700 | Juli 2016

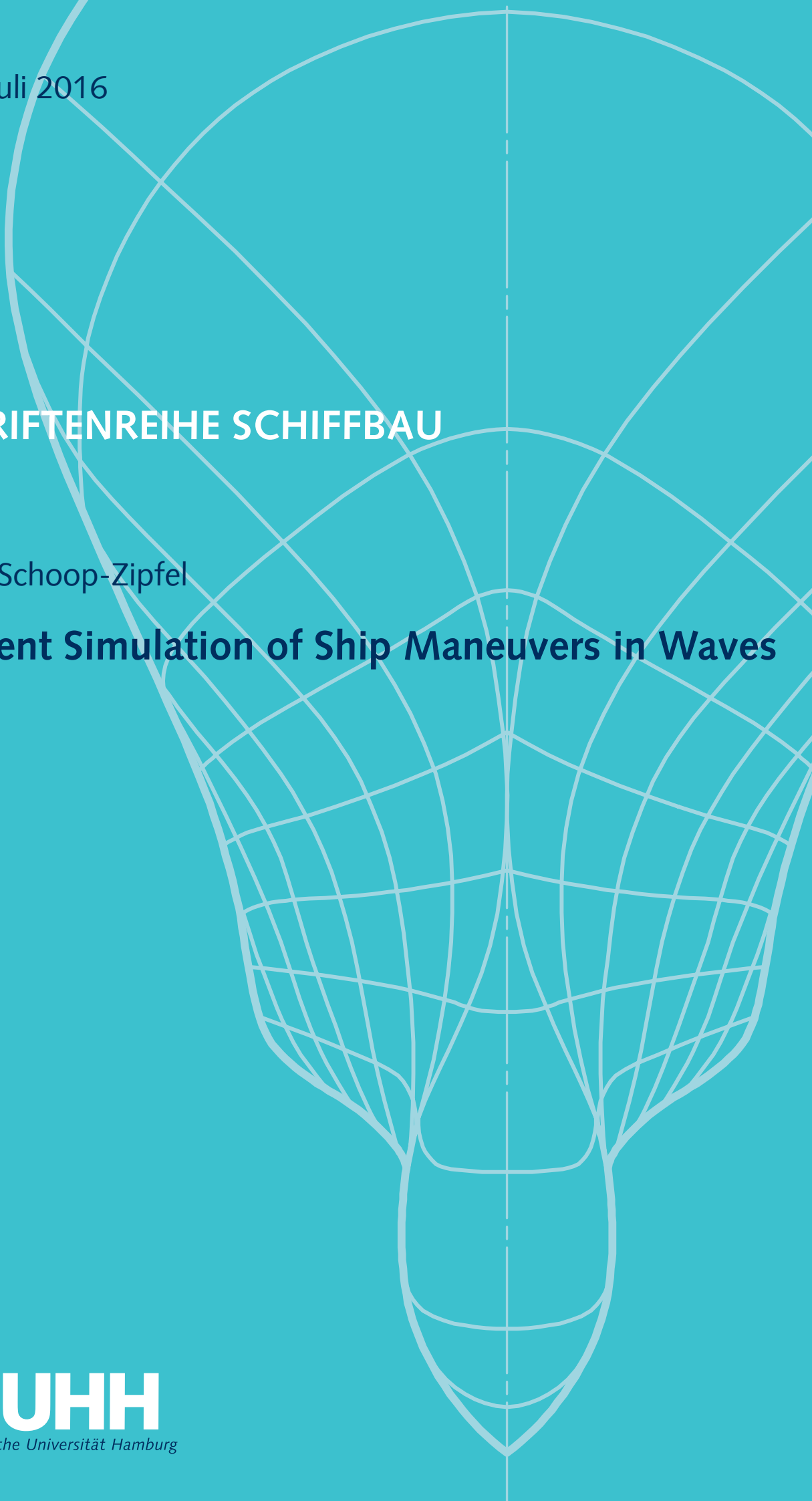

SCHRIFTENREIHE SCHIFFBAU

Karl J. Schoop-Zipfel

Efficient Simulation of Ship Maneuvers in Waves

TUHH
Technische Universität Hamburg

Efficient Simulation of Ship Maneuvers in Waves

Vom Promotionsausschuss der
Technischen Universität Hamburg-Harburg

zur Erlangung des akademischen Grades

Doktor-Ingenieur (Dr.-Ing.)

genehmigte Dissertation

von
Karl Jochen Schoop-Zipfel

aus
Hamburg

2016

Vorsitzender des Prüfungsausschusses:
Prof. Dr.-Ing. Edwin Kreuzer

Gutachter:
1. Gutachter: Prof. Dr.-Ing. Moustafa Abdel-Maksoud
2. Gutachter: Prof. Dr.-Ing. Stefan Krüger

Tag der mündlichen Prüfung:
15. Juli 2016

Schwarzenbergstraße 95C
D-21073 Hamburg
www.tuhh.de/vss

Bericht Nr. 700
ISBN 978-3-89220-700-9

Abstract

The description of ship motion dynamics is typically divided into two separate categories of inquiry: maneuvering in calm water and seakeeping at straight course. Combining both fields of investigation is not a trivial process because the hydrodynamic forces function differently. This thesis reports on the development of two numerical models to simulate the maneuvering motion of ships in waves. In order to simulate the motions, a precise description of the forces is necessary. In both approaches, the rudder forces are calculated with state-of-the-art procedures. For the propulsion, a numerical model is developed based on the propeller open-water diagram. An engine model is developed to determine the propeller rate of rotation for diesel-electric engines. A comparison with sea trial measurements reveals a very satisfactory representation of the propulsion and engine characteristics with the numerical model. The hydrodynamic forces acting on the hull are generally dependent on the motion frequency. Hence, the seakeeping motion is often solved in frequency domain. For the maneuvering case, the zero-frequency hydrodynamic forces are of interest. A two-time scale model is introduced that divides the basic motion equations into two groups - the zero-frequency maneuvering motion and the high-frequency wave-induced motion. Each group is solved separately and certain parameters are exchanged. Additionally, a unified theory is presented. This approach unifies both theories by extending the seakeeping theory. It is based on the impulse-response function, in which the retardation functions are built up for the entire motion frequency range and integrated during the time simulation over the elapsed time. The zero-frequency damping forces are incorporated into the retardation functions or added directly to the motion equations during time domain. They are calculated either with the slender-body theory or taken from the literature. A validation with experimental data from the literature is conducted with both methods. The simulated turning circles of the S-175 container ship and the KVLCC2 tanker in regular waves show satisfactory agreement with the measurements for both theories. Both methods capture the maneuvering motion in waves as well as the wave-induced motion during turning. Slight differences between the two models occur in the average track due to additional nonlinear effects in the unified theory. The simulated oscillatory wave-induced motion is very comparable between the two theories and shows reasonably well agreement with the measurements.

Acknowledgement

I would like to express my gratitude to my supervisor Prof. Dr.-Ing. Moustafa Abdel-Maksoud for his support, encouragement and many fruitful ideas and discussions throughout all stages of this research. I deeply appreciated the freedom and confidence that he provided me.

Additional thanks go to Prof. Dr.-Ing. Stefan Krüger and Prof. Dr.-Ing. Edwin Kreuzer for their work related to the examination process.

Special thanks go to my colleagues from the Institute for Fluid Dynamics and Ship Theory for creating an inspiring atmosphere on deck five. Especially I would like to thank my room mate Thierry Maquil for the numerous hours we spent together and the various on- and off-topic discussions.

In particular, I would like to thank my parents, Bernadette, Paula and Luise for their continuous support.

Contents

List of Figures

List of Tables

Nomenclature

The following notation is adopted throughout the thesis, unless otherwise explicitly stated. It is not exhaustive. Any other notation introduced will be defined when required.

General

- Vectors are denoted as boldface, lower-case letters
- Matrices are denoted as boldface, capital letters
- Time derivatives are marked by a dot, e.g. $\dot{f}$
- The dimensionless form is marked by a prime, e.g. Y'

Latin symbols

$\boldsymbol{a}$	Frequency-dependent sectional added mass matrix
$\boldsymbol{a}^0$	Sectional added mass matrix for zero-frequency
A_D	Advance of turning circle
A_R	Rudder area
$\boldsymbol{A}$	Frequency-dependent added mass matrix
$\boldsymbol{A}^0$	Added mass matrix for zero-frequency
$\overline{\boldsymbol{A}}$	Added mass matrix in time domain
B	Ship breadth
$\boldsymbol{B}$	Frequency-dependent damping matrix
c	Rudder chord length
C_B	Block coefficient of ship hull
C_D	Drag coefficient
c_{F0}	Skin friction resistance coefficient
C_M	Block coefficient of main frame

c_R	Residual resistance coefficient
c_{Th}	Propeller thrust loading coefficient
$\boldsymbol{C}$	Restoring matrix
$\boldsymbol{C}_A^*$	Linearized Coriolis and centripetal force matrix due to added mass
d	Sectional ship draft
D_P	Propeller diameter
dt	Time step size
D_T	Tactical diameter of turning circle
e	Mean distance between the leading edge of the rudder and the aft and of the hull
$\overline{f_x}$	Longitudinal mean wave drift force
$\overline{f_y}$	Transverse mean wave drift force
F_n	Froude number
$\boldsymbol{f}$	Force vector
$\boldsymbol{f}_e$	Wave excitation force vector
$\boldsymbol{f}_{e,A}$	Wave excitation force amplitude vector
g	Gravity
$\overline{GM}$	Transverse metacentric height
h_R	Rudder helm rate
H_D	Drifting distance
H_R	Rudder height
I	Moment of inertia
i_{xx}	Inertia radius around the x-axis
i_{yy}	Inertia radius around the y-axis
i_{zz}	Inertia radius around the z-axis
$\boldsymbol{I}$	Rigid-body inertia tensor
J	Propeller advance coefficient
k	Wave number
k_T	Thrust coefficient
$\boldsymbol{K}$	Matrix of retardation functions
L_{OA}	Ship length over all
L_{PP}	Ship length between perpendiculars
m	Rigid-body mass
$\overline{m_z}$	Mean wave drift yaw moment
$\boldsymbol{m}$	Moment vector
$\boldsymbol{M}$	Rigid-body mass matrix
n	Propeller rate of rotation
N	Hydrodynamic yaw moment in maneuvering
R_{F0}	Skin friction resistance
R_n	Reynolds number

R_R	Residual resistance
S_W	Wetted hull surface
$\boldsymbol{S}$	Rotation matrix
t	Thrust deduction factor
T	Ship draft
T_P	Propeller thrust
u	Ship velocity in longitudinal direction
U	Absolute ship velocity
u_A	Propeller speed of advance
$\boldsymbol{u}$	Absolute ship velocity vector
v	Ship velocity in transverse direction
w_p	Wake fraction
X	x-component of hydrodynamic force in maneuvering
x_G	x-component of the rigid body's center of gravity
x_m	x-component of the position where the flow presumably separates
Y	y-component of hydrodynamic force in maneuvering
y_G	y-component of the rigid body's center of gravity
z_D	z-component of the point of attack of the drag force
z_G	z-component of the rigid body's center of gravity

Greek symbols

β	Drift angle
δ	Rudder angle
ϵ	Wave excitation force phase angle
ζ_A	Wave amplitude
η	Wave angle relative to the Earth-fixed frame
$\boldsymbol{\eta}$	Position and rotational orientation vector in spatial frame
λ	Wave length
Λ	Rudder aspect ratio
μ_D	Drifting direction
$\boldsymbol{\nu}$	Linear and angular velocity vector in body-fixed frame
$\boldsymbol{\xi}$	Position vector in seakeeping frame
ρ	Mass density of fluid (water)
χ	Wave encounter angle
ψ	Ship heading angle
ψ_{OS1}	First overshoot angle
ψ_{OS2}	Second overshoot angle

ω	Motion frequency
ω_0	Wave frequency
ω_e	Frequency of encounter
$\boldsymbol{\omega}$	Angular velocity vector

Abbreviations

3DOF	Three degrees of freedom
4DOF	Four degrees of freedom
6DOF	Six degrees of freedom
CFD	Computational fluid dynamics
CPP	Controllable-pitch propeller
EEDI	Energy Efficiency Design Index
FFT	Fast Fourier transform
HSVA	The Hamburg Ship Model Basin
IACS	International Association of Classification Societies
IMO	International Maritime Organization
ITTC	International Towing Tank Conference
LF	Low-frequency
MEPC	Marine Environment Protection Committee
MMG	Maneuvering Modeling Group
MOERI	Maritime & Ocean Engineering Research Institute, South Korea
PMM	Planar-Motion Mechanism
RANS	Reynolds-averaged Navier-Stokes
RAO	Response amplitude operator
WF	Wave-frequency

1 Introduction and State of the Art

Figure 1.1.: Illustration of maneuvering in waves; source: www.crships.org and www.sintef.no

1.1 Background and motivation

Ship motion dynamics are typically divided into two fields of study: maneuvering in calm water and seakeeping at straight course. This division appears reasonable. The classical maneuvering regards course changes, turning, stopping, etc. These operations are generally performed in calm water environments. Seakeeping, in contrast, is associated with straight motion in a seaway. During voyages overseas the ship keeps its course and its speed mainly constant. Both fields are well developed and accurate models exist to simulate the motion of the ship in each.

In regards to ship safety, however, the maneuvering behavior of a ship in waves takes on special meaning. Waves may substantially influence the hydrodynamic forces and thereby change the maneuvering behavior, and vice versa.

Since the Energy Efficiency Design Index (EEDI) has come into effect, serious concerns regarding the maneuverability of ships in waves have been brought to the forefront. In 2012 the Marine Environment Protection Committee (MEPC) of the International Maritime Organization (IMO) passed the EEDI, which stipulates a limit for the specific CO_2-emissions of ships. If the ship marginally passes the relevant EEDI criterion, it is questionable whether the propulsion power and the steering devices are sufficient to maintain the maneuverability of the ship in adverse conditions and, subsequently, the safety of the ship.

To avoid negative effects on safety, such as under-powered ships, the International Association of Classification Societies (IACS) has proposed to add a provision to regulation 21 in chapter 4 of the MARPOL Annex VI text: *"For each ship to which this regulation applies, the installed propulsion power shall not be less than the propulsion power needed to maintain the maneuverability of the ship under adverse conditions as defined in the guidelines to be developed by the Organization."* However, standard maneuvers that demonstrate the capability of maneuvering in adverse conditions are not existent; adverse conditions are not defined; model tests are possible but not practical for routine ship design purposes; and the existing numerical simulation tools are not sophisticated enough for routine ship design purposes as reported by the Manoeuvring Committee at the 25th International Towing Tank Conference (ITTC) [52]. This clearly demonstrates the need for extensive research in this field.

Investigations on ship safety in waves are mainly based on statistical evaluations. To conduct statistical analyses a large amount of calculations is needed, so that short computational times for the individual computations are inherent. This, in turn, yields the necessity for developing bespoke mathematical models for the description of maneuvering motion in waves.

Combining the mathematical models for maneuvering and for seakeeping is not a trivial process due to the very different nature of the hydrodynamic forces. The forces due to maneuvering motion are dominated by viscosity. The fluid actions in maneuvering are expressed in terms of slow motion derivatives. Viscous forces, on the other hand, play only a minor role in seakeeping. Seakeeping performance can be sufficiently calculated with potential theory. The fluid actions during seakeeping are expressed in terms of frequency-dependent hydrodynamic coefficients. A unifying theory that describes the maneuvering of a ship in waves must combine the traditional theory of seakeeping associated with a vessel travelling along a prescribed course in waves and the theory of ship maneuvering in calm water. Such a model needs to describe the ship motions accurately for different speeds, sea states and operations.

A further application of the mathematical models can be the use in real-time training simulators. These simulators are often used to facilitate the training of ship masters and navigation officers. The mathematical models need to simulate in real-time or even faster while retaining a high accuracy.

Developing a numerical model for simulating the maneuvering in waves incorporates multiple

disciplines within ship hydrodynamics, including resistance, propulsion, calm water maneuvering, and seakeeping. It is necessary to find a balance between the accuracy of each module in the analysis and the computational effort.

1.2 Review on previous work

Before giving a review on the combined maneuvering and seakeeping methods, an overview on each field is given separately. In this work, the maneuvering motion is regarded in more detail than the seakeeping motion. Also, the review on previous work in maneuvering is more extensive, while the section on seakeeping is given in a brief and succinct overview.

1.2.1 Maneuvering simulation models

According to the Manoeuvring Committee of the ITTC [1], a maneuvering simulation model can be used for different purposes. They distinguish between:

- Models to predict ship maneuverability; needed at the design stage to ensure that a ship has acceptable maneuvering behavior.
- Models to use in simulators; used for the training of navigation officers or for the investigation of specific ships operating in specific harbors or channels.

The acceptable ship maneuvering characteristics are stated in the IMO maneuvering regulations [50] and possibly in specific contract requirements between a ship yard and a ship owner. They are mostly quantified by global parameters such as the overshoot angles in zig-zag maneuvers or the tactical diameter in a turning circle maneuver.

In order to develop ship maneuvering simulators, it is necessary to use mathematical models capable of calculating ship motion with a high degree of accuracy and in real-time. Most of the mathematical models need to be adjusted by human experience to obtain the required accuracy.

Simulation models for maneuvering motion are typically based on Newton's second law, i.e. the rate of change of the momentum of a body is equal to the resultant force acting on the body and is in the same direction. The mass properties of the vessel are generally well known. It is therefore important to have a correct description of the forces to accurately determine the motion. The forces are mainly due to hydrodynamics and include effects of the flow on the hull, the steering devices and the propulsors. The accuracy of the various forces and moments greatly influences the accuracy of the simulations.

The Manoeuvring Committee of the ITTC [1] distinguishes between various sources for estimating the hydrodynamic forces and moments:

- databases,
- regression equations from database,
- captive model tests,
- free model tests with system identification,
- full scale trials with system identification,
- calculation of forces resulting from prescribed kinematics within computational fluid dynamics (CFD),
- on-line application of CFD during simulation.

The hydrodynamic forces acting on the ship can be represented mathematically in many forms. Typically, the forces are described with hydrodynamic derivatives, look-up tables for the forces, algebraic equations or direct simulation [1]. Each mathematical model must be able to reproduce the original data with sufficient accuracy.

The first workshop on verification and validation of ship maneuvering simulation methods (SIMMAN) was held in 2008 [99]. Its purpose was to benchmark prediction capabilities of different ship maneuvering simulation methods and to clarify the accuracy of each method. However, Stern et al. [100] have summarized that the workshop highlighted many questions regarding the reliability of the procedures and the experimental data. There are a large number and variety of methods capable of predicting standard maneuvers, but their results were surprisingly scattered, as the workshop made apparent. For models based on captive model test data, it is essential that there is consistency between the model test program and the applied mathematical model. Extrapolation outside the range of the model test data should be avoided. Methods to predict maneuvers are not applicable outside the combination of motion parameters where the mathematical model is created. Furthermore, it is clearly demonstrated that e.g. a database consisting only of full form tankers cannot be used to predict forces on a container ship. The adequacy of a database for a given vessel can be assessed by comparing appropriate parameters such as T/L, B/T, c_B, approach speed, etc.

The SIMMAN 2008 workshop clearly demonstrates the large differences in performance between models with four degrees of freedom (4DOF) and three degrees of freedom (3DOF) for ships with low GM and higher speeds, implying that it is important to include roll into the simulations.

The most important differences between ship and model with respect to the scale effect are:

- The larger wake at the rudder in model scale reduces rudder effectivity.
- The larger propeller load in model scale increases slip stream velocity and thereby rudder effectivity.

- The resistance forces due to separation in an oblique flow depend on the Reynolds number, which is smaller in model scale than in real scale.

The forces can be divided into forces acting on the hull, the rudder and the propeller. However, interaction effects play an important role. The following sections discuss each point separately while keeping the interactions in mind.

Hull forces

There are many publications on experimental or theoretical work for determining the hydrodynamic forces and moments on the hull due to sway and yaw motions, which are the predominant motions in maneuvering.

Chislett and Strøm-Tejsen [18] have shown that it is possible to determine the hydrodynamic derivatives with captive model tests using a Planar-Motion Mechanism (PMM). The PMM device is mounted to the towing carriage and oscillates the ship model in transverse direction while it is towed with a constant speed in longitudinal direction. The measured forces can subsequently be fitted to polynomials to be available for maneuvering simulations. Maneuvering simulations based on these model test results confirm a satisfactory agreement with full scale measurements. The PMM has since become the standard in ship model testing.

In 1981 Wolff [118] used the computerized planar motion carriage (CPMC) (Oltmann [80]) at the Hamburg Ship Model Basin (HSVA) to investigate the maneuvering behavior of five ship models representing various ship types. The hydrodynamic derivatives are determined using force measurements on captive models. Maneuvering simulations with the gained derivatives show satisfactory agreement with free running models.

Computations of hull forces have been largely based on slender-body theories. Söding has shown the possibility of simulating maneuvering motion based on the slender-body theory ([104] and [105]). According to the slender-body theory, the water accelerated by a drifting or yawing ship induces a force per length acting on the hull. The cross-force per unit length is equal to the substantial time derivative of the cross-momentum, which is due to the added mass per unit length times the relative velocity in cross-direction. Söding has introduced some correction factors to account for the finite slenderness and for three-dimensional effects. Furthermore, viscosity is considered in the form of empirical corrections. Krüger [62] has used the body force model developed by Söding to simulate different standard maneuvers and compares these with sea trial measurements. His simulations show the principle validity of the force model. When the input parameters are properly known, simulation of the maneuvers is possible with acceptable accuracy for practical application. However, the calculations need a lot of assumptions, and according to Krüger [62], it is likely that good results are only achieved because many errors cancel each other. Subsequently, Krüger [62] suggests different

expansions of his work: for a satisfactory determination of the hull forces, potential theory might not be feasible and viscous methods or model tests should be conducted; the control mode of the main engine significantly influences the maneuvers and has to be respected by dynamic simulations; the actual thrust during sea trials is not known but has a major influence on the maneuvering behavior. Further investigations of the flow phenomena behind the ship are necessary. A recent publication by Krüger [63] shows that the results of maneuvering prediction based on the slender-body theory can be satisfactory when these deficiencies are considered in more detail.

Lin et al. [70] use the so-called blocking theory to calculate the hydrodynamic forces acting on a ship hull and rudder which is based on potential theory. The pressure loss due to flow separation is obtained in this theory by integrating the pressure only over the effect area. The pressure on the ship's surface can in a real fluid be written as p'_s. In a potential flow the pressure increases due to the absence of viscosity and turbulence to p_s so that $p'_s < p_s$. This is due to the separation. The total pressure force on the ship can be calculated with the area of the surface A_r:

$$\int_{A_r} \boldsymbol{n} p'_s ds \ . \tag{1.1}$$

When using potential theory, p_s is calculated instead of p'_s. Then the object surface area can be reduced from A_r to $A_r - A_e$ in order to obtain the total pressure force correctly. The total pressure force acting on the ship becomes

$$\int_{A_r - A_e} \boldsymbol{n} p_s ds \approx \int_{A_r} \boldsymbol{n} p'_s ds \tag{1.2}$$

with

$$A_e = L_{object} W_{block} \ . \tag{1.3}$$

W_{block} follows to

$$\begin{aligned} W_{block} &= c_1(\theta_m \omega)[1 + a_1(\theta_m \omega)^2 + a_2(\theta_m \omega)^4 + a_3(\theta_m \omega)^6 + ...] \\ &= \sum_{k=0}^{K} c_{2k+1}(\theta_m \omega)^{2k+1} \ , \end{aligned} \tag{1.4}$$

where c_i are constants and K is the truncation order as defined by Lin and Kuang [71]. The method is applied to simulate ship steering maneuvers. The results of the steering and the associated roll motions agree reasonably well with experimental data.

For the simulation of resistance tests, i.e. a ship moving with constant speed in calm water, CFD has become standard (e.g. Greve et al. [36]). Significant progress has been made by applying Reynolds-averaged Navier-Stokes (RANS)-based CFD codes. Recently, RANS based methods have also shown to be promising for computing complex hydrodynamic forces

for steady and unsteady maneuvers. The CFD simulations provide an insight into the entire flow structure around the hull, and the simulation results can be used to compute the forces and moments acting on the hull and to determine hydrodynamic derivatives. El Moctar [26] applies a RANS method to compute a cargo ship and a tanker in steady drift and steady turning. It focuses on the influence of draft and heel on hull forces. The ruder is modelled geometrically and the propeller by body forces, while free-surface and dynamic trim and sinkage are neglected. The acting forces can be determined with high accuracy and the simulations provide a profound insight into the flow details. Cura Hochbaum [21], [22] shows the possibility of replacing entire captive towing tank tests with simulations using a viscous RANS solver. Common maneuvering derivatives can be determined from virtual CPMC tests simulated with RANS with enough accuracy to get the required information about the maneuverability of a vessel. Similar investigations are conducted by Manzke et al. [72] and by Schoop-Zipfel and Abdel-Maksoud [93], who also apply RANS to determine the hydrodynamic derivatives. The hydrodynamic derivatives are then used to simulate standard maneuvers. A comparison of the simulated maneuvers with free-running model tests shows a satisfactory agreement. The computational effort is, however, still extremely high and determining all necessary derivatives requires an enormous amount of computational time. In these simulations the propeller can either be modelled directly, or its effect is regarded with a propeller model, modelling the body forces as source term in the impulse equation (Berger et al. [11], Wöckner et al. [119]). The results in the literature show that the interactions between hull, propeller and rudder have an important influence on the ship's track.

CFD methods were investigated and compared at the SIMMAN 2008 workshop [99], and as an outcome, finer grids, more advanced propeller and turbulence models, and additional verification and validation were suggested for the improvement of CFD-based methods (Stern et al. [100]). Finer grids should especially be used at the rudder, the appendages and at large vorticity regions, and verification and validation should follow the procedures proposed by Stern et al. [101]. Moreover, free surface capturing methods can be helpful to improve the accuracy of the results. To obtain the maneuvering derivatives from the force trajectories, multiple-run CFD/EFD curve fitting methods generally provide better results than single-run methods. It is stated that the best test of applicability is a comparison of actual maneuvers against free running model test data.

Rudder forces

The rudder, as one of the main steering devices, has a strong impact on the maneuvering behavior. Determining the rudder forces precisely is therefore of great importance.

Söding [106] has derived formulae from experiments and potential flow theory. These formulae are only valid below stall angle and do not consider specific rudder shape, profile thickness or Reynolds number. However, El Moctar [25] has confirmed with viscous flow computations that these formulae give a good agreement in the valid regimes for NACA 0015 profiles.

The propeller slipstream exerts considerable influence on the rudder forces. A panel method developed by Söding [108] computes rudder lift and drag with good accuracy. However, all potential flow methods are incapable of determining stall and thus the maximum lift. This is of special importance for yaw-checking when the angle of attack at the rudder becomes maximal [108].

Rudder flows feature high Reynolds numbers and are fully turbulent. Therefore, RANS computations should give better estimates than potential flow codes. El Moctar [26] has presented RANS simulations for a rudder and propeller interacting. The effect of the ship hull is not included. The numerical simulations show that the rudder lift forces increase by a factor of 2.3 in the propeller slipstream.

In most CFD simulations the propeller effect is simply modelled by body forces in RANS codes. The propeller forces are circumferentially averaged. El Moctar [26] has investigated the effect of simplified propeller modelling on rudder forces. In general, the computed rudder forces are increased by 10% when using body forces. This mainly results from the neglected hub. If considering the hub in the body force model, the deviation can be decreased to 4%.

Propeller

To determine the propeller forces, numerical methods based on potential theory can be used. These have much shorter computational times compared with RANS methods (see e.g. Lan [66] and Abdel-Maksoud et al. [3]).

However, the popularity of using viscous RANS methods to determine propeller flows is due to its increased computational power (Berchiche [10]). This can be especially beneficial when regarding all four quadrants of the propeller motion. Potential theory cannot capture the separation effects occuring for large angles of attack. The empirical models used in potential theory are mainly valid in the standard operating condition.

To determine the interaction of hull, propeller and rudder, it is still beneficial to simplify the propeller in order to save computational costs. Phillips et al. [83] couple a propeller model in the blade element momentum theory (BEMT) with the solution of the RANS equations.

The maneuvering derivatives of a self-propeller ship at straight ahead motion, at a drift angle and for different rudder angles can be determined with this approach. The computational uncertainty is reported to be typically 2-3% for the side force and the yaw moment. The approach allows for capturing the interaction effects between hull, propeller and rudder.

In reality, propeller blades always operate in oblique flow due to the aftbody shape, ship motions in maneuvering and seakeeping, etc. El Moctar [26] concludes in his investigations on oblique flow that the mean thrust and torque coefficients increase with increasing angle of attack. The Reynolds number effect on thrust and eccentricity is rather small. Similar results are reported by Vorhölter [116]. He shows that the wake fraction significantly influences the maneuvering behavior. The flow situation is very complex, so CFD computations are needed to determine the wake fraction sufficiently.

RANS methods can be applied to determine the interaction of the hull and the propeller. Examples can be found in Jensen et al. [56] and Xing-Kaeding [120], where steady and unsteady maneuvers are simulated.

Engine characteristics

Simulating maneuvers requires that the dynamic behaviors of the prime mover and the automatic control of the propulsion system are taken into account (Krüger [62]). When regarding maneuvering in waves, it is important to note that engine behavior may have a considerable influence on the motion of the ship.

Mathematical models for simulating the engine, the automation of controllable pitch propellers (CPP) and the engine control have been presented by different authors. Some focus on the behavior of the engine and others investigate the interaction of the engine and the maneuvering behavior of the ship.

Hanouneh [42] simulates crash stop maneuvers for ships with fixed-pitch propellers (FPPs). He develops a detailed model for the diesel engine, which is based on a cyclic process. Eyberg [27] concentrates on the automation of CPPs and the engine. Both studies drastically simplify hydrodynamic aspects. Zheng [128] develops a numerical model to describe the behavior of CPPs during crash stop maneuvers, but does not use a controller for the propeller pitch. Benvenuto [9] presents a detailed engine model for maneuver simulation of ships with CPPs and FPPs. He mainly investigates crash stop and turning circle maneuvers. The simulations are carried out based on a coefficient model. The propeller-hull interaction parameters are not taken into account during the simulation of the crash stop maneuvers.

Haack [39] develops an engine model for dynamic simulations during maneuvering motion. The maneuvering model is based on the work of Krüger [62]. With the models it is possible to simulate the total system for arbitrary maneuvers and for numerous system configurations.

Modelling of hydrodynamic forces

One of the most common concepts used to describe the hydrodynamic forces acting on a maneuvering ship has been proposed by Abkowitz [4]. According to this concept, the forces acting on a ship depend, at any instant, on the ship velocities and accelerations at that instant but not on their history, i.e. higher time derivatives. There are a few works that raise concerns over this assumption of quasi-stationarity; e.g. Newman [74] shows that memory effects due to separation, free-surface wave motions and the non-analytic dependence of the nonlinear forces on drift angle require a more complicated mathematical model for the force and moment. According to his work, history should not be neglected. These history effects could be taken into account by impulse-response functions. Bishop et al. [13] develop an unique formulation of the fluid forces and moments acting on a ship in terms of Volterra series. With this formulation the assumption of quasi-stationarity is relaxed. Burcher [17] and Nomoto [78] show that the history effects play a minor role in the steered motions of a ship in calm water. Regarding the practical use of the model test results, the history effects are rather unimportant for simulating realistic maneuvers. They arise due to the small motion amplitudes in combination with unrealistic high motion frequencies during the tests. Nomoto shows with a numerical example that the hydrodynamic derivatives at zero frequency can be used to get the ship response. Nevertheless, the fluid forces acting on a ship have significant time history effects. So care has to be taken in experiments and their analyses to avoid problems arising from the more complex nature of the forces. When doing so, higher frequency components play only a slight role and can be neglected.

1.2.2 Seakeeping simulation methods

According to the Seakeeping Committee of the ITTC [55], sea trials are believed to provide the most reliable and realistic data with respect to ship behavior in various environments. However, there are uncertainties that need to be considered when examining the results. As an example, the lack of control over the ocean environment creates uncertainties in defining the sea parameter.

For the computational determination of the motion behavior of ships in waves, the fluid dynamic loads have to be determined. This can be done either in frequency domain or in time domain.

Frequency-domain approaches

The Seakeeping Committee of the ITTC [55] states that frequency-domain approaches provide a quick but accurate solution. Frequency-domain solutions are typically used in the early stages of ship design. The frequency-based solution is advantageous in evaluating hydrodynamic and structural concerns involving natural frequency and modal problems. For multi-body problems, the frequency domain provides a much less intensive approach to assess interactions.

Time-domain approaches

Time-domain approaches solve the motions of the ship as a time-evolving process. They can be extended to the analysis of nonlinear motion and can be coupled with external or internal forces. Time-domain formulations for seakeeping problems have been introduced by some pioneering researchers, such as Cummins [20] and Liapsis and Beck [69]. An overview on different time-domain approaches given by the Seakeeping Committee of the ITTC can be found in Table 1.1.

Wave drift forces

Wave drift forces are the time-averaged wave forces acting on a body. They are approximately proportional to the square of the wave amplitude. In contrast with the short-time scale first-order wave loads, whose mean value over the wave period is zero, the mean second-order wave loads are able to produce a long-term steady wave effect. It is often believed that these forces play the major role for maneuvering in waves concerning the wave loads (Artyszuk [5]).

According to Clauss et al. [19], there are basically two methods for determining wave drift forces. One determines the velocity potential and integrates it over a control surface that is far away from the body. It is based on the asymptotic behavior of the potential ad infinitum. The calculations are mainly conducted for a monochromatic wave field, i.e. smooth Airy waves of constant period. The other method integrates the pressure up to the second order over the wetted surface of the body. The choice of a method depends on the wave characteristics, the Froude number and the slenderness of the ship hull.

Early known work on hydrodynamic drift forces and moments on a single body is from Maruo [73]. He has developed a three-dimensional far-field method that can determine the wave drift forces on a ship with zero forward speed in the horizontal plane. Newman [75] has used the fluid momentum conservation and the slender-body theory to derive the mean drift forces and moment. The work of Newman has been extended by Salvesen [87], whereby he establishes a hull pressure/integration method. However, Skejic [96] reports that the method seems to give

Table 1.1.: Time-domain approaches for seakeeping according to the ITTC [55]

Numerical method	**Advantage**	**Disadvantage**	**CPU capacity and time**
Impulse-response-function	Easy to implement Fast computation Requires small computer memory	Need pre-computed hydrodynamic coefficients Limited applicability	Minimal
Strip/sectional-based	2D BVP Fast computation Requires small computer memory	Limitation as 2D sectional method Poor accuracy in low frequency	Minimal
Transient wave Green function	Radiation condition automatically satisfied Panel distribution only on body surface	Hard to compute Green function for non-zero speed Limited application	Moderate
Rankine panel method	Good practicality Easy extension to nonlinear analysis Good overall accuracy	Difficulty in 3D geometric modelling and panel generation Needs a numerical method for radiation condition	Moderate
CFD method solving field equations	Capability for violent ship motion Can include viscous effects	Huge computational time and effort Poor accuracy in memory flow	Heavy
Hybrid method combining two methods	Taking advantage of combined method	No benefits in many combinations Additional effort for combinations	(Varying)

inadequate estimates of the mean wave loads when the ship is not slender enough. A three-dimensional near-field direct pressure integration method is applied by Pinkster [84]. Here the mean drift loads are obtained by integrating the pressure distribution on the instantaneous wetted hull surface. A direct pressure integration method for bodies with forward speed is developed by Faltinsen et al. [30]. Boese [15] proposes a simple method to estimate the added resistance in waves. First, the pressure is integrated up to the still water line. Under the assumption that the harmonic pressure variations are known on the hull, the longitudinal forces and the added resistance can be determined. Furthermore, the wetted water line oscillates around the still water line. This generates more components that need to be taken into account. Both components yield an average longitudinal force of second order. Söding and Bertram [111] extend the work of Boese [15] to also determine drift forces in transverse direction and the mean yaw moment. Several details are modified and the stationary pressure term in Bernoulli's equation is taken into account. When the wave lengths are small compared to the ship length, all mentioned theories are not applicable since the main contribution to the mean wave loads comes from the reflection of the incident waves by the ship. Faltinsen et al. [30] propose the asymptotic theory, which is applicable in cases when the ship experiences regular waves with short wave lengths.

1.2.3 Combination of maneuvering and seakeeping models

Maneuvering motion in a seaway has been a topic of discussion within the last years. Different approaches can be found in the literature for combining these two fields of hydrodynamics. The Maneuvering Committee of the ITTC [54] classifies the different approaches as:

- experimental methods,
- methods based on two-time scale models,
- methods based on unified theory,
- other simulation methods,
- methods using CFD.

The experimental methods use model tests to investigate the maneuvering behavior in waves. These tests investigate either the acting forces on restrained models or measure the trajectories of free-running models in different wave states. For the former case, the wave drift forces are of major interest. For the latter case, arbitrary combinations of wave lengths, heights and even wave spectra with maneuvering parameters, such as rudder angle control, initial heading, final heading, etc., can be assumed. Since it is not clear in advance which are the crucial cases, a very high number of different tests is necessary for a proper investigation.

Methods based on two-time scale models divide the combined maneuvering and seakeeping problem into the low-frequency maneuvering motion and the high-frequency motion due to the wave encounter frequency. Each problem is solved separately and the necessary information is transferred to the other problem. The drawback of this method is that the linear effects of the waves are only by means of an oscillatory displacement from the low-frequency ship motion. Critical situations that arise due to the first-order wave forces are hard to capture with these kinds of models.

From a physical point-of-view, wave loads should be modelled as forces acting on the ship through Newton's second law (Fossen [32]). This is done in unified methods. Unified methods try to unify both problems in one theory. Mainly, the impulse-response function is used to transform the frequency-domain coefficients to time domain. The low-frequency maneuvering parameters are brought into the coefficients by ramp functions. A closed set of equations can be derived in this way. Accurate retardation functions are needed to obtain reliable results. Their accuracy very much depends on the asymptotic behavior of the frequency-dependent added mass and damping coefficients (Skejic and Faltinsen [97]). Forward speed effects further complicate the evaluation of the retardation functions. Also, a high computational time is needed to solve the impulse-response functions due to the time integral over all past effects.

CFD can be used to solve the total fluid problem directly and it further provides a deep insight into complex flow phenomena. Due to the high computational costs, however, it is not feasible for a high amount of computations, and the same problem for model tests also arises. Moreover, much experience and a high degree of expert knowledge is needed for modelling the waves, especially those of short wave lengths. Numerical diffusion might play a significant role.

Below, the different approaches as classified by the ITTC are recapitulated and a review on previous work is given.

Experimental methods

Lee et al. [68] measure the forces and moment acting on the KVLCC (a very large crude-oil carrier designed at Maritime & Ocean Engineering Research Institute, South Korea (MOERI)) at various wave lengths and amplitudes. The experiments are carried out with two different wave amplitudes, various wave lengths and various wave encounter angles in order to study the influence of the wave amplitude as well as the influence of the wave length. The tests show that the first-order wave surge force becomes minimal when the wave incident angle is 90°, while the sway force is at a maximum. The first-order wave yaw moment is nearly zero at encounter angles of 0°, 90° and 180°. The magnitudes of the second-order forces are much smaller. Its surge force is nearly zero for an incident angle of 90°, while the magnitude of the sway force is at its maximum. The sway force is nearly zero for incident angles of 0° and 180°.

The yaw moment has its maximum at 70° and 110°. The results are, however, questionable for maneuvering ships. The tests are carried out at zero ship speed but this assumption is violated in real maneuvering motion and forward-speed effects may significantly change the wave drift forces.

Subsequent simulations by Lee et al. [68], which consider the measured forces and yaw moment, show that the wave drift forces have a strong effect on the trajectory of the ship. The simulations are conducted by solving the equations of motion in three degrees of freedom, while the forces comprise of the hull, propeller, rudder and wave force. In the simulations only the second-order forces are regarded for the wave effects. The first-order wave forces are supposed to cause high-frequency oscillations that are imposed upon the maneuvering kinematic data but keep their original average values for the calm water condition. The simulations show that the ship drifts towards the direction of the waves. This effect increases with increasing wave height. Similar results are found for 10°/10° and 20°/20° zig-zag maneuvers.

Xu et al. [121] perform towing tests with a PMM in still water and in waves. The model is towed with a small constant forward speed while a forced sway oscillation at low frequency is superimposed. During the test the forces and horizontal motions are measured and analyzed with Fourier analysis. Three force components can be observed in the fast Fourier transform (FFT) spectrum of the measured forces: at zero frequency, which is the wave drift force; at the low frequency of the sway oscillation; and at the wave encounter frequency. The significance of the wave-drift damping and the wave-drift added mass is examined by comparing them with the corresponding values in still water. It is found that the significance of the wave-drift damping is small; it is comparable with the damping measured in still water. For the wave-drift added mass, a value is found that is less than 10% of the value measured in still water. For further investigations, an improvement of the measurement accuracy is recommended by the authors.

Ueno et al. [114] conduct free-running model tests in regular waves using a VLCC model ship. They compare the measurement results in different wave length to ship length ratios and different encounter angles with measurement results in calm water. Straight runs, turning circles, zig-zag and stopping maneuvers are performed. The results can be summarized as the following:

Straight running

- Ship speed ratio U/U_0 becomes smallest in head wave condition for $\lambda/L = 1.0$ due to the large added resistance.
- For $\lambda/L = 0.4$ and 0.6 in beam, bow and quartering wave conditions, the speed loss is attributed to a combined effect of the added resistance due to reflected waves on the hull surface and oblique motion including rudder force.
- The oblique angle β and the counter rudder angle δ_C are large for short wave lengths, especially in beam wave condition due to the large wave drift force and moment compared with that of long waves.
- The ship bow tends to turn in the wave propagating direction for most cases.

Turning tests

- The drifting distance becomes large for short waves and the average ship speed ratio U_{ave}/U_0 shows larger values in 0.4 wave length ratio condition than in 1.0 wave length ratio.
- The drift direction is not necessarily the wave propagating direction.
- The average yaw rate r_{ave} shows a slightly decreasing tendency in the short wave region.

Zig-zag

- Overshoot angles in beam sea condition show large deviations from those in calm water condition.
- Overshoot angles are larger in following sea than in head sea.
- The wave effect is larger on the ship in full load condition than in ballast condition.

Stopping

- The waves reduce the track reach in head and in beam waves due to the added resistance in head waves and the wave reflection on the hull surface in beam waves.
- The final state heading angle is smaller in head and in beam waves due to the wave drift moment causing the ship to direct toward the wave propagating direction.

Yasukawa [122], [123] and Yasukawa and Nakayama [124] present experimental results of turning circles of the S-175 container ship in waves. The free-running tests are carried out with a model equiped with rudder, propeller and diverse measurement equipment. The propeller revolution in the tests is set to accomplish a Froude number of $Fn = 0.15$ in still water. In

the model tests, the carriage tracks the ship model automatically by using a speed control unit which receives feedback from the position signal from an optical position measuring equipment. The measured items are:

- all six degrees of ship motion at the center of gravity of the model,
- acceleration of vertical and horizontal motions of the bow,
- propeller revolution, propeller thrust and propeller torque,
- rudder angle, rudder normal force and rudder torque,
- ship position, ship speed and yaw rate.

For the turning motion, two encounter wave directions are investigated: namely, head waves and side waves in the initial condition. Four ratios between wave length and ship length for each wave direction are set $\lambda/L = 0.5$, 0.7, 1.0 and 1.2. The height ratio of the incident waves aims to be $H_W/L = 0.02$. The time to start the steering is the moment in which the incident wave bottom passes the midship of the model. The experimental data is compared with the results of a numerical method based on a two-time scale model that is described in the following section.

Two-time scale models

Two-time scale models basically divide the ship motions into slowly varying maneuvering motion and rapidly varying motion due to seakeeping effects. Each problem is solved separately and provides the relevant parameters to the other problem.

Skejic [96] and Skejic and Faltinsen [97] present a model to describe the maneuvering behavior of an advancing ship in regular deep water waves. The effect of the seakeeping on the maneuvering analysis is in terms of the slowly varying mean second-order wave loads. These account for the changing ship speed and wave heading. The more rapidly varying linear wave loads make the ship oscillate around a mean average value and do not change the ship's track. Skejic [96] and Skejic and Faltinsen [97] deduce from this to disregard the first-order wave loads in the time-domain simulation. The computational algorithm used by Skejic [96] and Skejic and Faltinsen [97] is sketched in figure 1.2.

Yasukawa and Nakayama [124] also assume the ship motion to be the sum of the maneuvering motion and the wave-induced motion, where each problem is solved separately. The method coincides with the time-domain strip method when a ship is assumed to move straight and with the maneuvering simulation method, the so-called MMG model, when the wave height is set to be zero. The six degrees of freedom (6DOF) motion of the ship in waves can be obtained from solving ten motion equations in total, i.e. four for the low-frequency maneuvering motion and six for the wave-induced motions. Additionally, the ship position, including the wave-induced

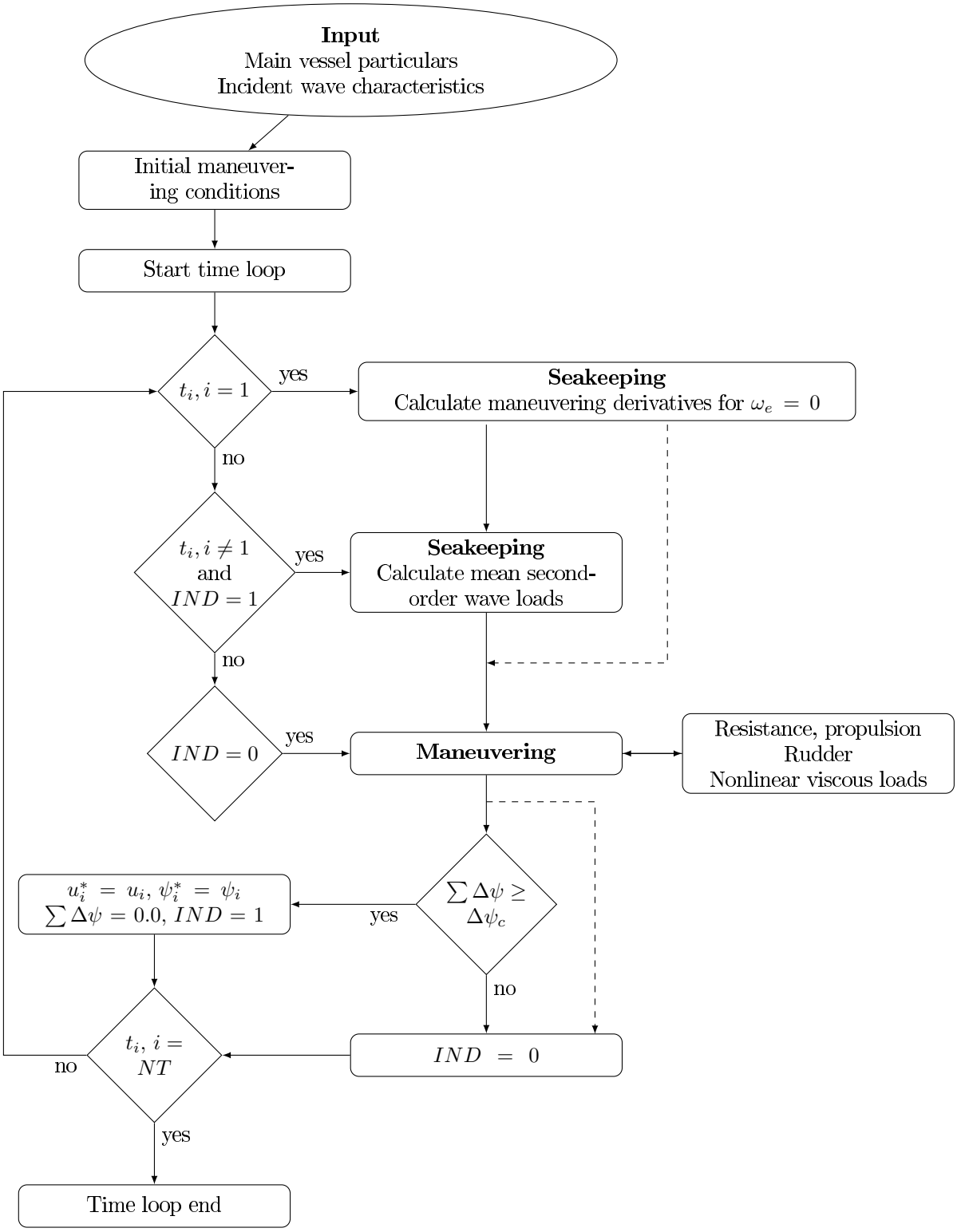

Figure 1.2.: Computational algorithm used by Skejic [96] and Skejic and Faltinsen [97]

motion component, is derived by adding the displacement from

$$\dot{X}_1 = (\dot{\xi}_1 + V_0\psi_1)\cos(\psi_0) - (\dot{\xi}_2 - U_0\psi_1)\sin(\psi_0) \tag{1.5}$$

$$\dot{X}_1 = (\dot{\xi}_1 + V_0\psi_1)\sin(\psi_0) + (\dot{\xi}_2 - U_0\psi_1)\cos(\psi_0) \tag{1.6}$$

$$\dot{Z}_1 = \dot{\xi}_3 \tag{1.7}$$

to the position from

$$\dot{X}_0 = U_0\cos(\psi_0) - V_0\sin(\psi_0) \tag{1.8}$$

$$\dot{X}_0 = U_0\sin(\psi_0) + V_0\cos(\psi_0)\ . \tag{1.9}$$

A comparison with experimental data shows that the method can simulate the general tendencies of the 6DOF motion during turning in regular waves.

Likewise, Seo and Kim [95] divide ship motions in waves into the linear wave-induced motion regarded as high-frequency motion and the maneuvering motion regarded as low-frequency motion. The two sets of equations are regarded separately while some coupling effects are considered: the seakeeping motion of the ship depends on the wave encounter angle and frequency, which are functions of the maneuvering motion and, on the other hand, the maneuvering motion is affected by the wave drift forces. The coupling is performed stepwise. First, the maneuvering module is applied to determine the velocity and the position of the ship in space-fixed coordinates. Velocity and position are used then to define the incident wave condition. Secondly, the boundary value problem in seakeeping is solved to obtain the ship motion response to the waves. Moreover, the second-order mean wave drift forces, the diffraction and the radiation forces are calculated in this step and transferred to the maneuvering module where they are used in the first stage of the next time step. Together with other maneuvering forces they are used to calculate the new ship velocity and position. This is continued until the end of the simulation. Due to the different time behavior of the seakeeping and the maneuvering module, different time step sizes need to be applied so that for the seakeeping problem multiple time steps are solved within one time step of the maneuvering motion. A flow chart of the computational algorithm can be found in Figure 1.3.

Since the two-time scale models divide the motion in maneuvering motion and seakeeping motion, the models used for each motion can be regarded and described separately. A description of the models used by the authors mentioned above is given below.

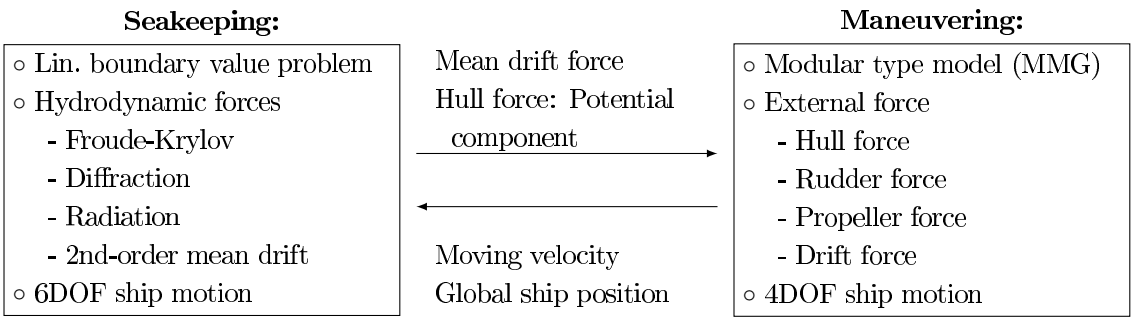

Figure 1.3.: Computational algorithm used by Seo and Kim [95]

Maneuvering The maneuvering motion is in all two-time scale models known considered as a 4DOF problem. The hydrodynamic forces in this low-frequency component are the sum of the hydrodynamic forces acting on the hull, the propeller, the rudder and the second-order mean wave drift forces. To solve this motion, the following set of equations can be applied:

$$\begin{aligned} m(\dot{u}_0 - v_0 r_0) &= X_H + X_P + X_R + X_W \\ m(\dot{v}_0 - u_0 r_0) &= Y_H + Y_P + Y_R + Y_W \\ I_{xx}\dot{p}_0 &= K_H + K_P + K_R + K_W \\ I_{zz}\dot{r}_0 &= N_H + N_P + N_R + N_W \end{aligned} \tag{1.10}$$

where the subscripts H, P and R denote the hydrodynamic forces on the ship hull, propeller and rudder, respectively. The subscript W denotes the second-order mean wave drift force which is obtained from the seakeeping analysis.

Skejic [96] and Skejic and Faltinsen [97] follow a modular approach. In this approach, the forces and moments due to the rudder, resistance, propulsion, and nonlinear viscous loads are described in separate modules. Söding's [104] slender-body theory is applied to determine the linear maneuvering derivatives. They are calculated with the two-dimensional added mass coefficients (a^0_{jk}) that are determined from the two-dimensional boundary value problem for zero encounter frequency $\omega_e = 0$. Strong nonlinearities occur during tight maneuvers so that nonlinear terms need to be applied in the equation of motion. They are obtained by applying a cross-flow drag model. However, it is difficult to establish an appropriate drag coefficient C_D. Within the rudder module the rudder-propeller-hull interactions are taken into account. The rudder forces and the interaction effects are calculated with semi-empirical formulae. The calm water resistance is calculated with the Holtrop-Mennen method [46]. In the propulsion module, an equilibrium between the calm water resistance and the propulsion is assumed in the case of the ship sailing straight at cruising speed without rudder helm and in calm water. The propulsion machinery is not modelled and the propeller rate of rotation is assumed to be constant. The thrust of the propeller is calculated with the thrust coefficient of an open-water

propeller.

Yasukawa and Nakayama [124] separate the added mass in zero frequency from the hydrodynamic forces of the maneuvering problem. So, the hull, propeller, rudder and wave forces include no acceleration effects. A further description of the hydrodynamic forces is only given in Japanese.

Seo and Kim [95] determine some parts of the hull force with potential theory while the other parts are obtained from empirical formulae or model tests. They split the hull force in the 4DOF maneuvering motion in the hydrodynamic force due to potential flow and viscous effects. The viscous effects that cannot be determined with potential theory are the hull lift force and additional viscous damping forces on the ship hull. Seo and Kim obtain the potential force directly by using their potential flow code WISH. The lift force is modelled as a lift force on an equivalent plate. Furthermore, nonlinear components are included with hydrodynamic derivatives based on the MMG approach. The forces of the propeller and rudder are calculated with empirical formulae.

Seakeeping To simulate the ship motion trajectories correctly it is necessary to accurately predict the wave drift forces.

Skejic [96] and Skejic and Faltinsen [97] have used different methods to compute the second-order mean wave drift forces. A comparison of the different methods is provided which shows a strong dependence of the results on the wave length. Subsequently, four different theories are applied to determine the wave drift forces in different wave lengths so that the entire wave length range of interest is covered. The ship's forward speed and the wave heading are taken into account within the models. For the maneuvering simulations in waves, the oscillatory wave-induced motion of first order is not considered.

Yasukawa and Nakayama [124] estimate the hydrodynamic forces for the high-frequency component based on the strip method. The wave exciting forces are expressed as the sum of Froude-Krylov and scattering force components. The added mass and wave damping coefficients are treated quasi-steadily for simplicity. Memory effects with respect to changing frequency of encounter are omitted. The method used to determine the wave drift forces is not further specified.

Seo and Kim [95] use potential theory to solve the wave-induced motion. The boundary value problem is linearized with the Neumann-Kelvin linearization method. The ship motion is simulated by solving the equation of motion:

$$\boldsymbol{M}\ddot{\boldsymbol{r}} = \boldsymbol{f}_{FK} + \boldsymbol{f}_{HD} + \boldsymbol{f}_{Res} \tag{1.11}$$

where $\boldsymbol{M}$ is the mass matrix of the ship and $\boldsymbol{f}_{FK}$, $\boldsymbol{f}_{HD}$, $\boldsymbol{f}_{Res}$ are the Froude-Krylov, hydro-

dynamic and restoring forces, respectively. $\boldsymbol{r}$ denotes the displacements of the wave-induced body motion in the body-fixed coordinate system. The seakeeping problem is solved with the time-domain Rankine panel method WISH, which uses a constant ship speed to solve the seakeeping behavior. It is extended to include lateral and rotational motions of the ship. The second-order mean wave drift forces are calculated with a near-field method that directly integrates the pressure over the body surface. The second-order boundary value problem does not need to be solved completely because only the linear solution is needed to calculate the the wave drift forces.

All two-time scale models demonstrate the importance of the wave influence on the maneuvering behavior of ships. The mean second-order wave drift forces as well as the yaw moment significantly change the motion trajectories of the maneuvering ship.

Methods based on unified theory

Maneuvering motion is classically described in a body-fixed frame of reference, while seakeeping analysis is performed in an equilibrium frame of reference. Bailey et al. [7] derive relations between the fluid actions defined for a maneuvering analysis using a body-fixed frame of reference and the fluid actions defined for a seakeeping analysis using an equilibrium frame of reference. A comparison of measured PMM data with data predicted by potential flow theory shows differences at low frequencies of oscillation. Bailey et al. introduce a linear viscous ramp to adjust the predicted damping data so that the values of the damping are equal at zero frequency. A much better agreement between the data sets over a wide range of frequencies is achieved in this way. Furthermore, the acceleration hydrodynamic coefficients are affected, so that they satisfy the transform relations. The equations of motion are set up either based on the maneuvering theory variables or on the seakeeping theory variables. The basic characteristics of maneuvering theory are retained by incorporating slow motion derivatives within the impulse-response functions and those of the seakeeping theory by including frequency hydrodynamic coefficients.

Fossen [32] derives a unified model using a state-space approach. The model is capable to describe ship maneuvering, station-keeping and control in waves. The relationship between frequency-dependent oscillatory derivatives, hydrodynamic derivatives and frequency-dependent hydrodynamic coefficients can be explained exemplarily with one degree of freedom, the sway motion:

$$[m + A_{22}(\omega)]\dot{v} + B_{22}(\omega)v = \tau_{2,FK+diff} + \tau_2 \tag{1.12}$$

The hydrodynamic added mass and damping coefficients are functions of the motion frequency. The frequency-dependent damping can be split into a potential part $B_{22p}(\omega)$ and a viscous

part $B_{22v}(\omega)$:

$$B_{22}(\omega) = B_{22p}(\omega) + B_{22v}(\omega) \tag{1.13}$$

The potential damping is zero when the motion frequency is zero ($B_{22p}(\omega = 0) = 0$). However, the viscous damping $B_{22v}(\omega)$ has a non-zero value for $\omega = 0$. This viscous damping is decaying with increasing ω and is modelled by Fossen as an exponentially decaying function:

$$B_{22v}(\omega) = \beta_{22} e^{-\alpha\omega} \tag{1.14}$$

A linear, potential flow strip theory formulation based on the theory of Salvesen et al. [88] is used to calculate the hydrodynamic forces in frequency domain. Impulse-response functions or state-space models are used then to transform the frequency-dependent equations to time domain. For the retardation function, an alternative representation is derived where the convolution integral is over $\mathbf{B}^*(\omega) - \mathbf{B}^*(\infty)$, since this term is zero at $\omega = \infty$. The nonlinear damping terms are found from PMM experiments. Wave drift forces and moments are not included in the simulation model. Furthermore, no results are presented for a ship under forward speed. The validity is subsequently not proven.

Yen et al. [126] develop and validate a method for the direct simulation of ship maneuvering in calm water and in waves, called LAMP (Large Amplitude Motion Program). The seakeeping and maneuvering models are formulated in the same framework of time-domain hydrodynamics and rigid-body dynamics. Forces due to viscous flow effects and other external forces such as hull lift, propulsors and rudders are modelled using other computation methods or with empirical or semi-empirical formulae and are added to the potential solution. The 6DOF forces and moments acting on the ship are computed in the time domain, including the following force components:

- wave-body hydrodynamic forces,
- hydrostatic and Froude-Krylov wave forces,
- hull lift,
- hull drag,
- additional viscous damping forces,
- other external forces due to control surfaces, propulsion systems, wind forces, etc.

Hydrodynamic forces are evaluated with an initial boundary value problem for a disturbance velocity potential. The effects of forward speed, radiation and diffraction are included in this. Nonlinear effects due to large amplitude motions and the coupling between diffraction and radiation are considered directly by satisfying the three-dimensional body boundary condition completely. Wave drift forces are determined with respect to the perturbation elevation at the hull waterline and are implemented for both body-linear and body-nonlinear wave-body

hydrodynamics. The hull is regarded as a low aspect ratio lifting surface to determine the lift force:

$$L_v = \frac{\rho}{2} C_v^{hull} |V_e|^2 T L_{pp} \tag{1.15}$$

$$L_r = \frac{\rho}{4} C_r^{hull} u r T L_{pp}^2 \tag{1.16}$$

C_v^{hull} and C_r^{hull} are similar to the linear hydrodynamic maneuvering derivatives Y_v' and Y_r'. These coefficients can be adjusted when forces and moments are available from external sources such as model tests or CFD calculations. The drag of the hull consists of lift-induced drag, viscous drag and wave drag. A validation is performed for maneuvering in calm water and for straight ahead motion in waves. The maneuvering results in calm water are comparable to results from systems-based methods. For the straight ahead motion in waves, the resulting motion amplitudes mostly follow the experimental data. The approach appears to be valid for at least ship maneuvering in moderate seas. For ship dynamic stability in severe seas, including extreme roll motions and capsizing, the authors state that it is necessary to investigate to what extent it is valid and applicable.

Methods using CFD

Greeley and Willemann [35] present procedures for and results of maneuvering force calculations in still water and in waves using lifting potential flow techniques. They follow the original Hess approach [43] for the formulation of the panel method. The nonlinear Kutta condition equations are solved together with the normal velocity equations, using repeated linearization of the nonlinear Kutta condition at each matrix iteration. For slender bodies, the trailing vorticity from the lifting surface trailing edges follow the body flow streamlines, which results in excellent agreement with experimental results. The potential flow is first calculated around the unappended hull and then this calculated body flow field is used to trace out the correct geometric positions of the trailing vortex wake from the keel. For full-form ships, attached flow is unlikely to occur and thus the applicability of potential flow techniques is questionable. However, according to Greeley and Willemann [35], for many hull forms, the separated flow is not due to gross smooth surface flow separation but rather to side-edge separation from a longitudinal geometric feature. In the case of bilge keels, Bollay's model [16] is used to determine the behavior of the shed vorticity near the bilge keels.

CFD methods using the RANS equations provide an adequate description of all physics. However, they are highly challenging from a computational point of view. Another problem is connected to difficulties in applying an appropriate turbulence model. This is especially difficult in the case of curvilinear motion of a surface displacement ship, since the flow around the ship's hull is strongly influenced by separations, re-attachments, vortex formation and

substantial interaction with the rudder and propeller (Tello Ruiz et al. [112]).

Xing-Kaeding [120] presents a computational procedure for the prediction of the motion of rigid bodies floating in viscous fluids and subjected to currents and waves. The rigid-body equations of motion in 6DOF are coupled iteratively with the RANS equations describing the turbulent fluid flow. The method is used to compute the motion of floating ships subjected to waves. Turning circles and zig-zag maneuvers are simulated with the ship hull and the rudder modelled geometrically while the propeller effect is substituted by a body force model. The results show favorable agreement with experiments.

Manzke et al. [72] show the application of efficient approaches to perform maneuvering simulations in challenging operating conditions, i.e. in seaway and restricted water. A RANS solver is applied to solve the hydrodynamic forces. The computational domains are kept very compact by coupling the method to an inviscid description of the waves in the far field. This reduces the amount of cells and subsequently the computational time.

1.3 Present work

The objective of this work is to develop computationally efficient state-of-the-art methods to simulate ship maneuvering motion in a seaway. A method based on a two-time scale model and a method based on a unified theory are introduced. Both methods are validated and compared with each other. The advantages of each method are identified but the limitations of their use are also determined and listed.

1.3.1 Contributions in the present work

The major contributions in the present work can be summarized as follows:

- A motion solver is implemented to determine arbitrary motions of rigid bodies. The 6DOF motion solver is based on quaternions in order to avoid the limitations of the gimbal lock. The equations are solved in global coordinates to obtain a universal validity. Due to the large dependence of the fluid force on the body's acceleration, instabilities are likely to occur and special attention is paid to the numerical stability.
- A modular concept is applied to solve the maneuvering motion of ships. The hull, propeller and rudder effects are accounted for in separate modules which interact with each other during the simulation of ship maneuvering. The reliability and accuracy within engineering practice is demonstrated for each module. The estimation of the hull forces is carried out by using modern methods commonly used in the maneuvering research field. Different methods are presented and compared with regards to the applicability

of real time simulations of maneuvering in waves. A numerical model to describe the ship propulsion is developed and validated with sea trial measurements. This model incorporates the behavior of the propeller rate of rotation for diesel-electric propulsion trains.

- Numerical methods to simulate the motion of ships in waves are outlined. A time-domain approach based on the impulse-response function is derived, following the concept of Fossen [33]. A structured verification and validation for different ships is presented.
- The maneuvering behavior of displacement ships in regular waves is analyzed with two different mathematical models:
  - a two-time scale model that splits the combined maneuvering and seakeeping motion into its components and solves each component separately, while certain parameters are exchanged.
  - a model based on unified theory that combines the maneuvering and seakeeping model into one set of equations. Based on the zero-speed approach of Fossen [32], which is mainly intended to simulate dynamic positioning, forward speed effects and additional terms due to maneuvering motion are incorporated.

  A theoretical derivation of each model is given and followed by a validation with experimental data from literature. The models are compared in detail and their advantages and disadvantages are highlighted.

1.3.2 Layout of the thesis

The remainder of the thesis is divided into the following chapters:

Chapter 2 - Fundamentals introduces the general notations and definitions of the present work. The fundamental equations used in the present work to describe ship motions are derived and verified.

Chapter 3 - Maneuvering outlines different models to describe the still water maneuvering motion of ships. A model to describe the propulsion is developed that includes the engine characteristics of diesel-electric engines. The influence of the rudder and the hull on the maneuvering motion is regarded.

Chapter 4 - Seakeeping deals with the simulation of ship motions in waves. A brief summary on state-of-the-art seakeeping simulation models is given. The impulse-response function is deduced according to the fundamentals that are defined in Chapter 2. The seakeeping models are verified and validated for straight motion in waves. Furthermore, mean second-order wave drift forces are introduced and the procedure of their determination is described.

In **Chapter 5 - Maneuvering in Waves**, two different approaches are derived to simulate the maneuvering motion of ships in waves and the wave-induced motion during maneuvering. Standard maneuvers in regular waves are simulated with two different ships and compared with model test results from the literature. A direct comparison of the two approaches is drawn.

Finally, **Chapter 6 - Conclusion and Perspective** presents a summary, conclusions and an outlook on possible future work.

2 Fundamentals

The investigation of the ship motion dynamics can be divided into separate fields of study: kinematics and kinetics, whereat the former treats the geometrical aspects of the motion and the latter analyzes the forces that cause the motion. This chapter provides the description fundamentals for the ship motions; and after introducing the general notation and the coordinate systems used in this work, the kinematic and kinetic equations are derived. In conjunction, the acting forces are of major interest. A short overview on the problem of force determination is given, while the following chapters deal with the forces in more detail.

2.1 General notations

The used notation complies with SNAME standards [113]. The six motion components of a ship are defined accordingly as surge, sway, heave, roll, pitch and yaw (see Table 2.1 and Figure 2.1).

Table 2.1.: Nomenclature of ships according to SNAME [113]

	Surge	**Sway**	**Heave**	**Roll**	**Pitch**	**Yaw**
DOF	1	2	3	4	5	6
Force/Moment	X	Y	Z	K	M	N
Linear/angular velocity	u	v	w	p	q	r
Positions/Euler angles	x	y	z	ϕ	θ	ψ

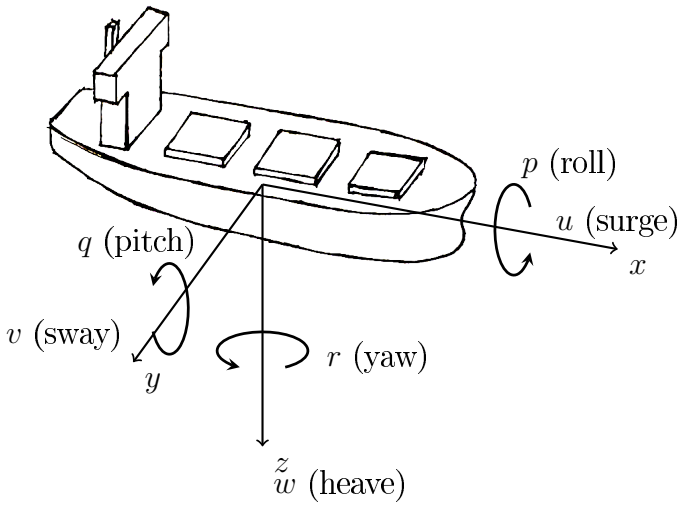

Figure 2.1.: Definition of the 6DOF motion components of ships

2.2 Coordinate systems

Two orthogonal coordinate systems are introduced to describe the position and the motion of ships (note that another coordinate system will be introduced in Chapter 4). The coordinate systems are (see also Figure 2.2):

- The global frame $K\{O, \boldsymbol{i}_{x_0}, \boldsymbol{i}_{y_0}, \boldsymbol{i}_{z_0}\}$ that is fixed to the earth, with z_0 pointing downward. The position $\boldsymbol{r}^K = (x_0\ y_0\ z_0)^T$ and the orientation in Euler angles $\boldsymbol{\Theta} = (\phi\ \theta\ \psi)^T$ within the K frame are summarized in a vector

$$\boldsymbol{\eta} = ((\boldsymbol{x}_0^K)^T\ \boldsymbol{\Theta}^T)^T = (x_0\ y_0\ z_0\ \phi\ \theta\ \psi)^T\ . \tag{2.1}$$

- The body-fixed frame $\hat{K}\{C, \boldsymbol{i}_x, \boldsymbol{i}_y, \boldsymbol{i}_z\}$ is fixed to the hull. The coordinates of the center of gravity with respect to the origin C are $\boldsymbol{r}_{G/C}^{\hat{K}} = (x_G\ y_G\ z_G)^T$. The x-axis is positive towards the bow, the y-axis is positive towards starboard and the z-axis is positive downwards. The linear velocities $\boldsymbol{u}_{C/K}^{\hat{K}} = (u\ v\ w)^T$ are given in C and the angular velocities $\boldsymbol{\omega}_{\hat{K}/K}^{\hat{K}} = (p\ q\ r)^T$ are defined relative to the global frame. They are summarized as

$$\boldsymbol{\nu} = ((\boldsymbol{u}_{C/K}^{\hat{K}})^T\ (\boldsymbol{\omega}_{\hat{K}/K}^{\hat{K}})^T)^T = (u\ v\ w\ p\ q\ r)^T\ . \tag{2.2}$$

The notation for marine craft is adopted from Fossen [32], [33] and can be explained examplarily as follows:

$\boldsymbol{u}_{C/K}^{K}$ = linear velocity of the point C wih respect to K expressed in K.

$\boldsymbol{\omega}_{\hat{K}/K}^{\hat{K}}$ = angular velocity of $\hat{K}$ wih respect to K expressed in $\hat{K}$.

$\boldsymbol{f}_{C}^{\hat{K}}$ = force attacking at the point C expressed in $\hat{K}$.

$\boldsymbol{m}_{C}^{\hat{K}}$ = moment about the point C expressed in $\hat{K}$.

$\boldsymbol{\Theta}_{K/\hat{K}}$ = Euler angles between K and $\hat{K}$.

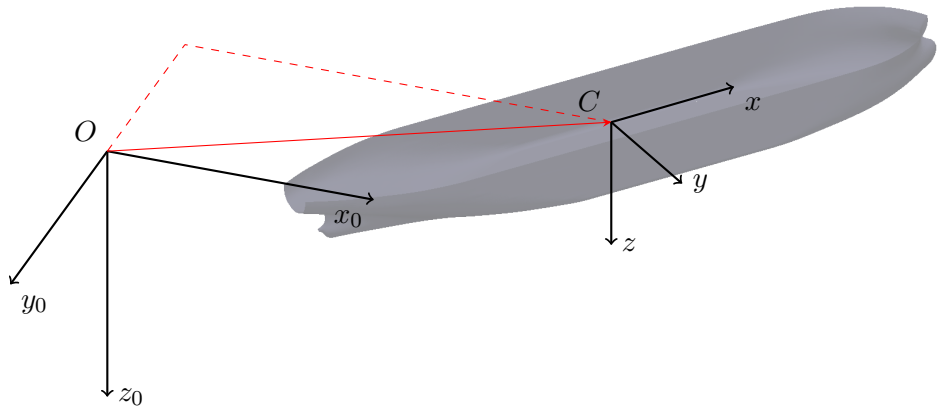

Figure 2.2.: Coordinate system

2.3 Kinematics

To give a unique description of the position of any point on the body, it is enough to know the translation, the rotation of the local system to the global system and the local coordinates. The rotation of $\hat{K}$ to K is specified by the rotation matrix $\boldsymbol{S}$. For $O = C$, the position vector of a point P can be described in coordinates $\boldsymbol{r}^{\hat{K}} = (x\ y\ z)^T$ of the $\hat{K}$-system as well as in coordinates $\boldsymbol{r}^{K} = (x_0\ y_0\ z_0)^T$ of the K-system. For the relation between $\boldsymbol{r}^{K}$ and $\boldsymbol{r}^{\hat{K}}$, the following applies:

$$\boldsymbol{r}^{K} = \boldsymbol{S} \cdot \boldsymbol{r}^{\hat{K}} \ . \tag{2.3}$$

Since $\boldsymbol{S}$ is an orthogonal matrix, it follows that

$$\boldsymbol{r}^{\hat{K}} = \boldsymbol{S}^{T} \cdot \boldsymbol{r}^{K} \ . \tag{2.4}$$

2.3.1 Unit quaternions

According to Euler's rotation theorem, a coordinate transformation can be performed by a single rotation around an appropriate axis. The transformation can therefore be described by four parameters: three parameters to describe the axis, and one parameter for the angle. Naming the axis $\boldsymbol{n}$ and the rotational angle ϕ, the rotation of a point P' with the position vector $\boldsymbol{s}'$ to the point P with the position vector $\boldsymbol{s}$ yields

$$\boldsymbol{s} = \boldsymbol{s}' \cos\phi + \boldsymbol{n}(\boldsymbol{n} \cdot \boldsymbol{s}')(1 - \cos\phi) + \boldsymbol{n} \times \boldsymbol{s}' \sin\phi \; . \tag{2.5}$$

By introducing the unit quaternion

$$e_0 = \cos\frac{\phi}{2} \tag{2.6}$$

$$\boldsymbol{e} = (e_1 \; e_2 \; e_3)^T = \boldsymbol{n} \sin\frac{\phi}{2} \tag{2.7}$$

Eqn. (2.5) can be rewritten as

$$\boldsymbol{s} = (2e_0^2 - 1)\boldsymbol{s}' + 2\boldsymbol{e}(\boldsymbol{e} \cdot \boldsymbol{s}') + 2e_0\boldsymbol{e} \times \boldsymbol{s}' \; . \tag{2.8}$$

By introducing the 3×3 unit matrix $\boldsymbol{I}$ and the skew symmetric cross product matrix

$$\tilde{\boldsymbol{E}} = \begin{pmatrix} 0 & -e_3 & e_2 \\ e_3 & 0 & -e_1 \\ -e_2 & e_1 & 0 \end{pmatrix} \tag{2.9}$$

the equation can be rewritten further as

$$\boldsymbol{s} = [(2e_0^2 - 1)\boldsymbol{I} + 2\boldsymbol{e}\boldsymbol{e} + 2e_0\tilde{\boldsymbol{E}}]\boldsymbol{s}' \; . \tag{2.10}$$

Comparing this with Eqn. (2.3) yields

$$\boldsymbol{S} = (2e_0^2 - 1)\boldsymbol{I} + 2(\boldsymbol{e}\boldsymbol{e} + e_0\tilde{\boldsymbol{E}}) \; . \tag{2.11}$$

In full, the rotation matrix becomes

$$\boldsymbol{S} = \begin{pmatrix} 2(e_0^2 + e_1^2) - 1 & 2(e_1e_2 - e_0e_3) & 2(e_1e_3 + e_0e_2) \\ 2(e_1e_2 + e_0e_3) & 2(e_0^2 + e_2^2) - 1 & 2(e_2e_3 - e_0e_1) \\ 2(e_1e_3 - e_0e_2) & 2(e_2e_3 + e_0e_1) & 2(e_0^2 + e_3^2) - 1 \end{pmatrix} \; . \tag{2.12}$$

The unit quaternion can be written in a four-line vector $\boldsymbol{p}$

$$\boldsymbol{p} = (e_0 \; e_1 \; e_2 \; e_3)^T \; . \tag{2.13}$$

2.3.2 Euler angles

Alternative to the description of rotations based on unit quaternions, Euler angles can be used to describe the rotatory situation of the body. Roll (ϕ), pitch (θ) and yaw (ψ) describe the rotation around the global x-, y- and z-axis, respectively:

$$\boldsymbol{\Theta} = \begin{pmatrix} \phi \\ \theta \\ \psi \end{pmatrix} . \tag{2.14}$$

Each rotation in space can be performed by a rotation around z with the angle ψ, followed by a rotation around the newly generated axis y' with the angle θ, and finally, a rotation around the new axis x'' with the angle ϕ. This is the so-called zyx convention. The rotation matrix resulting from these rotations yields

$$\boldsymbol{S}(\psi,\theta,\phi) = \begin{pmatrix} \mathrm{c}\psi\mathrm{c}\theta & -\mathrm{s}\psi\mathrm{c}\phi + \mathrm{c}\psi\mathrm{s}\theta\mathrm{s}\phi & \mathrm{s}\psi\mathrm{s}\phi + \mathrm{c}\psi\mathrm{c}\phi\mathrm{s}\theta \\ \mathrm{s}\psi\mathrm{c}\theta & \mathrm{c}\psi\mathrm{c}\phi + \mathrm{s}\phi\mathrm{s}\theta\mathrm{s}\psi & -\mathrm{c}\psi\mathrm{s}\phi + \mathrm{s}\theta\mathrm{s}\psi\mathrm{c}\phi \\ -\mathrm{s}\theta & \mathrm{c}\theta\mathrm{s}\phi & \mathrm{c}\theta\mathrm{c}\phi \end{pmatrix} . \tag{2.15}$$

In this equation, c stands for cos() and s for sin().

The body-fixed angular velocity $\boldsymbol{\omega} = (p\ q\ r)^T$ and the Euler rate vector $\dot{\boldsymbol{\Theta}} = (\dot{\phi}\ \dot{\theta}\ \dot{\psi})^T$ are related through a transformation matrix $\boldsymbol{T}_\Theta(\boldsymbol{\Theta})$:

$$\dot{\boldsymbol{\Theta}} = \boldsymbol{T}_\Theta(\boldsymbol{\Theta})\boldsymbol{\omega} . \tag{2.16}$$

The transformation matrix $\boldsymbol{T}_\Theta(\boldsymbol{\Theta})$ can be derived in several ways, e.g.

$$\boldsymbol{\omega} = \begin{pmatrix} \dot{\phi} \\ 0 \\ 0 \end{pmatrix} + \boldsymbol{S}_1(\phi) \begin{pmatrix} 0 \\ \dot{\theta} \\ 0 \end{pmatrix} + \boldsymbol{S}_2(\theta) \begin{pmatrix} 0 \\ 0 \\ \dot{\psi} \end{pmatrix} = \boldsymbol{T}_\Theta^{-1}(\boldsymbol{\Theta})\dot{\boldsymbol{\Theta}} . \tag{2.17}$$

Expanding this equation yields the desired rotation matrix

$$\boldsymbol{T}_\Theta^{-1}(\boldsymbol{\Theta}) = \begin{pmatrix} 1 & 0 & -\mathrm{s}\theta \\ 0 & \mathrm{c}\phi & \mathrm{c}\theta\mathrm{s}\phi \\ 0 & -\mathrm{s}\phi & \mathrm{c}\theta\mathrm{c}\phi \end{pmatrix} \quad \Rightarrow \quad \boldsymbol{T}_\Theta(\boldsymbol{\Theta}) = \begin{pmatrix} 1 & \mathrm{s}\phi\mathrm{t}\theta & \mathrm{c}\phi\mathrm{t}\theta \\ 0 & \mathrm{c}\phi & -\mathrm{s}\phi \\ 0 & \mathrm{s}\phi/\mathrm{c}\theta & \mathrm{c}\phi/\mathrm{c}\theta \end{pmatrix} . \tag{2.18}$$

For $\theta = \pm 90°$ and subsequently $\cos\theta = 0$, $\boldsymbol{T}_\Theta(\boldsymbol{\Theta})$ is undefined, which is often referred to as the gimbal lock. For the motion of surface ships, this is not a problem since it means a pitch angle of 90°. However, for other objects (e.g. underwater vehicles) this might gain importance. To avoid the gimbal lock, the kinematics can be described using the quaternion

representation.

Quaternions to Euler angles

The Euler angles ϕ, θ and ψ (zyx convention) can be derived from the unit quaternions e_i, $i = 0, ..., 3$ by requiring that the associated rotation matrices ((2.15) and (2.12)) are equal (Fossen [33]):

$$\boldsymbol{S}(\boldsymbol{\Theta}) = \boldsymbol{S}(\boldsymbol{p}) \; . \tag{2.19}$$

A component-wise formulation yields nine equations with three unknowns:

$$\begin{pmatrix} \mathrm{c}\psi\mathrm{c}\theta & -\mathrm{s}\psi\mathrm{c}\phi + \mathrm{c}\psi\mathrm{s}\theta\mathrm{s}\phi & \mathrm{s}\psi\mathrm{s}\phi + \mathrm{c}\psi\mathrm{c}\phi\mathrm{s}\theta \\ \mathrm{s}\psi\mathrm{c}\theta & \mathrm{c}\psi\mathrm{c}\phi + \mathrm{s}\phi\mathrm{s}\theta\mathrm{s}\psi & -\mathrm{c}\psi\mathrm{s}\phi + \mathrm{s}\theta\mathrm{s}\psi\mathrm{c}\phi \\ -\mathrm{s}\theta & \mathrm{c}\theta\mathrm{s}\phi & \mathrm{c}\theta\mathrm{c}\phi \end{pmatrix} = \begin{pmatrix} S_{11} & S_{12} & S_{13} \\ S_{21} & S_{22} & S_{23} \\ S_{31} & S_{32} & S_{33} \end{pmatrix} \; . \tag{2.20}$$

One of the possible solutions to this equation is

$$\phi = \mathrm{atan2}(S_{32}, S_{33}) \; , \tag{2.21}$$

$$\theta = \arcsin(S_{31}); \quad \theta \neq \pm 90^\circ \; , \tag{2.22}$$

$$\phi = \mathrm{atan2}(S_{21}, S_{11}) \; . \tag{2.23}$$

2.3.3 Velocities in local body-fixed coordinates

To describe the velocities of a point P in local body-fixed coordinates, the velocity follows to

$$\boldsymbol{u}_{P/K}^{\hat{K}} = \boldsymbol{u}_{C/K}^{\hat{K}} + \boldsymbol{\omega}_{\hat{K}/K}^{\hat{K}} \times \boldsymbol{x}_{P/C}^{\hat{K}} \; , \tag{2.24}$$

with $\boldsymbol{u}_{C/K}^{\hat{K}}$ being the velocity of the body origin C and $\boldsymbol{x}_{P/C}^{\hat{K}}$ being the vector to the center of gravity of the body in local body-fixed coordinates (Abdel-Maksoud [2]). The relationship between acceleration $\boldsymbol{b}_{P/K}^{\hat{K}}$ (relative to the earth and expressed in body-fixed coordinates) yields

$$\boldsymbol{b}_{P/K}^{\hat{K}} = \boldsymbol{\omega}_{\hat{K}/K}^{\hat{K}} \times \boldsymbol{u}_{P/K}^{\hat{K}} + \dot{\boldsymbol{u}}_{P/C}^{\hat{K}} \; . \tag{2.25}$$

When substituting (2.24) into (2.25), one obtains

$$\boldsymbol{b}_{P/K}^{\hat{K}} = \boldsymbol{\omega}_{\hat{K}/K}^{\hat{K}} \times \boldsymbol{u}_{C/K}^{\hat{K}} + \boldsymbol{\omega}_{\hat{K}/K}^{\hat{K}} \times (\boldsymbol{\omega}_{\hat{K}/K}^{\hat{K}} \times \boldsymbol{x}_{P/C}^{\hat{K}}) + \dot{\boldsymbol{u}}_{C/K}^{\hat{K}} + \dot{\boldsymbol{\omega}}_{\hat{K}/K}^{\hat{K}} \times \boldsymbol{x}_{P/C}^{\hat{K}} \; . \tag{2.26}$$

The rigid-body kinetics are calculated with respect to the body's center of gravity as described in the following. To obtain the velocity and acceleration of its coordinate origin C, Eqn. (2.24)

and Eqn. (2.26) have to be reformulated to

$$\boldsymbol{u}_{C/K}^{\hat{K}} = \boldsymbol{u}_{G/K}^{\hat{K}} - \boldsymbol{\omega}_{\hat{K}/K}^{\hat{K}} \times \boldsymbol{x}_{G/C}^{\hat{K}} \,, \tag{2.27}$$

$$\dot{\boldsymbol{u}}_{C/K}^{\hat{K}} = \boldsymbol{b}_{G/K}^{\hat{K}} - \boldsymbol{\omega}_{\hat{K}/K}^{\hat{K}} \times \boldsymbol{u}_{C/K}^{\hat{K}} - \boldsymbol{\omega}_{\hat{K}/K}^{\hat{K}} \times (\boldsymbol{\omega}_{\hat{K}/K}^{\hat{K}} \times \boldsymbol{x}_{G/C}^{\hat{K}}) - \dot{\boldsymbol{\omega}}_{\hat{K}/K}^{\hat{K}} \times \boldsymbol{x}_{G/C}^{\hat{K}} \,. \tag{2.28}$$

The hydrodynamic forces in maneuvering and seakeeping are generally given in ship-fixed coordinates, relative to the local origin located at the main frame. The rigid-body kinetics are derived for the motion of the body's center of gravity, see Section 2.4. Therefore, this coordinate transformation is of importance.

2.4 Rigid-body kinetics

For the rigid-body kinetics, all forces and moments are calculated with respect to the body's center of gravity. The two coordinate systems $K\{O, \boldsymbol{i}_{x_0}, \boldsymbol{i}_{y_0}, \boldsymbol{i}_{z_0}\}$ and $\hat{K}\{C, \boldsymbol{i}_x, \boldsymbol{i}_y, \boldsymbol{i}_z\}$ with the origins O and C, respectively, have been introduced in Section 2.2. System K is the inertial frame that is not accelerated and system $\hat{K}$ is moved arbitrarily but fixed to the body. A detailed derivation of the following is given in Koliha [59].

2.4.1 Translation

For translatory motion of the body's center of gravity, Newton's second law applies:

$$\boldsymbol{f}_G^K = m\ddot{\boldsymbol{r}}_{G/O}^K \,, \tag{2.29}$$

with the external force $\boldsymbol{f}_G^K$ acting on the center of gravity, the body mass m and the absolute acceleration of the body $\ddot{\boldsymbol{r}}_{G/O}^K$ with respect to the earth-fixed frame in global coordinates.

2.4.2 Rotation

Generally speaking, the time rate of change of the angular momentum $\boldsymbol{l}$ equals the external moment acting on the body. With the inertia tensor $\boldsymbol{I}$ and the angular velocity $\boldsymbol{\omega}$, the angular momentum $\boldsymbol{l}$ yields

$$\boldsymbol{l} = \boldsymbol{I} \cdot \boldsymbol{\omega} \tag{2.30}$$

and subsequently

$$\frac{d\boldsymbol{l}}{dt} = \frac{d(\boldsymbol{I} \cdot \boldsymbol{\omega})}{dt} = \boldsymbol{m} \,, \tag{2.31}$$

with the external moment $\boldsymbol{m}$. When writing this equation in local body-fixed coordinates with the local mass moment of inertia, the inertia tensor $\boldsymbol{I}^{\hat{K}}$ is constant and the equation

yields

$$\boldsymbol{I}^{\hat{K}} \cdot \dot{\boldsymbol{\omega}}^{\hat{K}}_{\hat{K}/K} + \boldsymbol{\omega}^{\hat{K}}_{\hat{K}/K} \times (\boldsymbol{I}^{\hat{K}} \cdot \boldsymbol{\omega}^{\hat{K}}_{\hat{K}/K}) = \boldsymbol{m}^{\hat{K}}_{G} \ , \tag{2.32}$$

with the local moment $\boldsymbol{m}^{\hat{K}}_{G}$ and the local angular velocity $\boldsymbol{\omega}^{\hat{K}}_{\hat{K}/K}$.

2.4.3 Time integration

To obtain the time-dependent position of the body, the accelerations known from Eqn. (2.29) and (2.32) need to be integrated. For notational convenience, the global position of the body's center of gravity in global coordinates ($\boldsymbol{r}^{K}_{G/O}$) is denoted $\boldsymbol{r}$ and the angular velocity is denoted $\boldsymbol{\omega}$ in global coordinates ($\boldsymbol{\omega}^{K}_{\hat{K}/K}$) and $\boldsymbol{\omega'}$ in local coordinates ($\boldsymbol{\omega}^{\hat{K}}_{\hat{K}/K}$). The following derivation is based on the work of Koliha [59].

Translatory quantities

For the translatory quantities, the following applies:

$$\dot{\boldsymbol{r}}(t) = \int_0^t \ddot{\boldsymbol{r}}(\tau) d\tau \ , \tag{2.33}$$

$$\boldsymbol{r}(t) = \int_0^t \dot{\boldsymbol{r}}(\tau) d\tau \ . \tag{2.34}$$

Rotatory quantities

The rotatory quantities of the body are:

- angular acceleration $\dot{\boldsymbol{\omega}}$,
- angular velocity $\boldsymbol{\omega}$,
- the vector $\boldsymbol{p}$, describing the rotatory position.

The angular body velocity $\boldsymbol{\omega}$ cannot be integrated directly since finite rotations are not summable. Therefore, the vector $\dot{\boldsymbol{p}}$ needs to be introduced. The integration of $\dot{\boldsymbol{p}}$ to $\boldsymbol{p}$ is possible. The integration of the rotatory quantities can now be performed following

$$\boldsymbol{m'} \rightarrow \text{Eqn. (2.32)} \rightarrow \dot{\boldsymbol{\omega}} \rightarrow \int \rightarrow \boldsymbol{\omega} \rightarrow \dot{\boldsymbol{p}} = f(\boldsymbol{\omega'}) \rightarrow \int \rightarrow \boldsymbol{p} \ . \tag{2.35}$$

The function $f(\boldsymbol{\omega}')$ must be derived. With the skew symmetric cross product matrix of the angular velocity $\boldsymbol{\omega}$

$$\tilde{\boldsymbol{\Omega}} = \begin{pmatrix} 0 & -\omega_3 & \omega_2 \\ \omega_3 & 0 & -\omega_1 \\ -\omega_2 & \omega_1 & 0 \end{pmatrix} \tag{2.36}$$

it can be shown that (Nikravesh [77])

$$\dot{\boldsymbol{S}} = \tilde{\boldsymbol{\Omega}}\boldsymbol{S} \, , \tag{2.37}$$

which, multiplied by $\boldsymbol{S}^T$ yields,

$$\dot{\boldsymbol{S}}\boldsymbol{S}^T = \tilde{\boldsymbol{\Omega}} \, . \tag{2.38}$$

$\boldsymbol{S}$ can be written as the product of two matrices

$$\boldsymbol{S} = \boldsymbol{G}\boldsymbol{L}^T \, , \tag{2.39}$$

with

$$\boldsymbol{G} = \begin{pmatrix} -e_1 & e_0 & -e_3 & e_2 \\ -e_2 & e_3 & e_0 & -e_1 \\ -e_3 & -e_2 & e_1 & e_0 \end{pmatrix} \tag{2.40}$$

and

$$\boldsymbol{L} = \begin{pmatrix} -e_1 & e_0 & e_3 & -e_2 \\ -e_2 & -e_3 & e_0 & e_1 \\ -e_3 & e_2 & -e_1 & e_0 \end{pmatrix} \, . \tag{2.41}$$

Because $\boldsymbol{G}\dot{\boldsymbol{L}}^T = \dot{\boldsymbol{G}}\boldsymbol{L}^T$ the time integration of $\boldsymbol{S}$ becomes

$$\dot{\boldsymbol{S}} = 2\dot{\boldsymbol{G}}\boldsymbol{L}^T \tag{2.42}$$

and subsequently

$$2\dot{\boldsymbol{G}}\boldsymbol{L}^T\boldsymbol{L}\boldsymbol{G}^T = \tilde{\boldsymbol{\Omega}} \, . \tag{2.43}$$

When taking into account that $\boldsymbol{L}^T\boldsymbol{L}$ is the sum of the 4×4 identity matrix and $-\boldsymbol{p}\boldsymbol{p}^T$ and that $\boldsymbol{G}\boldsymbol{p} = 0$, it follows that

$$2\dot{\boldsymbol{G}}\boldsymbol{G}^T = \tilde{\boldsymbol{\Omega}} \, . \tag{2.44}$$

With $\boldsymbol{G}\dot{\boldsymbol{G}}^T = -\dot{\boldsymbol{G}}\boldsymbol{G}^T$ and $-\dot{\boldsymbol{G}}\boldsymbol{G}^T = \tilde{G}\dot{\boldsymbol{p}}$, one obtains

$$\boldsymbol{\omega} = 2\boldsymbol{G}\dot{\boldsymbol{p}} \, . \tag{2.45}$$

The tilde shows that the matrix has the form of a cross product matrix.

It can be shown that $\boldsymbol{p}^T\boldsymbol{p} = 1$ and subsequently

$$\frac{d(\boldsymbol{p}^T\boldsymbol{p})}{dt} = \dot{\boldsymbol{p}}^T\boldsymbol{p} + \boldsymbol{p}^T\dot{\boldsymbol{p}} = \dot{\boldsymbol{p}}^T\boldsymbol{p} + \dot{\boldsymbol{p}}^T\boldsymbol{p} = 0 \quad \Rightarrow \quad \dot{\boldsymbol{p}}^T\boldsymbol{p} = 0\ . \tag{2.46}$$

Using $\boldsymbol{G}^T\boldsymbol{G} = \boldsymbol{L}^T\boldsymbol{L}$ and Eqn. (2.46), one obtains by multiplying Eqn. (2.45) with $\boldsymbol{G}^T$

$$\dot{\boldsymbol{p}} = \frac{1}{2}\boldsymbol{G}^T\boldsymbol{\omega}\ . \tag{2.47}$$

$\boldsymbol{\omega}$ can be substituted by $\boldsymbol{S}\boldsymbol{\omega}'$ and $\boldsymbol{S}$ by $\boldsymbol{G}\boldsymbol{L}^T$, so that with $\boldsymbol{L}\boldsymbol{p} = 0$

$$\dot{\boldsymbol{p}} = \frac{1}{2}\boldsymbol{L}^T\boldsymbol{\omega}'\ . \tag{2.48}$$

This equation represents the desired function $f(\boldsymbol{\omega}')$.

Numerical integration

To obtain the position of the body in each time step, numerical integration needs to be applied to the linear and angular acceleration.

The Runge-Kutta method can be used for the time integration of initial value problems:

$$\dot{y}(t) = f(t, y(t)), \quad y(0) = y_0, \quad y : \mathbb{R} \to \mathbb{R}^d \tag{2.49}$$

Runge-Kutta methods are one-step procedures with

$$y_{n+1} = y_n + \Delta t \sum_{j=1}^{s} b_j k_j\ . \tag{2.50}$$

Δt is the time step size given as $\Delta t = t_{n+1} - t_n$. The coefficients b_j define the procedure. The values k_j contain the values of the function f at discrete intermediate steps:

$$k_j = f(t_n + \Delta t c_j,\ y_n + \Delta t \sum_{l=1}^{s} a_{jl} k_l),\ j = 1, ..., s \tag{2.51}$$

c_j and A_{jl} are further characteristic coefficients of the procedure. The coefficients of the procedure can be given in so-called Butcher arrays, according to Table 2.2. Table 2.3 shows examplarily the characteristic values for the explicit Euler scheme, the implicit Euler scheme and the fourth-order Runge-Kutta scheme.

The implicit method uses the time derivative of the new time step to calculate the values of the new time step. Since this time derivative is not known in advance, an iteration process is necessary.

Table 2.2.: Butcher array (Goettsche [38])

c_1	a_{11}	a_{12}	$\cdots$	a_{1s}
c_2	a_{21}	a_{22}	$\cdots$	a_{2s}
$\vdots$	$\vdots$	$\vdots$	$\ddots$	$\vdots$
c_s	a_{s1}	a_{s2}	$\cdots$	a_{ss}
	b_1	b_2	$\cdots$	b_s

Table 2.3.: Butcher array for first-order explicit Euler scheme (left), first-order implicit Euler scheme (center) and fourth-order Runge-Kutta scheme (right)

0	
	1

1	1
	1

0				
$\frac{1}{2}$	$\frac{1}{2}$			
$\frac{1}{2}$	0	$\frac{1}{2}$		
1	0	0	1	
	$\frac{1}{6}$	$\frac{1}{3}$	$\frac{1}{3}$	$\frac{1}{6}$

In this special case, the equations of motion are of interest, so y is not a scalar but includes as a vector $\boldsymbol{y} \in \mathbb{R}^{13}$ the translatory position $\boldsymbol{r} \in \mathbb{R}^3$, the orientation describing quaternion $\boldsymbol{p} \in \mathbb{R}^4$, the translatory velocity $\dot{\boldsymbol{r}} \in \mathbb{R}^3$ and the angular velocity in local coordinates $\boldsymbol{\omega}' \in \mathbb{R}^3$. It can be written as

$$\boldsymbol{y} = \begin{pmatrix} \boldsymbol{r} \\ \boldsymbol{p} \\ \dot{\boldsymbol{r}} \\ \boldsymbol{\omega}' \end{pmatrix} . \tag{2.52}$$

The time differential $\dot{\boldsymbol{y}}$ subsequently yields

$$\dot{\boldsymbol{y}} = \begin{pmatrix} \dot{\boldsymbol{r}} \\ \dot{\boldsymbol{p}} \\ \ddot{\boldsymbol{r}} \\ \dot{\boldsymbol{\omega}}' \end{pmatrix} . \tag{2.53}$$

The terms of $\dot{\boldsymbol{y}}$ are determined as follows:

- The velocity $\dot{\boldsymbol{r}}$ is directly taken from $\dot{\boldsymbol{r}}$, i.e. from lines 8 to 10 of $\boldsymbol{y}$.
- $\dot{\boldsymbol{p}}$ is calculated with Eqn. (2.48) out of $\boldsymbol{p}$ and $\boldsymbol{L}^T$ (built with $\boldsymbol{p}$) and $\boldsymbol{\omega}'$.
- The acceleration $\ddot{\boldsymbol{r}}$ can be calculated with Eqn. (2.29), in which the external force is in global coordinates $\boldsymbol{f}$.
- The angular acceleration $\dot{\boldsymbol{\omega}}'$ is calculated with Eqn. (2.32), in which the external moment is in local coordinates $\boldsymbol{m}'$.

2.4.4 Instabilities due to added mass effects

For the motion of a rigid body in a fluid of substantial density like water, there is a linear dependence of the fluid force $\boldsymbol{f}$ on the acceleration $\ddot{\boldsymbol{r}}$ and $\dot{\boldsymbol{\omega}}'$,

$$\boldsymbol{f} = \bar{\boldsymbol{f}} - \boldsymbol{A}\ddot{\boldsymbol{r}} \; , \tag{2.54}$$

where $\bar{\boldsymbol{f}}$ does not depend on the acceleration and $\boldsymbol{A}$ is the added mass matrix. Subsequently, Newton's equation (2.29) (the same applies for Eqn. (2.32)) can be rewritten as

$$(\boldsymbol{M} + \boldsymbol{A})\ddot{\boldsymbol{r}} = \boldsymbol{f} + \boldsymbol{A}\ddot{\boldsymbol{r}} = \bar{\boldsymbol{f}} \; . \tag{2.55}$$

However, because $\boldsymbol{A}$ is usually unknown, it is common to apply numerical integration schemes directly to Eqn. (2.29) (and Eqn. (2.32)). As shown by Söding [109], explicit Euler integration methods become unstable if the added mass exceeds the real mass of the body. For implicit integration schemes, the iteration converges slowly (for small relaxation factors) or is not robust (for larger relaxation factors). A robust and economic method requires determining an approximation of the added mass matrix $\boldsymbol{A}$ so that Eqn. (2.55), instead of Eqn. (2.29), can be used.

The added mass can be determined from the flow computations for preceding time steps and iteration steps within an implicit integration method, as recommended by Söding [109]. If one distinguishes these different flow computations by the index k, Eqn. (2.54) becomes

$$\boldsymbol{f}_k = \bar{\boldsymbol{f}}_k - \boldsymbol{A}\ddot{\boldsymbol{r}}_k \; . \tag{2.56}$$

For the first implicit step, zero acceleration is used within each time step. By taking the difference between body forces determined in later implicit steps and in the first implicit step within the same time step, $\bar{\boldsymbol{f}}_k$ is eliminated from Eqn. (2.56), yielding

$$\Delta\boldsymbol{f}_k = -\boldsymbol{A}\ddot{\boldsymbol{r}}_k \; . \tag{2.57}$$

This is an over-determined linear equation system for $\boldsymbol{A}$ when having a sufficient number of k values. By minimizing the sum over k of weighted squared errors of these equations, separately for each line i, one obtains the following linear equation system for $\boldsymbol{A}$, where the elements of $\boldsymbol{A}$ are denoted by A_{ij}:

$$\sum_k (g\ddot{\boldsymbol{r}}_l \ddot{\boldsymbol{r}}_j)_k A_{ji} = -\sum_k (g\ddot{\boldsymbol{r}}_l \Delta f_i)_k \; , \tag{2.58}$$

where $A^T_{ji} = A_{ij}$.

2.4.5 Verification of rigid-body motion

Different test cases are calculated in order to verify the implementation of the methods described above. First, the equations for the rigid-body motion are verified. The excitation follows from unit forces in these cases. Then, a potential flow is taken into account and different floating cases are presented. For these cases, the influence of the different time integration schemes is shown. Finally, a verification of the calculation of the added mass is presented.

For the verification of the rigid-body kinetics, different procedures proposed in Koliha [59] are adopted. The first test case serves to check the integration schemata of normally integratable quantities and the behavior of numerical errors. A unit force is acting on a unit mass at rest. For this case, the numerical integration schemes are describing the analytical solution of the velocity exactly. For the position, the numerical error per time step can be determined as

$$\epsilon = \frac{f}{2m} dt^2 \,, \tag{2.59}$$

with the acting force f and the body mass m. Subsequently, the error after n time steps becomes

$$Err(n) = n\epsilon = \frac{t}{dt}\epsilon = \frac{dtf}{2m} t = Err(t) \,. \tag{2.60}$$

For the implicit time integration, it can be shown that $\epsilon_{impl} = -\epsilon_{expl}$. The fourth-order Runge-Kutta integration scheme gives the exact solution of the position. Figure 2.3 shows the deviation of the numerical solution from the analytical solution of the position and the velocity. It reveals zero deviation for the velocity and linear deviation with a gradient of $\frac{dtf}{2m}$ for the position determined with the Euler integration schemes and zero deviation when determined with the fourth-order Runge-Kutta integration scheme.

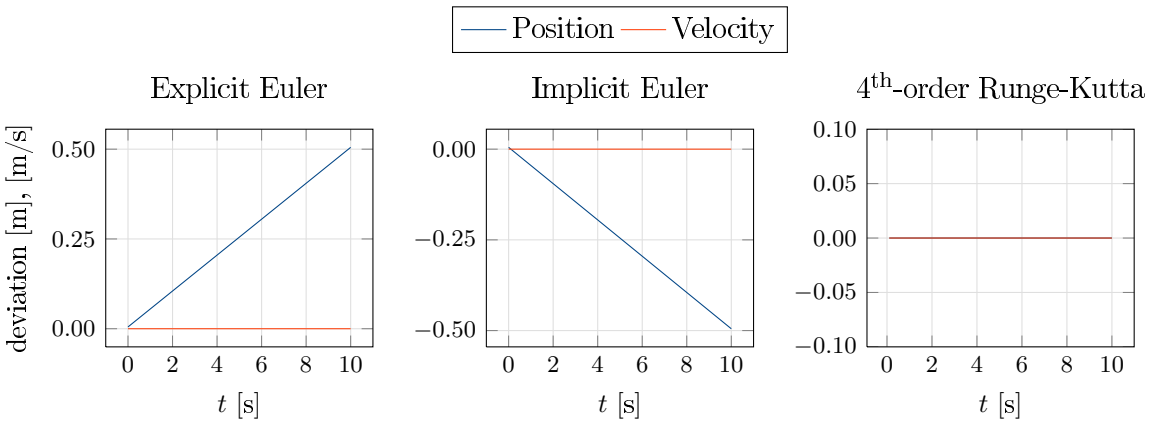

Figure 2.3.: Translatory acceleration; difference of the numerical and the analytical solution

The second test case considers a space gyro. A rotationally symmetric body shall be considered

with a local inertia of

$$\boldsymbol{I}' = \begin{pmatrix} 1 & 0 & 0 \\ 0 & 1 & 0 \\ 0 & 0 & 2 \end{pmatrix} \text{ kg m}^2 \tag{2.61}$$

and a mass of $m = 1\text{kg}$. In the beginning of the simulation, the local coordinate system is rotated by $\alpha = 45°$ around the x-axis. The initial predefined angular velocity in local coordinates is

$$\boldsymbol{\omega}' = \begin{pmatrix} \pi & 0 & 2\pi \end{pmatrix}^T 1 \text{ /s} . \tag{2.62}$$

The constant angular momentum in local coordinates follows to

$$\boldsymbol{l}' = \boldsymbol{I}'\boldsymbol{\omega}' = \begin{pmatrix} \pi & 0 & 4\pi \end{pmatrix}^T \text{Nms} . \tag{2.63}$$

Figure 2.4 shows the rotation components of the space gyro.

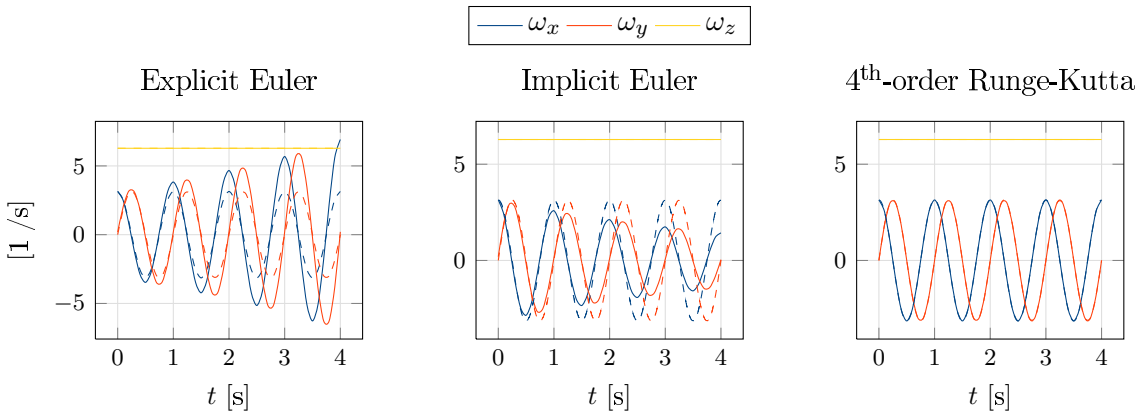

Figure 2.4.: Rotation of a space gyro; Numerical (solid) and analytical (dashed) solution; $dt = 0.01\text{s}$

The figure shows that the rotation is in phase with the analytical solution and reveals an increasing deviation for the Euler integration schemes. However, it further reveals that the conserved quantity ω_3' is reproduced exactly.

Further details on the verification procedure can be found in Koliha [59].

To demonstrate the different time integration schemes and the calculation of added mass according to Section 2.4.4, the oscillatory motion of a cube in water is calculated with the potential flow solver *pan*MARE. The panel code *pan*MARE (**pan**el code for **M**aritime **A**pplications and **RE**search) is a command-based program for the simulation of potential flows in maritime applications. The program is based on a three-dimensional panel method of first order, where the geometry of the body is discretized into flat quadrilateral elements. Adequate boundary conditions are defined on the disretized body and a linear equation system is set up. Solving the equation system yields the local velocity and pressure distribution on the body (Bauer

and Abdel-Maksoud [8]).

A box with dimensions of $length \times width \times height = 1\text{m} \times 1\text{m} \times 0.5\text{m}$ and a mass of $m = 300\text{kg}$ is put into water with a draft of $d_0 = 0.25\text{m}$. Due to the higher weight, no hydrostatic equilibrium is achieved in this state and the box starts to oscillate.

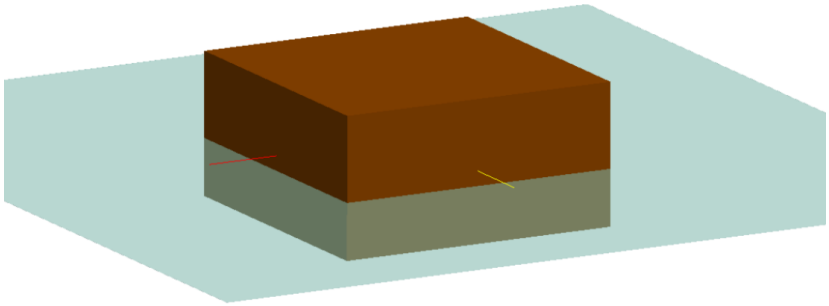

Figure 2.5.: Oscillating cube

No friction forces are acting and no free-surface is modelled, i.e. no real damping exists. Subsequently, the damping is due to numerics (artificial damping). It can be shown that the damping increases with decreasing time step size, see Figure 2.6. For explicit time integration, the damping appears to be negative, as can be seen from Figure 2.6. Since the added mass is not calculated in explicit calculations, a fixed value of $A_{33} = 500\text{kg}$ is set. Without the usage of the added mass, the calculations become unstable and no result can be obtained.

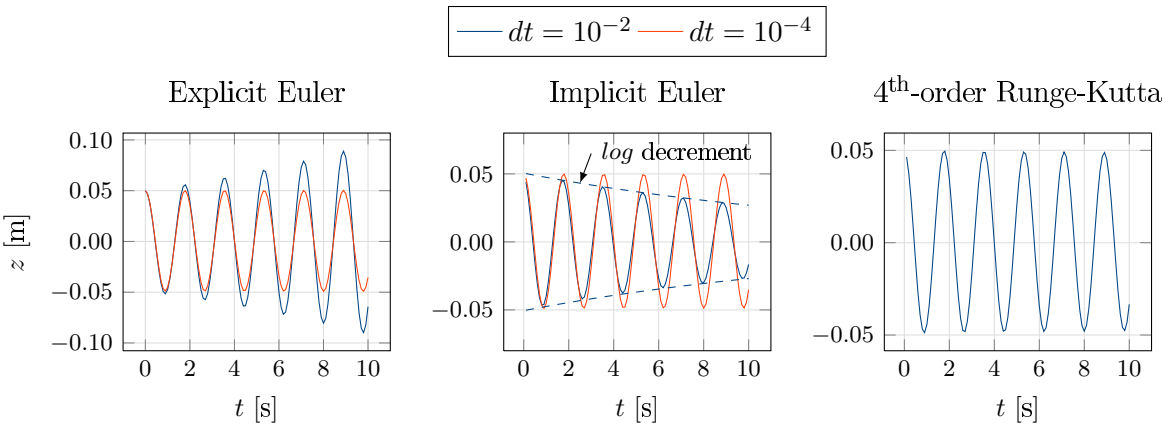

Figure 2.6.: Oscillating displacement of a cube

Furthermore, the calculation of the added mass can be verified. The total mass term of an oscillating system yields

$$M_{33} = \frac{C_{33}}{\omega_0^2} \,. \tag{2.64}$$

The mass term M_{33} includes the real body mass and added mass terms and C_{33} is the restoring

term. To obtain the undamped Eigenfrequency, the logarithmic decrement of the oscillation is determined:

$$\theta = \delta \cdot T_S = \ln \frac{x_n}{x_{n+1}} \,, \tag{2.65}$$

with x_n and x_{n+1} being arbitrary neighboring extrema. The logarithmic decrement is shown in Figure 2.6. With the period of oscillation T_S, the damping constant δ can be found. The frequency of the damped oscillation is in relation with the undamped Eigenfrequency:

$$\omega^2 = \omega_0^2 - \delta^2 \,. \tag{2.66}$$

The restoring term follows from hydrostatic considerations to

$$C_{33} = \rho \cdot g \cdot A_{WL} = 9810\mathrm{N\,m^{-1}} \,, \tag{2.67}$$

with the water plane area A_{WL}.

The added mass is then the difference of the mass term M_{33} and the real mass m

$$A_{33} = M_{33} - m = 487\mathrm{kg} \,. \tag{2.68}$$

Figure 2.7 shows the numerically and the analytically determined added mass as described above. The figure shows that the mean value of the added mass fits well with the analytical result. For the case that the acceleration becomes zero, the added mass becomes infinite.

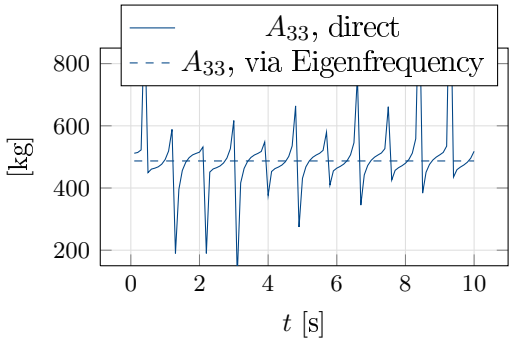

Figure 2.7.: Calculated added mass during oscillation of a cube

2.5 External forces

The external forces acting on the vessel are basically the hydrodynamic forces. Other forces, such as wind forces, tug forces or arbitrary loads, can be added easily but are not part of this work. To determine and describe these hydrodynamic loads, different approaches can be found in the literature. An overview is given in the review on previous work, see Section 1.2.

Assuming that the system is linear, the forces acting on the ship can be regarded as the superposition of two components: the forces due to the forced body motion in calm water and the wave forces acting on the restrained body, see e.g. Journée and Pinkster [58]. Subsequently, for the external forces acting on a ship, it can be assumed that:

- The motion of the ship in water causes a hydrodynamic reaction, which induces the hydrodynamical forces and moments.
- Incoming waves that act on the restrained ship cause the wave excitation forces and moments.

The former hydrodynamical forces and moments depend on the ship motion and thus can be described as a function of these:

$$\boldsymbol{f}_{hydrodynamical} = f(\boldsymbol{y}, \dot{\boldsymbol{y}}) \tag{2.69}$$

With $\boldsymbol{y}$ and $\dot{\boldsymbol{y}}$ according to Eqn. (2.52) and Eqn. (2.53), respectively. The forces connected with the acceleration of the body are called *added mass terms* ($\boldsymbol{A} \cdot \dot{\boldsymbol{\nu}}$) and those connected with the velocity are the *damping terms* ($\boldsymbol{B} \cdot \boldsymbol{\nu}$). Furthermore, *restoring terms* ($\boldsymbol{C} \cdot \boldsymbol{\eta}$) are present due to the hydrostatics. An important fact is that the hydrodynamic added mass and damping coefficients are dependent on the motion frequency of the body. This is mainly due to free surface effects and has therefore a special meaning for ships. Figure 2.8 illustrates this dependency for motion in sway. In this figure, only potential components are regarded. The curves are computed using PDSTRIP [111], a strip theory program that is further described in Chapter 4.

Examplarily for the ship moving in sway, the equation of motion yields

$$m\dot{v} = f_{y,additional} + f_{y,hydrodynamical} \tag{2.70}$$

$$\Leftrightarrow \quad m\dot{v} = f_{y,additional} - A_{22}(\omega)\dot{v} - B_{22}(\omega)v \tag{2.71}$$

$$\Leftrightarrow \quad [m + A_{22}(\omega)]\dot{v} + B_{22}(\omega)v = f_{y,additional}\ . \tag{2.72}$$

The additional forces can be caused by arbitrary loads and the mass and damping forces ($A_{22}(\omega)\dot{v}$ and $B_{22}(\omega)v$) are due to the ship motion.

The frequency-dependent damping consists of potential and viscous effects. The potential

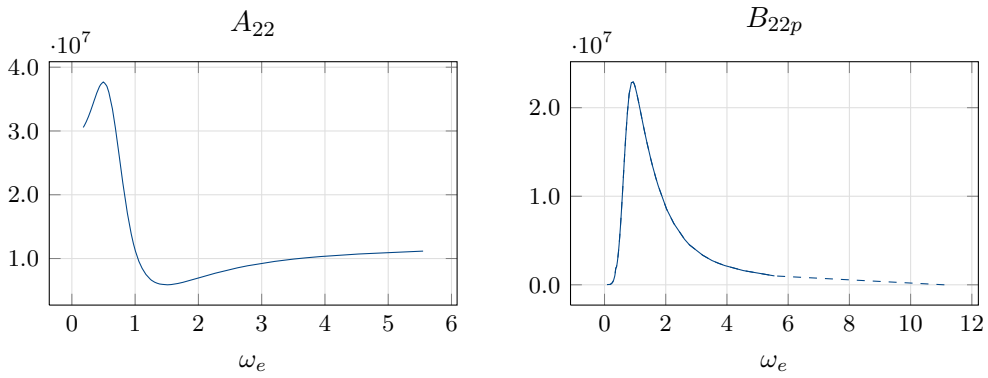

Figure 2.8.: Added mass and potential damping of the S-175 container ship

component in sway can be denoted as $B_{22p}(\omega)$ and the viscous component as $B_{22v}(\omega)$, following Fossen [32]. Both components are frequency-dependent. Subsequently, the total frequency-dependent linear damping coefficient is

$$B_{22}(\omega) = B_{22p}(\omega) + B_{22v}(\omega) \ . \tag{2.73}$$

The potential damping $B_{22p}(\omega)$ can be determined with potential theory, however, the viscous part $B_{22v}(\omega)$ needs more sophisticated tools. The potential damping becomes zero for zero frequency ($B_{22p}(0) = 0$), while the viscous part has its maximum for this frequency.

Maneuvering

For a ship moving in calm water, i.e. $\omega = 0$, the wave excitation force has to be separated from the additional forces. The remaining model can be designated as low-frequency (LF) model. Eqn. 2.72 then yields

$$(m - Y_{\dot{v}})\dot{v}_{LF} - Y_v v_{LF} = f_{y,additional} \ , \tag{2.74}$$

where v_{LF} is the LF velocity in sway.

The hydrodynamic derivatives are the zero-frequency hydrodynamic coefficients:

$$-Y_{\dot{v}} \triangleq A_{22}(0) \tag{2.75}$$

$$-Y_v \triangleq B_{22}(0) = B_{22v}(0) \tag{2.76}$$

The hydrodynamic derivatives can be determined with model tests or with viscous flow computations. However, linear terms are not always sufficient to describe the acting forces with enough accuracy. To describe the forces acting on a maneuvering ship, higher-order damping terms should be considered.

The maneuvering models used in the work are presented in Chapter 3 .

Seakeeping

For seakeeping calculations, the frequency dependence of the hydrodynamic coefficients needs to be regarded.

The frequency dependence of the body's motion can be solved directly with Eqn. (2.72). This is valuable for evaluating natural frequency and modal problems. If the frequency of encounter of the waves is known as well as the added mass and damping terms for this frequency, the equation can also be solved in the time domain. The frequency of encounter yields

$$\omega_e = \omega_0 - \frac{\omega_0^2 U}{g} \cos\beta \ . \tag{2.77}$$

An equation that is valid for arbitrary motion frequency can be found by using the approach of Cummins [20] and Ogilvie [79]. They have derived a time-domain equation based on the frequency-dependent coefficients $A_{22}(\omega)$ and $B_{22}(\omega)$:

$$[m + A_{22}(\infty)]\dot{v}_{WF} + B_{22}(\infty)v_{WF} + \int_{-\infty}^{t} K_{22}(t-\tau)v_{WF}(\tau)d\tau = f_{y,additional} \ . \tag{2.78}$$

The additional forces contain the linear Froude-Krylov forces and diffraction forces as well as the second-order mean wave loads, often called wave drift forces.

A detailed description and derivation of the seakeeping models is given in Chapter 4.

Two-time scale theory

The Eqns. (2.74) and (2.78) can be combined to describe the maneuvering motion in waves. Following the principle of linear superposition (proposed by Denis and Pierson [23]) yields

$$y = y_{LF} + y_{WF} \ . \tag{2.79}$$

In this model, the effect due to linear waves is considered as oscillatory motion with a zero mean value added to the low-frequency ship motions.

Two-time scale models are further investigated in Chapter 5.

Unified theory

To derive a unified theory, Bailey et al. [7] suggest a linear viscous ramp to adjust the damping data such that the values of the damping at zero frequency are equal to the viscous part. This viscous ramp is decaying with increasing ω. Fossen [32] models the viscous damper with an exponentially decaying function

$$B_{22v}(\omega) = \beta_{22} e^{-\alpha\omega} \,, \tag{2.80}$$

with β_{22} being the zero-frequency damping coefficient, i.e. $B_{22v}(0) = \beta_{22}$ and α being a constant that predefines the amount of decaying whereas $\alpha > 0$. The linear maneuvering derivative can be used to unify the seakeeping and the maneuvering theory. Furthermore, the nonlinear maneuvering derivatives have to be included into the equation of motion.

A complete derivation of the unified model is given in Chapter 5.

3 Maneuvering

This chapter provides the maneuvering models applied in this study. Maneuvering generally includes course keeping, course changing, track keeping and changing the ship's speed (especially stopping). It is characterized by a high degree of complexity due to the large number of factors influencing the maneuvering motion, including maneuvering devices such as rudders and movable thrusters, as well as the propulsion units and the hull. Furthermore, these components are interacting with one another.

In general, Newton's second law is applied in order to simulate the maneuvering motion, as described in Chapter 2. The mass properties are mainly well known, which means that correctly determining the hydrodynamic loads is essential for creating a reliable simulation of the ship motions. Once the forces are determined, a numerical model in dependence of the motion parameters must be defined to describe the forces during the time-domain maneuver simulation.

According to the Manoeuvring Committee of the ITTC [1], the generation of a maneuvering model can be divided into different steps. The model includes the prediction of the hydrodynamic forces, the modelling of these forces with a mathematical model, the numerical integration method included in the simulation software and the subsequent simulation of maneuvers. Each step needs to be validated and documented separately.

The present work utilizes different maneuvering simulation models. In the following, the different models and their most important derivation steps are presented. In the beginning of the chapter, the fundamentals of the maneuvering theory are defined. Since the way in which the hydrodynamic forces are modelled also affects the procedure to determine the forces, the modelling of the forces is first described, followed by the prediction methods of the hydrodynamic forces. Afterwards, the numerical methods used to solve the equations of motion are presented. Each step is accompanied by simulation examples and validation.

3.1 Definitions

The motions are generally limited to four degrees of freedom, i.e. translatory motion in longitudinal and transverse direction and rotatory motion around the longitudinal and the vertical axis (surge, sway, roll and yaw, respectively). When regarding maneuvering motion in calm water, no heave or pitch motion are expected.

The ship's track is described in the earth-fixed frame K. The origin of the body-fixed frame $\hat{K}$ is typically at the main frame, in the water plane area and amidships. The rudder angle is positive towards starboard according to the SIMMAN workshop [81]. The course angle ψ is the angle between the ship's longitudinal axis x and the global x_0-axis, while the drift angle β is between the ship's longitudinal axis x and the ship's velocity vector $\boldsymbol{u}$, specified by

$$\beta = \arctan(\frac{-v}{u}) \, . \tag{3.1}$$

The absolute ship velocity is denoted with a capital U:

$$U = \sqrt{u^2 + v^2} \, . \tag{3.2}$$

The definitions are shown in Figure 3.1.

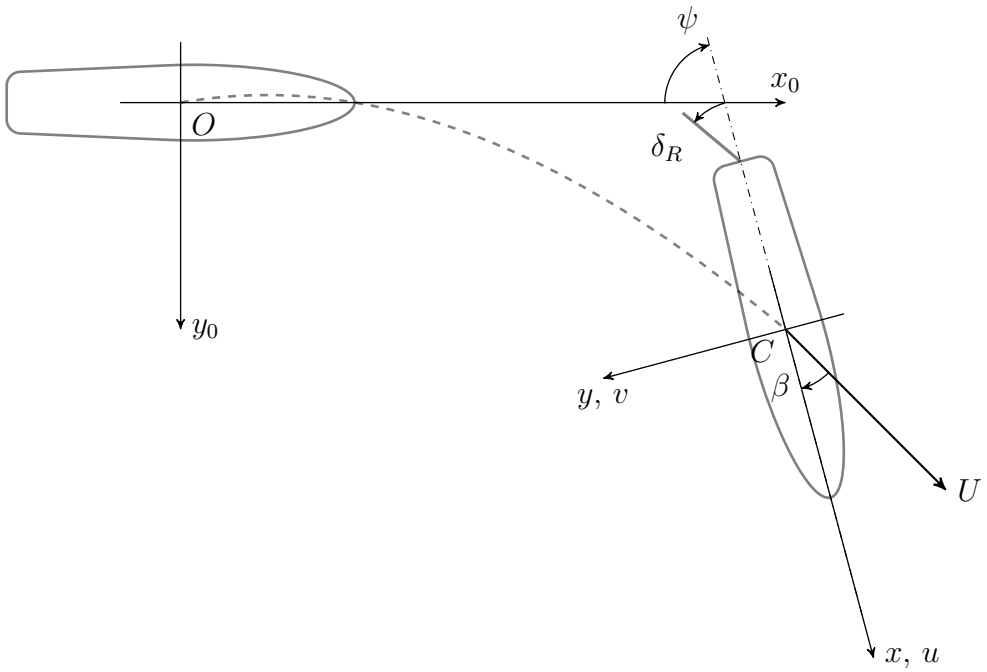

Figure 3.1.: Velocity components and angles in maneuvering

The hydrodynamical forces are defined in the body-fixed frame with X being the force in

longitudinal direction and Y the force in transverse direction. K is the roll moment and N is the yaw moment with respect to the main frame at $L_{PP}/2$. The forces and moments are generally non-dimensionalized as shown in the following equations. The non-dimensional version is denoted by a prime ($'$).

$$X' = \frac{X}{0.5\rho U^2 L_{PP} T} , \qquad Y' = \frac{Y}{0.5\rho U^2 L_{PP} T} , \tag{3.3}$$

$$K' = \frac{K}{0.5\rho U^2 L_{PP}^2 T} , \qquad N' = \frac{N}{0.5\rho U^2 L_{PP}^2 T} . \tag{3.4}$$

The velocity components can also be given in a non-dimensional form as

$$u' = \frac{u}{U} , \qquad v' = \frac{v}{U} , \qquad p' = \frac{pL_{PP}}{U} , \qquad r' = \frac{rL_{PP}}{U} , \tag{3.5}$$

$$\dot{u}' = \frac{\dot{u}L_{PP}}{U} , \qquad \dot{v}' = \frac{\dot{v}L_{PP}}{U} , \qquad \dot{p}' = \frac{\dot{p}L_{PP}^2}{U^2} , \qquad \dot{r}' = \frac{\dot{r}L_{PP}^2}{U^2} . \tag{3.6}$$

The IMO has developed a set of criteria for achieving satisfactory maneuvering behavior [49], which includes turning ability, initial turning ability, yaw-checking and course-keeping abilities and stopping ability. The standard maneuvers identify significant qualities for the evaluation of ship maneuvering characteristics.

Different test procedures have been established by the IMO to support the application of maneuvering standards, and to this end, they also provide standard procedures for testing trials. The IMO guide includes trial procedures that need to be performed in order to provide sufficient data for assessing ship maneuvering behavior with the defined criteria. The tests comprise turning circle maneuvers, zig-zag maneuvers and stopping tests. A detailed description of the different standard maneuvers is given by the IMO [48].

3.2 Modelling of hydrodynamic forces

When applying computationally fast simulation methods, e.g. the slender-body theory (see Section 3.3), the forces can be directly calculated during the time simulation. However, for more expensive methods, it is preferable to predetermine the forces and make them available during the time simulation. The hydrodynamic forces can be modelled in different ways to be available during the time simulation.

Generally, whole ship models, in which all components are modelled in one set of equations, are distinguished from MMG models, a modular concept in which each single component comprising of the hull, propeller and rudder is regarded separately (named after the Japanese Maneuvering Modeling Group (MMG), see Yasukawa and Yoshimura [125]).

The equation of motion for whole ship models can be written as

$$\boldsymbol{M}\dot{\boldsymbol{\nu}} = \boldsymbol{f}(u, v, p, r, \dot{u}, \dot{v}, \dot{p}, \dot{r}, \delta) \,, \tag{3.7}$$

where $\boldsymbol{f}$ denotes the hydrodynamic force acting on the entire system as a function of the velocity (u, v, p, r), the acceleration ($\dot{u}$, $\dot{v}$, $\dot{p}$, $\dot{r}$) and the rudder angle (δ).

For MMG models, the equation of motion is

$$\boldsymbol{M}\dot{\boldsymbol{\nu}} = \boldsymbol{f}_H + \boldsymbol{f}_P + \boldsymbol{f}_R \,, \tag{3.8}$$

with H denoting the hull, P the propeller and R the rudder.

The most popular method for modelling the hydrodynamic forces using the whole ship model is based on hydrodynamic derivatives and has been proposed by Abkowitz [4]. This approach is derived in the following. The MMG models concept is picked up in Section 3.3, where the forces acting on each separate component are deduced.

Following the concept of Abkowitz [4], the forces $\boldsymbol{f}$ in the 4DOF relevant for maneuvering can be described as a polynomial of u, v, p, r, $\dot{u}$, $\dot{v}$, $\dot{p}$, $\dot{r}$ and δ:

$$\boldsymbol{f} = (X(\boldsymbol{x})\; Y(\boldsymbol{x})\; K(\boldsymbol{x})\; N(\boldsymbol{x}))^T \,, \tag{3.9}$$

with

$$\boldsymbol{x} = (u\; v\; p\; r\; \dot{u}\; \dot{v}\; \dot{p}\; \dot{r}\; \delta)^T \,. \tag{3.10}$$

The forces include the effects of all participating components such as hull, rudder and propeller.

Building a Taylor-series expansion of the hydrodynamic force functions $X(\boldsymbol{x})$, $Y(\boldsymbol{x})$, $K(\boldsymbol{x})$ and $N(\boldsymbol{x})$ at

$$\boldsymbol{x}_0 = (u_0\; 0\; 0\; 0\; 0\; 0\; 0\; 0\; 0)^T \tag{3.11}$$

gives

$$X(\boldsymbol{x}) \approx X(\boldsymbol{x}_0) + \sum_{i=1}^{n} \left(\frac{\partial X(\boldsymbol{x})}{\partial x_i}|_{x_0}\Delta x_i + \frac{1}{2}\frac{\partial^2 X(\boldsymbol{x})}{(\partial x_i)^2}|_{x_0}\Delta x_i^2 + \frac{1}{6}\frac{\partial^3 X(\boldsymbol{x})}{(\partial x_i)^3}|_{x_0}\Delta x_i^3 \right) \,, \tag{3.12}$$

$$Y(\boldsymbol{x}) \approx Y(\boldsymbol{x}_0) + \sum_{i=1}^{n} \left(\frac{\partial Y(\boldsymbol{x})}{\partial x_i}|_{x_0}\Delta x_i + \frac{1}{2}\frac{\partial^2 Y(\boldsymbol{x})}{(\partial x_i)^2}|_{x_0}\Delta x_i^2 + \frac{1}{6}\frac{\partial^3 Y(\boldsymbol{x})}{(\partial x_i)^3}|_{x_0}\Delta x_i^3 \right) \,, \tag{3.13}$$

$$K(\boldsymbol{x}) \approx K(\boldsymbol{x}_0) + \sum_{i=1}^{n} \left(\frac{\partial K(\boldsymbol{x})}{\partial x_i}|_{x_0}\Delta x_i + \frac{1}{2}\frac{\partial^2 K(\boldsymbol{x})}{(\partial x_i)^2}|_{x_0}\Delta x_i^2 + \frac{1}{6}\frac{\partial^3 K(\boldsymbol{x})}{(\partial x_i)^3}|_{x_0}\Delta x_i^3 \right) \,, \tag{3.14}$$

$$N(\boldsymbol{x}) \approx N(\boldsymbol{x}_0) + \sum_{i=1}^{n} \left(\frac{\partial N(\boldsymbol{x})}{\partial x_i}|_{x_0}\Delta x_i + \frac{1}{2}\frac{\partial^2 N(\boldsymbol{x})}{(\partial x_i)^2}|_{x_0}\Delta x_i^2 + \frac{1}{6}\frac{\partial^3 N(\boldsymbol{x})}{(\partial x_i)^3}|_{x_0}\Delta x_i^3 \right) \,, \tag{3.15}$$

where $\Delta\boldsymbol{x} = \boldsymbol{x} - \boldsymbol{x}_0 = (\Delta x_1\ \Delta x_2\ ...\ \Delta x_9)^T$.

In principal, higher-order Taylor-series expansions can be derived. An important issue that must be addressed is the exact degree to which it needs to be extended in order to ensure that the principal nonlinear hydrodynamic effects are described correctly. However, it is also necessary to consider to what extent it is necessary to retain a great number of terms for a reasonably accurate description of maneuvers.

Abkowitz assumes that a third-order Taylor series can describe most ship maneuvers. For the acceleration terms, only first-order approximations are considered and a coupling between the acceleration and the velocity terms can be neglected.

A port/starboard symmetry yields further simplifications. For the symmetric force X, the symmetric motion (u) only has odd powers; while the asymmetric motions (v, r, δ) only have even powers. The other way around is valid for the asymmetric forces Y, K, N. Constant terms are kept to describe the force and moment due to asymmetric effects from single-screw propellers.

Several authors report that simulations of standard ship maneuvers using these assumptions yield satisfactory results (see e.g. Fossen [33], Cura Hochbaum [21], Schoop [89], Schoop-Zipfel et al. [93], Stern et al. [100]). When applying the assumptions, the forces $X(\boldsymbol{x})$, $Y(\boldsymbol{x})$, $K(\boldsymbol{x})$ and $N(\boldsymbol{x})$ can be written as

$$\begin{aligned} X =& X_0 + X_{\dot{u}}\dot{u} + X_u\Delta u + X_{uuu}\Delta u^3 + X_{vv}v^2 + X_{rr}r^2 \\ &+ X_{\delta\delta}{\delta_R}^2 + X_{vvu}v^2\Delta u + X_{rru}r^2\Delta u + X_{\delta\delta u}{\delta_R}^2\Delta u \\ &+ X_{v\delta}v\delta_R + X_{r\delta}r\delta_R + X_{vru}vr\Delta u + X_{v\delta u}v\delta_R\Delta u + X_{r\delta u}r\delta_R\Delta u + X_{r\delta v}r\delta_R v\ , \end{aligned} \tag{3.16}$$

$$\begin{aligned} Y =& Y_0 + Y_{\dot{v}}\dot{v} + Y_{\dot{r}}\dot{r} + Y_{uu}\Delta u^2 + Y_v v + Y_{vvv}v^3 + Y_{vrr}vr^2 \\ &+ Y_{v\delta\delta}v{\delta_R}^2 + Y_{vu}v\Delta u + Y_{vuu}v\Delta u^2 + Y_r r + Y_{rrr}r^3 + Y_{rvv}rv^2 \\ &+ Y_{r\delta\delta}r{\delta_R}^2 + Y_{ru}r\Delta u + Y_{ruu}r\Delta u^2 + Y_\delta\delta_R + Y_{\delta\delta\delta}{\delta_R}^3 \\ &+ Y_{\delta vv}\delta_R v^2 + Y_{\delta rr}\delta_R r^2 + Y_{\delta u}\delta_R\Delta u + Y_{\delta uu}\delta_R\Delta u^2 + Y_{vr\delta}vr\delta_R\ , \end{aligned} \tag{3.17}$$

$$\begin{aligned} K =& K_0 + K_{\dot{v}}\dot{v} + K_{\dot{r}}\dot{r} + K_{uu}\Delta u^2 + K_v v + K_{vvv}v^3 + K_{vrr}vr^2 \\ &+ K_{v\delta\delta}v{\delta_R}^2 + K_{vu}v\Delta u + K_{vuu}v\Delta u^2 + K_r r + K_{rrr}r^3 + K_{rvv}rv^2 \\ &+ K_{r\delta\delta}r{\delta_R}^2 + K_{ru}r\Delta u + K_{ruu}r\Delta u^2 + K_\delta\delta_R + K_{\delta\delta\delta}{\delta_R}^3 \\ &+ K_{\delta vv}\delta_R v^2 + K_{\delta rr}\delta_R r^2 + K_{\delta u}\delta_R\Delta u + K_{\delta uu}\delta_R\Delta u^2 + K_{vr\delta}vr\delta_R\ , \end{aligned} \tag{3.18}$$

$$
\begin{aligned}
N =& N_0 + N_{\dot{v}}\dot{v} + N_{\dot{r}}\dot{r} + N_{uu}\Delta u^2 + N_v v + N_{vvv}v^3 + N_{vrr}vr^2 \\
&+ N_{v\delta\delta}v{\delta_R}^2 + N_{vu}v\Delta u + N_{vuu}v\Delta u^2 + N_r r + N_{rrr}r^3 + N_{rvv}rv^2 \\
&+ N_{r\delta\delta}r{\delta_R}^2 + N_{ru}r\Delta u + N_{ruu}r\Delta u^2 + N_\delta \delta_R + N_{\delta\delta\delta}{\delta_R}^3 \\
&+ N_{\delta vv}\delta_R v^2 + N_{\delta rr}\delta_R r^2 + N_{\delta u}\delta_R \Delta u + N_{\delta uu}\delta_R \Delta u^2 + N_{vr\delta}vr\delta_R \, .
\end{aligned} \tag{3.19}
$$

The hydrodynamic derivatives are defined using the notation

$$
F_0 = F(\boldsymbol{x}_0) \, , \qquad F_{x_i} = \frac{\partial F(\boldsymbol{x})}{\partial x_i}|_{\boldsymbol{x}_0} \, ,
$$

$$
F_{x_i x_j} = \frac{1}{2}\frac{\partial^2 F(\boldsymbol{x})}{\partial x_i \partial x_j}|_{\boldsymbol{x}_0} \, , \qquad F_{x_i x_j x_k} = \frac{1}{6}\frac{\partial^3 F(\boldsymbol{x})}{\partial x_i \partial x_j \partial x_k}|_{\boldsymbol{x}_0} \, ,
$$

for $F \in \{X, Y, K, N\}$ and $i,\ j,\ k = 1...9$.

The hydrodynamic derivatives are generally given in the $\hat{K}$ frame, i.e. in body-fixed coordinates, while the origin C is at the main frame ($L_{PP}/2$).

Simulation example

The hydrodynamic derivatives presented by Cura Hochbaum et al. [22] are used to calculate the hydrodynamic forces acting on the KVLCC2 during standard maneuvers. The resulting turning circle and zig-zag maneuvers are shown in Figures 3.2 and 3.3, respectively. The figures compare the simulated results with measured maneuvers (benchmark data from SIMMAN 2008 [99]).

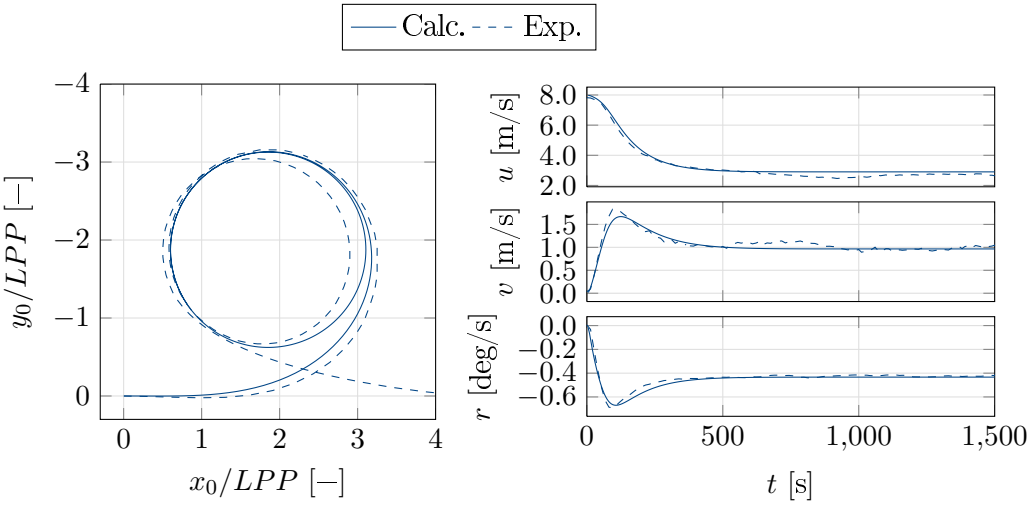

Figure 3.2.: −35° turning circle of KVLCC2 calculated with derivatives from Cura Hochbaum et al. [22]; measurements from MARIN [99]

The simulated turning circle maneuver shows a very good agreement with the measured data.

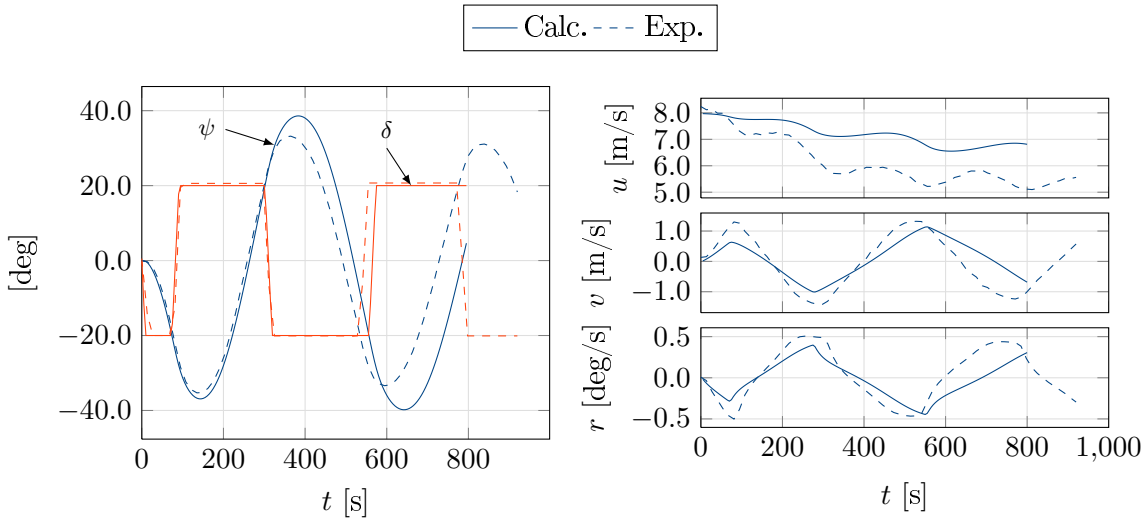

Figure 3.3.: $-20°/-20°$ zig-zag maneuver of KVLCC2 calculated with derivatives from Cura Hochbaum et al. [22]; measurements from MARIN [99]

However, deviations can be seen in the zig-zag maneuver. Despite the large amount of used hydrodynamic derivatives and the extensive computational effort in connection with this (see Section 3.3), there is a considerable deviation of the overshoot angles. Even more derivatives are needed to achieve a better agreement in this maneuver.

Ćoncluding, it can be said that hydrodynamic derivatives can be a useful basis for determining arbitrary maneuvers, but an extensive computational effort is necessary for determining a total set of derivatives.

3.3 Prediction of hydrodynamic forces

The forces acting on different hulls and their appendages are introduced in this section. Further, methods for identifying the forces are given.

3.3.1 Propulsion

In maneuvering model tests, the propeller rate of rotation is classically kept constant at the self-propulsion point of either the model or of the full scale ship (ITTC Manoeuvring Committee [53]). However, this will not be the case for real ship maneuvers. The varying flow situations at the propeller during the maneuver will result in a fluctuating torque. Depending on the installed engine, these torque variations will result in a change of the propeller rate of rotation. This becomes even more important in a seaway due to the oscillatory motion of the waves.

Mathematical models for simulating the engine are presented by different authors. A short review on different models is given in the review on previous work, see Section 1.2. For the present work, it is not necessary to model the engine in each detail since only the effect on the propulsion is of interest, i.e. the dynamic rate of rotation of the propeller. In the present work, a model for diesel-electric engines is developed and implemented. Models to describe the behavior of diesel engines can e.g. be found in Haack [39] and Wirz [117].

A diesel-electric transmission system consists of a diesel engine, a generator and an electric traction motor. The diesel engine powers the generator to produce electricity for the traction motor. For the behavior of the propulsion, the electrical generator is of minor interest and it is assumed that enough electrical power is delivered to the traction motor.

The hydrodynamic torque at the propeller due to the inflow and the number of revolutions is available as dimensionless coefficient in the open water diagram of the propeller. The open water diagram can be obtained with open water tests in a model basin (see e.g. Kuiper [64]) or from numerical calculations (see e.g. Hundemer [47]). This torque is the torque demand of the propeller and is opposed to the torque generated by the engine. If these torques are equal, the propeller rate of rotation is constant. The change of the propeller rate of rotation can be computed with the equation of motion, using the difference in the torque of the propeller and the engine. The time derivative of the speed of rotation of the propeller yields

$$\frac{dn}{dt} = \frac{Q_m - Q_p}{2\pi(I_{Shaft} + I_{Prop})} \,. \tag{3.20}$$

Q_m and Q_p are the torque of the engine and the propeller, respectively, and I is the moment of inertia of the propeller, shaft, gearbox and engine. Added mass effects have to be considered since these will significantly change the moment of inertia. The moment of inertia of the propeller I_{Prop} is described as a function of the current pitch ratio. The moment of inertia of the shaft I_{Shaft} is fixed and also includes the gearbox and the rotating parts of the engine. The added mass is considered as a ratio of the mass inertia of the propeller and is generally given by the propeller manufacturer.

The simulation model distinguishes between two different operation modes. As long as the propeller has a positive torque, the speed of rotation of the propeller shaft is estimated with respect to the available power. When the torque becomes negative, wind-milling occurs and the propeller is driven by the inflow. For wind-milling, the engine torque is set to zero and the speed of rotation increases due to torque generated by the propeller inflow.

The computational algorithm used for the propulsion determination is given in Figure 3.4.

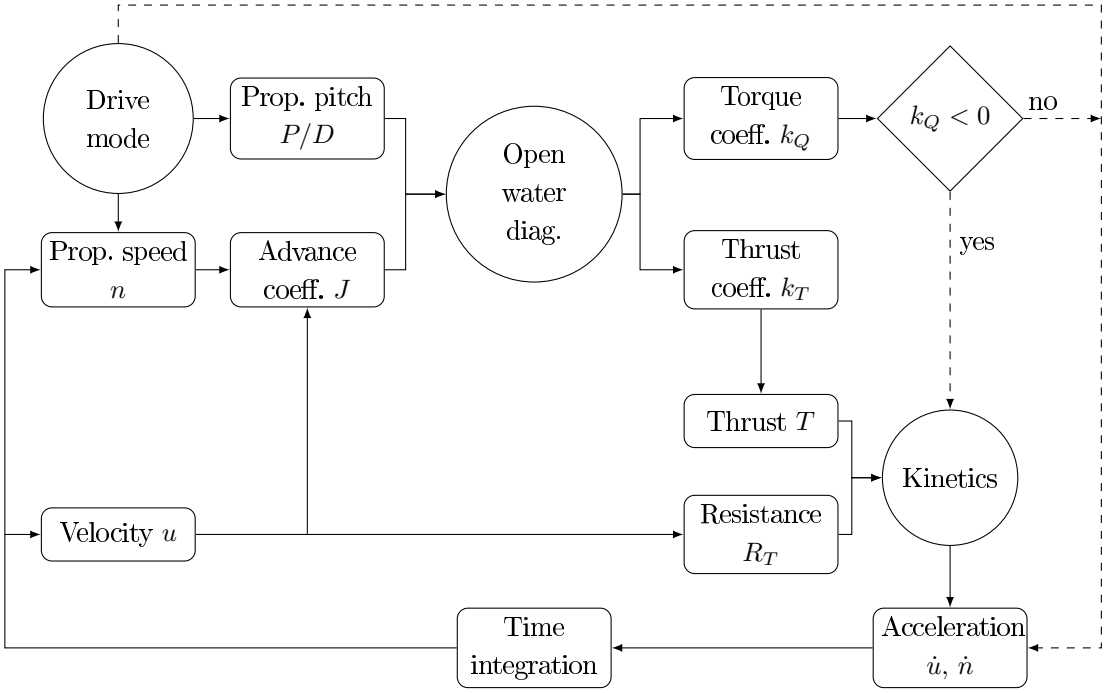

Figure 3.4.: Computational algorithm of propulsion

Motor

Alternative current motors exist in two main types: synchronous and asynchronous motors. Figure 3.5 shows a typical behavior of an asynchronous drive, where Q is the torque and ω the angular frequency.

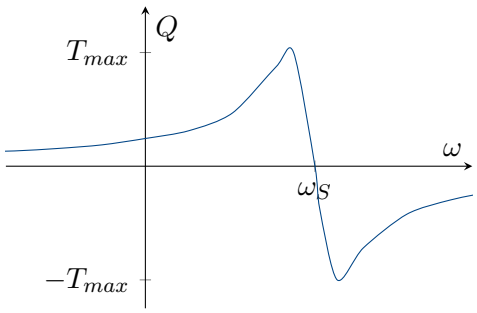

Figure 3.5.: Typical RPM to torque line for an asynchronous motor

The frequency ω_S where the curve crosses the abscissa is called synchronous frequency (where the slip is zero). The motor is generally operated at a frequency a little below ω_S, so that the motor produces a torque but still has enough reserve until reaching the maximum torque Q_{max}. The synchronous frequency can be set by regulating the electrical AC frequency using the transformer (see Figure 3.6).

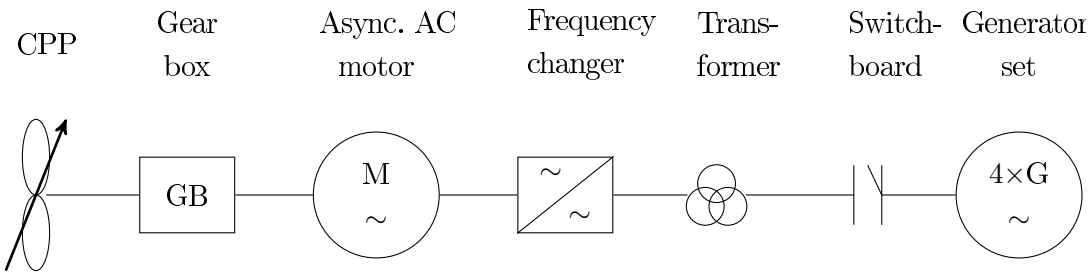

Figure 3.6.: Arrangement for a propulsion string

The frequency changer controls the electrical frequency, which is equal to the synchronous frequency of the motor. It is therefore possible to control the rate of rotation independently of the load torque, assuming an appropriate behavior on the generator side.

However, the electrotechnical specificities are not necessary to be implemented in the numerical model for the maneuvering simulations. The engine, its supply and the controller can be modelled by a common control model.

Engine control

The engine and frequency changer are controlled by a PI-controller, as shown in Figure 3.7. It is characterized by two constants, K_n (proportionality constant) and T_n (integration time). Q is the torque and n the shaft revolutions. A star $*$ means the target values. Further, t is the current time and h is the time step.

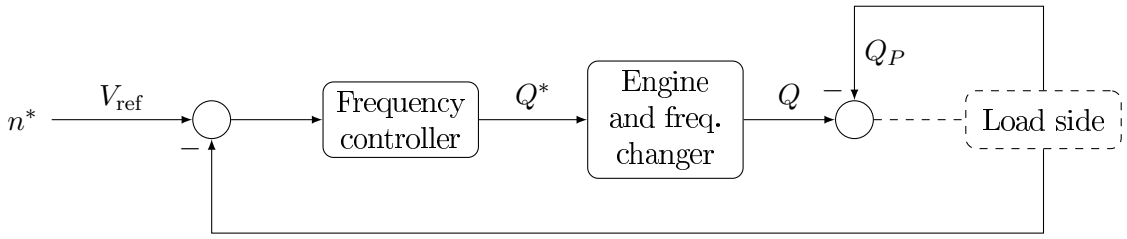

Figure 3.7.: Control strategy for the engine

The PI law is given by

$$Q^*(t) = K_p e(t) + \frac{K_p}{T_n} \int_0^t e d\tau \ , \tag{3.21}$$

where $e(t) = n^* - n$. If both sides are differentiated with respect to time, it becomes

$$\dot{Q}^*(t) = K_p \dot{e}(t) + \frac{K_p}{T_n} e(t) \ . \tag{3.22}$$

Applying the first-order approximation gives

$$\frac{Q^*(t) - Q^*(t-h)}{h} = K_p \frac{e(t) - e(t-h)}{h} + \frac{K_p}{T_n} e(t) \,, \tag{3.23}$$

which can be rewritten as

$$Q^*(t) = Q^*(t-h) + K_p(e(t)(1 + \frac{h}{T_n}) - e(t-h)) \,. \tag{3.24}$$

Engine response and latency

The control value of the torque is given by the PI controller, but the engine does not instantaneously produce this torque. Therefore, an engine lag time is defined. In practice, this means that the engine will use the target torque of a past timestep (called $n_{eng.lag}$). For a 5MW engine, the lag time usually lies around $T_1 = 250$ms.

The torque difference to the propeller torque is related to the rate of change of the shaft revolutions by means of the inertia,

$$\dot{n} = \frac{Q^*(n_{eng.lag}) - Q_{Prop}}{2\pi(I_{Shaft} + I_{Prop})} \cdot 60 \,. \tag{3.25}$$

Propeller Forces

Thrust and torque of the propeller are determined from the open water diagram, see Figure 3.4. The advance coefficient J yields

$$J = \frac{u_A}{n \cdot D} \,, \tag{3.26}$$

with n being the number of revolutions of the propeller and D its diameter. For a given propeller, the thrust and the torque can be calculated via the indices k_T and k_Q from the open water diagram. Subsequently, thrust and torque can be calculated:

$$T_P = \rho \cdot k_T \cdot n \cdot |n| \cdot D^4 \,, \tag{3.27}$$

$$Q = \rho \cdot k_Q \cdot n \cdot |n| \cdot D^5 \,. \tag{3.28}$$

The thrust coefficient k_T can be described by a cubic function of the advance coefficient J for a fixed pitch as

$$k_T = k_{T,0} - k_{T,1} J - k_{T,2} J^2 \,. \tag{3.29}$$

An interpolation procedure is applied to obtain the thrust and torque coefficients for varying

pitch ratios of the propeller. The thrust for each pitch can be determined with the equation given above.

Interaction of hull and propeller

The thrust deduction due to the interaction of the hull and the propeller is accounted for with the help of the thrust deduction factor t, reducing the thrust to

$$T_P \rightarrow (1-t) \cdot T_P \; . \tag{3.30}$$

Therefore, the force on the hull is assumed to be linearly proportional to the thrust. This is a common practice and is valid for forward thrust, but in the case of negative thrust, the problem has to be studied anew. In this case, the force on the hull is not a suction anymore but a thrust. Nevertheless, it counteracts the effect of the propeller and reduces the absolute value of the thrust in the same way as it does for forward thrust.

Haack [39] investigates this effect on a single and a double screw ship with a potential method. He concludes that the use of a thrust deduction coefficient is still valid but it should be different from the one at forward thrust. The effect is greater than in normal condition, thus the coefficient has to be greater.

Generally, the thrust deduction factor from the open water test with design condition yields a shorter stopping distance in a crash stop maneuver [39]. Calculations of Haack [39] with a newly developed CFD-method show a three to five times larger thrust deduction than the thrust deduction factor from design condition. Haack shows that this results in a much better agreement of the simulations with full scale measurements. Gronarz [37] states that increasing the resistance by 20% for a backing ship gives realistic results.

Another influence of the hull is that the wake generates a non-homogeneous inflow at the propeller. This is simplified to an equivalent inflow speed u_A defined by Son and Nomoto [98] as

$$u_A = u[(1-w_p) + \tau(v + x_p \cdot r)^2] \; , \tag{3.31}$$

where w_p is the wake fraction and τ is an experimental constant. This effect is not affected by the direction of the thrust, as the inflow does not change its direction.

Simulation example

The developed engine model is applied to simulate crash stop maneuvers for the seismic research vessel HAI YANG SHI YOU 720. It is a twin-screw ship and due to the symmetry, no course deviation is assumed during stopping. Therefore, only the resistance is included as hull forces.

The vessel was built in 2011 by Shanghai Shipyard. It is equipped with a diesel-electric engine manufactured by Siemens. Sea trial measurements of the engine characteristics during the crash stop maneuvers are available for validation (see Schoop-Zipfel et al. [94]).

The vessel has a length between perpendiculars of 96.6m. It is equipped with a diesel-electric propulsion system combined with two electric motors, each with a rating of 4500kW driving two controllable-pitch propeller (CPP) in a nozzle. The main dimensions and a picture of the vessel can be found in Table 3.1.

Table 3.1.: Main dimensions of HAI YANG SHI YOU 720 (Image source: www.cosl.com.cn)

Length L_{OA}	[m]	108.3
Breadth B	[m]	24.0
Draft D	[m]	9.6
Speed U	[kn]	16
Displacement m	[t]	ca. 5000
Gross tonnage	[t]	ca. 13000
Towing capacity	[t]	min. 100

Different scenarios of stopping the ship are investigated. The scenarios are simulated and the results of the simulations are compared to the measurements taken during sea trial. The ship speed, the speed of rotation and the pitch angle of the propeller are varied during the simulation. The four test cases (A, B, C and D) are summed up in Table 3.2.

In the first test case A, the electric motors are decoupled at a ship speed of 16 knots. In this sailing mode, the shaft speed directly depends on the ship's speed, as the torque from the engine is zero. Due to technical reasons, the pitch angle is reduced to zero when the engine is decoupled. In cases B and C, the target number of revolutions is kept constant during the stop maneuver, while reducing the pitch angle to the maximum negative value. In case D, the target number of revolutions is increased during the stop maneuver in order to increase the backward thrust and decrease the possibility of wind-milling.

Table 3.2.: Testing conditions for stop maneuver of HAI YANG SHI YOU 720

Case	Initial ship speed [kn]	Propeller revolutions [rpm]	Initially delivered power [kW]	Propeller pitch [P/D]
A	16	145	2x 0	from 1.1767 to 0
B	12.8	129.1	2x 2,173	from 1.0297 to -0.6556
C	16	145	2x 4,500	from 1.1767 to -0.6556
D	12.8	from 129.1 to 145	2x 2,173	from 1.0297 to -0.6556

Case A In case A, the electric motor is electrically decoupled from the propellers when the maneuver starts. As stated above, the propeller pitch angle is reduced to zero when the electric motor is decoupled.

Figure 3.8 shows the behavior of different characteristic values during the stopping process. Important parameters during stopping are ship speed, propeller speed of rotation, propeller pitch ratio, torque and power. The solid curves represent the calculated values and the dashed curves are the results from the sea trial measurements. Because the vessel has two propellers, for each measured value there are two curves: one for the portside propeller and the other for the starboard side propeller. In the simulations, no distinction is made between the propellers due to symmetry.

Before beginning the maneuver, there is perfect agreement between the calculated and the measured values. Once the maneuver starts it can be seen that the calculated and measured values of torque and power instantly fall to zero. Calculated and measured pitch change with the same gradient. The curve of the propeller rate of rotation indicates that wind-milling occurs shortly after the maneuver begins. This tendency is captured by the measurements and the calculations, but the calculated rate of rotation increases more than the measured values. The results show that the initial value is not exceeded, so no danger for the propulsion system should be expected. After approximately 120s, an unplanned switch on of the electric motor drive was initialized. This resulted in an oscillation in the measured torque. Simultaneously, the measured rate of rotation increases, which indicates a torque intake condition. This scenario can be excluded from the dynamic analysis.

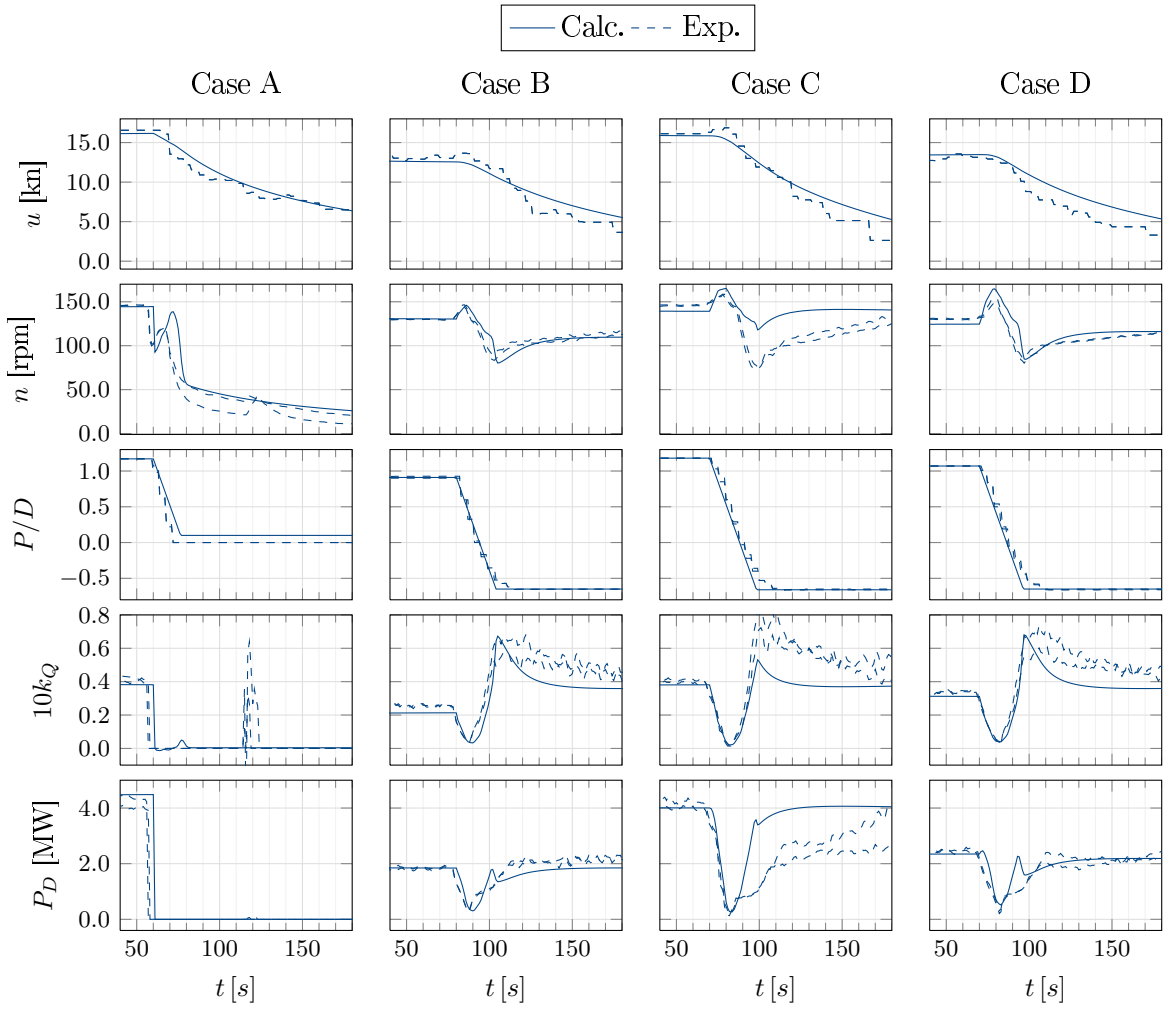

Figure 3.8.: Stopping simulation of HAI YANG SHI YOU 720

Case B In case B, the target propeller rate of rotation is held constant during the entire maneuver. With the beginning of the maneuver, the propeller pitch angle is decreased. The different values over time are also plotted in Figure 3.8.

Due to the descreasing hydrodynamic torque at the propeller, the propeller speed increases until the engine control counterbalances. At approximately 90s, the torque starts increasing due to the inflow condition at the propeller. This results in a decrease of the propeller speed. Due to the predefined control parameters, the propeller speed increases very slowly and does not reach the target value within the time of the maneuver.

Case C Case C is similar to case B. The target rate of rotation is kept constant while the propeller pitch is decreased. However, the approach speed is higher. Similar tendencies as in case B can be seen for the characteristic parameters (Figure 3.8).

Case D Stopping is performed by constantly decreasing the pitch angle while increasing the target propeller rate of rotation to a predefined value. The behavior of the characteristic values is very comparable to case B, as seen from Figure 3.8. The increase of the propeller speed with the beginning of the maneuver is higher than in case B due to the higher target rate of rotation. However, the drop of the propeller speed and the behavior of the torque and power are almost equal to case B. Again, the propeller rate of rotation does not reach the target value.

Concluding remarks The numerical model used to desribe the ship propulsion is applied to the seismic research vessel HAI YANG SHI YOU 720. Special attention is paid to the behavior of the propeller rate of rotation. A satisfactory correlation is found between the simulations and the measurements. Wind-milling can be reliably predicted. The general trends of the engine control can be captured.

3.3.2 Rudder forces

The rudder force calculation is based on semi-empirical formulae, following the approach proposed by Söding [105]. Further details are also given in Bertram [12]. The velocity and the radius of the propeller slipstream far behind the propeller are, according to the slipstream theory,

$$u_\infty = u_A\sqrt{1+c_{Th}}\,, \tag{3.32}$$

$$r_\infty = r_0\sqrt{0.5(1+u_A/u_\infty)}\,. \tag{3.33}$$

r_0 is the radius of the propeller $(D/2)$ and c_{Th} is the thrust loading coefficient:

$$c_{Th} = \frac{T}{\frac{1}{2}\rho u_a^2(0.25\pi D^2)}\,. \tag{3.34}$$

Usually, the slipstream is not completely contracted at the rudder. Its radius and axial velocity can then be approximated as

$$r_x = r_0\frac{0.14(r_\infty/r_0)^3 + r_\infty/r_0\cdot(x/r_0)^{1.5}}{0.14(r_\infty/r_0)^3+(x/r_0)^{1.5}}\,, \tag{3.35}$$

$$u_x = u_\infty\frac{r_\infty^2}{r_x^2}\,, \tag{3.36}$$

where x is denoting the position behind the propeller plane. Söding proposes to use the position of the rudder's centre of area within the slipstream to calculate the rudder force and moment.

The rudder inflow is not uniform due to the finite lateral extent of the propeller slipstream so that the rudder lift has to be corrected. This is done by multiplying the rudder lift that is determined with the velocity within the slipstream by the correction factor λ:

$$\lambda = (\frac{u_A}{u_x})^f \ , \quad \text{with} \quad f = 2(\frac{2}{2 + d/c})^8 \ . \tag{3.37}$$

Here u_A is the rudder approach speed outside of the propeller slipstream. d is the slipstream radius and c is the rudder chord length in the region of the slipstream.

The angle of attack follows from the rudder angle δ, the mean longitudinal flow speed u_x and the mean transverse flow speed at the rudder $v_R = -(v + x_R \cdot r)$ to

$$\alpha = \delta + \arctan(\frac{v_R}{u_x}) \ . \tag{3.38}$$

The coefficients of the lift, drag and moment of the rudder can be approximated according to Söding [107] as

$$C_L = 2\pi \frac{\Lambda(\Lambda + 0.7)}{(\Lambda + 1.7)^2} \sin\alpha + C_Q \sin\alpha |\sin\alpha| \cos\alpha \ , \tag{3.39}$$

$$C_D = 1.1 \frac{C_{L1}^2}{\pi\Lambda} + C_Q |\sin\alpha|^3 + C_{D0} \ , \tag{3.40}$$

$$C_M = (C_{L1}\cos\alpha + C_{D1}\sin\alpha)\left(0.47 - \frac{\Lambda + 2)}{4(\Lambda + 1)}\right) + 0.75(C_{L2}\cos\alpha + C_{D2}\sin\alpha) \ . \tag{3.41}$$

The lift and drag forces are determined from these coefficients. Whereas the propeller inflow velocity u_A is used outside of the propeller slipstream and for the force inside of the stream, the propeller slipstream velocity is approximated using Söding's formulae [105]. The lift is acting perpendicular to, and the drag in the direction of the local inflow given by $\arctan(\frac{v_R}{u_x})$. Lift and drag are then separated in x- and y-direction. The y-component is multiplied by the factor $(1 + a_H)$ to account for the influence of the hull in front of the rudder.

$$a_H = (1 + (4.9e/T + 3c/T)^2)^{-1} \tag{3.42}$$

Here T is the draft of the ship and e the mean distance between the leading edge of the rudder and the aft end of the hull.

The yaw moment due to the rudder follows from multiplying the y-component of the rudder

force with the x-coordinate of the attack point. This is assumed to be

$$\delta x = \frac{0.3T}{e/T + 0.46} \tag{3.43}$$

in front of the rudder axis.

For the roll moment, the transverse force is assumed to attack at the barycenter of the rudder.

Figure 3.9 shows the total force on a KVLCC2 for different rudder angles. The simulated results are opposed to measurements from the Hyundai Maritime Research Institute, South-Korea (HMRI) [102] and the National Maritime Research Institute of Japan (NMRI) [127], published via the SIMMAN 2014 workshop [81]. The figure reveals that the influence of the rudder on the total forces can be predicted very well with the semi-empirical method of Söding [105].

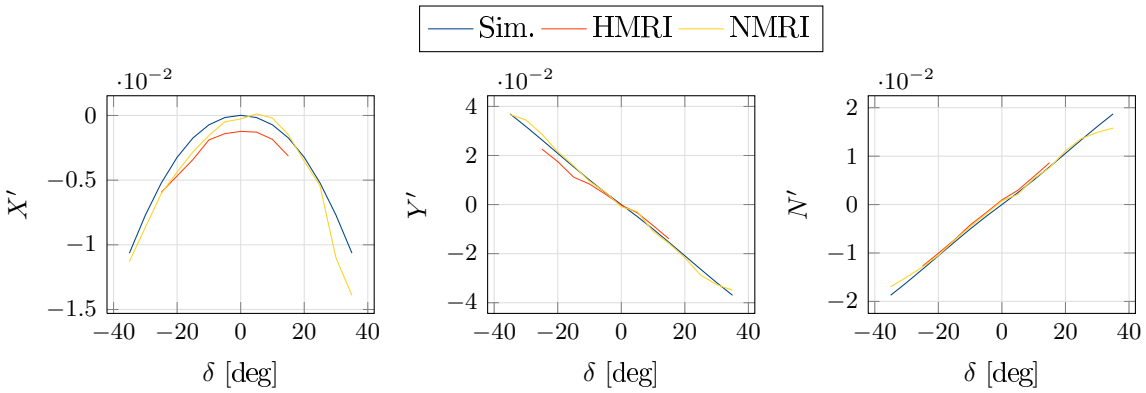

Figure 3.9.: Total force on KVLCC2 over rudder angle; measurements from HMRI [102] and NMRI [127]

3.3.3 Hull forces

The hull forces are generally split into velocity dependent damping forces and acceleration dependent added mass forces. The damping forces are influenced to a large degree by viscous effects such as friction and separation. These effects have a minor influence on the added mass forces. Subsequently, potential theory can properly determine the inertial forces. Corrections are necessary for properly determining the velocity-dependent forces with potential theory. These corrections can be applied in different ways.

Söding [105] proposes to simulate the hull forces based on slender-body theory. According to this theory, the transverse acceleration of the water next to the ship generates a horizontal force per ship length in transverse direction. This force can be integrated over the ship length to obtain the entire hull forces and moments. Söding [105] suggests different corrections to

this approach to model the effects of the real flow.

In three-dimensional potential theory, the velocity dependent forces can be calculated by modelling vortices for slender ships with salient hull features. Therefore, a wake sheet is shed from salient hull features (Greeley [35]). However, the strength of these vortices is difficult to determine for blunt bodies like ship hulls, which do not have a sharp edge leading to separation. Alternatively, a force correction based on the slender-body theory can be applied (Söding [110]).

RANS methods can determine the acting forces with very high accuracy. However, the computational effort increases with increasing accuracy. An extensive amount of time is needed to determine all the required forces of the maneuvering simulations.

Slender-body theory

The basis of the slender-body theory approach formulated by Söding [105] is the idea that the hull force in y-direction on a strip of length dx is equal to the change in time of the y-momentum of the water that is next to the hull at this strip. The amount of this water is the added mass of the specified hull section, the sectional added mass in sway $a_{22}^0(x)$. The added mass for zero frequency and low frequency, respectively, must be used for the maneuvering motion, which is denoted here with the superskript ^{0}.

The transverse momentum of the water per ship length follows subsequently to

$$a_{22}^0(x)(v + xr) \ . \tag{3.44}$$

The substantial derivative yields the force per length, which is integrated over the entire ship length L:

$$Y = \int_L (-\frac{\partial}{\partial t} + u\frac{\partial}{\partial x}) a_{22}^0(x)(v + xr)\, dx \ . \tag{3.45}$$

The minus sign is neccessary because the force of the water on the ship is considered and not the force of the ship on the water.

Equation (3.45) can be extended to obtain the moments around the x- and the z-axis, K and N, respectively. The force vector for all four degrees of freedom yields

$$\begin{pmatrix} X \\ Y \\ K \\ N \end{pmatrix} = \int_L \begin{pmatrix} 0 \\ 1 \\ 1 \\ x \end{pmatrix} (-\frac{\partial}{\partial t} + u\frac{\partial}{\partial x}) \left[\begin{pmatrix} 0 \\ a_{22}^0(x) \\ -z_y a_{22}^0(x) \\ a_{22}^0(x) \end{pmatrix} (v + xr) \right] dx \ , \tag{3.46}$$

where z_y is the z-coordinate of the center of the hydrodynamic mass in each section, i.e. the

height of the point of attack of the hydrodynamic transverse force and $z_y a^0_{22} = a^0_{42}$.

Söding [105] proposes empirical corrections to account for different influences.

The real flow is not only across the sections but also around the bow and the stern. To account for this fact, the terms including $\partial/\partial t$ are multiplied by the reduction factors k_1 and k_2. These factors are calculated for ellipsoids of revolution in Lamb [65] and can be approximated with:

$$k_1 = \sqrt{1 - 0.245\epsilon - 1.68\epsilon^2}\,, \qquad k_2 = \sqrt{1 - 0.76\epsilon - 4.41\epsilon^2}\,, \tag{3.47}$$

with $\epsilon = 2d/L$. So the acceleration part of the hull forces follows to

$$\begin{pmatrix} X_1 \\ Y_1 \\ K_1 \\ N_1 \end{pmatrix} = \int_L \begin{pmatrix} 0 \\ -k_1 a^0_{22}(x) \\ k_1 a^0_{42}(x) \\ -k_2 x a^0_{22}(x) \end{pmatrix} (k_1 \dot{v} + k_2 x \dot{r})\, dx\,. \tag{3.48}$$

For the parts including $u\partial/\partial x$, one has to distinguish if this term is applied to a^0_{22} and a^0_{42} or to $v + xr$. The derivatives of a^0_{22} and a^0_{42} have to be built on the fore ship, from the bow to the point where the flow presumably separates. These derivatives are omitted for the aft part of the ship because of the flow separation. This will generate a lifting effect comparable to the Kutta condition used in lifting foil theory.

The derivatives of $v + xr$ need to be integrated over the whole ship length. The steady part of the hull forces then becomes

$$\begin{aligned} \begin{pmatrix} X_2 \\ Y_2 \\ K_2 \\ N_2 \end{pmatrix} = u \begin{pmatrix} 0 \\ -a^0_{22}(x_m) \\ z_{ym} a^0_{22}(x_m) \\ -x_m a^0_{22}(x_m) \end{pmatrix} (v + x_m r) + ur \int_{x_a}^{x_m} \begin{pmatrix} 0 \\ a^0_{22}(x) \\ -a^0_{42}(x) \\ x a^0_{22}(x) \end{pmatrix} dx \\ - \int_{x_m}^{x_f} \begin{pmatrix} 0 \\ 0 \\ 0 \\ a^0_{22}(x) \end{pmatrix} (v + xr)\, dx\,. \end{aligned} \tag{3.49}$$

The index f means fore and the index a aft of the ship. m is the position where the flow presumably separates, i.e. where a^0_{22} has a large negative gradient, mainly at the aft end of the skeg or in front of the propeller.

The slender-body theory does not provide any longitudinal forces. The following forces from

three-dimensional potential theory are added:

$$\begin{pmatrix} X_3 \\ Y_3 \\ K_3 \\ N_3 \end{pmatrix} = \begin{pmatrix} -A_{11}^0 \dot{u} \\ -A_{11}^0 ur \\ 0 \\ A_{11}^0 uv \end{pmatrix} . \tag{3.50}$$

A_{11}^0 is the added mass for longitudinal acceleration of the ship. This will also be approximated with an empirical formula following Lamb [65]:

$$A_{11}^0 = \frac{m}{\pi\sqrt{\rho L^3/m} - 14} . \tag{3.51}$$

The particular force components can be summed up and written in matrix notation as

$$\begin{pmatrix} X \\ Y \\ K \\ N \end{pmatrix} = \begin{pmatrix} X_1 \\ Y_1 \\ K_1 \\ N_1 \end{pmatrix} + \begin{pmatrix} X_2 \\ Y_2 \\ K_2 \\ N_2 \end{pmatrix} + \begin{pmatrix} X_3 \\ Y_3 \\ K_3 \\ N_3 \end{pmatrix} = \boldsymbol{A} \cdot \begin{pmatrix} \dot{u} \\ \dot{v} \\ \dot{p} \\ \dot{r} \end{pmatrix} + \boldsymbol{B} \cdot \begin{pmatrix} u \\ v \\ p \\ r \end{pmatrix} , \tag{3.52}$$

with

$$\boldsymbol{A} = \begin{pmatrix} A_{11}^0 & 0 & 0 & 0 \\ 0 & -k_1^2 \int_L a_{22}^0(x)dx & 0 & -k_1 k_2 \int_L x a_{22}^0(x)dx \\ 0 & k_1^2 \int_L a_{42}^0(x)dx & 0 & k_1 k_2 \int_L x a_{42}^0(x)dx \\ 0 & -k_1 k_2 \int_L x a_{22}^0(x)dx & 0 & -k_2^2 \int_L x^2 a_{22}^0 dx \end{pmatrix} , \tag{3.53}$$

$$\boldsymbol{B} = u \cdot \begin{pmatrix} 0 & 0 & 0 & 0 \\ 0 & -a_{22,m}^0 & 0 & -a_{22,m}^0 x_m + \int_{x_a}^{x_m} a_{22}^0 dx - A_{11}^0 \\ 0 & a_{42,m}^0 & 0 & a_{42,m}^0 x_m - \int_{x_a}^{x_m} a_{42}^0 dx \\ 0 & -x_m a_{22,m}^0 - \int_{x_m}^{x_f} a_{22}^0 dx + A_{11}^0 & 0 & -x_m^2 a_{22,m}^0 + \int_{x_a}^{x_m} x a_{22}^0 dx - \int_{x_m}^{x_f} x a_{22}^0 dx \end{pmatrix} , \tag{3.54}$$

where

$$\begin{aligned} a_{22,m}^0 &= a_{22}^0(x = x_m) , \quad a_{22}^0 = a_{22}^0(x) , \\ a_{42,m}^0 &= a_{42}^0(x = x_m) , \quad a_{42}^0 = a_{42}^0(x) . \end{aligned}$$

The slender-body theory does not contain any nonlinear terms. These can be calculated

similar to rudder forces with the stagnation pressure, the area and a drag coefficient C_D:

$$\begin{pmatrix} X_{NL} \\ Y_{NL} \\ K_{NL} \\ N_{NL} \end{pmatrix} = \frac{1}{2}\rho \int_L \begin{pmatrix} 0 \\ -1 \\ z_D \\ -x \end{pmatrix} (v + xr)\,|v + xr|\,C_D\,d\,dx\ , \tag{3.55}$$

with d being the draft of the respective section and z_D the z-coordinate of the point of attack of the drag force.

However, some experience is needed with the cross-flow drag coefficient to obtain reliable results.

Resistance

The slender-body theory cannot determine any forces in longitudinal direction. The resistance has to be calculated separately.

The basis for estimating the ship resistance needs to be model experiments or extensive CFD-calculations. The resistance is calculated as the sum of the residual resistance R_R and the skin friction resistance R_{F0}. The residual resistance can be obtained by model tests or CFD-calculations. The skin friction resistance coefficient can be calculated by using the ITTC 1957 correlation line:

$$c_{F0} = \frac{0.075}{(log_{10}R_n - 2)^2}\ . \tag{3.56}$$

According to Söding [105], the dependence of the resistance on v and r has to be taken into account with the coefficients X_{vv}, X_{rr} and X_{vr} that can be determined with model experiments. The resistance force in longitudinal direction follows to:

$$X = \frac{1}{2}\rho u^2 S_w \cdot (c_{F0} + c_R) + X_{vv}v^2 + X_{rr}r^2 + X_{vr}vr\ . \tag{3.57}$$

The contribution of the ship resistance to the force in y-direction and the yaw moment must be considered:

$$Y = R_{F0}(v + xr)/u\ , \tag{3.58}$$

$$N = R_{F0}L^2 r/(6u)\ . \tag{3.59}$$

Simulation example KVLCC2

The slender-body theory is applied to simulate standard maneuvers with the KVLCC2 tanker ship. Extensive results for validation are available for this hull, e.g. from the SIMMAN workshop 2008 [99] and 2014 [81]. The KVLCC2 is a tanker ship with bulbous bow and stern. Her main dimensions and frame plan are shown in Table 3.3.

Table 3.3.: Main dimensions and frame plan of KVLCC2

Dimensions		
L_{PP}	[m]	320.0
B	[m]	58.0
D	[m]	20.8
C_B	[–]	0.8101
C_M	[–]	0.9980
F_n	[–]	0.142

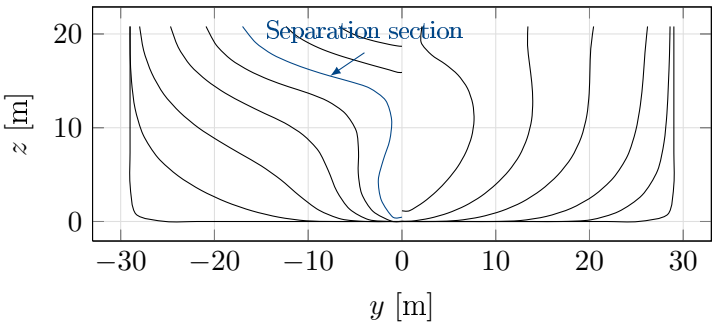

Figure 3.10 shows the distribution of the added mass over the ship length. The added mass is calculated using the open source strip methods PDSTRIP [111]. According to this figure, the sectional added mass is integrated from the bow to section 4 at $x_m = -150$m. This section is highlighted in the frame plan (Table 3.3) in blue. Figure 3.10 also shows the cross-flow drag coefficient per section of the KVLCC2.

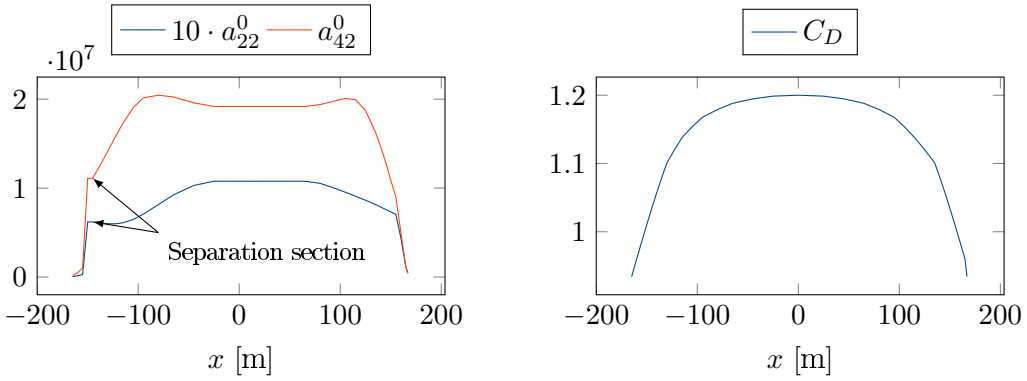

Figure 3.10.: Added mass (left) and cross-flow drag (right) per ship length of KVLCC2

The forces acting on the hull during pure drift and pure yaw motion are calculated and compared with measured results of NMRI [127]. Figure A.1 in Appendix A shows the comparison of the simulated and the measured drift force and yaw moment resulting from drift and from yaw motion. Most of the agreement appears to be fair. However, a deviation can be seen in the drift force resulting from yaw motion. The simulated drift force overestimates the

measured value. The uncertainty of the model test results is not known.

A direct maneuver simulation using the slender-body theory shows very promising results. A 35° turning circle maneuver is presented in Figure 3.11. The measurements were conducted at MARIN and published via the SIMMAN 2008 workshop [99]. The simulated tactical diameter deviates less than 1% from the measurements. However, the steady rate of turn is higher in the simulation.

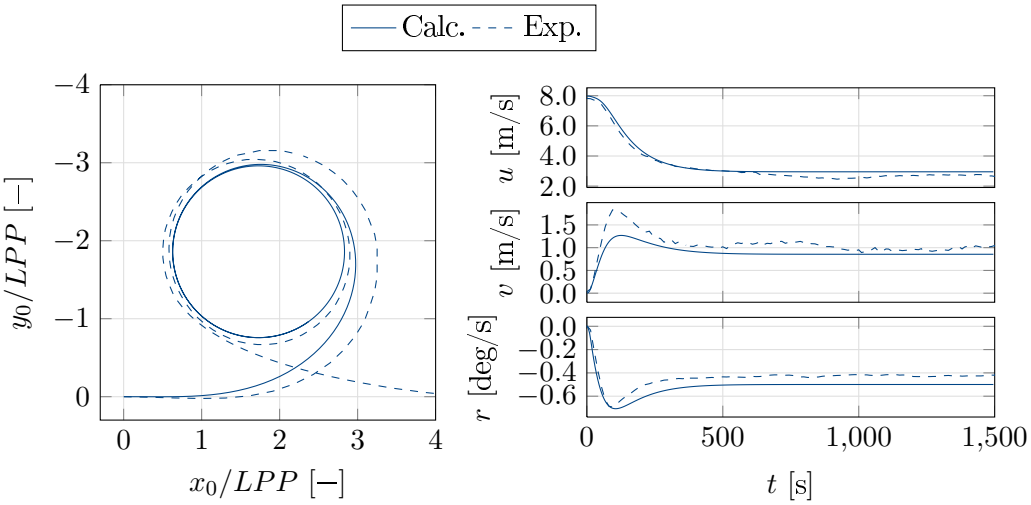

Figure 3.11.: −35° turning circle of KVLCC2; simulation with slender-body theory; measurements from MARIN [99]

The simulation of 20°/20° zig-zag maneuvers also shows acceptable agreement with measured results, see Figure 3.12. The first and the second overshoot angle have a deviation of 5% and 13%, respectively.

Simulation example S-175

Simulations of turning circle maneuvers are also presented for the S-175 container ship. The main dimensions and the frame plan are shown in Table 3.4. Yasukawa [122] conducted free-running model tests for this ship. The relevant data of the model and the resistance and thrust curves are given in Table 3.5. The added mass distribution is calculated with PDSTRIP and shown in Figure A.2 in Appendix A. The horizontal drag coefficient is assumed to be $C_D = 0.7$ over the entire ship length.

The simulation of port and starboard turning circle maneuvers shows satisfactory agreement with the measured data, see Figure 3.13.

With regards to the simplicity and the low computational effort, the results that can be obtained with the slender-body theory are very satisfactory. However, some experience is

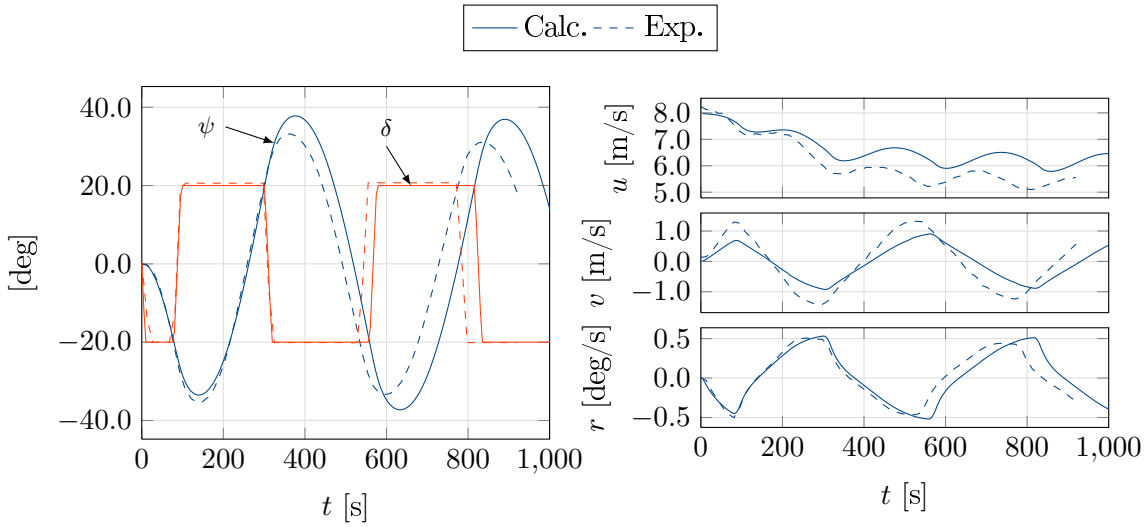

Figure 3.12.: $-20°/-20°$ zig-zag maneuver of KVLCC2; simulation with slender-body theory; measurements from MARIN [99]

needed with the transverse drag coefficient since it has a considerable influence on the motion of the ship.

Simulations with 3D potential theory

Determining the strength of the vorticity and the position where it leaves the hull is not a straightforward process for blunt ships. Therefore, it is easier but not less accurate to account for separation forces using semi-empirical formulae (Söding [110]). Following the slender-body theory, these forces can be calculated by specifying a separation point. Söding [110] recommends to use the aft end of the horizontal keel or the lower aft end of the rudder for ships. The force acting on this point can be calculated as:

$$F_{sep} = uva^0_{22,m} \tag{3.60}$$

with u being the ship's speed and v the transverse velocity at the separation point. $a^0_{22,m}$ is the sectional added mass at the separation point.

Similar to slender-body theory, additional nonlinear terms need to be applied for simulating narrow maneuvers. In Schoop-Zipfel and Abdel-Maksoud [92], additional nonlinear terms based on results obtained with a RANS method are introduced. Correction factors can be deduced by comparing the results of steady drift and of steady turning motion obtained with potential theory and with RANS. These nonlinear correction factors describe the difference of the damping forces obtained with potential theory and with RANS.

The computational effort is much lower than using RANS methods. However, the effort is

Table 3.4.: Main dimensions and frame plan of S-175 for maneuvering according to Yasukawa [122]

Dimensions		
L_{PP}	[m]	175.0
B	[m]	25.4
T	[m]	9.5
C_B	[-]	0.572
F_n	[-]	0.15

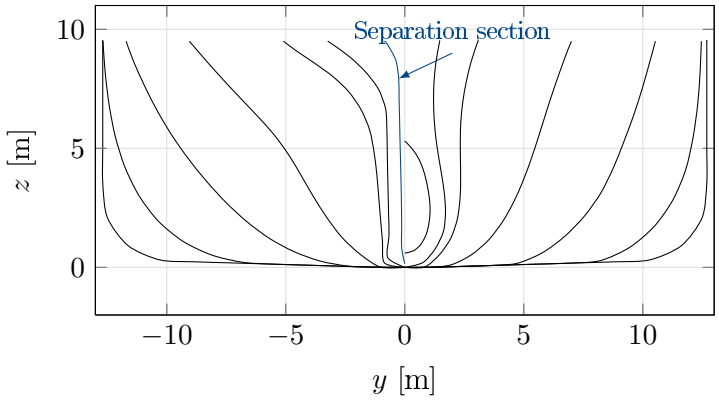

Table 3.5.: Data of S-175 for maneuvering simulations according to Yasukawa [122]

m	24801t	F_n	0.15	D_P	6.507
x_G	-2.545m	h_R	12.0deg/s	n	1.42
z_G	9.235m	H_R	7.7m	$k_{T,0}$	0.2932
$\overline{GM}$	1.005m	c	4.215m	$k_{T,1}$	0.1971
i_{xx}^2	110.3889m^2	A_R	32.46m^2	$k_{T,2}$	0.0481
i_{yy}^2	2216m^2			t	0.175
i_{zz}^2	2216m^2	w_p	0.1684	X'_{uu}	0.01563

nevertheless too large for real-time simulations.

RANS methods

Recent workshops (SIMMAN 2008 [99], SIMMAN 2014 [81], Gothenburg 2010 [67]) have shown that RANS solvers are capable of calculating flow forces with an accuracy comparable to model test measurements. Flow solvers based on the RANS equations are therefore adequate to determine the hull forces depending on arbitrary ship motions.

A further advantage of RANS is that it makes flow details available. E.g. vortices can be traced and the pressure distribution along the hull can be made visible.

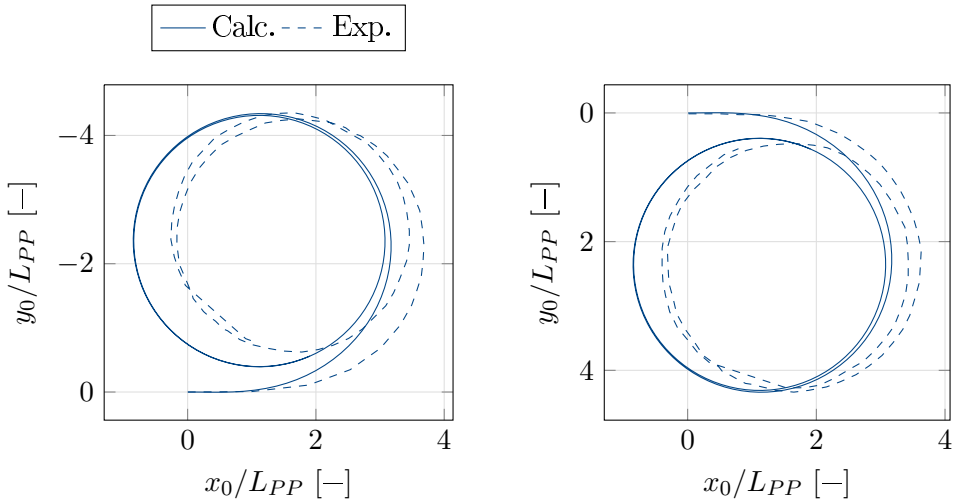

Figure 3.13.: ±35° turning circle of S-175; simulation with slender-body theory; measurements from Yasukawa [122]

3.3.4 Whole ship forces from captive motions

According to Stern et al. [100], the SIMMAN workshop [99] has shown that RANS CFD has the potential to provide data from maneuvering investigations that are fully equivalent to experimental data. The RANS method is applied in the present work to determine maneuvering forces. However, experiments would follow the same procedures.

The forces acting on the hull can be determined during captive motions. The dependence of the forces on the ship motions is classically described by hydrodynamic derivatives, see Section 3.2. The forces acting on the ship have to be determined for the entire range of motions that the ship will encounter during the maneuver to provide a proper basis for maneuvering simulations (Stern et al. [100]). Subsequently, these motions have to be simulated in advance. This leads to an extensive amount of calculations or measurements and is therefore inadequate in the early design stage.

Generally, the target of the force determination using RANS or model experiments is the use of the forces in a whole ship model. However, the forces acting on each component (hull, propeller, rudder) are available separately, so that the single components can also be used in the MMG model.

The simulations can be divided into quasi-stationary and transient ones. Both types are evaluated in a different way. Resistance and drift simulations are quasi-stationary as a stationary wave pattern develops after a certain simulation time at constant speed. The converging forces and moments at different speeds and drift angles form discrete sampling points, which can be approximated by a nth degree polynomial function. This function can, for instance, be found by applying a least-squares approximation.

In PMM tests, the ship moves along a sinusoidal path while forces and moments acting on the hull are measured. The time histories of the forces and moments acting on the ship are evaluated using Fourier analysis. From the coefficients of the Fourier analysis, the maneuvering derivatives can be determined. The hydrodynamic forces determined with transient motions show a dependence of the frequency due to free-surface effects. According to the Manoeuvring Committee of the ITTC [53], this frequency dependence should be checked and it should be ensured that the coefficients are equivalent to those at zero frequency.

In a pure sway test, the ship performs a sinusoidal motion with its bow pointing into the mean direction of travel i.e. the direction of the incoming flow (see Figure 3.14). The path can be described by amplitude η_0, velocity u and time period T.

In a pure yaw test, the ship performs a sinusoidal motion while moving tangent to its path (see Figure 3.14). Again, the path can be described by amplitude η_0, velocity u and time period T.

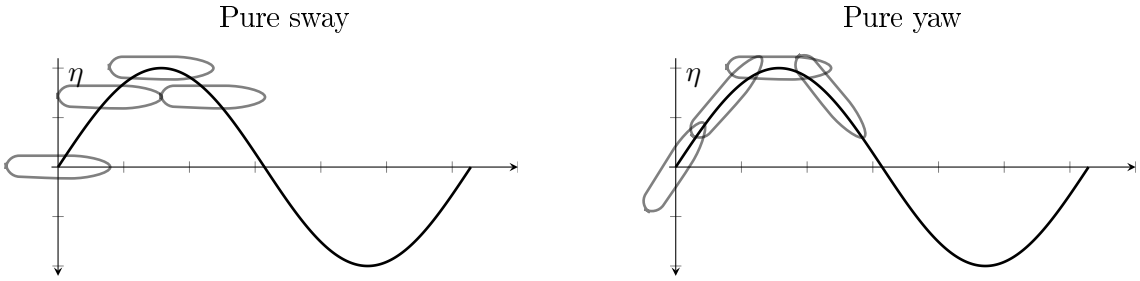

Figure 3.14.: Pure sway and pure yaw motion in PMM model tests

Further details on the derivation of maneuvering derivatives from the force tracks are given in Schoop [89] and Zinkmann [129]. In Schoop [89] and Schoop-Zipfel et al. [93], the maneuvering derivatives of the Series 60 ship are determined with virtual PMM tests. The captive motions are conducted on different water depths to investigate the influence of the water depth on the ship maneuvering motion. Zinkmann [129] conducts RANS simulations to determine the maneuvering derivatives of a catamaran. A comparison with model test measurements shows good agreement.

3.4 Solving the equation of motion

Once the hydrodynamic forces are properly determined, the motion of the vessel can be calculated using the rigid-body kinetics described in Section 2.4.

Pérez and Clemente [85] investigate the mathematical problems in maneuverability. They state that the most important part of the maneuverability is the physical problem; but once it is solved, the mathematical problem of solving the ordinary differential equations system can

be studied using different methods, such as the typical Runge-Kutta or Predictor-Corrector methods. They state that Runge-Kutta methods can be used when the goal is to obtain global parameters. Generally, the global parameters are of major interest, e.g. the rules given by the IMO [50] refer to global parameters as tactical diameter and overshoot angles. However, for a long time simulation, the trajectories can have a large deviation. For this case, they recommend to use multi-step methods, such as predictor-corrector methods.

3.5 Concluding remarks

For the subsequent simulations of maneuvering in waves, two methods are chosen. The slender-body theory based on the MMG concept yields acceptable results with a low computational effort. Furthermore, simulations based on hydrodynamic derivatives are conducted. Once the derivatives are known, the computational effort is very low and arbitrary maneuvers can be simulated in very short times.

4
Seakeeping

"The basic law of the seaway is the apparent lack of any law."

Lord Rayleigh (1842-1919)

This chapter discusses the simulation of ship motions in waves, and a general description of the adopted theory is given. Subsequently, a deeper insight into the time-domain solution using the impulse-response functions is provided. The simulation examples are meant to demonstrate both capabilities and validation.

Linear wave theory is often applied to determine the response of a ship in regular waves. Results in an irregular seaway can be obtained by linearly superposing the results in regular waves. Subsequently, it is sufficient from a hydrodynamical point of view to analyse the wave induced forces and the motion behavior of the ship in regular waves of small steepness (Faltinsen [28]). When presuming a steady state (no transient effects due to the initial condition and the motions and loads are oscillating with the same frequency as the waves) the hydrodynamic problem of a ship in regular waves can be split into two parts:

- A forced harmonically oscillating motion in calm water resulting in so-called hydrodynamical forces and moments; namely the added mass, damping and restoring terms.
- The restrained body in regular waves where the waves exert the so-called wave excitation forces.

Generally, linearity is assumed, so the forces obtained in these sub-problems can be added to give the total hydrodynamic forces.

4.1 Seakeeping coordinate system

The encounter angles between the ship, the earth and the waves are defined in Figure 4.1.

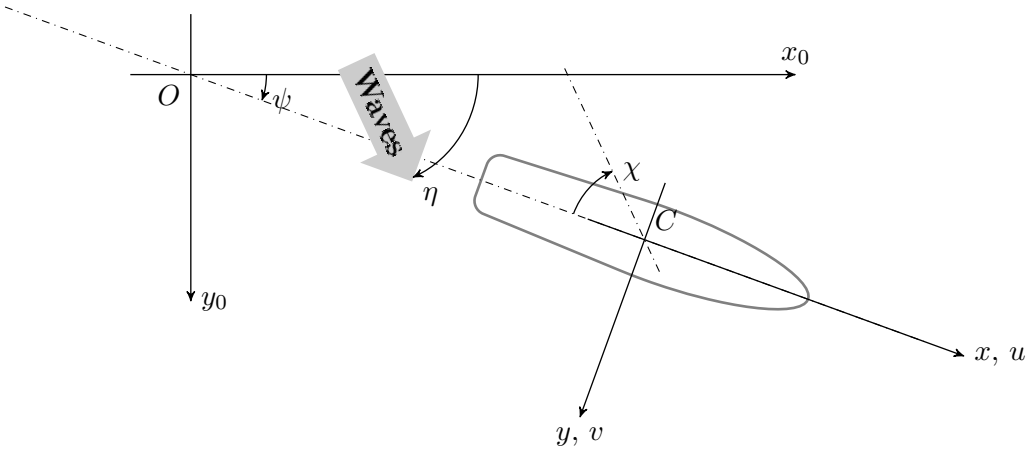

Figure 4.1.: Definitions for seakeeping

In seakeeping, the motion is often described relative to a coordinate system $\overline{K}$ fixed to an equilibrium virtual ship that moves at a constant speed and heading that corresponds to the average motion of the actual ship (Fossen [33]). In general, hydrodynamic computation methods use this coordinate system to compute the loads and motions of a ship in waves, see e.g. Söding and Bertram [111]. This is in contrast to maneuvering theory, where the equations of motion are described in a coordinate system fixed to the ship ($\hat{K}$).

The seakeeping coordinate system $\overline{K}\{S, x_S, y_S, z_S\}$ is not fixed to the simulated ship. It moves with the average ship velocity, but does not follow the wave-frequency oscillations of the ship. When no waves are present, its origin S equals the origin of the body-fixed coordinate system. Waves cause that the ship oscillates around this equilibrium condition. The position vector in the $\overline{K}$ coordinate system is defined as

$$\boldsymbol{\xi} = (\xi_1\ \xi_2\ \xi_3\ \xi_4\ \xi_5\ \xi_6)^T\ , \tag{4.1}$$

where the ξ_i are the positions/angles with respect to the body-fixed coordinate system.

4.2 Hydrodynamical forces and moments

The hydrodynamical forces are the so-called added mass and damping terms. These forces occur due to forced oscillatory motion of the ship without the presence of incoming waves, however, waves are radiating from the ship. The oscillating pressure field around the ship generates forces that can be calculated by integrating the pressure over the hull surface. The added mass is by definition the force term proportional to the body acceleration while the damping is proportional to its velocity. They can subsequently be written as

$$\boldsymbol{f}_{hydrodynamical} = -\boldsymbol{A}\frac{d^2\boldsymbol{\xi}}{dt^2} - \boldsymbol{B}\frac{d\boldsymbol{\xi}}{dt} \, . \tag{4.2}$$

The word 'added mass' may be misleading, since it is not a finite fluid mass that is oscillating together with the ship, which is a common misunderstanding. It can be shown, for instance, that for a catamaran, the heave added mass can be negative in a certain frequency domain (Faltinsen [29]).

Different physical effects cause a damping of the ship motion. Faltinsen [29] sums the four main sources of damping for a rigid ship as:

- wave radiation damping,
- hull-lift damping,
- foil-lift damping,
- viscous damping.

The former three can easily be calculated with potential theory, while the viscous damping is small when the flow does not separate and induces vortices.

Both the added mass and the damping terms are dependent on the frequency of the forced oscillation of the ship.

Furthermore, restoring terms are present. The restoring forces and moments are obtained by integrating the pressure loads due to the hydrostatic pressure. The force and moment components can be written as

$$\boldsymbol{f}_{restoring} = -\boldsymbol{C}\boldsymbol{\xi} \, . \tag{4.3}$$

4.3 Strip theory

Because it is necessary to both maintain a quick simulation time and an appropriate level of accuracy, a certain level of simplicity must be pursued. On account of this, strip theory methods are applied for the seakeeping calculations. 2D strip methods simplify the complex 3D problem of an advancing ship in waves by dividing the hull into a finite number of transverse strips. For slender bodies, the variation of the flow is much larger in transverse direction than in longitudinal direction of the body. It is therefore sufficient to compute the two-dimensional hydrodynamics of each strip and integrate them over the length of the ship to obtain the three-dimensional solution. The theory is explained by several authors, see e.g. Newman [76], Faltinsen [28], Journee and Massie [57].

In the present work, the strip theory program PDSTRIP [111] is used for the seakeeping calculations, which computes the seakeeping behavior of ships and other floating bodies according to the strip method. For the motions, a method from Söding [103] is applied, while a procedure of Hachmann [40] is used to determine the pressure. PDSTRIP considers mainly linear responses, but it takes into account some nonlinear effects. It gives the responses to regular waves as RAO.

Schoop-Zipfel and Abdel-Maksoud [90] use PDSTRIP for determining the RAO of a S-175 container vessel and a Wigley hull. The results agree well with experimental data. Recently, Gourlay et al. [34] have systematically compared the simulation results of PDSTRIP with the results of other seakeeping simulation codes and the results from model tests. The motions simulated with PDSTRIP are in good agreement with the results of the other codes and the measurements.

In principal, strip theory is valid for long and slender bodies. However, experiments have shown that strip theory gives reliable results for bodies with a length to breadth ratio larger than three (Journée and Massie [57]). It should further be noted that strip theory is basically a theory for the simulation of high-frequency motion (Faltinsen [28]), meaning that it is more applicable in head sea waves than in following sea for a ship with forward speed. Moreover, strip theory is suitable for the simulation of the ship motion at low Froude number. It does not properly account for the interaction between the steady wave system of the advancing ship and the oscillatory effects of ship motion. Another limitation of strip theory is the linearity between response and incident wave amplitude.

Strip theory codes do not compute the zero- and infinite-frequency cases. According to Perez and Fossen [82], a curve fitting can be applied to the hydrodynamic data to obtain values for $\omega = 0$ and $\omega = \infty$. The fact that the damping values are zero for $\omega = 0$ and $\omega = \infty$ can be exploited.

4.4 Hydrodynamical forces of S-175 container ship

Exemplarily, the added mass and damping terms are determined for the S-175 container ship. Table 3.4 has shown the main dimensions and the geometry of the hull. The linear strip theory code PDSTRIP is applied to determine the frequency-dependent added mass and damping terms. Figures 4.2 and 4.3 show the components of the main diagonal of the added mass and damping matrices, respectively. All components of the lateral and the longitudinal mode can be seen in the Appendix in Figures B.1 to B.4.

The calculated damping coefficients are extended to zero frequency and the double of the maximum calculated frequency. The damping values are zero for these frequencies. The values in between are interpolated by a piecewise cubic hermite interpolating polynomial. A zero gradient is enforced for the end values. The solid lines in the figures represent the calculated values as obtained with PDSTRIP and the dashed lines show the fitted graphs where the limits for $\omega = 0$ and $\omega = \infty$ are employed.

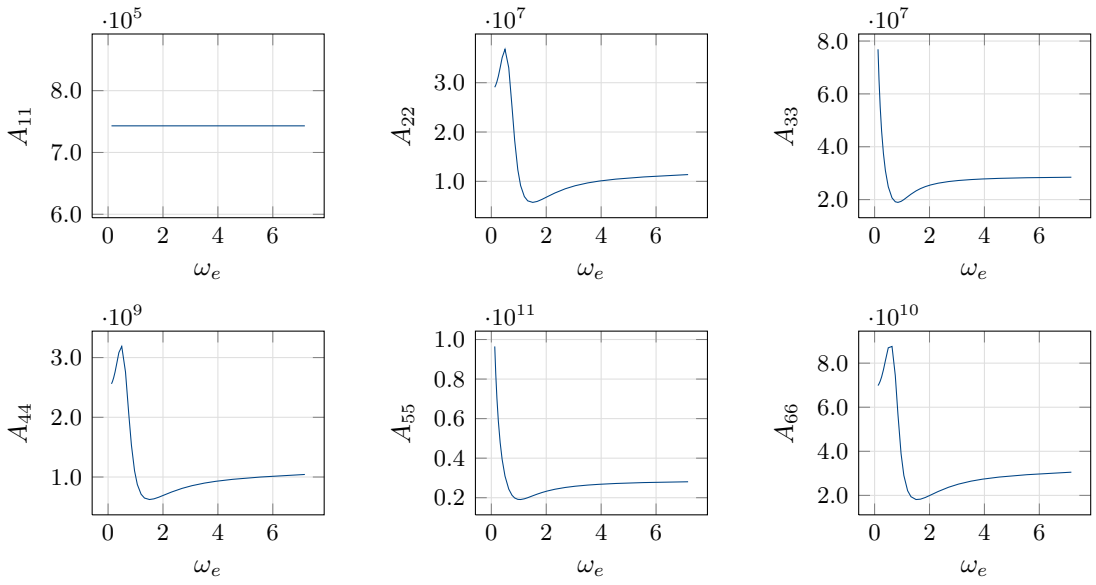

Figure 4.2.: Added mass of S-175 for zero speed

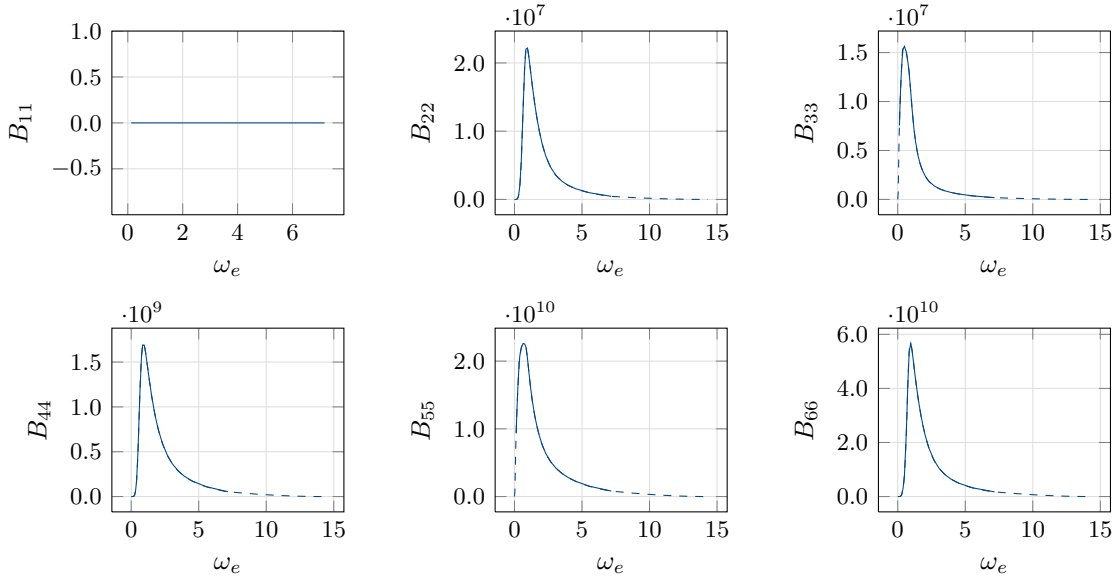

Figure 4.3.: Potential damping of S-175

4.5 Frequency-domain approach

The classical equation of motion in frequency domain yields

$$[\boldsymbol{M} + \boldsymbol{A}(\omega)]\ddot{\boldsymbol{\xi}} + \boldsymbol{B}(\omega)\dot{\boldsymbol{\xi}} + \boldsymbol{C}\boldsymbol{\xi} = \boldsymbol{f}_e \,, \tag{4.4}$$

where $\boldsymbol{A}(\omega)$ is the frequency-dependent added mass matrix, $\boldsymbol{B}(\omega)$ is the frequency-dependent potential damping matrix and $\boldsymbol{f}_e$ is the excitation force vector.

Solving this equation yields the motion amplitudes of the ship as a function of the wave encounter frequency, the so-called RAO. Once the RAOs are known, the ship motion can also be described with them. The wave elevation is $\zeta = \zeta_A \cos(\omega t)$, meaning that the motion and velocity of the ship yields

$$\boldsymbol{\eta} = \mathbf{RAO}\zeta_A \cos(\omega t + \boldsymbol{\epsilon}) \,, \tag{4.5}$$

$$\boldsymbol{\nu} = -\mathbf{RAO}\zeta_A \omega \sin(\omega t + \boldsymbol{\epsilon}) \,. \tag{4.6}$$

4.6 Time-domain approach

The time-domain approach is based on the work of Cummins [20]. The impulse-response function according to Cummins proves that the motion response of a ship on an impulse, i.e. an external load at time t, is comprised of the superposition of all fading impulses in preceding time steps up to the time t. The advantage of this approach is that the reaction on arbitrary loads can be determined if the reaction on the unit impulse is known. However, it has to be noted that nonlinear excitations also yield linear responses. The superposition of the fading impulses is often referred to as the memory effect.

Using the results of Cummins [20] and Ogilvie [79], the frequency-dependent coefficients $\boldsymbol{A}(\omega)$ and $\boldsymbol{B}(\omega)$ can be transformed for linear systems to a formulation in time-domain.

When applying Cummins' formulation [20], the hydrodynamical forces and moments acting on a ship due to time varying ship motions can be written as

$$\boldsymbol{f}_{hydrodynamical} = -\overline{\boldsymbol{A}}\ddot{\boldsymbol{\xi}} - \int_{-\infty}^{t} \overline{\boldsymbol{K}}(t-\tau)\dot{\boldsymbol{\xi}}(\tau)d\tau - \overline{\boldsymbol{C}}\boldsymbol{\xi} \ , \tag{4.7}$$

with the generalized hydrodynamic added mass matrix $\overline{\boldsymbol{A}}$, the spring stiffness matrix $\overline{\boldsymbol{C}}$, and a matrix of retardation functions $\overline{\boldsymbol{K}}(t-\tau)$. Rewriting the equation of motion by putting the hydrodynamical forces on the left hand side and adding additional external loads $\boldsymbol{f}_e$, one obtains the Cummins equation, in honor of his work:

$$[\boldsymbol{M} + \overline{\boldsymbol{A}}]\ddot{\boldsymbol{\xi}} + \int_{-\infty}^{t} \overline{\boldsymbol{K}}(t-\tau)\dot{\boldsymbol{\xi}}(\tau)d\tau + \overline{\boldsymbol{C}}\boldsymbol{\xi} = \boldsymbol{f}_e \tag{4.8}$$

To obtain the hydrodynamic coefficients $\overline{\boldsymbol{A}}$, $\overline{\boldsymbol{C}}$, and $\overline{\boldsymbol{K}}$, an approach proposed by Ogilvie [79] can be used. By assuming that the floating object carries out oscillations and then comparing Cummins equation (Eqn. 4.8) with the equation of motion in frequency domain (Eqn. 4.4), it is shown that the relation between the frequency-dependent hydrodynamic coefficient matrices $\boldsymbol{A}(\omega)$ and $\boldsymbol{B}(\omega)$ and the hydrodynamic coefficients in Cummins equation can be written as

$$\boldsymbol{A}(\omega) = \overline{\boldsymbol{A}} - \frac{1}{\omega}\int_{0}^{\infty} \overline{\boldsymbol{K}}(\tau)\sin(\omega\tau)d\tau\} \ , \tag{4.9}$$

$$\boldsymbol{B}(\omega) = \int_{0}^{\infty} \overline{\boldsymbol{K}}(\tau)\cos(\omega\tau)d\tau \ . \tag{4.10}$$

The first equation is valid for all ω so that $\omega = \infty$ can be chosen,

$$\overline{\boldsymbol{A}} = \boldsymbol{A}(\infty) \ . \tag{4.11}$$

The second equation can be rewritten by applying the inverse Fourier transform:

$$\overline{\boldsymbol{K}}(t) = \frac{2}{\pi}\int_0^\infty \boldsymbol{B}(\omega)\cos(\omega\tau)d\omega \ . \tag{4.12}$$

$\overline{\boldsymbol{K}}(t)$ is a matrix of retardation functions. The convolution integral in this equation captures the so-called fluid memory effects. The waves that are generated by the moving ship will last, in theory, for all susequent times and influence then the motion of the ship. Figure 4.4 shows the entries on the main diagonal of the retardation function matrix of the S-175.

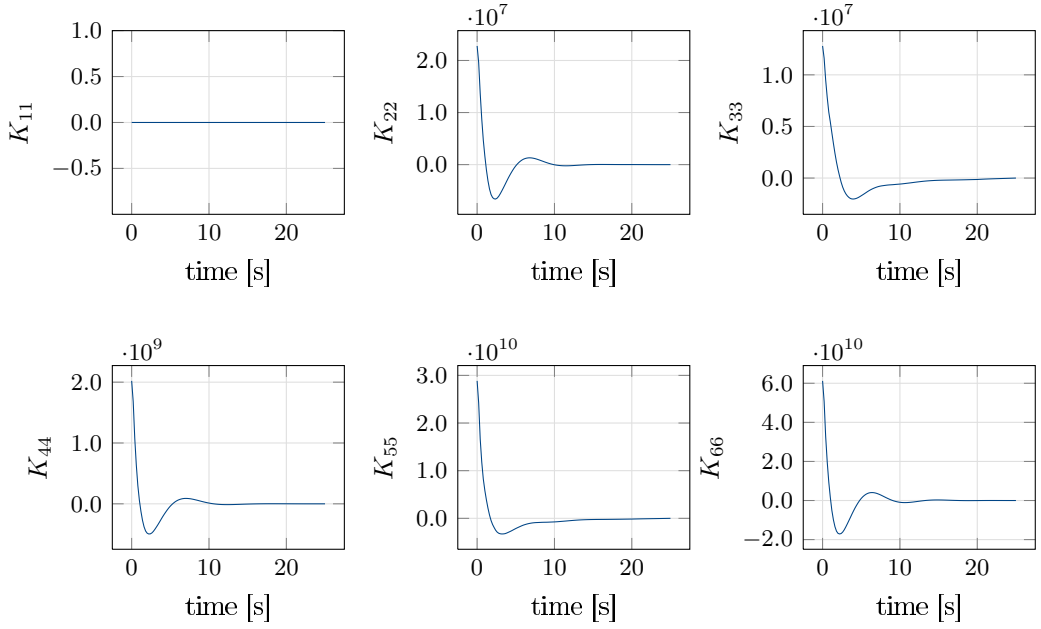

Figure 4.4.: Retardation functions of the potential damping of S-175

Fossen [32] states that from a numerical point of view it is better to integrate

$$\boldsymbol{K}(t) = \frac{2}{\pi}\int_0^\infty [\boldsymbol{B}(\omega) - \boldsymbol{B}(\infty)]\cos(\omega\tau)d\omega \ , \tag{4.13}$$

than to use Eqn. (4.12), because $\boldsymbol{B}(\omega) - \boldsymbol{B}(\infty)$ is zero at $\omega = \infty$. To include this in Cummins equation, Fossen [32] writes Eqn. (4.12) as

$$\begin{aligned}\overline{\boldsymbol{K}}(t) &= \frac{2}{\pi}\int_0^\infty [\boldsymbol{B}(\omega) - \boldsymbol{B}(\infty) + \boldsymbol{B}(\infty)]\cos(\omega\tau)d\omega \\ &= \boldsymbol{K}(t) + \frac{2}{\pi}\int_0^\infty \boldsymbol{B}(\infty)\cos(\omega\tau)d\omega\end{aligned} \tag{4.14}$$

which yields

$$\int_{-\infty}^{t} \overline{\boldsymbol{K}}(t-\tau)\dot{\boldsymbol{\xi}}(\tau)d\tau = \int_{-\infty}^{t} \boldsymbol{K}(t-\tau)\dot{\boldsymbol{\xi}}(\tau)d\tau + \boldsymbol{B}(\infty)\dot{\boldsymbol{\xi}} \ . \tag{4.15}$$

Here it is made use of the fact that the inverse Fourier transform of the constant $\boldsymbol{B}(\infty)$ is an impulse and that

$$\boldsymbol{B}(\infty)\dot{\boldsymbol{\xi}} = \int_{-\infty}^{t} (\frac{2}{\pi} \int_{0}^{\infty} \boldsymbol{B}(\infty) \cos(\omega\tau) d\omega) \dot{\boldsymbol{\xi}}(\tau) d\tau \ . \tag{4.16}$$

So, finally Cummins equation (Eqn. (4.8)) can be written as

$$[\boldsymbol{M} + \boldsymbol{A}(\infty)]\ddot{\boldsymbol{\xi}} + \boldsymbol{B}(\infty)\dot{\boldsymbol{\xi}} + \int_{-\infty}^{t} \boldsymbol{K}(t-\tau)\dot{\boldsymbol{\xi}}(\tau) d\tau + \boldsymbol{C}\boldsymbol{\xi} = \boldsymbol{f}_e \ . \tag{4.17}$$

The hydrodynamical forces can be summed up as:

$$\boldsymbol{f}_{hydrodynamical} = -\boldsymbol{A}(\infty)\ddot{\boldsymbol{\xi}} - \boldsymbol{B}(\infty)\dot{\boldsymbol{\xi}} - \int_{-\infty}^{t} \boldsymbol{K}(t-\tau)\dot{\boldsymbol{\xi}}(\tau) d\tau - \boldsymbol{C}\boldsymbol{\xi} \ . \tag{4.18}$$

For further details, reference is made to Fossen [32].

4.7 Time-domain equations in body-fixed coordinates

Hydrodynamic maneuvering derivatives are normally given in body-fixed coordinates, i.e. in the $\hat{K}$ coordinate system. To derive a unified theory, it is therefore useful to also represent the impulse-response function in the $\hat{K}$ coordinate system. Subsequently, Eqn. (4.18) needs to be transformed from $\overline{K}$ to the rotating coordinate system $\hat{K}$. With this transformation, Coriolis and centripetal forces appear due to the rotation of the body-fixed coordinate system around the inertial coordinate system.

The kinematic transformations are according to Fossen [33]:

$$\boldsymbol{\xi} := \delta\boldsymbol{\eta} \ , \tag{4.19}$$

$$\delta\boldsymbol{\nu} \approx \boldsymbol{\nu} + U(\boldsymbol{L}\delta\boldsymbol{\eta} - \boldsymbol{e}_1) \ , \tag{4.20}$$

$$\delta\dot{\boldsymbol{\nu}} \approx \dot{\boldsymbol{\nu}} + U\boldsymbol{L}\boldsymbol{\nu} \ , \tag{4.21}$$

with

$$\boldsymbol{e}_1 := \begin{pmatrix} 1 \\ 0 \\ 0 \\ 0 \\ 0 \\ 0 \end{pmatrix} \quad , \quad \boldsymbol{L} := \begin{pmatrix} 0 & 0 & 0 & 0 & 0 & 0 \\ 0 & 0 & 0 & 0 & 0 & 1 \\ 0 & 0 & 0 & 0 & -1 & 0 \\ 0 & 0 & 0 & 0 & 0 & 0 \\ 0 & 0 & 0 & 0 & 0 & 0 \\ 0 & 0 & 0 & 0 & 0 & 0 \end{pmatrix} \ . \tag{4.22}$$

Using this transformation yields for Eqn. (4.18)

$$\boldsymbol{f}_h = -\boldsymbol{A}[\dot{\boldsymbol{\nu}} + U\boldsymbol{L}\boldsymbol{\nu}] - \boldsymbol{B}(\infty)[\boldsymbol{\nu} + U(\boldsymbol{L}\delta\boldsymbol{\eta} - \boldsymbol{e}_1)] - \int_{-\infty}^{t} \boldsymbol{K}(t-\tau)\delta\boldsymbol{\nu}(\tau)d\tau - \boldsymbol{C}\delta\boldsymbol{\eta}\,. \quad (4.23)$$

Assuming a steady state, when no waves and wind are present, yields

$$\boldsymbol{f}_h = -\boldsymbol{A}(\infty)[\dot{\boldsymbol{\nu}} + U\boldsymbol{L}\boldsymbol{\nu}] - \boldsymbol{B}(\infty)[\boldsymbol{\nu} + U\boldsymbol{L}\delta\boldsymbol{\eta}] - \int_{-\infty}^{t} \boldsymbol{K}(t-\tau)\delta\boldsymbol{\nu}(\tau)d\tau - \boldsymbol{C}\delta\boldsymbol{\eta}\,. \quad (4.24)$$

The influence of $\delta\nu$ on the forward speed is rather small and therefore commonly neglected when computing the damping and retardation functions (Fossen [33]) such that

$$\delta\boldsymbol{\nu} \approx \boldsymbol{\nu} + U(\boldsymbol{L}\delta\boldsymbol{\eta} - \boldsymbol{e}_1) \approx \boldsymbol{\nu} - U\boldsymbol{e}_1 \quad (4.25)$$

and subsequently

$$\boldsymbol{f}_h = -\boldsymbol{A}(\infty)\dot{\boldsymbol{\nu}} - \boldsymbol{C}_A^*\boldsymbol{\nu} - \boldsymbol{B}(\infty)\boldsymbol{\nu} - \int_{-\infty}^{t} \boldsymbol{K}(t-\tau)[\boldsymbol{\nu}(\tau) - U\boldsymbol{e}_1]d\tau - \boldsymbol{C}\boldsymbol{\eta}\,, \quad (4.26)$$

where

$$\boldsymbol{C}_A^* = U\boldsymbol{A}(\infty)\boldsymbol{L} \quad (4.27)$$

which are the linearized Coriolis and centripetal terms due to the rotation of $\hat{K}$ about $\overline{K}$. More conveniently, the equation can be reformulated as

$$\boldsymbol{f}_h = -\boldsymbol{A}(\infty)\dot{\boldsymbol{\nu}} - \boldsymbol{D}\boldsymbol{\nu} - \int_{-\infty}^{t} \boldsymbol{K}(t-\tau)[\boldsymbol{\nu}(\tau) - U\boldsymbol{e}_1]d\tau - \boldsymbol{C}\boldsymbol{\eta}\,, \quad (4.28)$$

with

$$\boldsymbol{D} = \boldsymbol{C}_A^* + \boldsymbol{B}(\infty) \quad (4.29)$$

$$= U\boldsymbol{A}(\infty)\boldsymbol{L} + \boldsymbol{B}(\infty) \quad (4.30)$$

Now the body-fixed velocity $\boldsymbol{\nu}$ and acceleration $\dot{\boldsymbol{\nu}}$ (known from Eqn. (2.27) and (2.28)) can be used instead of $\boldsymbol{\xi}$ and its time derivatives.

When substituting the hydrodynamic coefficients with the terms obtained from strip theory, one obtains terms similar to the terms obtained for the slender-body theory in Chapter 3 (see

Fossen [32]).

$$\boldsymbol{D}(\omega_e) = \boldsymbol{B}(\omega_e) + U\boldsymbol{A}(\omega_e)\boldsymbol{L} \tag{4.31}$$

$$= \begin{pmatrix} B_{11} & 0 & B_{13} & 0 & B_{15} - UA_{13} & 0 \\ 0 & B_{22} & 0 & B_{24} & 0 & B_{26} + UA_{22} \\ B_{31} & 0 & B_{33} & 0 & B_{35} - UA_{33} & 0 \\ 0 & B_{42} & 0 & B_{44} & 0 & B_{46} + UA_{42} \\ B_{51} & 0 & B_{53} & 0 & B_{55} - UA_{53} & 0 \\ 0 & B_{62} & 0 & B_{64} & 0 & B_{66} + UA_{62} \end{pmatrix}. \tag{4.32}$$

Substituting the Salvesen, Tuck, Faltinsen (STF) strip theory coefficients (Salvesen et al. [88]) given in Appendix B.1 yields

$$\boldsymbol{D}(\omega_e) = U \begin{pmatrix} 0 & 0 & 0 & 0 & 0 & 0 \\ 0 & a_{22,A} & 0 & a_{24,A} & 0 & x_A a_{22,A} \\ 0 & 0 & a_{33,A} & 0 & -x_A a_{33,A} & 0 \\ 0 & a_{42,A} & 0 & a_{44,A} & 0 & x_A a_{42,A} \\ 0 & 0 & -x_A a_{33,A} & 0 & x_A^2 a_{33,A} & 0 \\ 0 & x_A a_{22,A} & 0 & x_A a_{24,A} & 0 & x_A^2 a_{22,A} \end{pmatrix} \tag{4.33}$$

$$+ \begin{pmatrix} 0 & 0 & 0 & 0 & 0 & 0 \\ 0 & B_{22} & 0 & B_{24} & 0 & B_{26} \\ 0 & 0 & B_{33} & 0 & B_{35} & 0 \\ 0 & B_{42} & 0 & B_{44} & 0 & B_{46} \\ 0 & 0 & B_{53} + UA_{33} & 0 & B_{55} + UA_{53} & 0 \\ 0 & B_{62} - UA_{22} & 0 & B_{64} - UA_{42} & 0 & B_{66} - UA_{62} \end{pmatrix}. \tag{4.34}$$

B_{ij} are the frequency-dependent damping terms for zero ship speed. The index $_A$ denotes the aft section.

4.8 Additional damping terms

The four main sources of damping are wave radiation damping, hull-lift damping, foil-lift damping and viscous damping as written previously. The wave radiation damping can be captured by the zero-speed potential theory. Additional corrections may be necessary for the other parts. Linear damping can be included directly into the damping terms and the retardation functions. Non-linear damping has to be added to the external forces on the right-hand side of Cummins equation (Eqn. (4.8)).

The linear damping can be introduced to the equation in different ways. Fossen [32] suggests using an exponentially decaying ramp to add the zero-frequency viscous damping terms (B_v) to the potential damping (B_p) (see Figure 4.5). The retardation functions then includes the additional damping terms. Alternatively, the additional damping terms can be directly added during the time-domain simulation. Ross and Fossen [86] have shown the equality of both approaches.

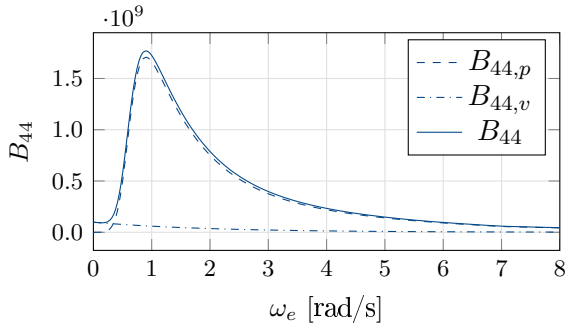

Figure 4.5.: Roll damping of S-175; potential ($B_{44,p}$) and additional viscous damping ($B_{44,v}$)

4.8.1 Roll damping

Roll damping is generated by wave radiation, vortex generation and the lift and friction on the hull, see Himeno [44]. In addition, ship appendages can have a noticeable effect on roll damping. For the consideration of the total roll damping, additional terms need to be embedded in the simulation method.

To take viscous roll damping into account, a quadratic coefficient approach according to Kröger [61] is used. The roll moment can be written as

$$m_\phi(\dot{\phi}) = (d_L + d_Q|\dot{\phi}|)\dot{\phi} \; . \tag{4.35}$$

The viscous roll damping content can be determined with experiments or numerical RANS computations (see e.g. Handschel et al. [41]). Alternatively, the coefficients proposed by Blume [14] can be used. In Blume, roll damping coefficients for different hull shapes and driving conditions are determined experimetally with model tests. Further information on the applied roll damping can be found in Detlefsen [24].

Figure 4.6 shows the roll motion of the S-175 container vessel. Two possibilities for applying the additional damping are compared and contrasted. For the results labeled with $\beta_4 e^{-\alpha\omega}$, an exponentially decaying linear damping is added to the potential damping before building the retardation functions. For the results labeled with β_4, the linear damping is added directly in the time domain. The figure shows that both approaches yield comparable results.

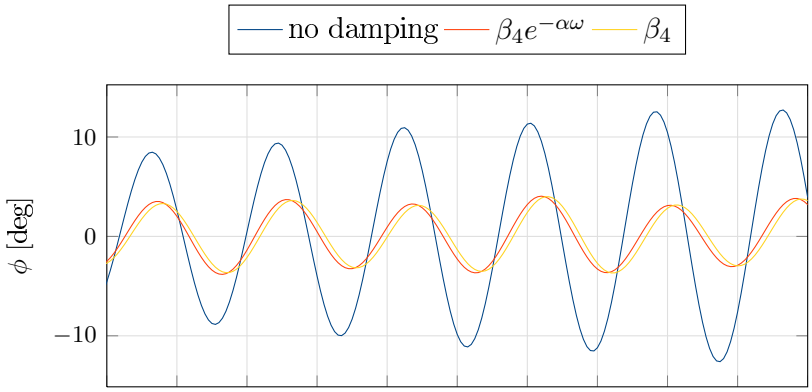

Figure 4.6.: Roll motion of S-175; different damping concepts; $\zeta_A = 1\text{m}$, $\chi = 60°$, $\lambda/L_{pp} = 1.57$

4.8.2 Sway and heave damping

For motion in transverse and vertical direction, an additional nonlinear viscous damping can be applied. As in the slender-body theory (see Section 3.3.3 and Söding [105]), the nonlinear viscous damping reads

$$f_{y,NL} = -\frac{1}{2}\rho \int_L (v + xr)\,|v + xr|\,C_{Dy}\,d\,dx\ . \tag{4.36}$$

Similarly, a force in vertical direction can be defined (Söding and Bertram [111]):

$$f_{z,NL} = -\frac{1}{2}\rho \int_L (w + xq)\,|w + xq|\,C_{Dz}\,d\,dx\ . \tag{4.37}$$

The cross-flow drag coefficients C_{Dy} and C_{Dz} can be determined with experiments or viscous RANS computations. For well rounded frame shapes, $C_{Dy} = 0.8$ is recommended by Söding and Bertram [111]. If bilge keels, a knuckle at the keel or a knuckle at the bilge are present, $C_{Dy} = 1.2$ can be assumed. For C_{Dz}, values between 0.4 and 0.8 are recommended; 0.4 can be used for sections which intersect the waterline at maximum breadth and 0.8 for fully submerged sections.

4.9 Additional restoring terms

To simulate straight motion, additional restoring terms have to be applied if the ship is not self-propelled and has no steering. Similar to the fastenings in model testing, springs have to be applied to the hull. Otherwise, the surge, sway and yaw motions will not be restored to the average and the ship will lose its mean track. However, the spring terms influence the motion of the ship, so care has to be taken when choosing the proper terms.

4.10 Wave excitation forces

Incoming waves cause a pressure variation along the ship hull which results in wave excitation forces. The forces can be split in parts that are linearly dependent on the wave elevation and nonlinear parts. Linear wave excitation forces of first order have a zero mean value. They are the Froude Krylov and the diffraction forces. The nonlinear components have a non-zero mean value and therefore produce non-oscillatory drift forces. Furthermore, the nonlinear components produce also oscillatory forces with energy at higher and lower frequency than the waves. Artyszuk [5] states that the forces at lower frequencies oscillate around the mean second-order forces and are not significant in ship maneuvering. According to Fossen [33] the nonlinear high-frequency forces are critical for oscillations in the structure (springing) but are also of no concern for maneuvering. The second-order mean wave drift forces are addressed in Section 4.13.

The linear exciting forces and moments are the loads of incident waves acting on a ship that is restrained from moving. The unsteady fluid pressure can be divided into two effects. One effect is the unsteady pressure induced by the undisturbed waves. The force due to the corresponding undisturbed pressure field is called a Froude-Krylov force. The second one is due to the changes of the wave shape by the structure and the associated change of the pressure field. This force is called diffraction force. Both forces are of similar orders of magnitude.

4.11 Solving the equation system

The simulation method is implemented into the potential framework *pan*MARE; however, the potential solution of *pan*MARE is not used in the present work. The frequency-dependent added mass and damping terms as well as the restoring terms and the wave excitation forces are determined with PDSTRIP.

Figure 4.7 shows the workflow of the numerical simulation.

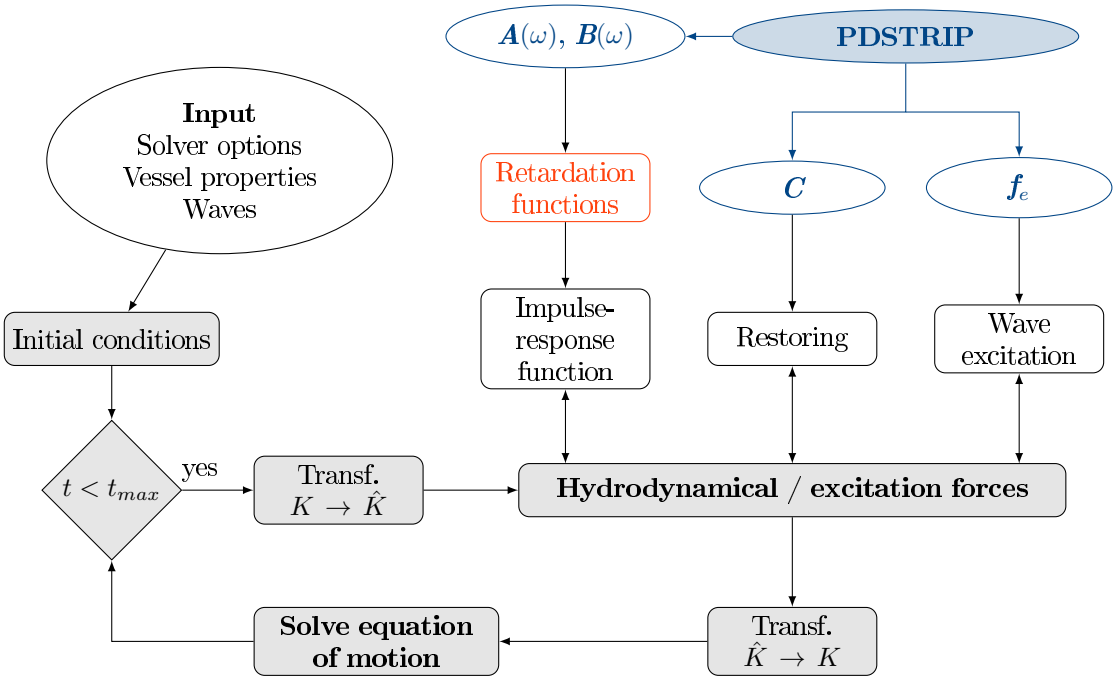

Figure 4.7.: Computational algorithm for the seakeeping simulation

For the time-domain simulations, the added mass, damping, restoring and wave excitation terms are predetermined and saved in a database. During the time-domain simulation, the hydrodynamic forces acting on the ship can be determined according to Eqn. 4.28. Alternatively, the associated added mass and damping terms can be directly retained from the database if the wave encounter frequency is known. Then Eqn. 4.4 instead of Eqn. 4.28 can be solved to obtain the hydrodynamic forces. However, this is only possible for regular waves with a known frequency.

The amplitudes and phase shifts of the linear wave excitation forces are stored for a set of encounter angles χ, wave lengths λ and forward speeds of the ship U. The wave excitation force can then be written as

$$\boldsymbol{f}_e = \boldsymbol{f}'_{e,A}\zeta_A \cos(\omega t - kx_0 \cos(\eta) - ky_0 \sin(\eta) + \boldsymbol{\epsilon}) \; . \tag{4.38}$$

Schoop-Zipfel and Abdel-Maksoud [92] show that the linear wave excitation forces acting on a Wigley hull in regular waves can be calculated with high accuracy using PDSTRIP.

The strong memory effects associated with the free-surface flow and the dependence of the fluid force upon the ship displacement, velocity and acceleration introduce a degree of complexity not encountered in ordinary differential equations free of strong memory effects. In Kring and Sclavounos [60], the numerical stability of Newton's rigid-body equations of motion for a ship advancing in waves in the time domain is studied. It is concluded that a fourth-order

Adams-Bashforth-Moulton method is optimal for practical work in terms of accuracy and efficiency. However, for small time steps, many integration methods are stable and therefore convergent. Therefore, a precise knowledge of the maximum time step of various integration methods, before instability sets in, is an essential prerequisite for the development of a robust and efficient seakeeping code. The problem of numerical instability is adressed in Section 2.4.4.

To solve the differential equation, the Runge-Kutta method of fourth order is applied, since it is essentially easier to implement than a multistep method as the fourth-order Adams-Bashforth-Moulton method. However, precise investigations of the time step size are conducted. Figure 4.8 shows exemplarily the heave and pitch motion of the S-175 in regular waves coming from bow quartering direction. The amplitudes are shown on the right hand side of the figure. The equation of motion is integrated with three different time integration schemes: explicit Euler (EE), implicit Euler (IE) and fourth-order Runge-Kutta (RK4). Three different time step sizes are used. The figure shows a clear convergence. Furthermore, the figure shows that the fourth-order Runge-Kutta method can be applied with large time steps, while still maintaining a high accuracy.

4.12 Verification and validation of seakeeping simulations

Extensive model test results for the S-175 container ship are available in the ITTC 1978 Proceedings [51]. The RAOs are measured for a large range of wave lengths and wave encounter angles. The mass distribution, as used in the experiments, is given in Table 4.1.

Table 4.1.: Mass distribution of S-175

m [kg]	x_G [m]	z_G [m]	$\overline{GM}$ [m]	i_{xx}^2 [m^2]	i_{yy}^2 [m^2]	i_{zz}^2 [m^2]
24609620	-2.55	9.375	0.891	69.3889	1764	1764

Figure 4.9 shows a comparison of the measured motion amplitudes with the simulation results in frequency-domain with PDSTRIP and the results using the time-domain approach based on impulse-response functions as described above.

The cases with $\chi = 0°$, $\chi = 30°$, $\chi = 90°$, $\chi = 120°$, $\chi = 150°$ and $\chi = 180°$ are given in Figure B.5 in Appendix B.

The figures reveal that the results of frequency domain determined with PDSTRIP are almost in perfect agreement with the experimental data. The general agreement of the time-domain

simulation results is satisfactory, also in the resonance region. The roll motion is very sensitive to additional damping and restoring terms. Some deviation of the roll motion can be observed in the cases with $\chi = 30°$ and $\chi = 60°$ in the resonance region. Interestingly, the roll motion in the resonance peak is overestimated for $\chi = 30°$ and underestimated for $\chi = 60°$. The simulated pitch motion in time domain shows a dent, where the frequency-domain result has its resonance peak.

The same trends can be found for different ship speeds.

When the regular wave characteristics are known, the best results can be achieved within frequency domain or by using the frequency-dependent hydrodynamic forces in time domain (Eqn. (4.4)). However, the impulse-response function (Eqn. (4.28)) offers a satisfactory basis to determine the hydrodynamic added mass and damping forces if the waves are unknown or irregular and/or additional external forces are acting on the ship.

4.13 Mean second-order wave loads

Wave drift forces are the time-averaged wave forces acting on a body. The body is not restrained from moving, unlike for the determination of the linear wave excitation forces. The wave drift forces are approximately proportional to the square of the wave amplitude. The methods that are usually used for the calculation of mean second-order wave loads can basically be divided into two categories: a method directly integrating the pressure and a method using the conservation of momemtum/energy. Their applicability depends on the wave characteristics, the Froude number and the slenderness of the ship hull.

Söding and Bertram [111] derive the most important part of the wave drift forces from the motions, pressures, etc. that depend linearly on the wave amplitude. Further parts of the wave drift forces, usually much smaller components, require more complex computations. The computations follow the approximations by Boese [15]. Boese proposes a simple method to estimate the added resistance in waves. First, the pressure is integrated up to the still water line. Under the assumption that the harmonic pressure variations are known on the hull, the longitudinal forces and the added resistance can be determined. Furthermore, the wetted water line oscillates around the still water line, which generates more components that have to be taken into account. Both components yield an average longitudinal force of second order. Söding and Bertram implement this method in PDSTRIP.

The drift forces can be displayed in dimensionless form denoted with a prime ($'$):

$$\overline{f_x}' = \frac{\overline{f_x}}{\rho g \zeta_a^2 \frac{B^2}{L}} , \qquad \overline{f_y}' = \frac{\overline{f_x}}{\rho g \zeta_a^2 \frac{B^2}{L}} , \qquad \overline{m_z}' = \frac{\overline{f_x}}{\rho g \zeta_a^2 B^2} . \tag{4.39}$$

Little experimental data on the mean second-order wave loads can be found in the literature. Generally, the wave drift forces are difficult to determine experimentally. The forces depend on the motion of the ship so that in experiments the hull may not be restrained from moving. However, some fastening is necessary to be able to measure the acting forces.

Figure 4.10 shows the wave drift forces and yaw moment acting on the S-175 hull. Experimental results of the wave drift forces are given in Yasukawa [122]. The mass distribution, as used in Yasukawa [122], is given in Table 4.2. The wave drift forces are determined and measured for the advancing ship with a Froude number of $Fn = 0.15$. The figure reveals a satisfactory agreement of the calculations with the experiments. The yaw moment is underestimated, but the general slope can be determined with the calculations.

Table 4.2.: Mass distribution of S-175 for drift force calculations according to Yasukawa [123], [122]

m [t]	x_G [m]	z_G [m]	$\overline{GM}$ [m]	i_{xx}^2 [m^2]	i_{yy}^2 [m^2]	i_{zz}^2 [m^2]
24801	-2.545	9.235	1.006	110.406	2216	2216

Also, in Schoop-Zipfel and Abdel-Maksoud [91], it is shown that the wave drift forces can be determined with satisfactory accuracy via Söding and Bertrams' theory [111] using PDSTRIP, see as well Figures B.8 and B.9 in Appendix B. Furthermore, Augener and Vorhölter [6] present very satisfactory results with the same theory. However, both references determine the mean wave drift forces acting on a ship with zero forward speed. This simplification is questionable for the maneuvering case. The forward speed can crucially influence the wave drift forces.

Comparable calculations in the literature (e.g. Skejic and Faltinsen [97]) show similar results to the present work.

Therefore, the application of PSDTRIP to determine the wave drift forces appears adequate, especially from an engineering point of view.

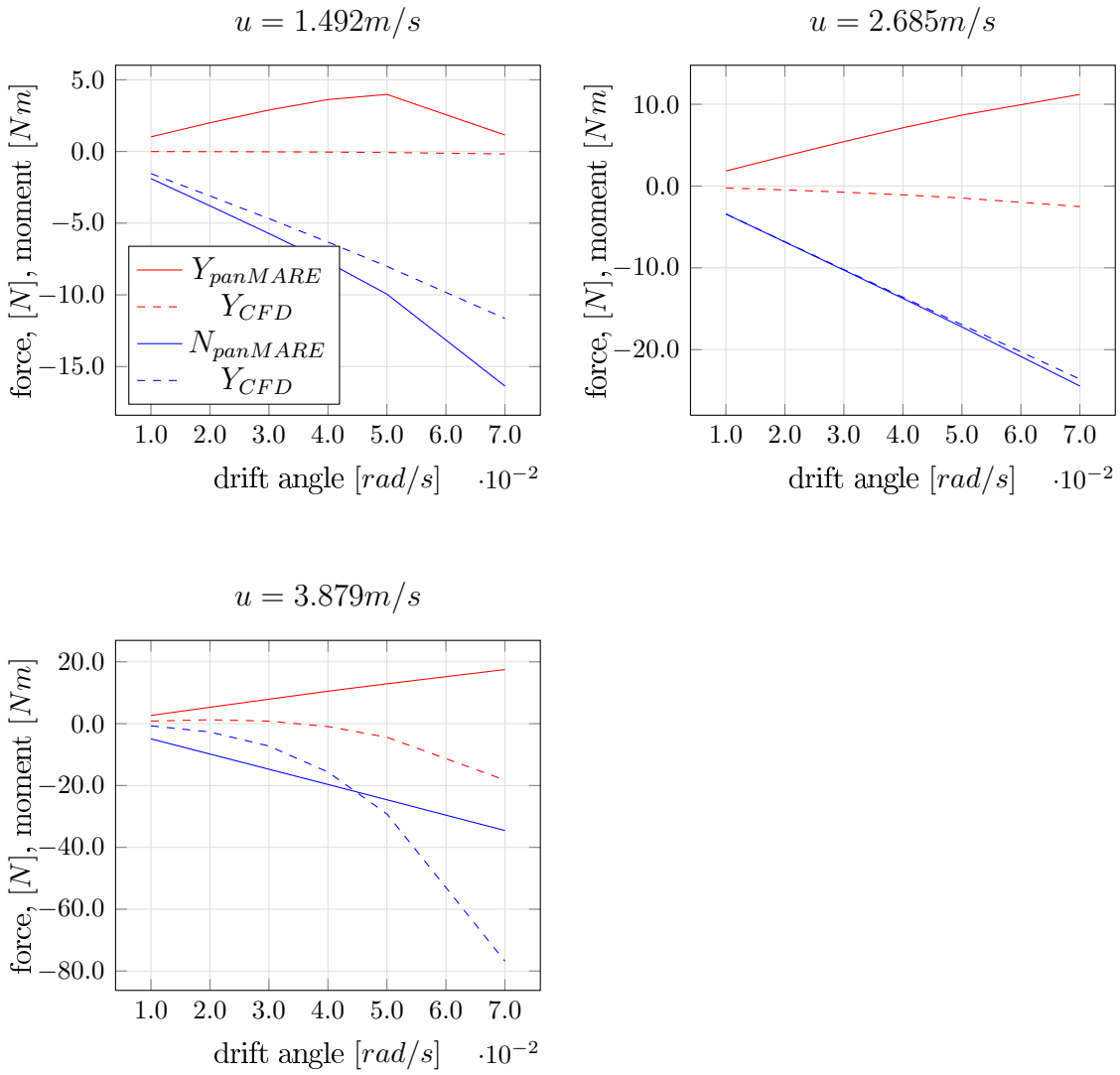

Figure 4.8.: Heave and pitch motion and amplitudes of S-175; different time integration schemes and time step sizes; $\zeta_A = 1\text{m}$, $\chi = 120°$, $\lambda/L_{pp} = 1.0$

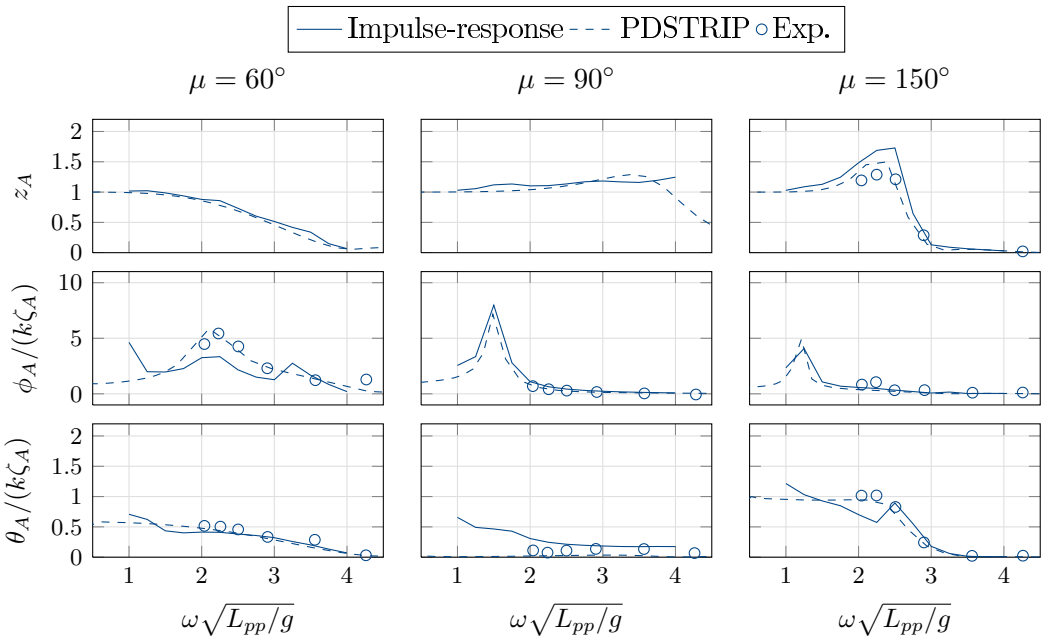

Figure 4.9.: Heave, pitch and roll RAO of S-175; calculated with impulse-response function and PDSTRIP; measurements from ITTC78 [51]

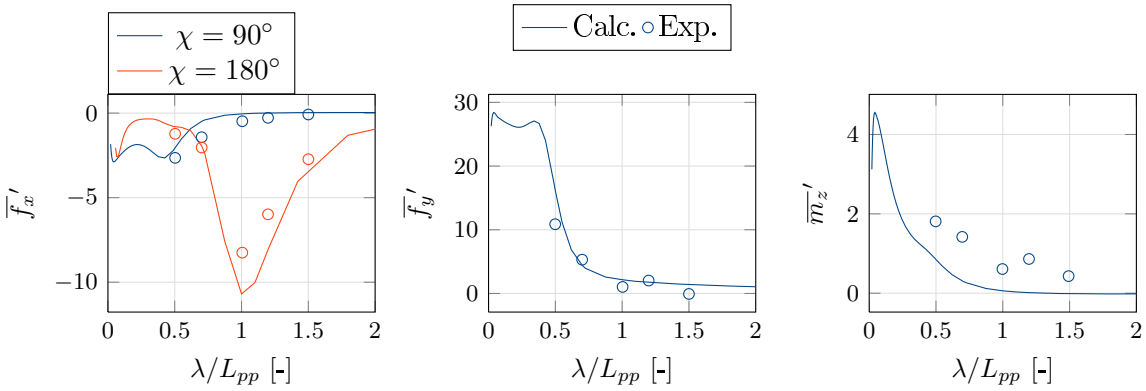

Figure 4.10.: Drift force on S-175 as a function of the wave length for different encounter angles; $Fn = 0.15$; measurements from Yasukawa [122]

5 Maneuvering in Waves

Two different approaches are developed to simulate the maneuvering behavior of ships in waves. First, the so-called two-time scale model is presented. This model splits the motion into a seakeeping and a maneuvering motion and solves each component separately, while certain parameters are exchanged. Secondly, a unified theory is introduced. This theory unifies the seakeeping and the maneuvering theories within one set of equations. Starting with the seakeeping equations, nonlinear terms are introduced to describe the maneuvering effects.

5.1 Two-time scale model

The maneuvering behavior of a ship in waves can be simulated by regarding the combined seakeeping and maneuvering as a two-time scale problem. The assumption behind this model is that the oscillating motion due to linear wave loads has a rapidly varying time-scale while the maneuvering varies slowly. The two time-scales can then be solved separately while some interaction effects have to be regarded. The maneuvering motion affects the rapidly varying wave-frequency problem in terms of changing heading angles and average ship speeds. On the other hand, the maneuvering analysis is influenced by the seakeeping in terms of the slowly varying mean second-order wave loads.

The total motion can be written as the sum of the low-frequency (LF) maneuvering motion and the wave-frequency (WF) seakeeping motion, following the principle of linear superposition (Denis and Pierson [23]):

$$y = y_{LF} + y_{WF} \ , \tag{5.1}$$

as illustrated in Figure 5.1.

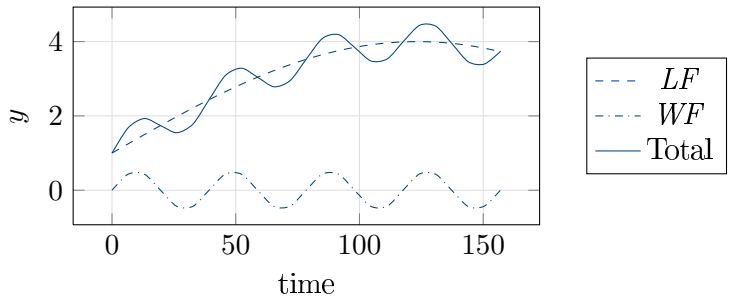

Figure 5.1.: Total motion as sum of LF and WF motion (Fossen [32])

The basic assumption is that the average track of the ship is not influenced by the linear wave loads, since these only produce an oscillatory motion. The only effect of the seakeeping on the maneuvering motion is due to the mean second-order wave drift forces that change slowly in time. The WF motion is influenced by the maneuvering through the changing angle of attack of the waves and the changing frequency of encounter. The LF maneuvering model is extended to account for the slowly varying wave drift forces and moments. They are the surge mean wave force $\overline{f}_x$, the sway mean wave force $\overline{f}_y$ and the yaw mean wave moment $\overline{m}_z$. The equation of motion for the LF motion can be written as (see Eqn. (3.7))

$$\boldsymbol{M}\dot{\boldsymbol{\nu}} = \boldsymbol{f}(u, v, p, r, \dot{u}, \dot{v}, \dot{p}, \dot{r}, \delta) + \boldsymbol{f}_W \ , \tag{5.2}$$

where the mean wave drift forces are marked with $_W$.

The motion equation for maneuvering, applying the MMG notation, is written as (see Eqn. (3.8))

$$\boldsymbol{M}\dot{\boldsymbol{\nu}} = \boldsymbol{f}_H + \boldsymbol{f}_P + \boldsymbol{f}_R + \boldsymbol{f}_W \ . \tag{5.3}$$

The motion equation for seakeeping in frequency domain has been derived as (see Eqn. (4.4))

$$\boldsymbol{M}\dot{\boldsymbol{\nu}} = \boldsymbol{f}_h = -\boldsymbol{A}(\omega)\ddot{\boldsymbol{\xi}} - \boldsymbol{B}(\omega)\dot{\boldsymbol{\xi}} - \boldsymbol{C}\boldsymbol{\xi} + \boldsymbol{f}_e \ . \tag{5.4}$$

When this equation is solved for the motion amplitudes and the RAOs are known, the motion can be solved directly as (see Eqn. (4.5) and Eqn. (4.6))

$$\boldsymbol{\eta} = \mathbf{RAO}\zeta_A \cos(\omega t + \boldsymbol{\epsilon}) \ , \tag{5.5}$$

$$\boldsymbol{\nu} = -\mathbf{RAO}\zeta_A \omega \sin(\omega t + \boldsymbol{\epsilon}) \ . \tag{5.6}$$

For irregular waves and when additional forces are applied, the impulse-response function has

been derived in Section 4.7 to determine the forces acting on the ship (see Eqn. (4.28)):

$$\boldsymbol{M}\dot{\boldsymbol{\nu}} = \boldsymbol{f}_h = -\boldsymbol{M}_A\dot{\boldsymbol{\nu}} - \boldsymbol{D}\boldsymbol{\nu} - \int_{-\infty}^{t} \boldsymbol{K}(t-\tau)[\boldsymbol{\nu}(\tau) - U\boldsymbol{e}_1]d\tau - \boldsymbol{C}\boldsymbol{\eta} + \boldsymbol{f}_e \,, \tag{5.7}$$

where the wave excitation forces $\boldsymbol{f}_e$ are added to the hydrodynamical forces.

When no waves are present, the equations become exactly the same as the still water maneuvering equations. The resulting motion is then the same motion as predicted using a maneuvering theory. Also, the other way around, when no steering is present, the results of the WF component equal the linear seakeeping solution. However, no direct interaction is regarded for the maneuvering in waves case.

5.1.1 Implementation

Both equations of motion are solved parallel to determine the maneuvering motion in waves. The mean heading, ship speed and position calculated in the LF model are transferred to the WF model after each iteration. Those values are used to determine the frequency of encounter, the wave excitation forces and the displacement within the WF-model. The latter is needed to calculate the restoring forces. The particular results of each component are summed up to obtain the total motion. The general computational procedure is sketched in Figure 5.2.

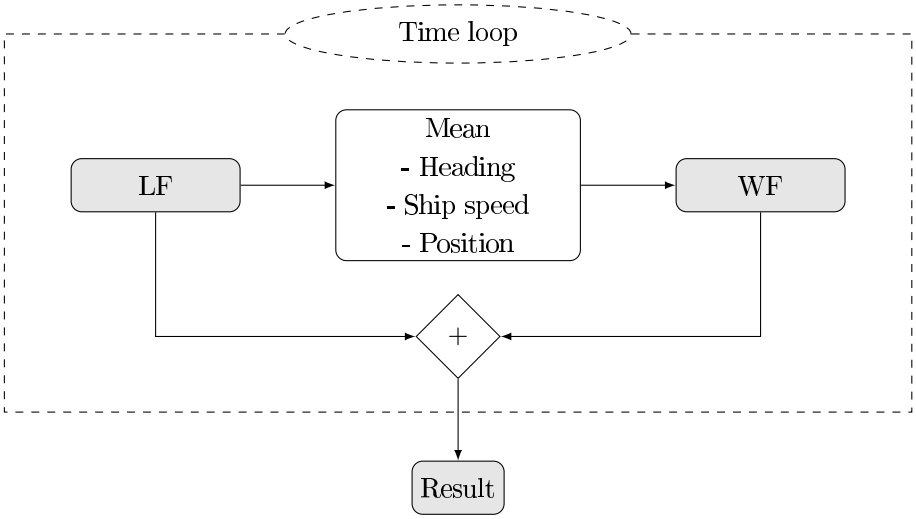

Figure 5.2.: Computational algorithm of the two-time scale simulation

WF model

The frequency of encounter depends not only on the wave frequency, but also on the global position of the ship:

$$\omega_e = \omega_0 t - kx_0 \cos(\eta) - ky_0 \sin(\eta) \ . \tag{5.8}$$

The motion of the ship can be solved by either using the RAOs with Eqns. (5.5) and (5.6) or by solving the equation of motion, Eqn. (5.4) or (5.7).

LF model

For the LF model, regular maneuvering simulations are conducted as described in Chapter 3. Additionally, the mean second-order wave drift forces are added to the hydrodynamic forces acting on the ship. The wave drift forces are predetermined with PDSTRIP and saved in a database. During the time simulation, the forces are available in this database.

5.2 Unified theory

For the unified theory, the time-domain seakeeping equations are used as the basis. The linear damping terms are modified to achieve agreement with the maneuvering theory in the calm water case and necessary nonlinear terms are added. History effects are already included with the retardation functions in the seakeeping equation. Linear and nonlinear wave loads are also kept from the seakeeping model. The time-domain transformations are given in Chapter 4. The approach is based on the results of Fossen [32], [33].

Reconsidering the time-domain equation derived in Chapter 4 based on the impulse-response function (Eqn. (4.28)) gives

$$\boldsymbol{M}\dot{\boldsymbol{\nu}} = \boldsymbol{f}_h = -\boldsymbol{A}(\infty)\dot{\boldsymbol{\nu}} - \boldsymbol{D}\boldsymbol{\nu} - \int_{-\infty}^{t} \boldsymbol{K}(t-\tau)[\boldsymbol{\nu}(\tau) - U\boldsymbol{e}_1]d\tau - \boldsymbol{C}\boldsymbol{\eta} + \boldsymbol{f}_e \ . \tag{5.9}$$

This equation has been derived using zero-speed potential coefficients. The remaining speed-dependent damping terms have to be added directly in time domain. Speed-independent damping terms can also be regarded by modifying the damping terms that provide the basis for the retardation functions (see Section 4.8). However, the maneuvering derivatives, which are of major interest in this work, are generally speed dependent, so that a direct inclusion in time domain is more reasonable.

In contrast to the two-time scale method, the unified theory provides a direct coupling of the low-frequency maneuvering motion and the wave-frequency motion. Subsequently, the maneuvering motion is also influenced by the first-order wave loads. The entire motion of the

ship is described with one set of equations.

Unified theory based on MMG model

To evolve the unified theory, the forces due to maneuvering motion have to be incorporated into Eqn. 5.9. Applying a MMG model, the forces of the propeller and the rudder and the mean wave drift forces are added as additional exciting forces. The hull forces consist of linear added mass forces and linear and nonlinear damping forces.

The motion equation then becomes

$$\boldsymbol{M}\dot{\boldsymbol{\nu}} = \boldsymbol{f}_H + \boldsymbol{f}_P + \boldsymbol{f}_R + \boldsymbol{f}_e + \boldsymbol{f}_W \ , \tag{5.10}$$

with

$$\boldsymbol{f}_H = -\boldsymbol{A}(\infty)\dot{\boldsymbol{\nu}} - \boldsymbol{D}\boldsymbol{\nu} - \int_{-\infty}^{t} \boldsymbol{K}(t-\tau)[\boldsymbol{\nu}(\tau) - U\boldsymbol{e}_1]d\tau - \boldsymbol{C}\boldsymbol{\eta} + \boldsymbol{f}_{NL,maneuvering}(\boldsymbol{\nu}) \ , \tag{5.11}$$

where

$$\boldsymbol{D} = \boldsymbol{C}_A^* + \boldsymbol{B}(\infty) \ , \tag{5.12}$$

$$\boldsymbol{C}_A^* = U\boldsymbol{A}(\infty)\boldsymbol{L} \ . \tag{5.13}$$

When using the slender-body theory to determine the forces due to maneuvering motion, the linear damping forces yield (see Eqn. (3.54))

$$\boldsymbol{B}_{maneuvering} = u \cdot \begin{pmatrix} 0 & 0 & 0 & 0 & 0 & 0 \\ 0 & -a^0_{22,m} & 0 & 0 & 0 & -a^0_{22,m}x_m + \int_{x_a}^{x_m} a^0_{22}dx - A^0_{11} \\ 0 & 0 & 0 & 0 & 0 & 0 \\ 0 & a^0_{42,m} & 0 & 0 & 0 & a^0_{42,m}x_m - \int_{x_a}^{x_m} a^0_{42}dx \\ 0 & 0 & 0 & 0 & 0 & 0 \\ 0 & -x_m a^0_{22,m} - \int_{x_m}^{x_f} a^0_{22}dx + A^0_{11} & 0 & 0 & 0 & -x_m^2 a^0_{22,m} + \int_{x_a}^{x_m} x a^0_{22}dx - \int_{x_m}^{x_f} x a^0_{22}dx \end{pmatrix} , \tag{5.14}$$

with a linear dependence on the forward speed u. The separation section is generally close to the stern of the ship. The integral along the hull behind the separation point ($\int_{x_a}^{x_m} a dx$) is subsequently small and can be neglected. The integral along the hull in front of the separation point equals approximately the entire ship's added mass. For the forward speed, it holds that $u \approx U$. So, the matrix equals the linear speed-dependent damping terms obtained in

seakeeping. These are (see Eqn. 4.33)

$$\boldsymbol{D}(\omega_e) = U \cdot \begin{pmatrix} 0 & 0 & 0 & 0 & 0 & 0 \\ 0 & a_{22,A} & 0 & a_{24,A} & 0 & x_A a_{22,A} \\ 0 & 0 & a_{33,A} & 0 & -x_A a_{33,A} & 0 \\ 0 & a_{42,A} & 0 & a_{44,A} & 0 & x_A a_{42,A} \\ 0 & 0 & -x_A a_{33,A} + A_{33} & 0 & x_A^2 a_{33,A} + A_{53} & 0 \\ 0 & x_A a_{22,A} - A_{22} & 0 & x_A a_{24,A} - A_{42} & 0 & x_A^2 a_{22,A} - A_{62} \end{pmatrix} . \tag{5.15}$$

The terms are integrated to the point where the flow presumably separates. In seakeeping theory, this is assumed to be the aft section, denoted by $_A$. In maneuvering theory, this section is specified and denoted by $_m$.

The zero-speed damping matrix $\boldsymbol{B}$ does not appear in maneuvering, since it is zero for $\omega = 0$.

In seakeeping, $\boldsymbol{D}$ is build for $\omega = \infty$. However, in maneuvering it is needed for $\omega = 0$. To achieve the maneuvering results with the unified theory and $\zeta_A = 0$, the additional damping terms are used with $\omega = 0$. Simulations with the S-175 and the KVLCC2 show that, otherwise, the turning rate is too small and subsequently the turning circles become too large.

The nonlinear maneuvering forces are calculated according to the nonlinear terms in slender-body theory. Similarly, results are found for the propeller and rudder forces ($\boldsymbol{f}_P$ and $\boldsymbol{f}_R$) according to Section 3.3.1 and Section 3.3.2.

Unified theory based on hydrodynamic derivatives

Alternatively, the maneuvering motion can be described based on a whole ship model using hydrodynamic derivatives. To unify this model and incorporate the wave-induced motion, some assumptions have to be made. To describe the hull forces, it is assumed that the matrix $\boldsymbol{D}$ in Eqn. 5.11 can be substituted by the linear hydrodynamic derivatives. Furthermore, the propeller, rudder and nonlinear hull forces are included in the hydrodynamic derivatives. The added mass terms included in the hydrodynamic derivatives are omitted and replaced by the infinite-frequency added mass from seakeeping theory. The equation of motion then yields

$$\begin{aligned} \boldsymbol{M}\dot{\boldsymbol{\nu}} = &- \boldsymbol{A}(\infty)\dot{\boldsymbol{\nu}} - \int_{-\infty}^{t} \boldsymbol{K}(t-\tau)[\boldsymbol{\nu}(\tau) - U\boldsymbol{e}_1]d\tau - \boldsymbol{C}\boldsymbol{\eta} \\ &+ \boldsymbol{f}(u,v,p,r,\delta) + \boldsymbol{f}_e + \boldsymbol{f}_W \ , \end{aligned} \tag{5.16}$$

with the term $\boldsymbol{f}(u,v,p,r,\delta)$ as described in Section 3.2 but not including added mass terms.

Other than in the two-time scale model, the equations do not fall back on the maneuvering equations when no waves are present. Also, the equations are different to the linear seakeeping equations when no steering is performed. However, the maneuvering and seakeeping effects are directly coupled and interaction effects are not neglected.

5.3 Results

Simulations are conducted for the S-175 container ship and the KVLCC2 tanker ship. Experimental data is available for the S-175 in Yasukawa [122]. Ueno et al. [114] perform model tests of maneuvering in waves for a VLCC tanker comparable to the KVLCC2.

A ship in waves does not necessarily drift towards the wave propagating direction. The turning circles in waves can be characterized by the drifting distance H_D and the drifting direction μ_D. Ueno et al. [114] define the drifting distance H_D as the distance between successive ship positions, in which the wave encounter angle χ is equal to 90°. The drifting direction μ_D is defined as the offset angle between the wave propagating direction and the moving direction of ship positions, in which the wave encounter angle χ is equal to 90°. The two parameters are shown in Figure 5.3. They are almost independent of the initial wave encounter angle.

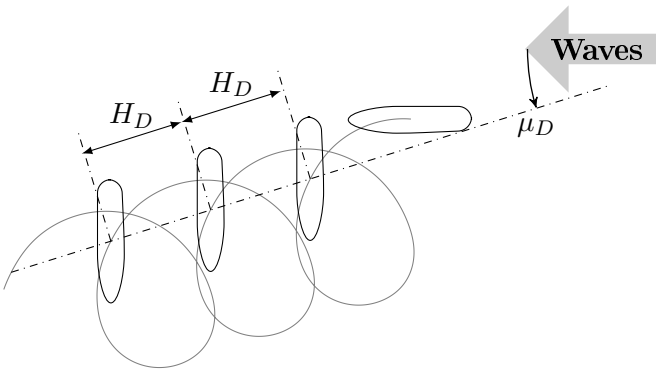

Figure 5.3.: Definition of drifting distance H_D and drifting direction μ_D

Furthermore, the waves influence the classical maneuvering characteristic parameters, i.e. advance and tactical diameter in turning circle maneuvers and overshoot angles and times in zig-zag maneuvers. These influences are strongly dependent on the initial wave encounter angle.

5.3.1 S-175

The results of the two-time scale model and the unified theory are shown for the S-175 container ship. The main dimensions and the hull geometry have been introduced in Table 3.4. The simulations are conducted with a mass distribution according to Table 4.2. Measurements of the hull drift forces and turning circles in waves are given in Yasukawa [122] and are borrowed in the present work for validation.

The work by Yasukawa [122] is the most extensive experimental work on ship maneuvering motion in waves known to the author.

The LF-component of the two-time scale model is calculated with the slender-body theory, whereas the wave drift forces are additionally added. The turning circles without the influence of the waves have been presented in Figure 3.13. The second-order wave drift forces are determined with PDSTRIP (see Section 4.13). Figure 4.10 has shown a comparison of the simulated forces with the measured results from Yasukawa [122]. The influence of the ship speed on the wave drift forces and the yaw moment can be seen in Figure B.6 in the appendix.

The simulations with the unified theory are based on the MMG model using the slender-body theory. The unified theory based on the whole ship model, using hydrodynamic derivatives is applied for the KVLCC2 tanker.

First, maneuvers in calm water simulated with the unified theory are presented to exemplify the influence of the impulse-response function on the still water maneuvering motion. The inclusion of the retardation function, in comparison to the maneuvering equations used in Chapter 3, influences the simulation results. Figure 5.4 shows the simulated $-35°$ turning circle. The simulation with straight-forward unified theory shown with solid blue lines is opposed to the results from Chapter 3 shown with dashed blue lines. The figure shows that the speed loss, the transverse velocity and the yaw rate are clearly higher when using the unified theory. This indicates that the retardation function introduces an additional negative damping in this case. By increasing the cross flow drag coefficient C_D, the calm water maneuvering characteristics equal the results from the maneuvering simulations. The results with the artifically increased C_D are labeled as 'unified tuned' in the figure. This engineering approach allows for comparing the results of the unified theory with the still water maneuvering.

Similarly, zig-zag maneuvers are simulated, see Figure 5.5. The straight-forward unified result deviates only slightly from the maneuvering result. However, using the increased cross-flow drag coefficient C_D as for the turning circle, the deviation becomes smaller and the agreement is satisfactory.

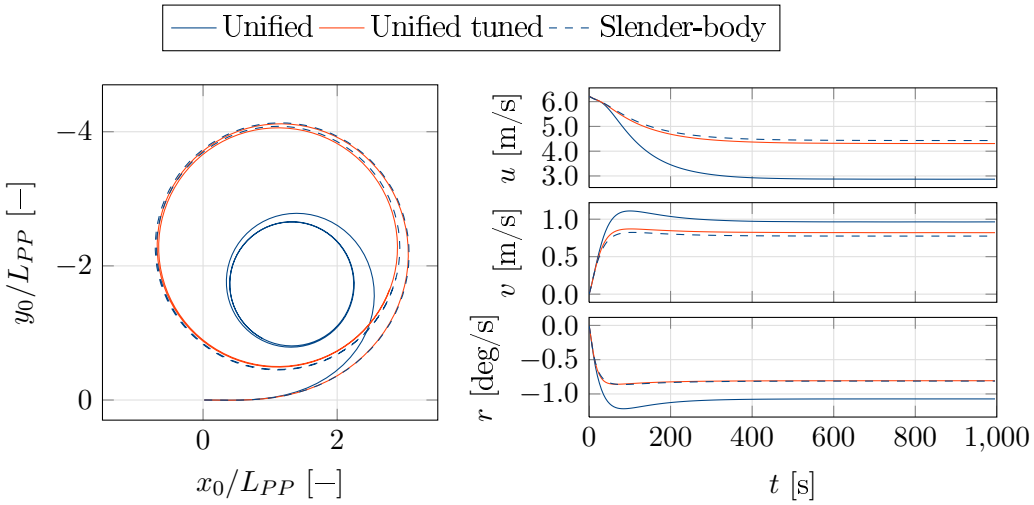

Figure 5.4.: −35° turning circle of S-175; comparison of unified theory with maneuvering theory

Turning circles in regular waves

Subsequently, the influence of the waves on the turning circle maneuver is shown. First, the two-time scale model is applied and the results are compared to experimental data. Then, the unified theory is used to simulate turning circles in regular waves. Differences to the results of the two-time scale model are highlighted.

Two-time scale model Figure 5.6 shows the average track during port and starboard turning circle maneuvers in regular waves of different lengths with an amplitude of $\zeta_A = 1.75$m. The LF component is simulated with three degrees of freedom in these simulations. The heel is neglected. Start of the maneuver is the time instant when the midship is in a wave trough. Measurements (Yasukawa [122]) are compared to the simulations. The figures reveal that the simulations roughly capture the turning motion in regular waves. The wave drift forces show a strong dependence on the wave length (which can e.g. be seen in Figure B.6), which results in the varying turning motion in the different wave length cases. Simulations with different wave lengths indicate that the wave length dependence might be shifted in the simulations. The measurements for $\lambda/L_{PP} = 0.7$ show a slightly better agreement with the simulations for $\lambda/L_{PP} = 1.0$ and the measurements for $\lambda/L_{PP} = 1.0$ show a slightly better agreement with simulations for $\lambda/L_{PP} = 1.1$, as shown with red curves in the figures. The drifting direction can be reproduced very well within the simulations.

In the case with $\lambda/L_{PP} = 0.7$, the ship is not able to turn against the waves within the simulations. In this case, the longitudinal drift force and the drift yaw moment have the largest maximum values (see Figure B.6). Those occur at an encounter angle of $\chi = 130°$ as

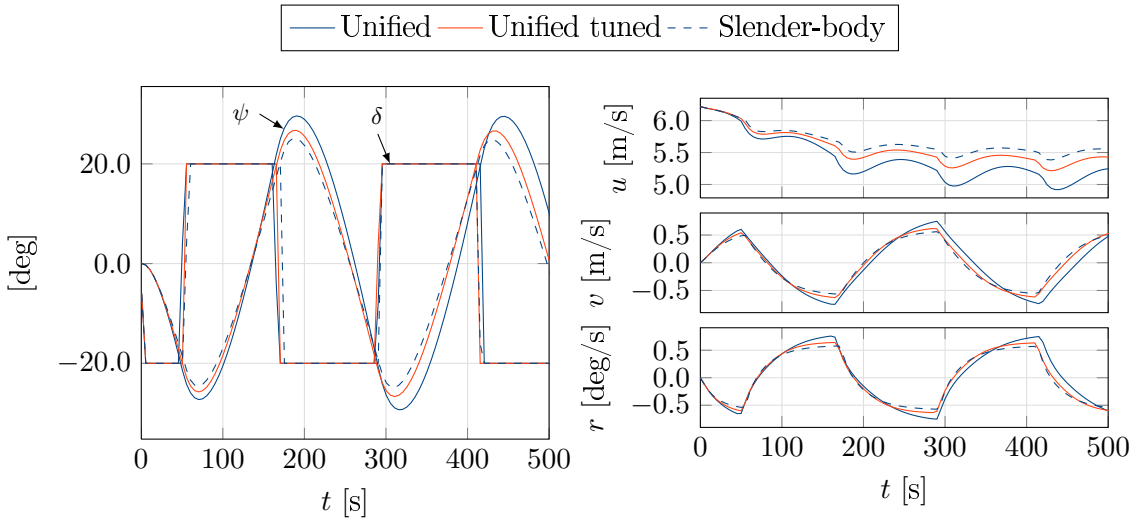

Figure 5.5.: $-20°/-20°$ zig-zag maneuver of S-175; comparison of unified theory with maneuvering theory

well as $\chi = 230°$ for $\overline{f_x}$ and $\chi = 120°$ as well as $\chi = 240°$ for $\overline{m_z}$. The turning stops at an encounter angle of $\chi = 118°$.

It is difficult to judge the drifting distance and direction, since the exact positions with $\chi = 90°$ are not known from the experiments. Furthermore, a maximum of two complete turns are measured for each wave condition, usually even less. Therefore, a comparison of the advance and the tactical diameter of the turning circles in regular waves is shown in Figure 5.7. The figure shows the simulated values contrasted with the measured values from Yasukawa [122]. Furthermore, the still water values are shown in the figure. The simulated values agree very well with the measurements. The qualitative dependence on the wave length is reproduced in all cases. Some quantitative deviation can be observed in the tactical diameter of the 35° turning circle with a wave angle of $\eta = 270°$. In this case, the simulated tactical diameter is under-predicted at all wave lengths. The starboard and port turns show almost equal characteristic parameters for $\eta = 180°$ due to the symmetry.

The behavior of the WF component for the $-35°$ turning circle in regular waves with $\lambda/L_{PP} = 0.7$, $\zeta_A = 1.75$m and $\eta = 270°$ can be seen in Figure 5.8. However, the results are achieved with the drift force for $\lambda/L_{PP} = 1.0$, since the turning trajectories show a slightly better agreement with the measurements of Yasukawa [122] and the turning motion is not stopped due to large wave drift forces and moment, as described above. The wave-induced high-frequency motion is simulated with the RAO using Eqn. 5.5 and Eqn. 5.6. These equations do not include the memory effects of the fluid.

The results of ship speed, drift angle, heave motion, roll and pitch angle as well as yaw rate during the port turn in beam sea generally reproduce the increases and decreses of the

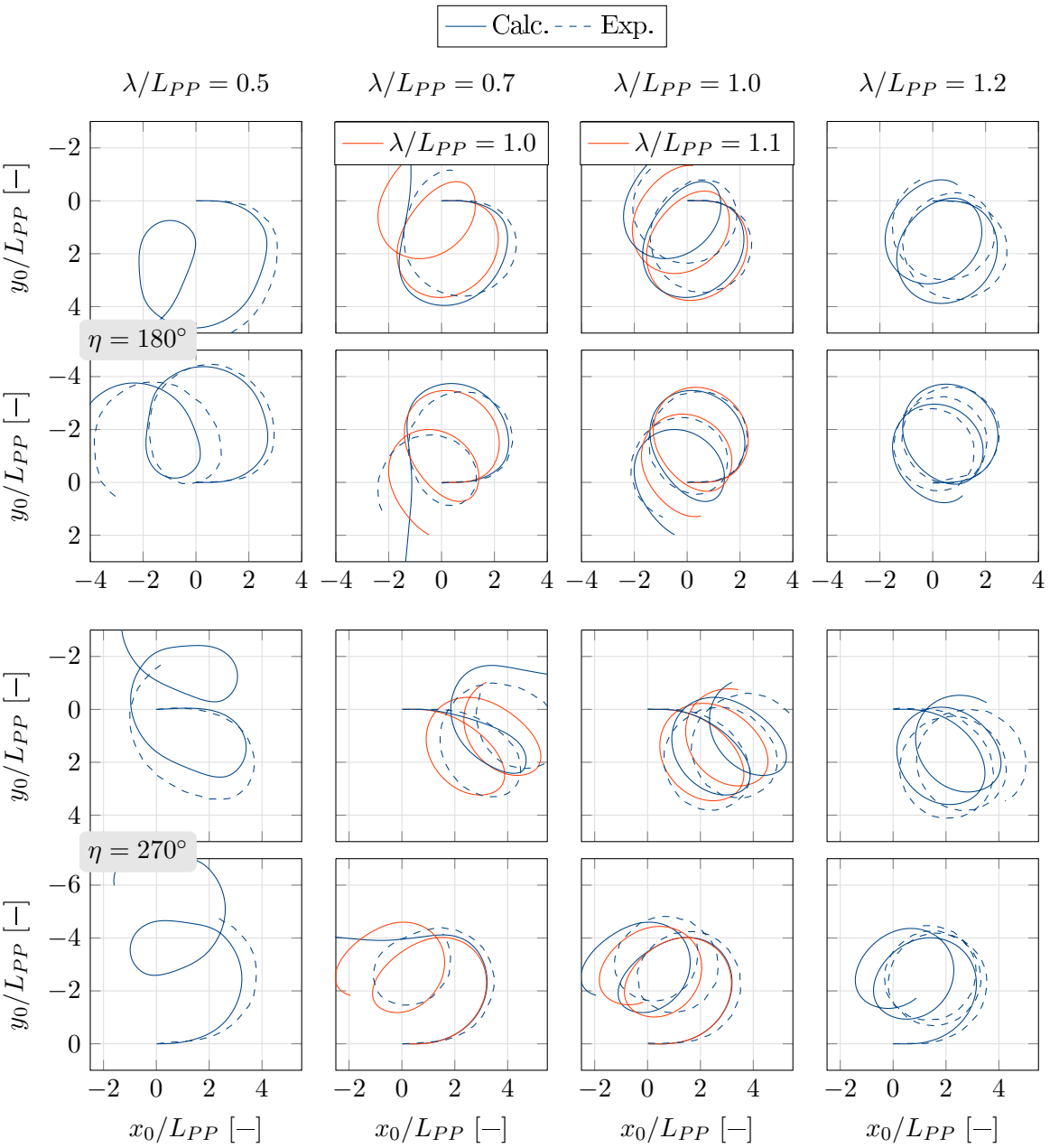

Figure 5.6.: ±35° turning circles of S-175 in regular waves using the two-time scale model; $\zeta_A = 1.75$m; measurements from Yasukawa [122]

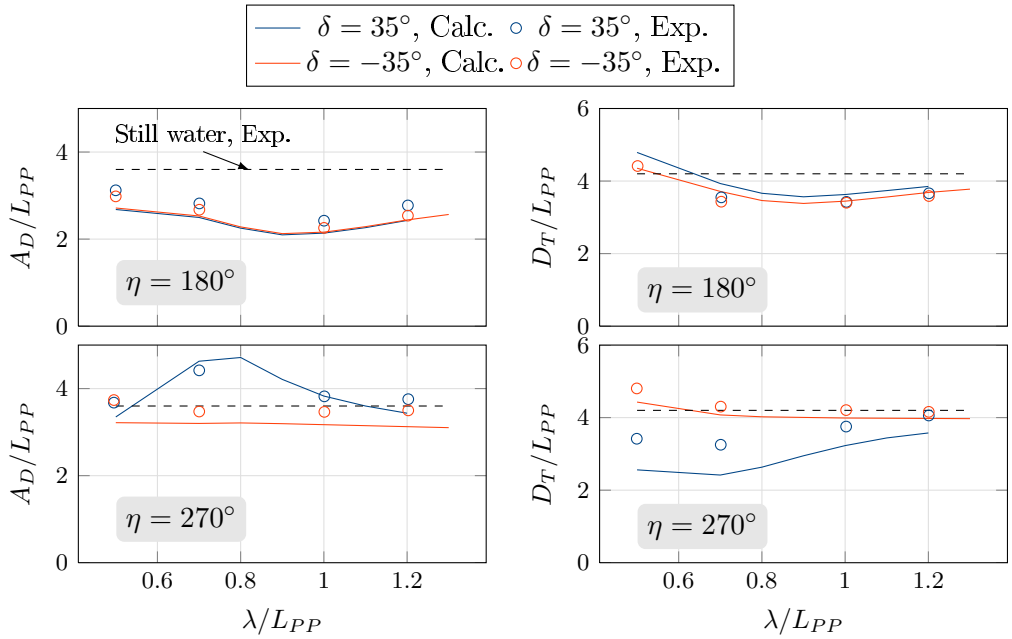

Figure 5.7.: Advance A_D and tactical diameter D_T of S-175 in regular waves; calculations with two-time scale model; $\zeta_A = 1.75$m; measurements from Yasukawa [122]

motion. However, a time shift between the simulations and the experiments can be observed. The simulations have an increasing time delay meaning that the simulated yaw rate is larger than the one of the experiment. Apart from this time shift, the agreement is satisfactory. The maximum amplitudes are in fair agreement for each motion component.

Unified theory The same turning circle maneuvers in regular waves are simulated as in the two-time scale model. The approximations described above are applied for the simulations. Figure 5.9 shows the $\pm 35°$ turning circles with wave angles of $\eta = 180°$ and $\eta = 270°$. The figure compares the simulation results with the results of the two-time scale model and the experimental results given in Yasukawa [122].

The results obtained with the unified theory are very similar to the results of the two-time scale model. The most significant difference is that the turning motion in the case with $\lambda/L_{PP} = 0.7$ is not trapped but the ship conducts the entire turn. Obviously, the linear wave loads cause the moments supporting the turning direction to exceed the counteracting wave drift moments. Besides this case, the linear wave loads - and subsequently the WF motion - seem to have a minor influence on the average track of the ship.

Figure 5.10 opposes the advance and tactical diameter simulated with the unified theory to the values from the two-time scale model and the experimental values. For the case with $\eta = 180°$, the results are very comparable to the results obtained with the two-time scale

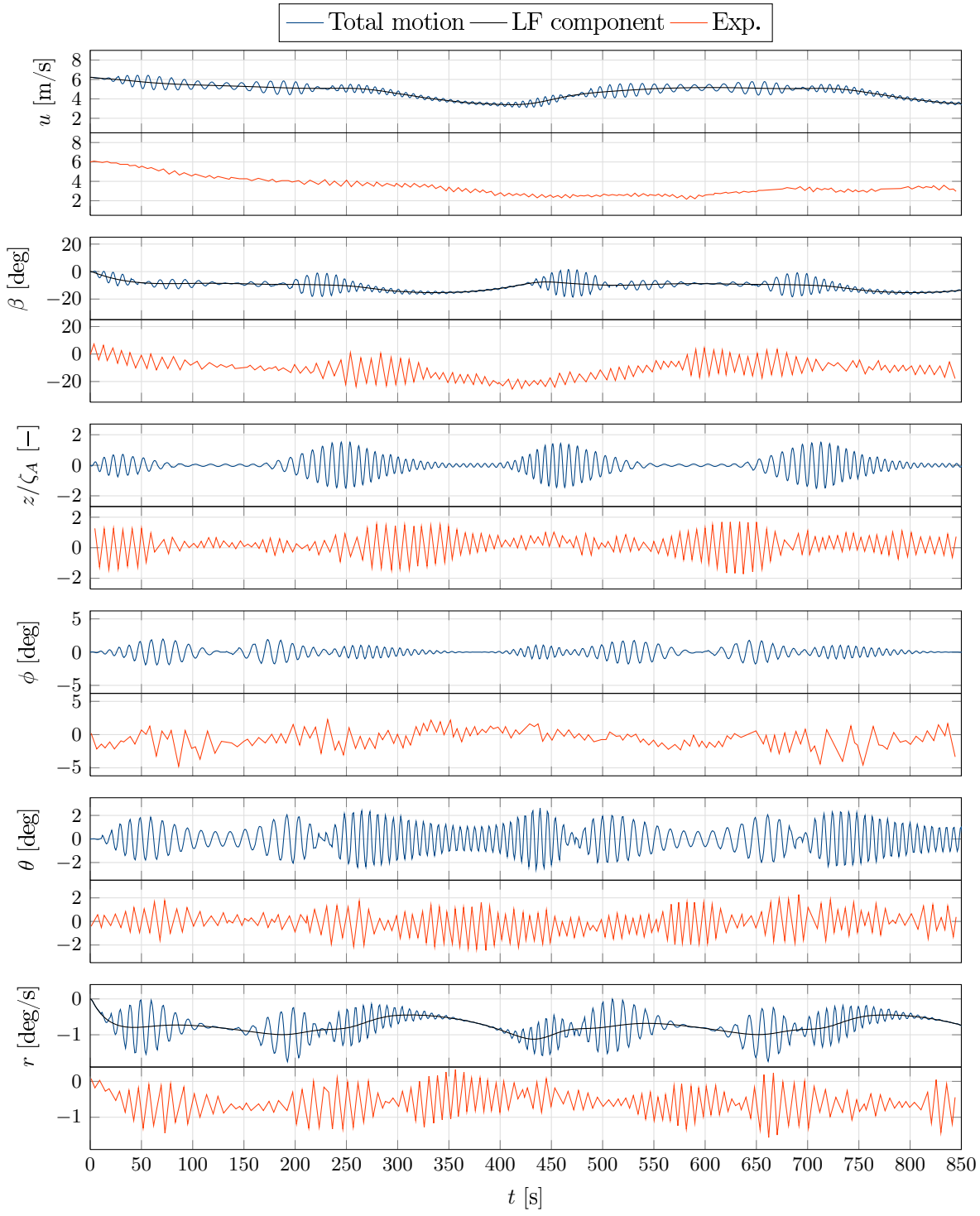

Figure 5.8.: Motion components during $-35°$ turning circle of S-175 in regular waves with two-time scale model; $\zeta_A = 1.75$m, $\lambda/L_{PP} = 1.0$, $\eta = 270°$; WF simulated with RAO

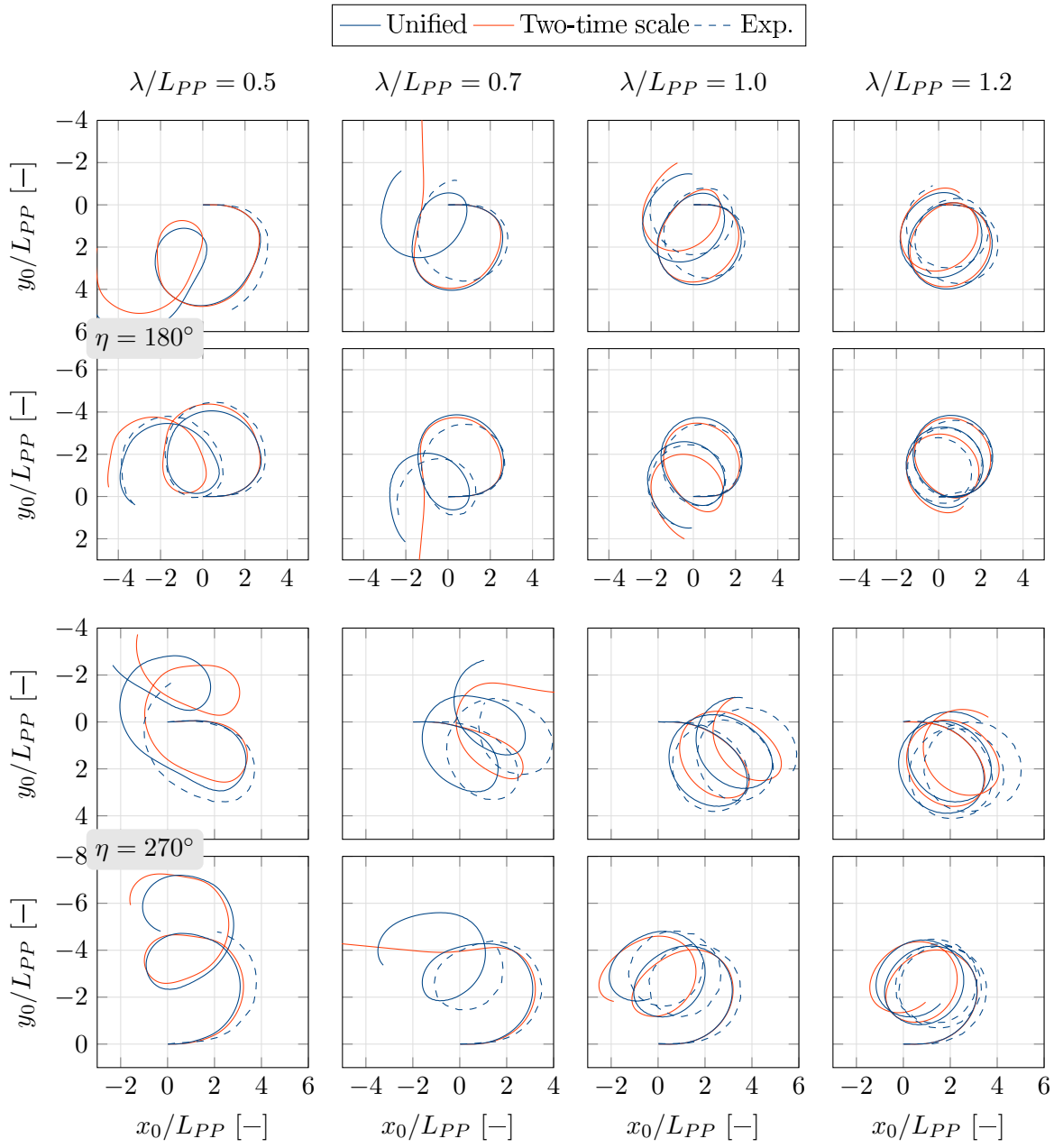

Figure 5.9.: ±35° turning circles of S-175 in regular waves; comparison of unified model, two-time scale model and experiment; $\zeta_A = 1.75$m; measurements from Yasukawa [122]

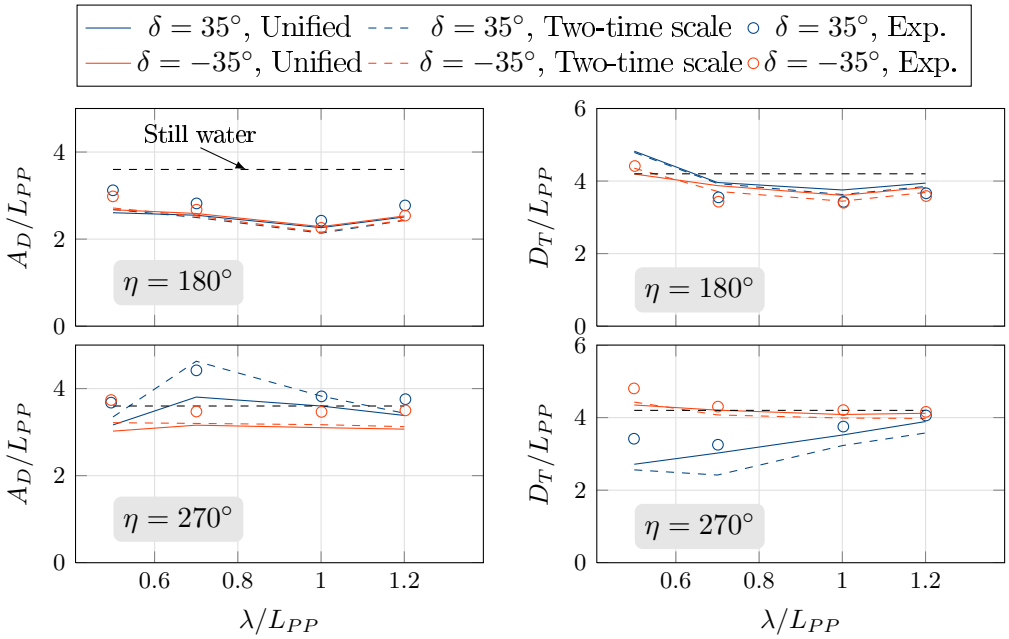

Figure 5.10.: Advance and tactical diameter of S-175 in regular waves; calculations with unified model and two-time scale model; $\zeta_A = 1.75$m; measurements from Yasukawa [122]

model. This is not true for the case with beam waves. The advance of the starboard turns are clearly smaller than the values obtained with the two-time scale model and the experimental results for $\eta = 270°$. Especially for $\lambda/L_{PP} = 0.7$, the advance simulated with the unified theory is smaller than the two-time scale results and the experimental value. This can also be observed in Figure 5.9. However, the tactical diameter shows a better agreement with the experiments than the two-time scale model. Further, the overall track is in better agreement with the measurement, as can be seen in Figure 5.9.

The individual motion components are shown in Figure 5.11 for a wave length ratio of $\lambda/L_{PP} = 0.7$ and a wave angle of $\eta = 270°$. The figure also shows the results of the two-time scale model for comparison. Figure C.3 in the appendix contrasts and compares the simulation results to the experimental data of Yasukawa [122]. As described previously, the result with the two-time scale model is obtained with the wave drift force of $\lambda/L_{PP} = 1.0$. The average rate of turn in the current simulation is slightly lower than in the simulation with the two-time scale model. This is, however, also the case without waves, see Figure 5.4. Furthermore, a direct comparison of the average values is factually flawed due to the different wave drift forces. The temporal course of the values simulated with unified theory and with two-time scale model is very similar. The memory effect has little influence, at least in this case. The heave motion decays faster in the simulation with the two-time scale model. Besides this, no clear deviation can be observed.

Alternatively, the WF results of a hybrid theory are shown in Figure 5.12. The WF component of the two-time scale model is simulated with the impulse-response function (Eqn. (5.7)) in these simulations. The figure shows that the there is no noteworthy difference between the WF components and the result of the unified theory. In this way, the memory effects can also be included in the two-time scale model.

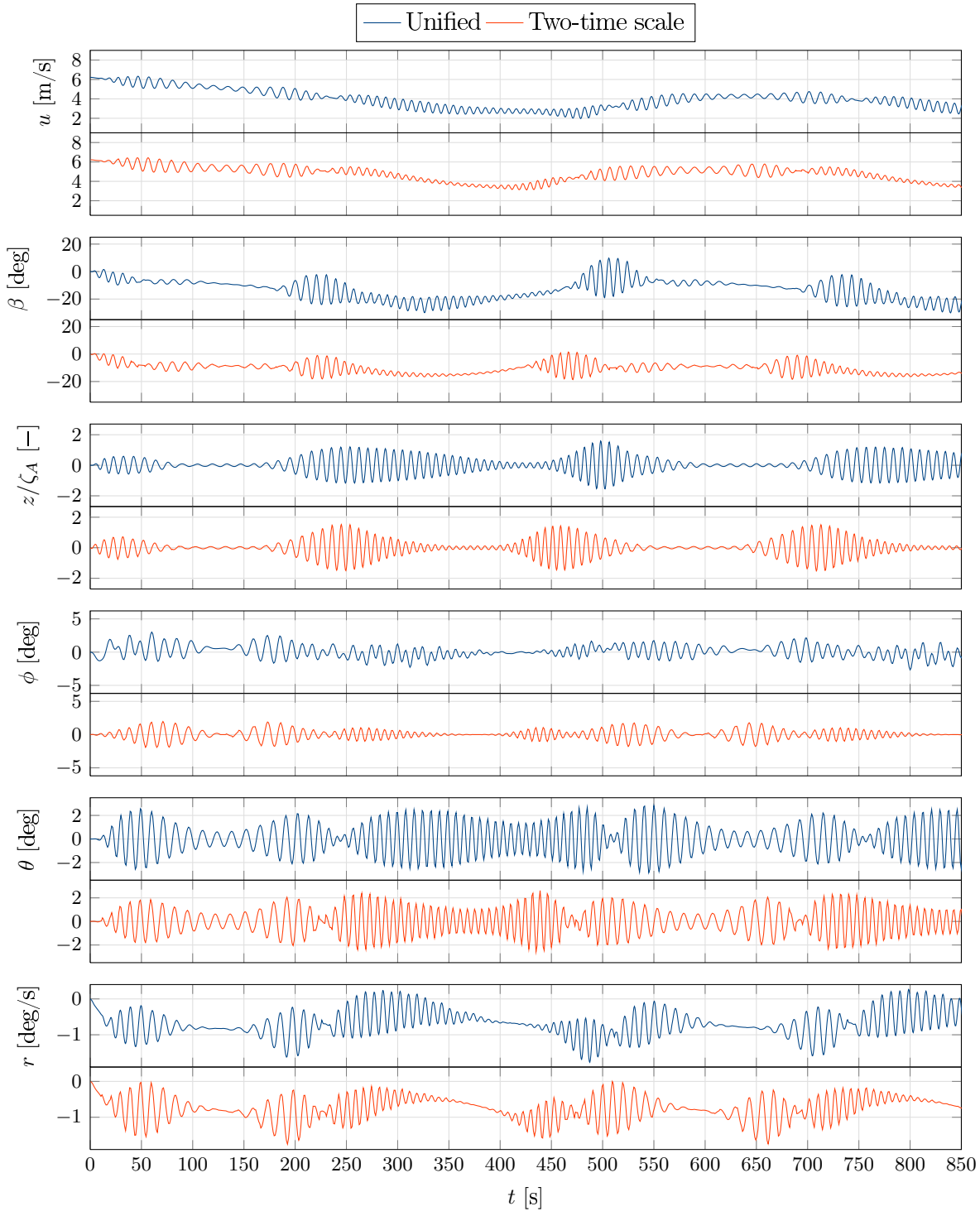

Figure 5.11.: Motion components during $-35°$ turning circle of S-175 in regular waves using unified and two-time scale theory (two-time scale results with drift forces for $\lambda/L_{PP} = 1.0$); $\zeta_A = 1.75$m, $\lambda/L_{PP} = 0.7$, $\eta = 270°$; WF simulated with RAO

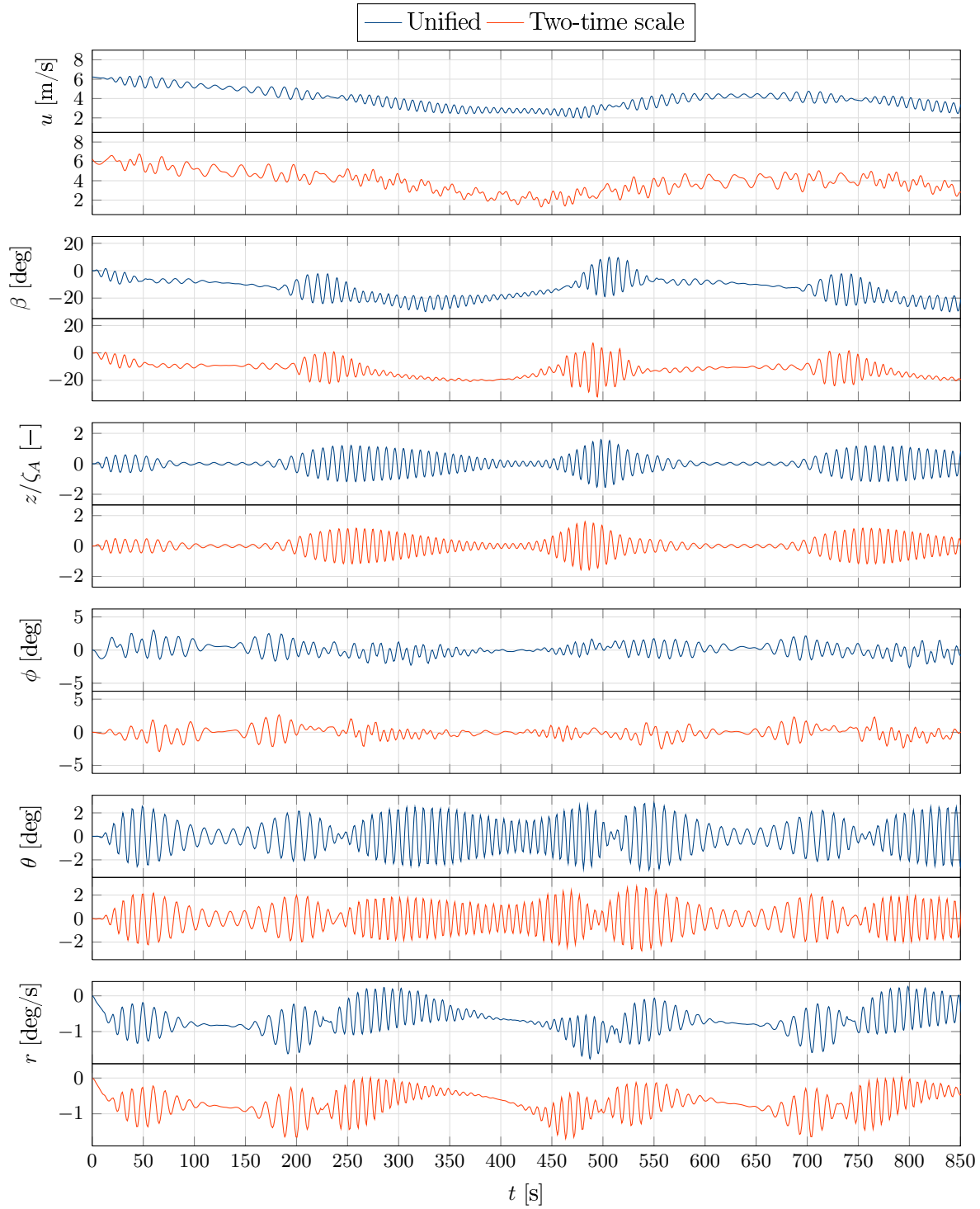

Figure 5.12.: Motion components during $-35°$ turning circle of S-175 in regular waves using unified and two-time scale theory (two-time scale results with drift forces for $\lambda/L_{PP} = 1.0$); $\zeta_A = 1.75$m, $\lambda/L_{PP} = 0.7$, $\eta = 270°$; WF simulated with impulse-response function

Zig-zag maneuvers in regular waves

$-20°/-20°$ zig-zag maneuvers are simulated in regular stern, beam and bow waves of different length and plotted in Figures C.4, C.5 and C.6 in the appendix. The figures show the simulation result of the unified theory and the two-time scale model in waves contrasted with the results in calm water. No experimental data is available for this case.

In stern and head waves, the effect of the waves on the maneuver rises with increasing wave length. Beam waves show an opposite trend; the maneuver is influenced more by short waves than by long waves. Stern waves ($\eta = 0°$) have the smallest effect on the zig-zag maneuvers. Both theories show a slight increase of the response time. The overshoot angles increase a little. The largest effects are in waves with a length of $\lambda/L_{PP} = 1.0$. The unified theory shows these effects more pronounced than the two-time scale model. However, the still water overshoot angles are also larger when simulated with the unified theory. For beam waves with a wave length of $\lambda/L_{PP} = 0.5$, the maneuver cannot be finished due to the large wave drift forces. The other wave length cases show a decrease of the overshoot angles due to the wave drift forces. The decrease predicted by the two theories is practically the same. The overshoot time, however, is somewhat larger in the results produced with the unified theory. Head waves lead to an increase of the overshoot angles. For $\lambda/L_{PP} = 0.5$, almost no effect of the waves on the maneuvers can be observed. Both theories predict the same increase of the overshoot angles and times in waves with $\lambda/L_{PP} = 1.2$. In the cases with $\lambda/L_{PP} = 0.7$ and $\lambda/L_{PP} = 1.0$, the largest deviation between the two theories occurs. In wave lengths of $\lambda/L_{PP} = 1.0$, the overshoot angles become very large and especially the overshoot times become extensive. Both theories show the same trend in this case.

The change of the oscillatory WF motion is rather small since the wave angle of encounter χ has only little variation over time. This results in small changes of the wave excitation forces and the results are similar to the straight-forward motion simulated in Chapter 4 and is not discussed here.

5.3.2 KVLCC2

The second simulation example considers the KVLCC2 tanker. Due to the lack of experimental data on the KVLCC2 performing maneuvers in waves, the results are compared with results from Ueno et al. [114]. Ueno et al. conduct an experimental study on the maneuvering motion of a VLCC model ship in regular waves. The present study is based on the KVLCC2 given in Table 3.3. The wave drift forces are calculated for the KVLCC2 hull geometry but with the mass distribution of the VLCC as presented in Ueno et al. [114].

The maneuvering simulations in the present study are based on the hydrodynamic derivatives given in Cura Hochbaum et al. [22], see Section 3.2. A validation of the seakeeping (straight

motion in waves and wave drift forces) is given in the appendix, see Section B.3.

Simulations with the two-time scale model and the unified theory are conducted. First, the unified model is used to simulate maneuvers with $\zeta_A = 0$. The results are compared with the still water results of Chapter 3. Subsequently, turning circle and zig-zag maneuvers are conducted in regular waves with different lengths and encounter angles. The results are contrasted with the experimental data given in Ueno et al. [114].

Figure 5.13 shows a $-35°$ turning circle simulated with unified theory. The maneuvering characteristics in calm water are again influenced by the impulse-response function.

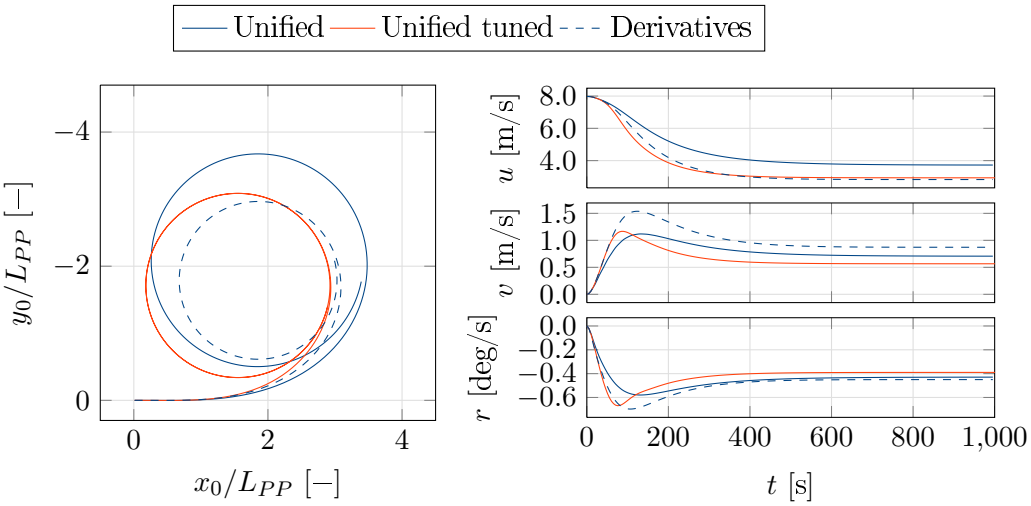

Figure 5.13.: $-35°$ turning circle of KVLCC2; comparison of unified theory with maneuvering theory

The maneuvering simulations are based on a set of 45 derivatives. A fine tuning is therefore not trivial. By increasing the linear X-derivatives, the simulation result can be improved slightly, as shown in Figure 5.13. However, Figure 5.14 reveals that the zig-zag maneuver is not significantly influenced by this increase. Investigations have shown that this "tuning" does not influence the trend induced by waves. So, for the present work, the still water results are regarded as sufficient. Only the effects generated by waves need to be assessed. The experimental data used in the present work (given in Ueno et al. [114]) is limited to the drifting distance and the drifting angle. A precise description of the calm water maneuvers is not necessary to assess this change. Furthermore, the maneuvering simulations are based on the KVLCC2; however, Ueno et al. [114] use a different hull geometry in their experiments. A deviation of the results is therefore expectable and only tendencies can be compared.

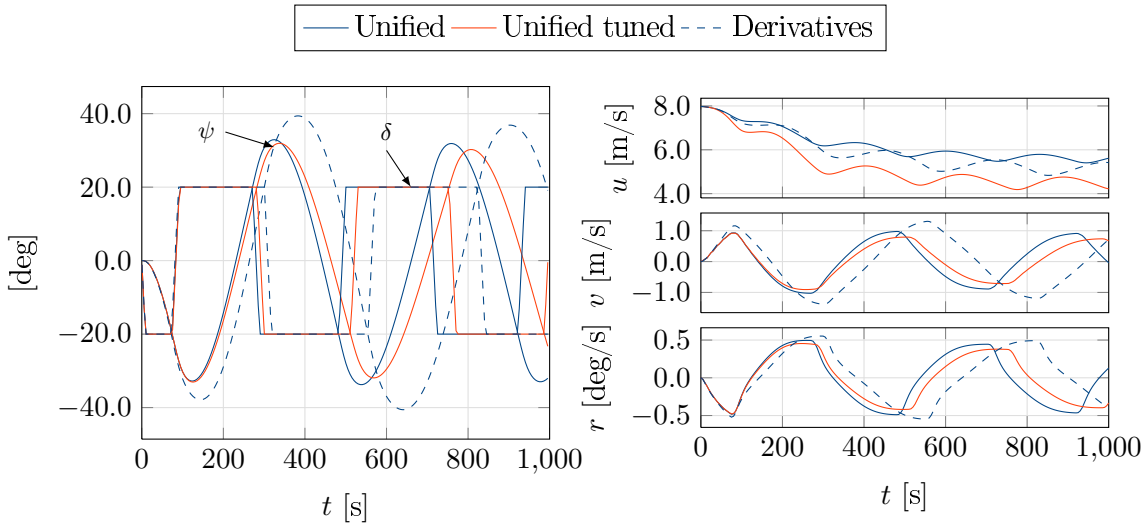

Figure 5.14.: $-20°/-20°$ zig-zag maneuver of KVLCC2; comparison of unified theory with maneuvering theory

Turning circles in regular waves

Turning circle maneuvers are simulated with the KVLCC2 in regular waves with an amplitude of $\zeta_A = 2.15$m and a wave angle of $\eta = 180°$ and $\eta = 270°$. Figure 5.15 shows exemplarily the port turning circle maneuvers in waves with an angle of $\eta = 270°$ and three different wave lengths ($\lambda/L_{PP} = 0.4$, $\lambda/L_{PP} = 0.6$ and $\lambda/L_{PP} = 1.0$). Starboard turning circles and turning circles with a wave angle of $\eta = 180°$ are shown in the appendix in Figure C.7. No experimental data is available for the track of the ship. However, Ueno et al. [114] show the drifting distance and direction for their VLCC in regular waves. Figure 5.16 compares the simulated values with the experimental data.

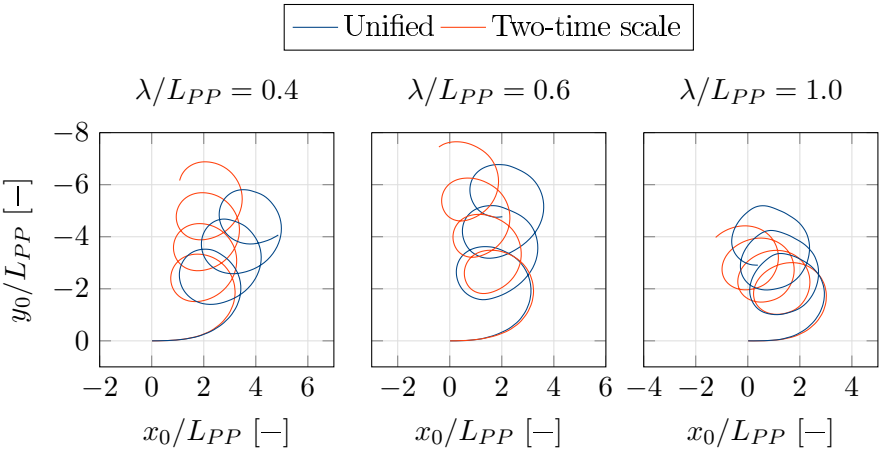

Figure 5.15.: $-35°$ turning circles of KVLCC2 in regular waves; comparison of two-time scale model and unified model; $\zeta_A = 2.15$m, $\eta = 270°$

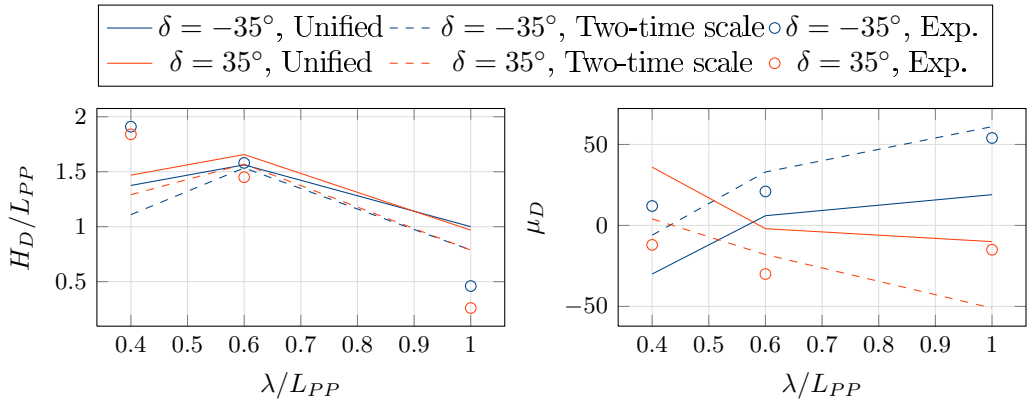

Figure 5.16.: Drifting distance and direction of KVLCC2 in regular waves; $\zeta_A = 2.15$m; measurements from Ueno et al. [114]

Comparison of unified and two-time scale theories The following section focuses on the differences between the unified theory and the two-time scale theory. A comparison with the experiments is then given.

The drifting distance calculated with unified theory is in good agreement with the results of the two-time scale model (see Figure 5.16). However, a deviation can be observed in the drifting direction. The equations of motion are solved in global coordinates. Due to the coordinate transformation from local to global coordinates, nonlinear terms arise, e.g. Coriolis and centripetal forces. These forces can have an average mean value in the horizontal plane induced by oscillatory motion in the vertical plane. However, these terms can be included in the drift forces. So, care has to be taken that they are not considered twice. These terms are not included in the drift forces used in the present work as determined with PDSTRIP. This implies that a small error is accepted in the two-time scale model. Furthermore, the nonlinear maneuvering derivatives can induce an average force in the lateral plane resulting from the wave-frequency motion of the ship. It is, however, rather small but it is also included in the wave drift forces and subsequently a small error is induced in the unified theory. Interestingly, the direction is more affected by this than the distance. These effects are not so pronounced in the simulations with the S-175.

Figure 5.17 shows the individual motion components of the KVLCC2 turning in regular waves with $\zeta_A = 2.15m$, $\lambda/L_{PP} = 0.6$ and $\eta = 270°$. The figure compares the result of the unified theory with the result of the two-time scale model. The WF motion in the two-time scale simulation is simulated with the RAO determined with PDSTRIP, according to Eqn. (5.5) and (5.6). The figure shows that the two-time scale model simulates a slightly larger rate of turn, so that after a while a time shift can be observed. However, the general motion components are in fair agreement. Some deviation can be observed in the heave motion. The maximum heave motion amplitudes are clearly larger when simulated with the unified theory.

This phenomenon can also be seen in the general RAO, see Figure B.7, where the peak of the heave motion is larger when determined with the impulse-response function. The roll motion has its maxima for stern quartering waves. It shows some extreme peaks in the two-time scale result after approximately 100s. These extreme peaks are not predicted by the unified theory. The second time when the waves come from stern quartering direction (after approximately 900s), the maximum roll amplitude is clearly less and even larger when simulated with the unified theory. The forward speed effect on the roll motion is subsequently less pronounced in the unified theory.

In contrast to the motion of the S-175, the phases with maximum amplitudes are much less. The S-175 shows large motion amplitudes over the entire maneuver, while the KVLCC2 has only some time instants with pronounced motion. However, the wave amplitude to ship length ratio is 50% larger in the simulations with the S-175.

Comparison of simulations and measurements In the following, the similarities and differences of the simulations and the measurements shall be pointed out.

Figure 5.16 reveals that in the experiments the drifting distance becomes large for short waves. Generally, this effect is captured by the simulations. However, the simulations show a larger drifting distance for $\lambda/L_{PP} = 0.6$ than for $\lambda/L_{PP} = 0.4$. Within the experiments, the drifting distance is linearly increasing with decreasing wave length. The simulated drifting distance has a maximum at $\lambda/L_{PP} = 0.6$. The calculated transverse drift force and yaw moment have a maximum at around $\lambda/L_{PP} = 0.6$ for beam waves, as can be seen in Figure B.8. The measured force and moment does not show this maximum distinctively.

For the $+35°$ turn in waves of $\lambda/L_{PP} = 1.0$, the drifting direction is in the same order of magnitude as in the $-35°$ turn but with the opposite sign within the simulations. This is not the case in the experiments, where the magnitude of the drifting distance is small in the $+35°$ turn. Ueno et al. [114] state that the large value of drifting direction μ_D in the experiments for the $-35°$ turn in waves of 1.0 wave length ratio is of small importance because of its small drifting distance H_D. The same holds for the small drifting direction in the $+35°$ turn.

The drifting direction μ_D has a negative value in $+35°$ turning condition and a positive value in $-35°$ turning condition. The simulation results show a similar behavior. According to Ueno et al. [114], this is an inverted tendency in comparison to almost all experimental and calculated cases reported by Hirano et al. [45].

The general trends of the wave effects on the maneuvering motion are also confirmed by the simulations with the S-175. For the S-175, the simulations and experimental data show the largest drifting direction for wave lengths with $\lambda/L_{PP} = 1.0$, both for starboard and port turns, as stated previously. This is similar to the simulations with the KVLCC2 but different than in the experiments. The S-175 shows the same drifting directions as in the simulations

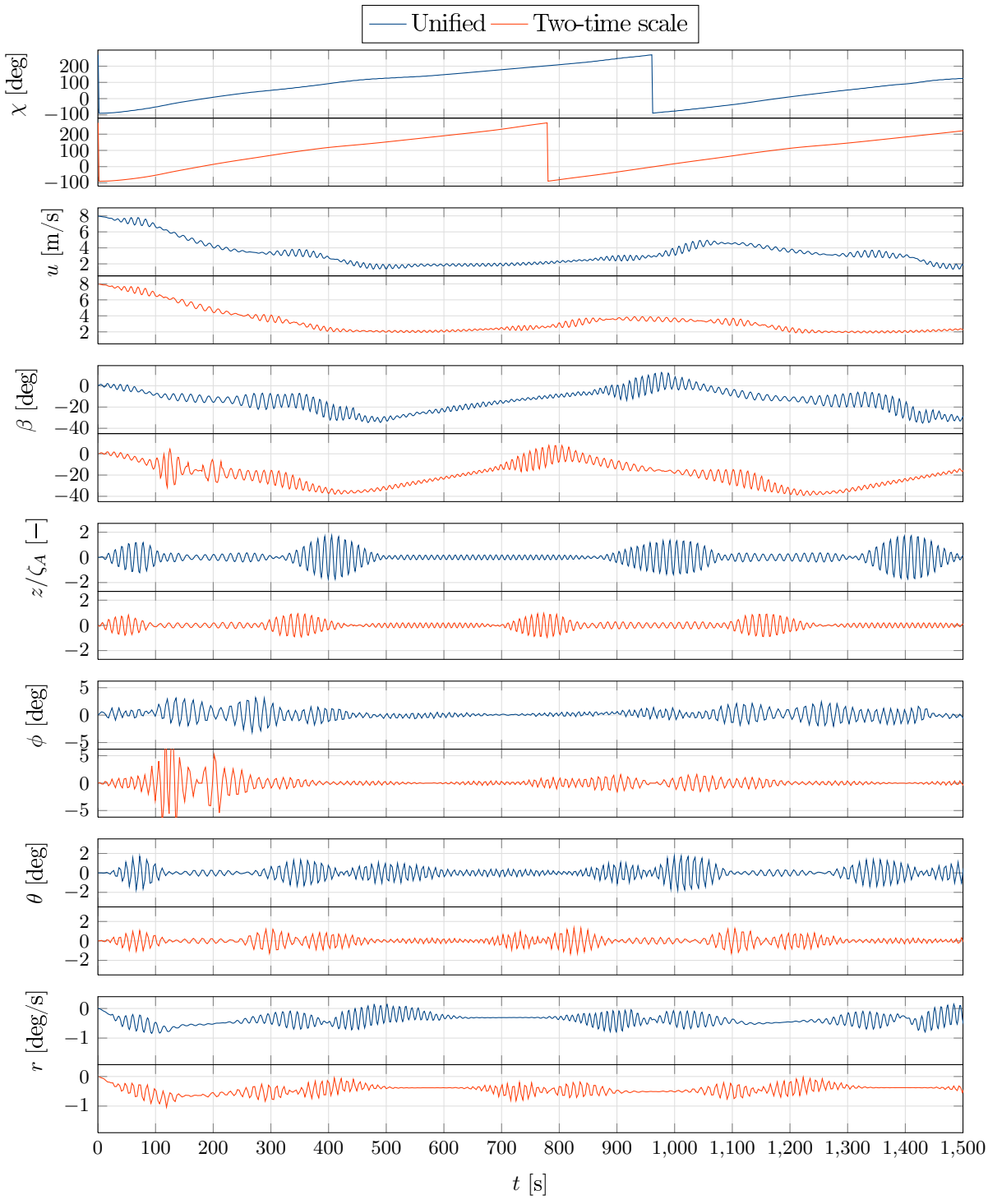

Figure 5.17.: Motion components during −35° turning circle of KVLCC2 in regular waves using unified and two-time scale theory; WF motion of two-time scale theory with RAO; $\zeta_A = 2.15$m, $\lambda/L_{PP} = 0.6$, $\eta = 270°$

with the KVLCCs, i.e. the starboard turn has mostly a positive drifting direction for the shortest wave length case and negative drifting directions for the longer wave lengths. The other way around is true for the port turns.

The results of the two-time scale model show a slightly better agreement with the experimental values.

Zig-zag maneuvers in regular waves

Zig-zag maneuvers in stern, head and quartering waves ($\eta = 0°$, $\eta = 180°$ and $270°$, respectively) with wave length to ship length ratios of $\lambda/L_{PP} = 0.4$, $\lambda/L_{PP} = 0.6$ and $\lambda/L_{PP} = 1.0$ are simulated. The simulated zig-zag maneuvers are shown in the appendix, see Figure C.8 to Figure C.13.

Experimental data for the KVLCC2 in waves are used from Ueno et al. [114]. Ueno et al. conduct $-10°/-10°$ and $20°/20°$ zig-zag maneuvers in regular waves of different wave length to ship length ratios with their VLCC. The simulated and measured overshoot angles are contrasted in Figure 5.18 and Figure 5.19 for the $-10°/-10°$ and the $20°/20°$ zig-zag maneuver, respectively. For the $-10°/-10°$ zig-zag test, the measurement is carried out two times for each wave length and wave encounter angle.

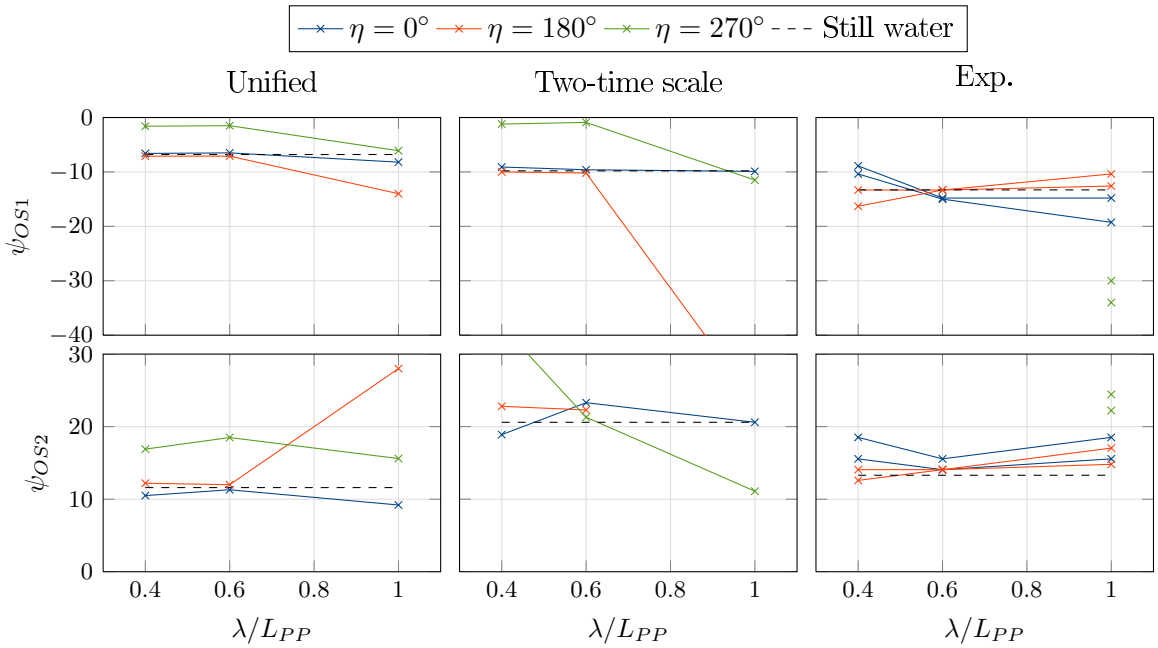

Figure 5.18.: Overshoot angle of $-10°/-10°$ zig-zag of KVLCC2 in regular waves; $\zeta_A = 2.15$m; measurements from Ueno et al. [114]

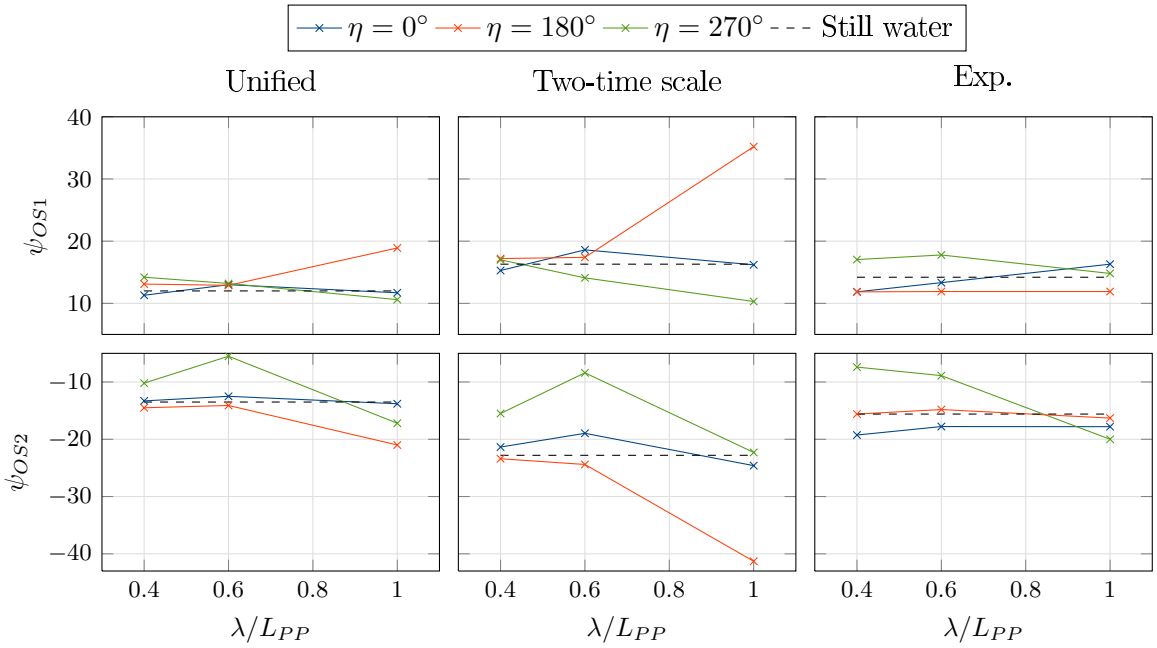

Figure 5.19.: Overshoot angle of 20°/20° zig-zag of KVLCC2 in regular waves; $\zeta_A = 2.15$m; measurements from Ueno et al. [114]

Comparison of unified and two-time scale theories The first overshoot angle determined with unified theory and the two-time scale model is in a comparable range for all wave conditions, both in the $-10°/-10°$ and in the $20°/20°$ zig-zag maneuver. In the $-10°/-10°$ zig-zag test, it is almost zero for short beam waves. In both zig-zag tests, the first overshoot angles nearly equal the calm water values for stern waves. For bow waves with $\lambda/L_{PP} = 1.0$, the first overshoot angle becomes very large, especially when predicted with the two-time scale model.

The second overshoot angles show similar trends in the $20°/20°$ zig-zag maneuver. They have the smallest values for beam waves with $\lambda/L_{PP} = 0.6$ and the largest value for head waves with $\lambda/L_{PP} = 1.0$. For the other wave conditions, the second overshoot angle is similar to the still water value. In the $-10°/-10°$ zig-zag maneuver, the agreement is not particularly distinctive. For stern and head waves with $\lambda/L_{PP} = 0.4$ and $\lambda/L_{PP} = 0.6$, the second overshoot angles are similar to the still water values. Beam waves with $\lambda/L_{PP} = 0.4$ and $\lambda/L_{PP} = 0.6$ show a significant influence on the zig-zag maneuvers, as can be seen from Figure C.9. The maneuver cannot be continued after the second overshoot.

Comparison of simulations and measurements The most significant feature of the experiments is that the $-10°/-10°$ zig-zag maneuver cannot be finished due to large wave drift forces and yaw moment in beam waves with a wave length to ship length ratio of $\lambda/L_{PP} = 0.4$ and $\lambda/L_{PP} = 0.6$. Also in the simulations, the entire zig-zag maneuver cannot be finished; however, the first and second overshoot angle can be determined. In longer beam waves with $\lambda/L_{PP} = 1.0$, the overshoot angles show a large deviation from those in still water within the experiments. This feature is not captured by the simulations. The simulations with the S-175 show similar results to the simulations with the KVLCC2. The maneuver cannot be finished in beam waves with a wave length of $\lambda/L_{PP} = 0.5$. The other wave lengths have only a minor influence on the overshoot angles.

The experimental results show for both zig-zag maneuvers that the overshoot angles in following waves are larger than those in head waves. This can neither be found in the simulations with the KVLCC2 nor in the simulations with the S-175.

The absolute value of the first overshoot angle in following waves becomes smaller in short waves and larger in long waves within the experiments. This effect is also seen in the simulations (both KVLCC2 and S-175), however, not as pronounced as in the experiments.

The simulated zig-zag maneuvers are considerably influenced by head waves with $\lambda/L_{PP} = 1.0$. Almost no influence of the waves in this case is seen in the experiments. Also, the simulations with the S-175 show a strong effect of the waves in this case.

The wave effect on overshoot angles in the $20°/20°$ zig-zag test in beam wave condition are much smaller than those in the $-10°/-10°$ zig-zag test.

A detailed explanation for the deviation is hard to find due to the lack of experimental data. First of all, it needs not be noted that different hull geometries are compared. The VLCC investigated by Ueno et al. [114] is not the KVLCC2, even if it is considered to be similar. Furthermore, the temporal course of the characteristic parameter within the experiments is not given. So the exact reason for the discrepancies is difficult to identify. More information is needed to explain the deviation of the overshoot angles.

No significant conclusion concerning the validation can be drawn due to the large deviation from the experimental values. Regarding the applied simplifications and the lack of information from the experiments, the simulations cannot be dismissed either. Further investigations are necessary for this case and are adressed in the outlook of the present work.

5.4 Concluding remarks

Two different methods are introduced to simulate the maneuvering motion in waves. One method is based on a two-time scale assumption, where the low-frequency motion and the oscillatory wave-frequency motion are separated and regarded individually. The other method unifies both motion components in one set of equations by applying the impulse-response function. The two-time scale method falls back to the maneuvering equations when no waves are present and to the seakeeping equations when there is no steering. This yields the exact solution for these cases. The unified theory does not give the exact still water maneuvering motion because the equations additionally include the impulse-response function. Furthermore, the maneuvering terms influence the wave effects. This is especially distinct for the second-order wave drift forces.

The lateral drift forces and the yaw drift moment are larger for shorter wave lengths. This results in larger drifting distances in the shorter wave length regions for turning circles. The turning trajectories are shifted in both the longitudinal and transverse direction with respect to the wave propagation direction. The overall agreement of the simulation results with the experiments is acceptable for turning circle maneuvers. The simulated results of the advances and tactical diameters are in good agreement with the experiments, both in head sea and in beam sea. In the head sea case, the advances and tactical diameters are smaller in waves than in calm water. In the beam sea case, the influence of the waves on the turning circle is different for the two turning directions. For the starboard turning, the advances are larger in waves than in calm water while the tactical diameters are smaller. The other way around is true for port turning.

Despite a time delay due to slightly different average yaw rates, both methods provide very encouraging results of the oscillatory wave-induced motion. The regions with increased amplitudes can be assigned to the wave encounter angle. A satisfactory agreement of the simulations and the experiments is present in these regions.

The unified and the two-time scale theories are in general agreement. A difference can be seen in the still water values; however, the deviation from these values due to waves is comparable. The track of the S-175 is almost identical, whether if simulated with the unified theory or with the two-time scale theory. For the KVLCC2, a deviation of the drifting direction is observed. Within the unified theory, additional drift forces are generated by the nonlinear maneuvering derivatives. These do not exist in the two-time scale model, where only the drift forces from the seakeeping theory are regarded. The simulations with the S-175 reveal a rather small influence of these terms. However, the motion of the KVLCC2 is clearly influenced by them.

Not all turning circle maneuvers of the S-175 can be completed with the two-time scale model. The wave drift forces and moment exceed the steering forces and moment. In the unified

theory, the linear wave excitation forces and/or the oscillatory motion make the completion of the maneuver possible. In two-time scale models, the results of the WF component generally do not influence the LF maneuvering motion.

The oscillatory wave-induced motion is very comparable between the two theories. The motion amplitudes decay faster when simulated with the RAO in the two-time scale theory. For the roll motion of the KVLCC2, a stronger influence of the forward speed on the amplitudes is observed. The oscillatory wave-induced motion is practically identical between the two theories when simulating the WF component in the two-time scale model with the impulse-response function. This can be regarded as a hybrid theory. However, additional damping and restoring terms need to be introduced. This can lead to instability effects. The unified theory is generally more stable.

Zig-zag maneuvers are simulated with the S-175 and the KVLCC2. The simulation results of the KVLCC2 are compared with measurements on a similar VLCC. A clear deviation of the simulations and the measurements is found. The reasons for the deviation cannot be clarified completely. The simulated KVLCC2 and the measured VLCC have different geometries. Furthermore, no detailed results are available from the experiments.

The two different simulation methods show for both ships the same tendencies of the wave influence on the zig-zag maneuvers. The overshoot angles are nearly the same for both theories. The unified theory predicts slightly larger overshoot times for the $20°/20°$ zig-zag maneuvers. However, for the differences between the two methods, no clear trend can be observed. The usage of the infinite-frequency added mass in the unified theory has only negligible influence.

Although there is room for improvement, both presented methods can capture the turning motion in waves as well as the wave-induced motion during turning. An advantage of the unified theory is that it incorporates all physical effects in one set of equations. Additional effects can easily be added as external forces. However, in the two-time scale model, all physical effects can clearly be assigned. This method is easy to implement and gives very satisfactory results with regard to the turning motion in waves. When the WF motion is solved with the impulse-response function, no clear differences to the result of the unified theory can be seen in the WF motion. It has to be kept in mind that all nonlinear wave effects have to be included in the wave drift forces then.

6
Conclusion and Perspective

Two simulation methods to determine the maneuvering motion of ships in waves have been presented. The derivation of the methods began with the maneuvering theory and the seakeeping theory. The general maneuvering theory describes the maneuvering motion of ships in still water, while the seakeeping theory deals with straight forward motion of ships in waves.

The motion equations have been derived by using the kinematic and kinetic equations. Arbitrary rigid-body motions due to the acting forces can be determined with these equations. Unit quaternions have been utilized to describe the rotatory position of the ship. They have the advantage that the so-called gimbal lock is avoided and no singularities due to the combination of different rotations occur. Newton's second law is the foundation of the rigid-body kinetics. When the mass properties of the ship are known, the main task for determining the ship motions is to determine and model the acting forces. Due to the strong dependence of the hydrodynamic forces on the acceleration of the body, the numerical solution of the equations of motion tends to become unstable. This has been avoided by subtracting the added mass terms from both sides of the motion equations.

The general difference of the maneuvering and the seakeeping theories is the nature of the acting forces.

The classical maneuvering motion is influenced by the propulsion forces, the rudder forces and the forces acting on the hull during arbitrary and slowly varying ship motions. The propulsion forces have been obtained from the open water diagram of the propeller. Therefore, it was necessary to know the propeller rate of rotation. An engine model to determine the behavior of diesel-electric propulsion trains has been developed and it shows satisfactory agreement to sea trial measurements. Wind-milling can be predicted reliably and the general trends of the engine control can be captured. The rudder forces have been calculated with semi-empirical formulae utilizing the propeller slipstream and the lift, drag and moment coefficients. A

comparison with measured forces shows good agreement. To determine the hull forces, the slender-body theory has been applied. This theory yields the hull forces with acceptable accuracy while being very computationally efficient. Simulated standard maneuvers with the S-175 and the KVLCC2 are in fair agreement with model test results. However, the forces determined with the slender-body theory depend to a large extent on the nonlinear cross-flow drag forces. Experience is needed to properly determine these forces. Alternatively, the maneuvering motion was described with so-called whole ship models, where the entire forces acting on the ship have been modelled with one set of equations that are generally based on hydrodynamic derivatives. These polynomials calculate the acting forces as function of the instantaneous motion parameters. An enormous computational effort is necessary to determine the derivatives. However, nearly arbitrary maneuvers can be simulated once they are known.

The motion of ships in waves can be described in frequency domain or in time domain. Time-domain equations have been applied in the present work since the temporal behavior is of interest. To determine the motion in time domain, the impulse-response function has been derived. This function describes the hydrodynamic reaction forces due to arbitrary motions, while also incorporating the history of the motion through the convolution integral over the retardation functions. A major advantage of the impulse-response function is that additional nonlinear loads can be applied. The impulse-response function has been applied to determine the RAO of the S-175 and the KVLCC2. They are in satisfactory agreement with the frequency-domain results and with model test measurements.

The track of the ship can strongly be influenced by second-order wave effects. Due to the time average of these effects, wave drift forces occur that can be regarded as a quasi-constant force acting on the ship. Mean second-order wave drift forces are very difficult to determine, both experimentally as well as numerically. They depend on the action of the waves on the ship, the influence of the ship on the waves and also on the interaction of these components. In the present work, PDSTRIP has been utilized to calculate the mean second-order wave drift forces. The forces acting on the S-175 under forward speed and the forces acting on the KVLCC2 without forward speed are in good agreement with model test results.

In order to combine the maneuvering and seakeeping theory as described above, two different approaches have been derived. The first approach considers the maneuvering and the seakeeping motions separately. The combined motion has been regarded as a two-time scale problem, where the linear, oscillatory wave-induced motion occurs on a more rapidly varying time scale than the maneuvering. The wave-frequency problem is affected by the slowly varying maneuvering motion in terms of the changing wave encounter angle and average ship speed. The maneuvering motion is influenced by the mean second-order wave drift forces. The other approach has unified both theories in one set of equations. In this approach, the impulse-response function has been extended to include the maneuvering forces and the non-

linear wave drift forces. This approach does not fall back to the maneuvering equations when no waves are present. This yields a different maneuvering behavior and necessitates an adaption of the maneuvering terms to obtain a satisfactory maneuvering prediction. In contrast to this, the two-time scale model gives the exact maneuvering results if no waves are present.

A validation with experimental data from literature has been conducted. Turning circles and zig-zag maneuvers in regular waves have been simulated with the S-175 and the KVLCC2. Both simulation methods show almost equal results for the S-175. The track of the ship is in satisfactory agreement with the model test results given in Yasukawa [122]. Also, the individual motion components are similar to the measured values.

The turning circles do not only drift in the wave propagating direction, but under an angle relative to this. The turning circles of the KVLCC2 show different drifting directions when simulated with the two-time scale method or the unified theory. The differences in the drifting direction demonstrate that additional nonlinear terms due to waves occur in the unified theory. These terms have not been included in the wave drift forces used in the two-time scale model. The nonlinear centripetal terms, for instance, may generate a transverse drift force due to combined heave and roll motion. Furthermore, nonlinear terms have been generated because of the nonlinear maneuvering derivatives that also result in drift forces due to the oscillatory wave-frequency motion. Subsequently, it is necessary to know which terms are included in the wave drift force terms so that no terms are considered twice.

The results of the simulations with the KVLCC2 have been compared with measurements of Ueno et al. [114], although some assumptions and simplifications have to be made. The agreement is fair for turning circles. The simulated zig-zag maneuvers, however, clearly deviate from the measurements. The reasons for the deviation cannot be clarified completely. The measurements have been conducted on a VLCC similar to the KVLCC2, so that differences in the geometry are present. Furthermore, no detailed results are available from the experiment.

Investigations on the S-175 have shown that only regarding the low-frequency components for the turning motion might not be sufficient in all cases. In the wave length regions, where the wave drift forces have their maximum, the turning motion gets trapped in the two-time scale model and the wave drift yaw moment exceeds the steering moment in this case. This does not happen with the unified theory since the linear, oscillatory wave loads also have instants of time where they act in the direction of the steering moments. This leads to an avoidance of the trapping. So, in this case, the linear wave forces play an important role for the turning motion, which is not captured by the two-time scale model.

The oscillatory wave-induced motion is very comparable between the two theories. The wave-frequency motion of the two-time scale model shows slight deviations from the unified theory and the experiments, when simulated with known RAO. Generally, the agreement is acceptable, especially with regards to the simplicity of the model. However, a hybrid theory has

been introduced where the wave-frequency motion of the two-time scale model is simulated with the impulse-response function. The resulting wave-frequency motion nearly equals the result of the unified theory. Some instability concerns have to be solved for this case since the ship needs to be kept on course in the wave-frequency component by artificial restoring terms.

The unified theory unifies the maneuvering and the seakeeping equations. All ship motions have been described with one set of equations, which allows for regarding further effects by just adding the forces due to these effects. No care has to be taken to split these influences into low-frequency and wave-frequency components.

Both methods capture the maneuvering motion in waves as well as the wave-induced motion during turning. It has been hard to justify the general validity of the methods due to the lack of experimental data. However, the obtained results are very promising.

For the present simulations with the two-time scale model, the heel has been neglected. This has been acceptable for the low speeds in the presented simulation examples. However, for higher speeds, the heel that arises from the maneuvering motion might be considerably large and a neglection is improper. More maneuvering derivatives are needed to include this fourth degree of freedom in the maneuvering equations. This yields an exponential increase in the simulations/measurements needed for determining the derivatives. Alternatively, the slender-body theory needs to be generalized and validated for four degrees of freedom.

Little experimental data is available for validation. Model tests on a maneuvering ship in waves are challenging. To conduct free-running maneuvers in waves, large model basins equipped with wave makers are necessary. Only a few basins exist that comply with this requirement. A large amount of different tests needs to be performed to obtain reliable and meaningful results. However, for a proper validation of the numerical models, they are irreplaceable. Especially for the zig-zag maneuvers, a large scatter between the simulations and the measurements occurs in the present work. Well-documented model tests are therefore desirable to clarify the differences.

To conduct realistic simulations and to assess the security in a seaway, it is desirable to include irregular waves. For the present approach, the wave excitation forces have to be adapted.

A
Maneuvering

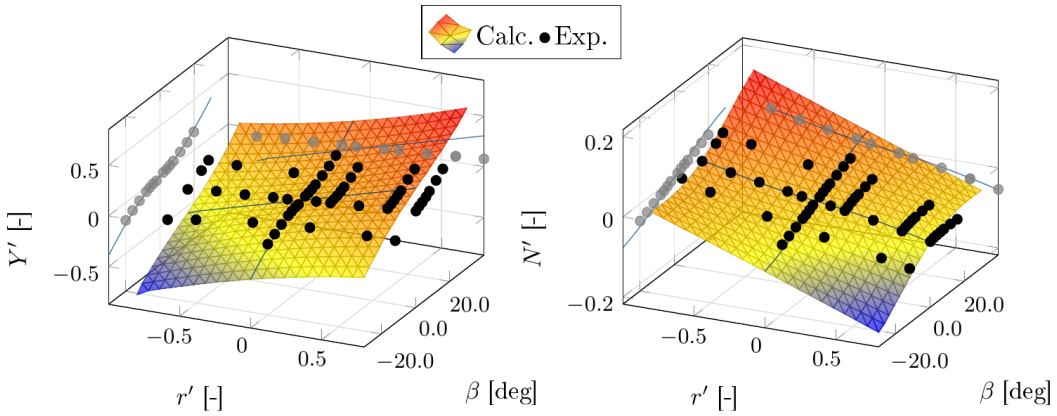

Figure A.1.: Hydrodynamic damping forces acting on KVLCC2; simulation with slender-body theory; measurements from circular motion tests at NMRI [127]

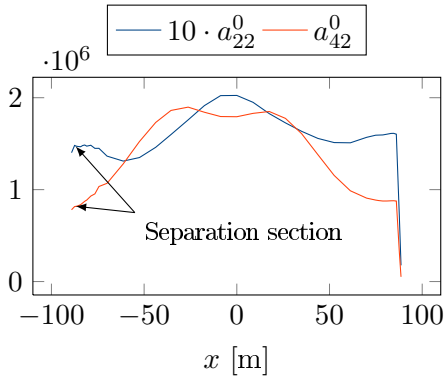

Figure A.2.: Added mass per ship length of S-175

B
Seakeeping

B.1 Strip theory coefficients

STF strip theory coefficients (Salvesen et al. [88], Fathi and Hoff [31], Skejic [96]):

$$A_{11} = \int_L a_{11}(x)dx - \frac{U}{\omega_e^2} b_{11}^A$$

$$B_{11} = \int_L b_{11}(x)dx + U a_{11}^A$$

$$A_{22} = \int_L a_{22}(x)dx - \frac{U}{\omega_e^2} b_{22}^A$$

$$B_{22} = \int_L b_{22}(x)dx + U a_{22}^A$$

$$A_{24} = A_{42} = \int_L a_{24}(x)dx - \frac{U}{\omega_e^2} b_{24}^A$$

$$B_{24} = B_{42} = \int_L b_{24}(x)dx + U a_{24}^A$$

$$A_{26} = \int_L x a_{22}(x)dx + \frac{U}{\omega_e^2} \int_L b_{22}(x)dx - \frac{U}{\omega_e^2} x_A b_{22}^A + \frac{U^2}{\omega_e^2} a_{22}^A$$

$$B_{26} = \int_L x b_{22}(x)dx - U \int_L a_{22}(x)dx + U x_A a_{22}^A + \frac{U^2}{\omega_e^2} b_{22}^A$$

$$A_{33} = \int_L a_{33}(x)dx$$

$$B_{33} = \int_L b_{33}(x)dx$$

$$A_{35} = -\int_L x a_{33}(x)dx + \frac{U}{\omega_e^2} B_{33}$$

$$B_{35} = -\int_L x b_{33}(x)dx - U A_{33}$$

$$
\begin{aligned}
A_{44} &= \int_L a_{44}(x)dx - \frac{U}{\omega_e^2} b_{44}^A \\
B_{44} &= \int_L b_{44}(x)dx + U a_{44}^A \\
A_{46} &= \int_L x a_{24}(x)dx + \frac{U}{\omega_e^2}\int_L b_{24}(x)dx - \frac{U}{\omega_e^2} x_A b_{24}^A + \frac{U^2}{\omega_e^2} a_{24}^A \\
B_{46} &= \int_L x b_{24}(x)dx - U\int_L a_{24}(x)dx + U x_A a_{24}^A + \frac{U^2}{\omega_e^2} b_{24}^A \\
A_{55} &= \int_L x^2 a_{33}(x)dx - \frac{U^2}{\omega_e^2} A_{33} \\
A_{53} &= -\int_L x a_{33}(x)dx - \frac{U}{\omega_e^2} B_{33} \\
B_{53} &= -\int_L x b_{33}(x)dx + U A_{33} \\
B_{55} &= \int_L x^2 b_{33}(x)dx - \frac{U^2}{\omega_e^2} B_{33} \\
A_{62} &= \int_L x a_{22}(x)dx - \frac{U}{\omega_e^2}\int_L b_{22}(x)dx - \frac{U}{\omega_e^2} x_A b_{22}^A \\
B_{62} &= \int_L x b_{22}(x)dx + U\int_L a_{22}(x)dx + U x_A a_{22}^A \\
A_{64} &= \int_L x a_{24}(x)dx - \frac{U}{\omega_e^2}\int_L b_{24}(x)dx - \frac{U}{\omega_e^2} x_A b_{24}^A \\
B_{64} &= \int_L x b_{24}(x)dx + U\int_L a_{24}(x)dx + U x_A a_{24}^A \\
A_{66} &= \int_L x^2 a_{22}(x)dx + \frac{U^2}{\omega_e^2}\int_L a_{22}(x)dx - \frac{U}{\omega_e^2} x_A^2 b_{22}^A + \frac{U^2}{\omega_e^2} x_A a_{22}^A \\
B_{66} &= \int_L x^2 b_{22}(x)dx + \frac{U^2}{\omega_e^2}\int_L b_{22}(x)dx + U x_A^2 a_{22}^A + \frac{U^2}{\omega_e^2} x_A b_{22}^A
\end{aligned}
$$

B.2 S-175

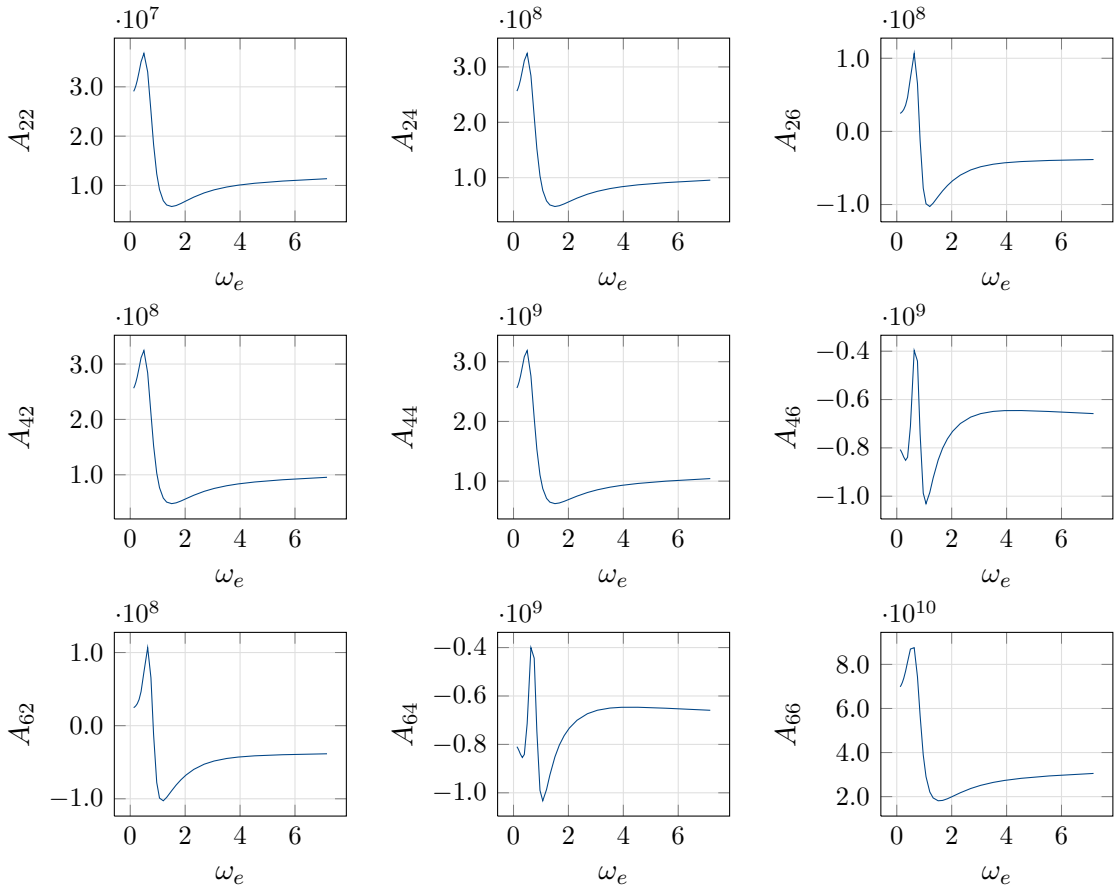

Figure B.1.: Added mass of S-175 in the lateral mode

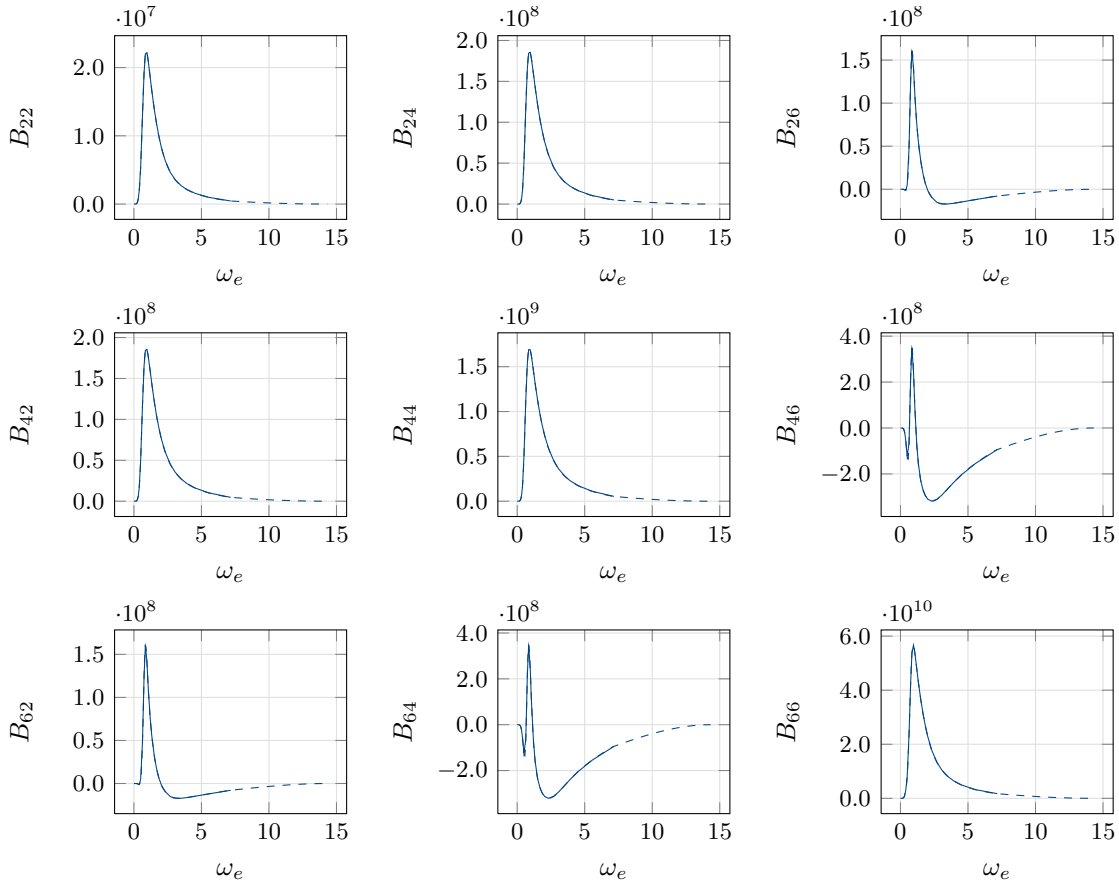

Figure B.2.: Potential damping of S-175 in the lateral mode

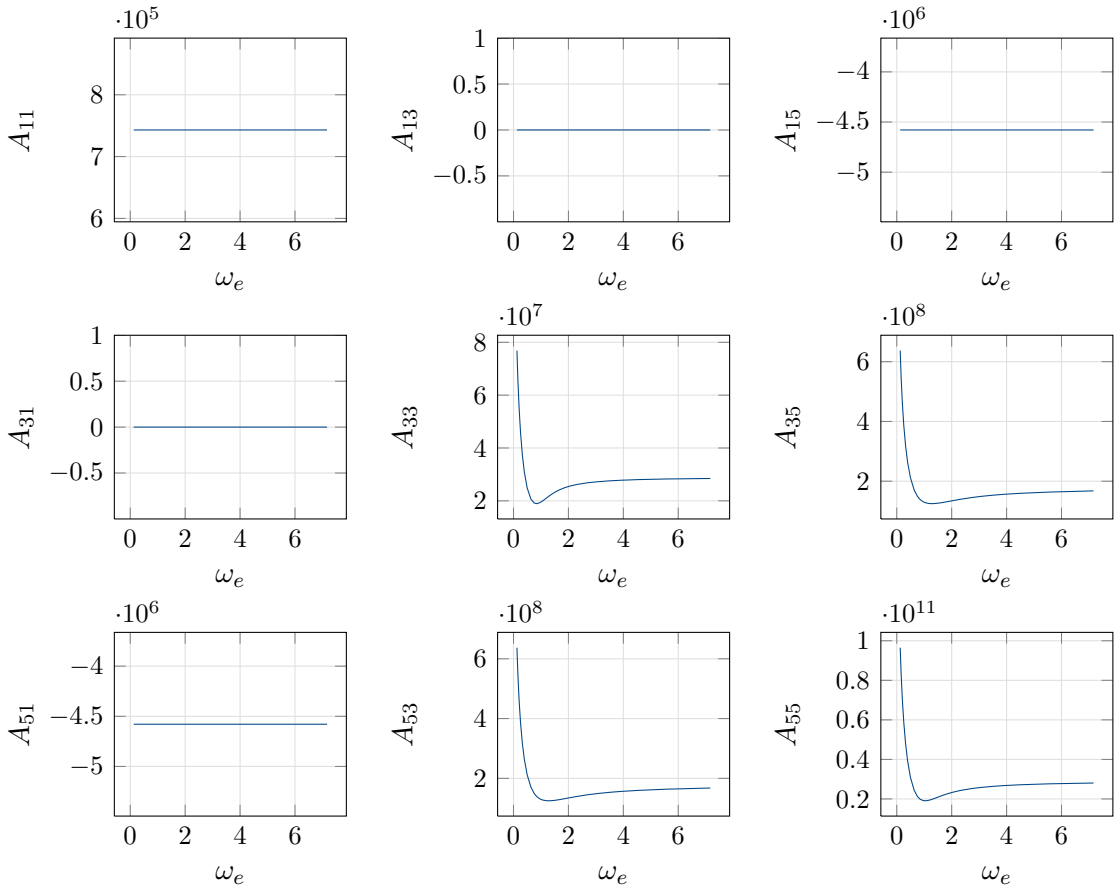

Figure B.3.: Added mass of S-175 in the longitudinal mode

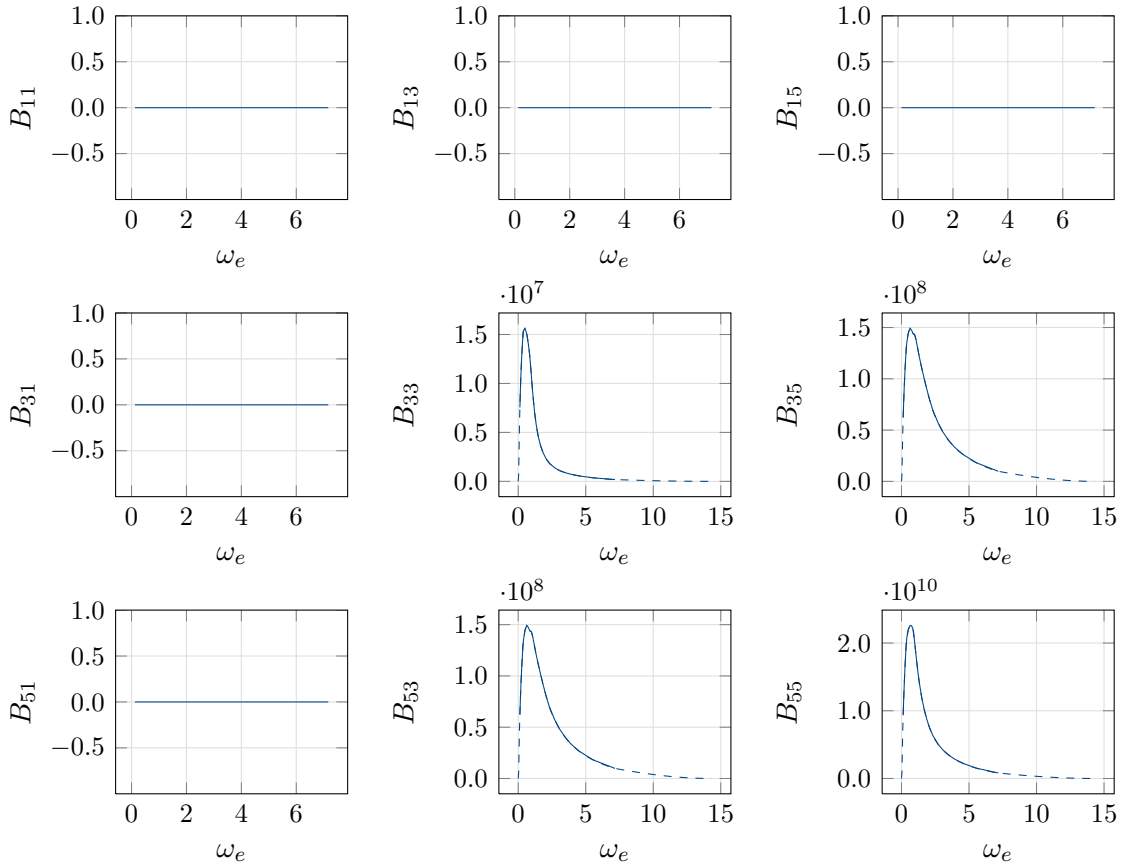

Figure B.4.: Potential damping of S-175 in the longitudinal mode

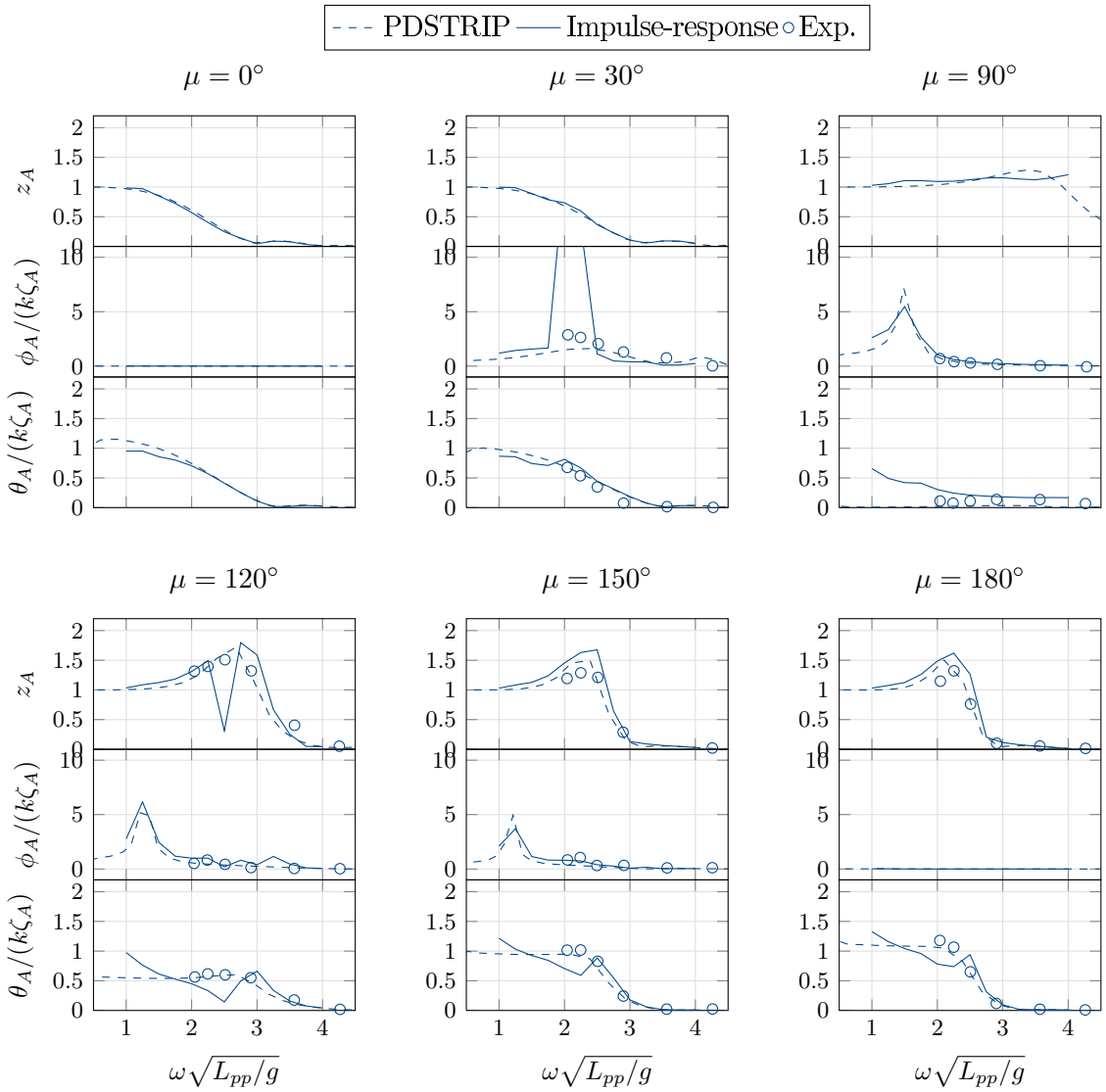

Figure B.5.: Heave, pitch and roll RAO of S-175; calculated with PDSTRIP and impulse-response function; measurements from ITTC78 [51]

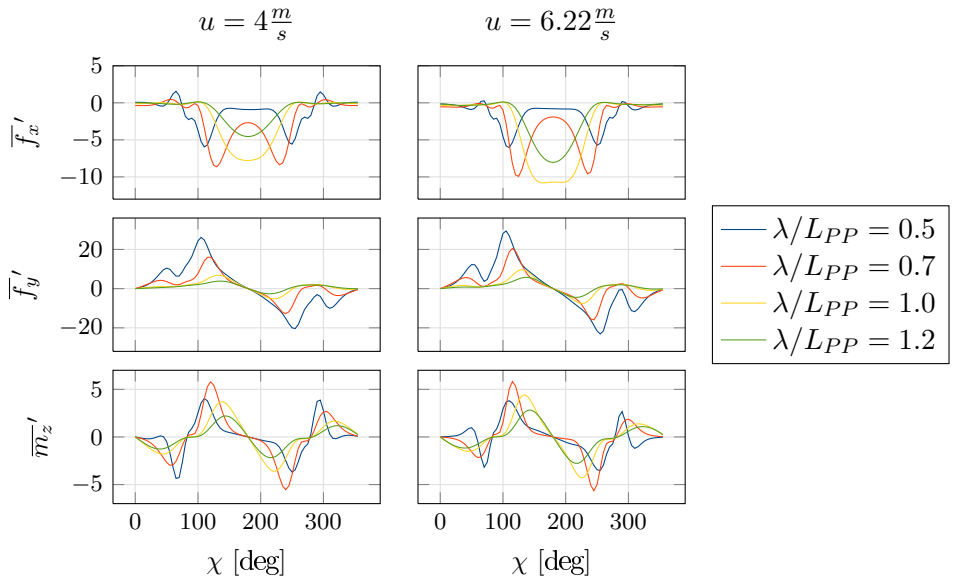

Figure B.6.: Drift forces and moment on S-175 as a function of the encounter angle for different wave lengths and forward speeds

B.3 KVLCC2

Figure B.7 shows the RAO of a very large crude oil carried (VLCC). The measurements are borrowed from Ueno et al. [114]. Unfortunately, not all details of the experiments are provided in the article, so that a few assumptions have to be made for the simulations. Since the exact geometry is not known, simulations are conducted for the KVLCC2 with the mass data provided in Ueno et al. [114]. The results calculated with PDSTRIP and the results determined with the impulse-response function are in good agreement with the measurements. The resonance peaks are determined for the same wave length and are in a comparable order of magnitude.

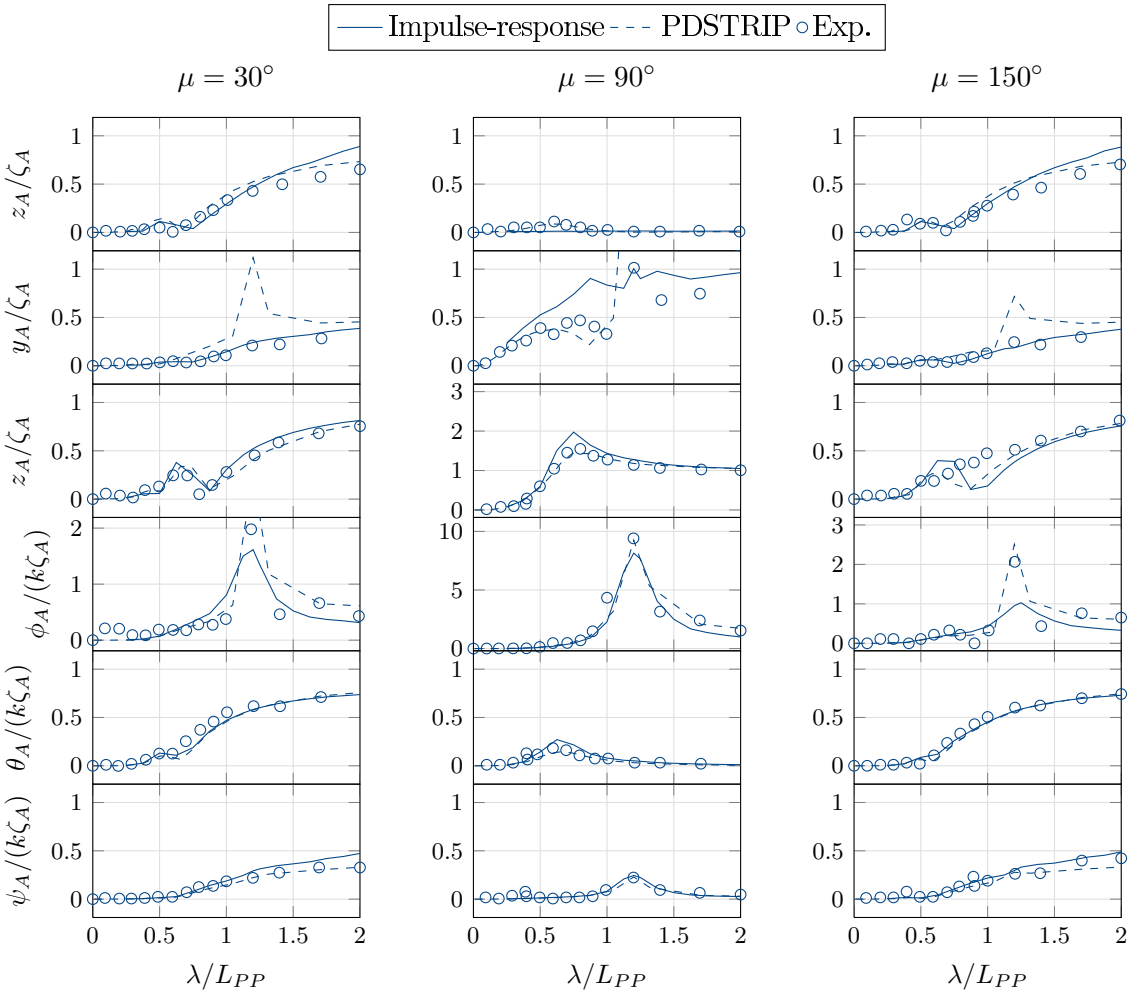

Figure B.7.: RAO of a VLCC according to Ueno et al. [115]; $Fn = 0$; calculated with PDSTRIP and impulse-response function; measurements from Ueno et al. [115]

Figure B.8 shows the wave drift forces acting on the VLCC. The results of the calculations show a satisfactory agreement with the experiments for the longitudinal and the transverse

force. The force peaks at $\lambda/L_{PP} = 1.2$ can be traced back to the resonance region of the ship motion. These peaks are not found in the measurements, possibly due to the fastening of the model. The yaw moments show a large deviation. The measured moments are almost zero over the entire range of wave lengths.

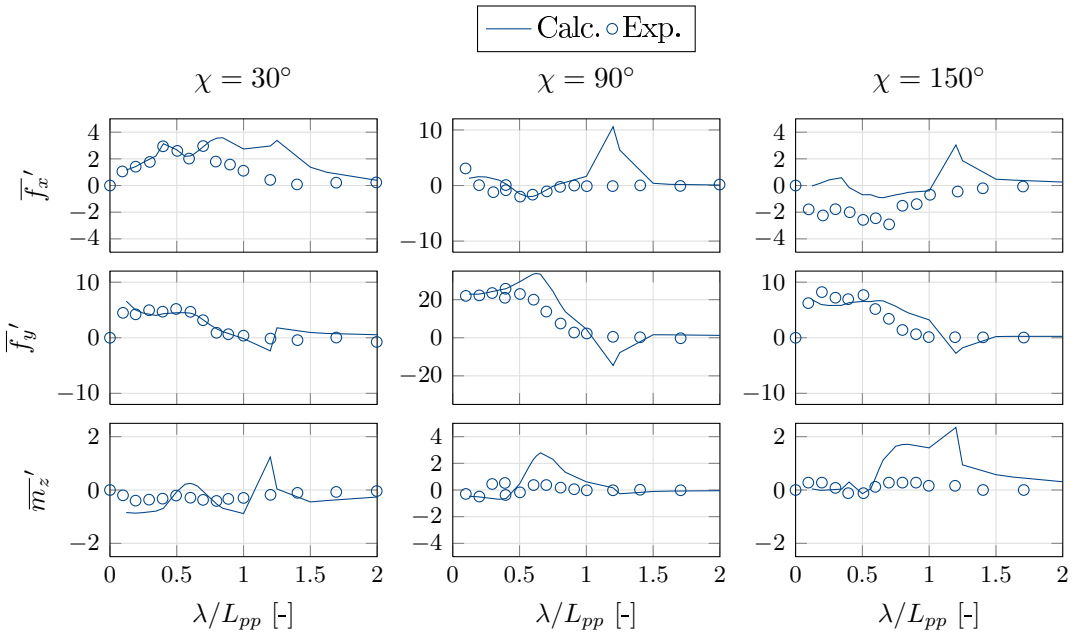

Figure B.8.: Drift forces and moment on a VLCC as function of the wave length for different encounter angles; $Fn = 0$; measurements from Ueno et al. [115]

Figure B.9 shows calculated values of the transverse force and the yaw moment acting on the KVLCC2 compared with experimental data from Lee et al. [68]. Again, not much details are known from the experiments, so that a few assumptions have to be made. In contrast to the measurements and simulations in Figure B.8, this figure shows an underestimation of the measured values.

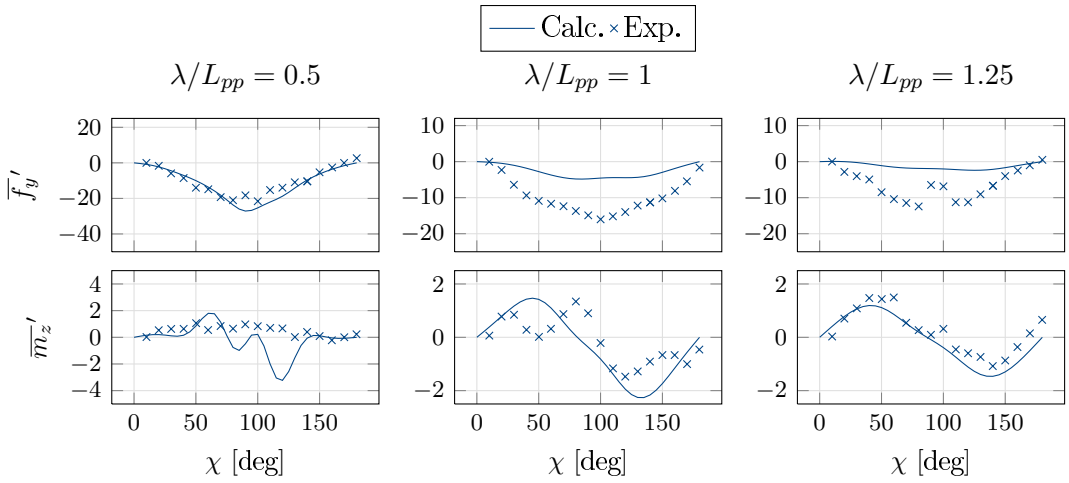

Figure B.9.: Drift forces and moment on KVLCC as a function of the encounter angle for different wave lengths; $Fn = 0$; measurements from Lee et al. [68]

C

Maneuvering in Waves

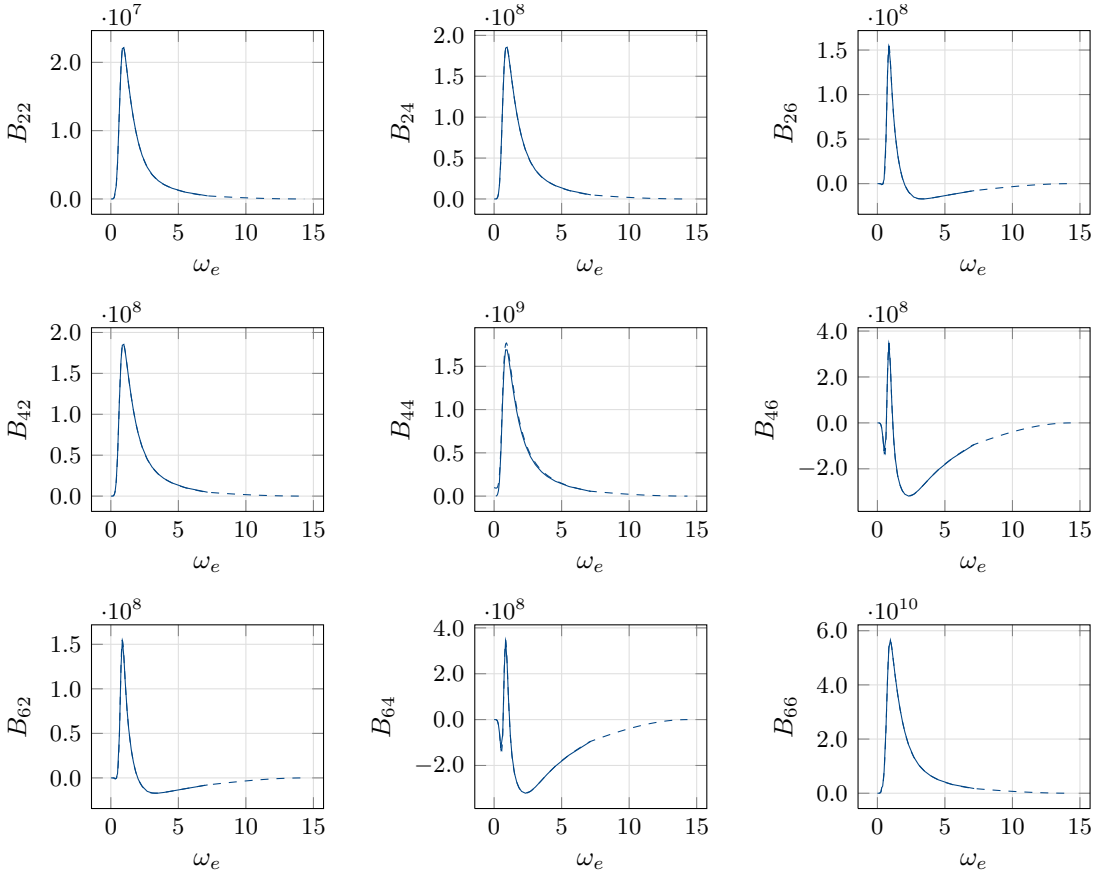

Figure C.1.: Potential damping of S-175 in the lateral mode for unified model

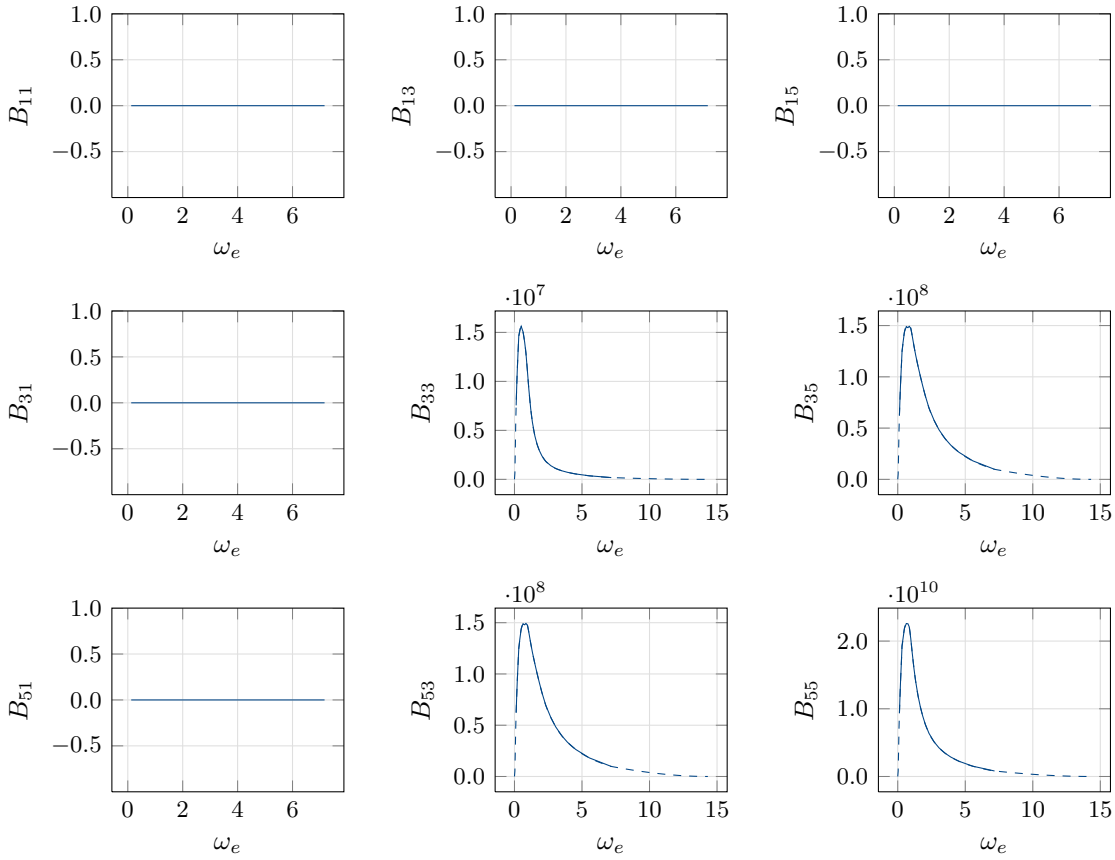

Figure C.2.: Potential damping of S-175 in the longitudinal mode for unified model

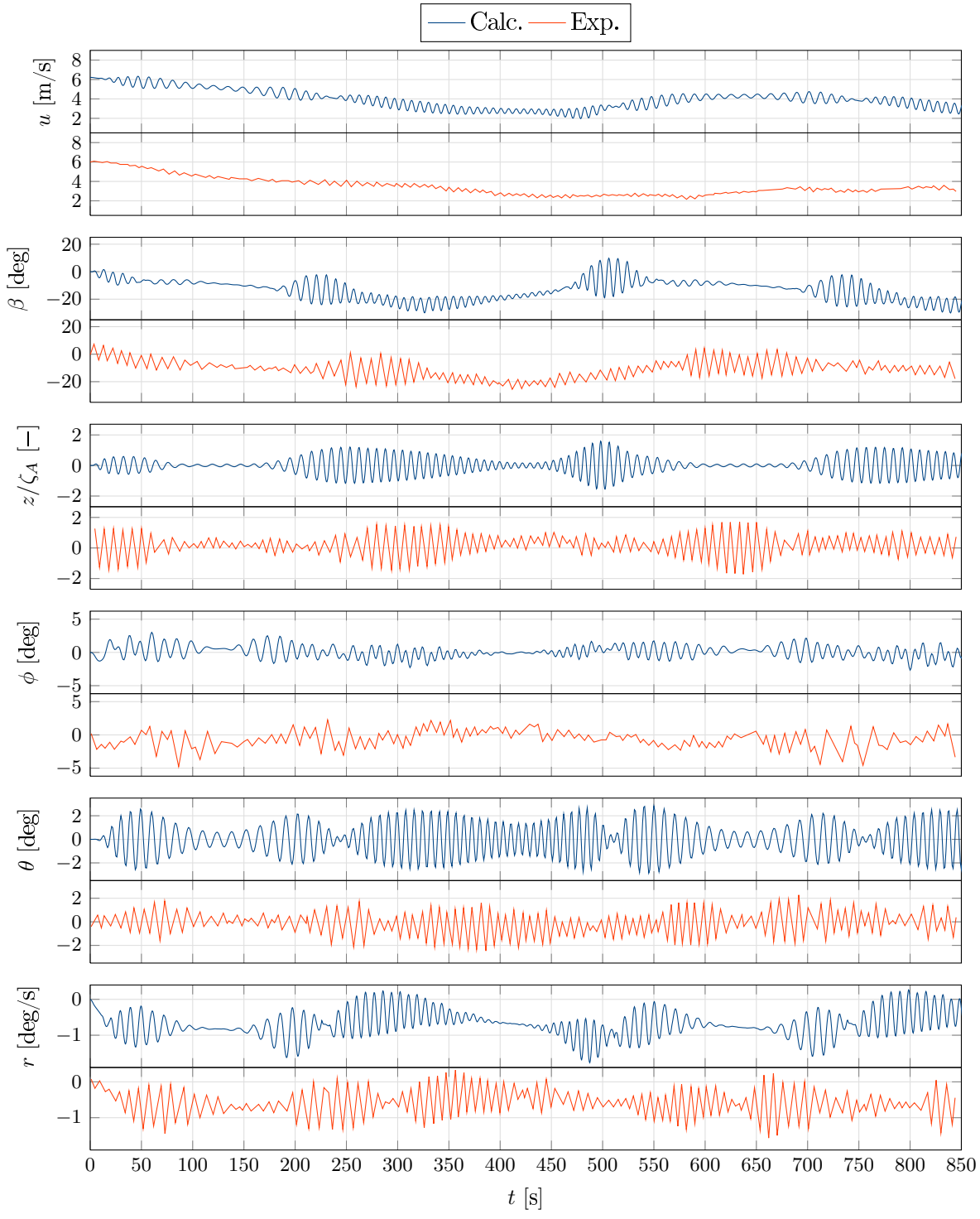

Figure C.3.: Motion components during $-35°$ turning circle of S-175 in regular waves using unified theory; $\zeta_A = 1.75m$, $\lambda/L_{PP} = 0.7$, $\eta = 270°$; measurements from Yasukawa [122]

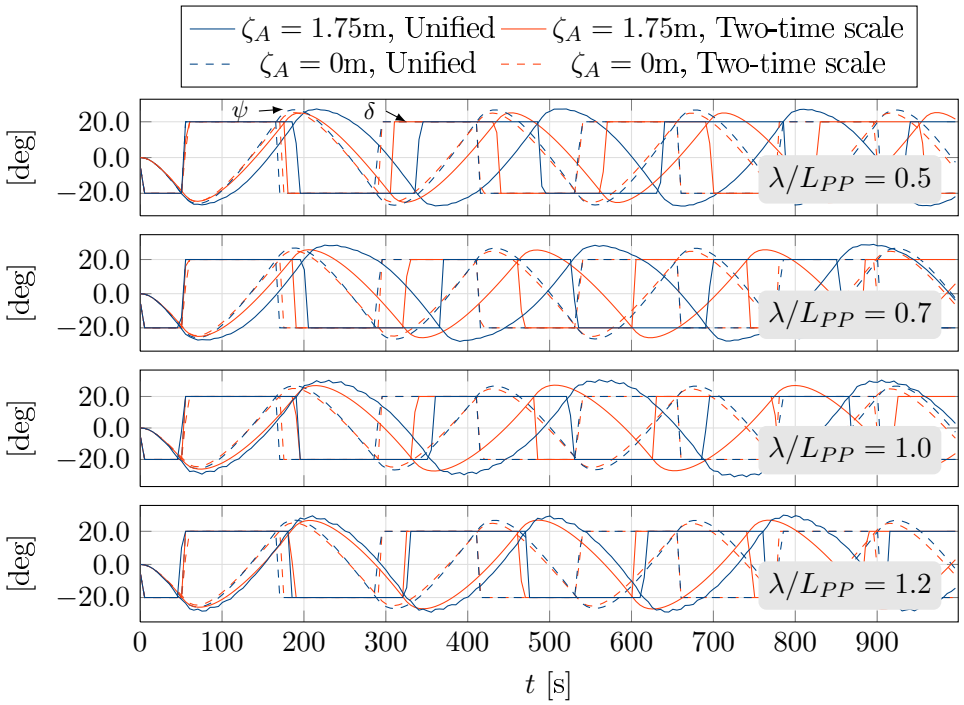

Figure C.4.: $-20°/-20°$ zig-zag maneuver of S-175 in waves; $\eta = 0°$

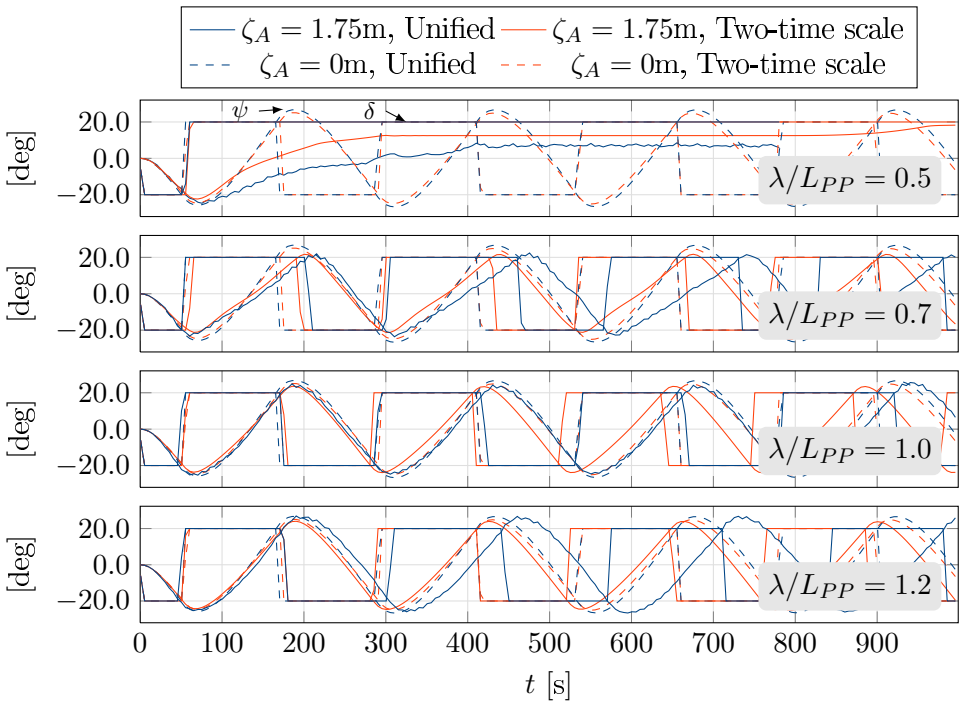

Figure C.5.: $-20°/-20°$ zig-zag maneuver of S-175 in waves; $\eta = 90°$

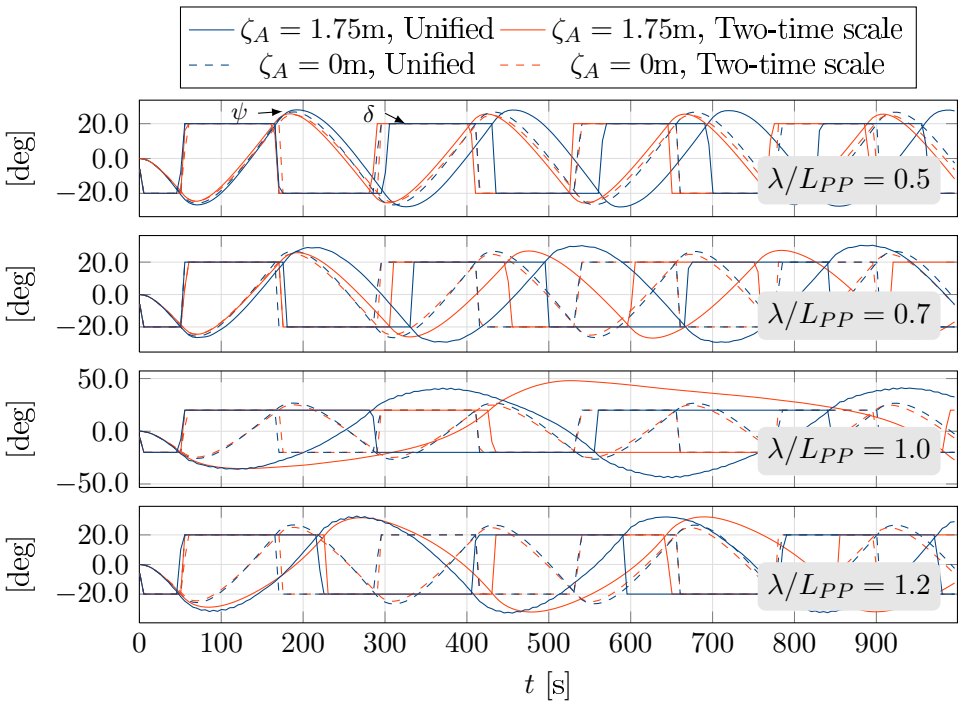

Figure C.6.: $-20°/-20°$ zig-zag maneuver of S-175 in waves; $\eta = 180°$

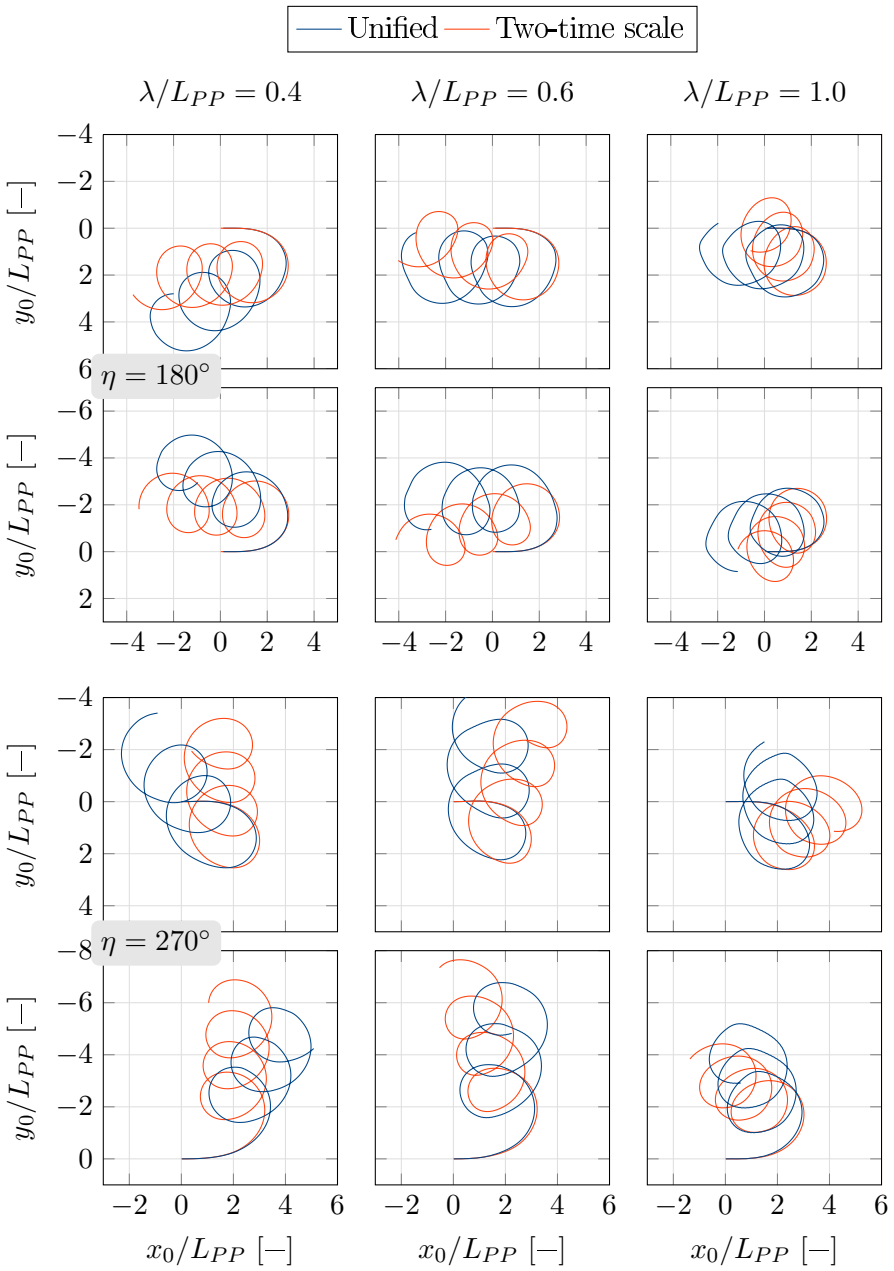

Figure C.7.: ±35° turning circles of KVLCC2 in regular waves; comparison of two-time scale model and unified model; $\zeta_A = 2.15$m

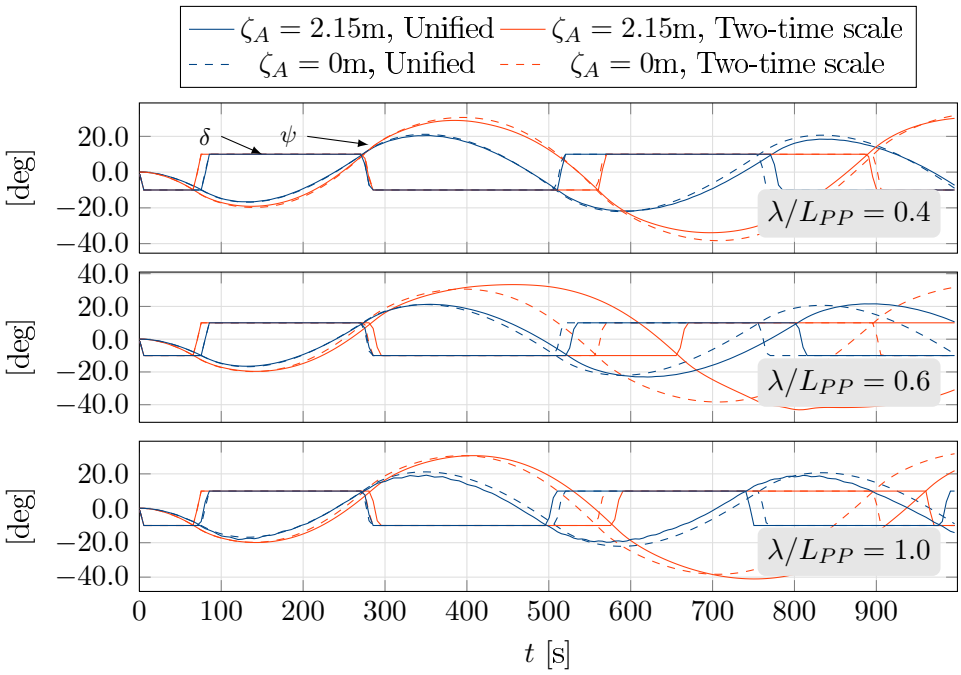

Figure C.8.: $-10°/-10°$ zig-zag maneuver of KVLCC2 in waves calculated with derivatives from Cura Hochbaum et al. [22]; $\eta = 0°$

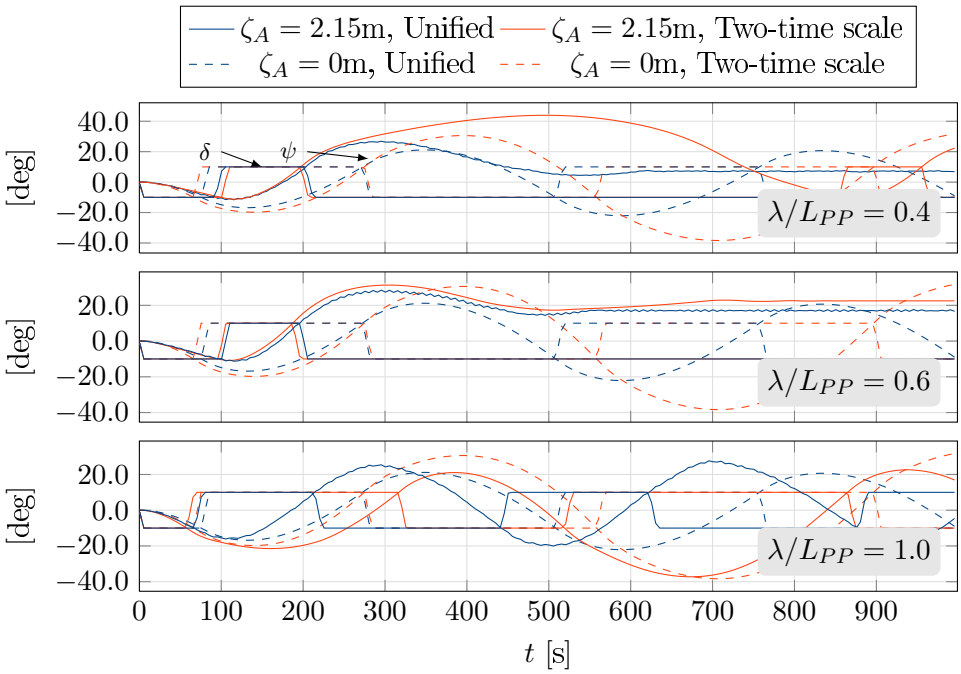

Figure C.9.: $-10°/-10°$ zig-zag maneuver of KVLCC2 in waves calculated with derivatives from Cura Hochbaum et al. [22]; $\eta = 270°$

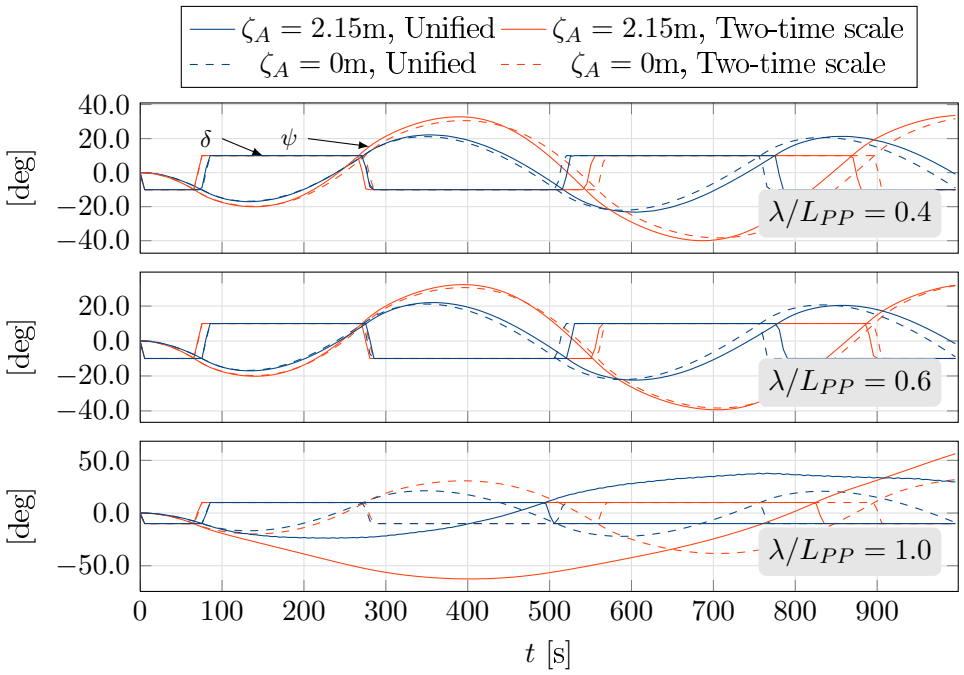

Figure C.10.: $-10°/-10°$ zig-zag maneuver of KVLCC2 in waves calculated with derivatives from Cura Hochbaum et al. [22]; $\eta = 180°$

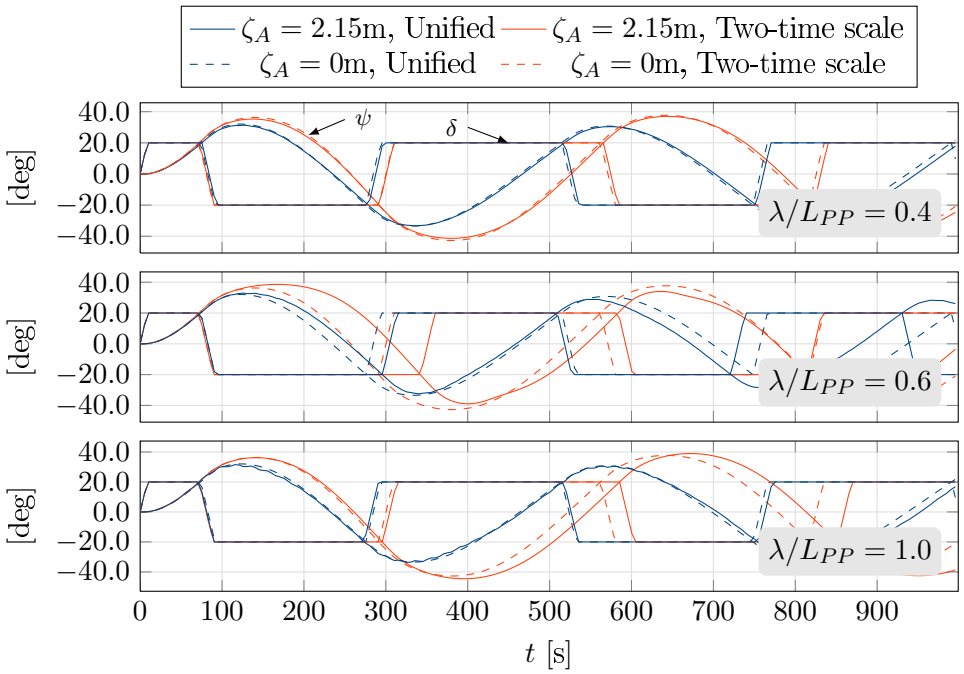

Figure C.11.: $20°/20°$ zig-zag maneuver of KVLCC2 in waves calculated with derivatives from Cura Hochbaum et al. [22]; $\eta = 0°$

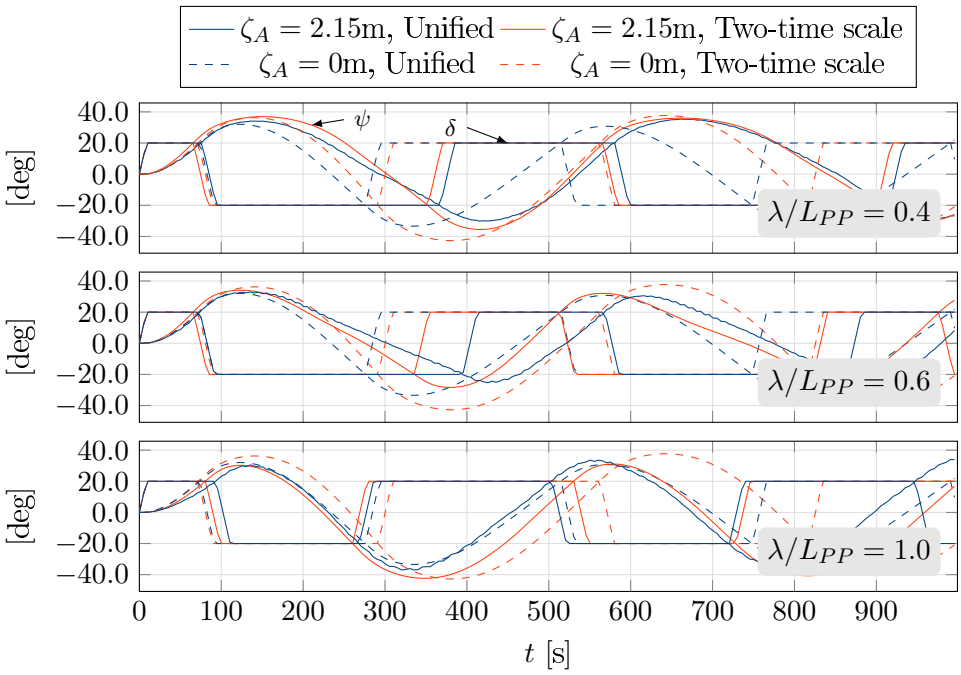

Figure C.12.: 20°/20° zig-zag maneuver of KVLCC2 in waves calculated with derivatives from Cura Hochbaum et al. [22]; $\eta = 270°$

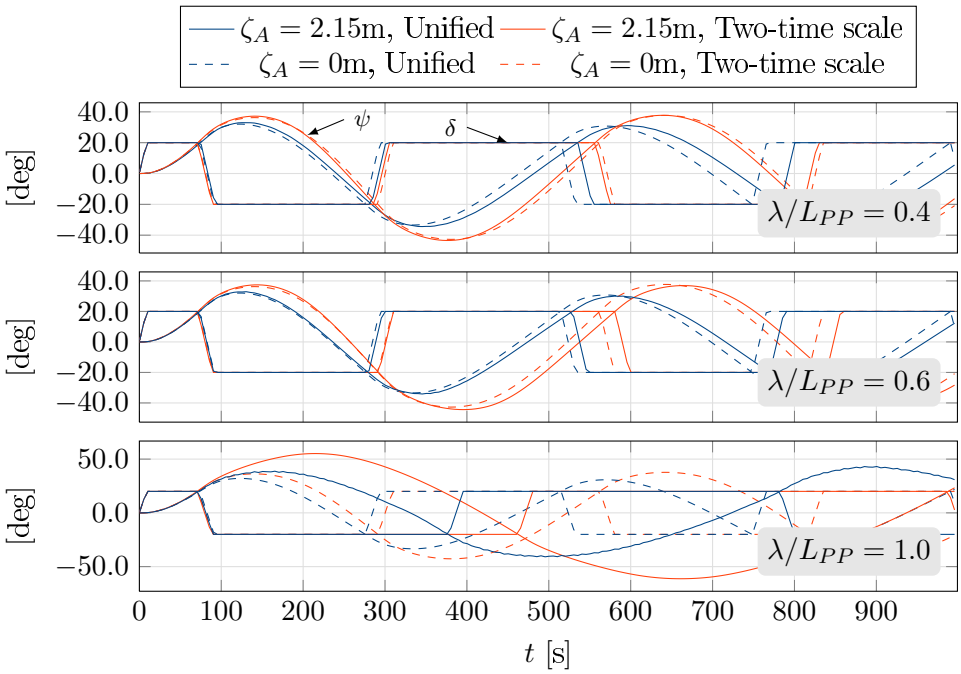

Figure C.13.: 20°/20° zig-zag maneuver of KVLCC2 in waves calculated with derivatives from Cura Hochbaum et al. [22]; $\eta = 180°$

Bibliography

[1] 26th ITTC Manoeuvring Committee. Validation of manoeuvring simulation models. Technical report, ITTC - Recommended Procedures and Guidelines, 2011.

[2] M. Abdel-Maksoud. Schiffsdynamik. Lecture Notes Hamburg University of Technology. in German.

[3] M. Abdel-Maksoud, M. Steden, and J. Hundemer. Design of a multi-component propulsor. In *28th Symposium on Naval Hydrodynamics*, Pasadena, USA, 2010.

[4] M. A. Abkowitz. *Lectures on Ship Hydrodynamics - Steering and Manoeuvrability.* Danish Technical Press, Lyngby, Denmark, 1964.

[5] J. Artyszuk. Wave effects in ship manoeuvring motion mm - a review analysis. In *International Conference on Marine Simulation and Ship Manoeuvrability, MARSIM*, 2003.

[6] P. Augener and H. Vorhölter. Determination of forces on offshore wind park installation vessels for dynamic positioning within the very early design stage. *Proceedings of the PRADS2013*, 2013.

[7] P. Bailey, W. Price, and P. Temarel. A unified mathematical model describing the manoeuvring of a ship travelling in a seaway. *Transactions of the Royal Institution of Naval Architects*, 140:131–149, 1997.

[8] M. Bauer and M. Abdel-Maksoud. A 3-d potential based boundary element method for the modelling and simulation of marine propeller flows. *7th Vienna Conference on Mathematical Modelling*, 2012.

[9] G. Benvenuto, S. Brizzolara, and M. Figari. Simulation of the propulsion system behaviour during ship standard manoeuvres. In *Proceedings of PRADS 2001, Conference on Practical design of ships and other floating structures*, 2001.

[10] N. Berchiche and C.-E. Janson. Flow simulation of a propeller in open water condition and experimental validation. In *8th Numerical Towing Tank Symposium*, 2005.

[11] S. Berger, M. Druckenbrod, M. Greve, L. Greitsch, and M. Abdel-Maksoud. An efficient method for the investigation of propeller hull interaction. In *14th Numerical Towing Tank Conference*, 2011.

[12] V. Bertram. *Practical Ship Hydrodynamics*. Butterworth-Heinemann, 2000.

[13] R. Bishop, R. Burcher, and W. Price. The fifth annual fairey lecture: On the linear representation of fluid forces and moments in unsteady flow. *Journal of Sound and Vibration*, 29:113–128, 1973.

[14] P. Blume. Experimentelle Bestimmung von Koeffizienten der wirksamen Rolldämpfung und ihre Anwendung zur Abschätzung extremer Rollwinkel. *Schiffstechnik*, 26:3–23, 1979. in German.

[15] P. Boese. Eine einfache Methode zur Berechnung der Widerstandserhöhung eines Schiffes im Seegang. *Schiffstechnik*, 17:29–35, 1970. in German.

[16] W. Bollay. *A New Theory for Wings of Small Aspect Ratio*. PhD thesis, California Institute of Technology, 1936.

[17] R. K. Burcher. Studies into the validity of quasi steady prediction techniques. *International Towing Tank Conference*, 14:404–407, 1975.

[18] M. S. Chislett and J. Strøm-Tejsen. Planar motion mechanism tests and full-scale steering and manoeuvring predictions for a mariner class vessel. Technical Report Hy-6, Hydro- og Aerodynamisk Laboratorium, Lyngby, Denmark, April 1965.

[19] G. Clauss, E. Lehmann, and C. Östergaard. *Meerestechnische Konstruktionen*. Springer-Verlag, 1988. in German.

[20] W. E. Cummins. The impulse response function and ship motions. *Schiffstechnik*, 47(9):101–109, 1962.

[21] A. Cura Hochbaum. Virtual pmm tests for manoeuvring prediction. In *26th Symposium on Naval Hydrodynamics*, 2006.

[22] A. Cura Hochbaum, M. Vogt, and S. Gatchell. Manoeuvring prediction for two tankers based on rans simulations. In *SIMMAN 2008 - Workshop on Verification and Validation of Ship Manoeuvring Simulation Methods*, 2008.

[23] M. Denis and W. Pierson. On the motions of ships in confused seas. *Transactions SNAME*, 61:280–357, 1953.

[24] O. Detlefsen. Enwicklung eines Verfahrens zur Simulation von Schiffsbewegungen und dynamischem Positionieren im Seegang unter Verwendung von Impuls-Antwort-Funktionen. Master's thesis, Hamburg University of Technology, 2014. in German.

[25] O. M. El Moctar. Viscous flow computations around rudders. In *1st Numerical Towing Tank Symposium*, 1998.

[26] O. M. El Moctar. *Numerische Berechnung von Strömungskräften beim Manövrieren von Schiffen*. PhD thesis, Hamburg University of Technology, 2001. in German.

[27] W. Eyberg. Berechnung einer selbsttätig adaptierenden Automation zur Minimierung des Treibstoffverbrauchs von Schiffsantrieben mit Verstellpropeller. *VDI-Verlag, Düsseldorf*, 1990. in German.

[28] O. M. Faltinsen. *Sea Loads on Ships and Offshore Structures*. Cambridge University Press, 1990.

[29] O. M. Faltinsen. *Hydrodynamics of High-Speed Marine Vehicles*. Cambridge University Press, 2005.

[30] O. M. Faltinsen, K. J. Minsaas, N. Liapsis, and S. O. Skj/ordal. Prediction of resistance and propulsion of a ship in a seaway. In *13th Symposium on Naval Hydrodynamics*, 1980.

[31] D. Fathi and J. R. Hoff. *ShipX Vessel Responses (VERES)*. Marintek AS, Trondheim, 2004.

[32] T. I. Fossen. A nonlinear unified state-space model for ship maneuvring and control in a seaway. *Journal of Bifurcation and Chaos*, 2005.

[33] T. I. Fossen. *Marine Craft Hydrodynamics and Motion Control*. John Wiley & Sons, Ltd, 2011.

[34] T. Gourlay, A. von Graefe, V. Shigunov, and E. Lataire. Comparison of aqwa, gl rankine, moses, octopus, pdstrip and wamit with model test results for cargo ship wave-induced motions in shallow water. In *34rd International Conference on Ocean, Offshore and Arctic Engineering (OMAE)*, 2015.

[35] D. S. Greeley and S. D. Willemann. Surface ship maneuvering forces in calm water and waves. *International Shipbuilding Progress*, 60:613–631, 2013.

[36] M. Greve, M. Abdel-Maksoud, S. Eder, and J. De Causmaecker. Unsteady viscous flow calculation around the kcs-model with and without propeller under consideration of the free surface. In *Workshop on CFD in Ship Hydrodynamics*, Gothenburg, Sweden, 2010.

[37] A. Gronarz. *Rechnerische Simulation der Schiffsbewegung beim Manövrieren unter besonderer Berücksichtigung der Abhängigkeit von der Wassertiefe*. PhD thesis, Gesamthochschule Duisburg, 1997. in German.

[38] U. Göttsche. Implementierung der instationären Randbedingung an der freien Wasseroberfläche in einem Randelementverfahren. Master's thesis, Hamburg University of Technology, 2014. in German.

[39] T. Haack. *Simulation des Manövrierverhaltens von Schiffen unter besonderer Berücksichtigung der Antriebsanlage*. PhD thesis, Hamburg University of Technology, 2006. in German.

[40] D. Hachmann. Calculation of pressures on a ship's hull in waves. *Ship Technology Research*, 38:111–133, 1991.

[41] S. Handschel, N. Köllisch, J. Soproni, and M. Abel-Maksoud. A numerical method for the estimation of ship roll damping for large amplitudes. In *29th Symposium on Naval Hydrodynamics*, 2012.

[42] M. Hanouneh. Ein Beitrag zur Untersuchung des dynamischen Verhaltens des Hauptantriebssystems von Schiffen unter besonderer Berücksichtigung der Umsteuerungsmanöver. Technical report, Fakultät der Ingenieurwissenschaften der Universität Rostock, 1997. in German.

[43] J. L. Hess. Calculation of potential flow about arbitrary three-dimensional lifting bodies. Technical Report MDC J5679/01, Douglas Aircraft Company, October 1972.

[44] Y. Himeno. Prediction of ship roll damping - state of the art. Technical report, The University of Michigan - The Department of Naval Architecture and Marine Engineering, 1981.

[45] M. Hirano, J. Takashina, K. Takeshi, and T. Saruta. Ship turning trajectory in regular waves. *Transactions of The West-Japan Society of Naval Architects*, 60:17–31, 1980.

[46] J. Holtrop and G. Mennen. An approximate power prediction method. *International Shipbuilding Progress*, 29:166–170, 1982.

[47] J. Hundemer. *Entwicklung eines Verfahrens zur Berechnung der instationären potenzialtheoretischen Propellerumströmung*. PhD thesis, Hamburg University of Technology, 2013. in German.

[48] International Maritime Organization (IMO). Explanatory notes to the standards for ship manoeuvrability. MSC/Circ.1053.

[49] International Maritime Organization (IMO). Interim standards for ship manoeuvrability. Resolution A.751(18).

[50] International Maritime Organization (IMO). Standards for ship manoeuvrability. Resolution A.137(76), 2002.

[51] ITTC. *Proceedings of the 15th ITTC*, The Hague, The Netherlands, May 1978.

[52] ITTC. *Proceedings of 25th ITTC. The Manoeuvring Committee. Final Report and Recommendations to the 25th ITTC*, volume 1, Fukuoka, 2008.

[53] ITTC. Testing and extrapolation methods manoeuvrability captive model test procedures. ITTC – Recommended Procedures and Guidelines, 2008.

[54] ITTC. *Proceedings of 26th ITTC. The Manoeuvring Committee. Final Report and Recommendations to the 26th ITTC*, volume 1, Rio de Janeiro, 2011.

[55] ITTC. *Proceedings of 26th ITTC. The Seakeeping Committee. Final Report and Recommendations to the 26th ITTC*, volume 1, Rio de Janeiro, 2011.

[56] G. Jensen, M. Klemt, and Y. Xing-Kaeding. On the way to the numerical basin for seakeeping and manoeuvring. In *9th Symposium on Practical Design of Ships and Other Floating Structures*, 2004.

[57] J. Journée and W. Massie. *Offshore Hydromechanics*. Delft University of Technology, 2001.

[58] J. Journée and J. Pinkster. *Introduction in Ship Hydromechanics*. Delft University of Technology, 2002.

[59] N. Koliha. Entwicklung eines 6DOF-Moduls auf Basis von Quaternionen zur Simulation freier Bewegungen schwimmender Körper. Bachelor's thesis. Hamburg University of Technology, 2011. in German.

[60] D. Kring and P. D. Sclavounos. Numerical stability analysis for time-domain ship motion simulations. *Journal of Ship Research*, 39:313–320, 1995.

[61] H.-P. Kröger. Simulation der Rollbewegung von Schiffen im Seegang. Technical Report 473, Institut für Schiffbau der Universität Hamburg, 1987. in German.

[62] S. Krüger. Manöversimulation auf der Basis von Großausführungsmessungen. *Jahrbuch der Schiffbautechnischen Gesellschaft*, 92:541–551, 1998. in German.

[63] S. Krüger. Manövrieren: Welche Ergebnisse kann man mit Streifenmethoden für naturgroße Schiffe erzielen? *Jahrbuch der Schiffbautechnischen Gesellschaft*, 108, 2014. in German.

[64] G. Kuiper. *The Wageningen Propeller Series*. MARIN, 1992.

[65] H. Lamb. *Hydrodynamics*. Dover Publications, Inc., 1945.

[66] C. E. Lan. A quasi-vortex-lattice method in thin wing theory. *Journal of Aircraft*, 11(9):518–527, 1974.

[67] L. Larson, F. Stern, and M. Visonneau, editors. *Gothenburg 2010, A Workshop on Numerical Ship Hydrodynamics*, 2010.

[68] S.-K. Lee, S.-H. Hwang, S.-W. Yun, K.-P. Rhee, and W.-J. Seong. An experimental study of a ship manoeuvrability in regular waves. In *International Conference on Marine Simulation and Ship Manoeuvrability, MARSIM*, 2009.

[69] S. Liapsis and R. Beck. Seakeeping computations using time-domain analysis. In *Proceedings of the Fourth International Conference on Numerical Ship Hydrodynamics*, pages 34–56. National Academy of Science, 1985.

[70] R.-Q. Lin, M. Hughes, and T. Smith. Prediction of ship steering capabilities with a fully nonlinear ship motion model. part 1: Maneuvering in calm water. *Journal of Marine Science and Technology*, 2010.

[71] R.-Q. Lin and W. Kuang. Modeling nonlinear roll damping with a self-consistent, strongly nonlinear ship motion model. *Journal of Marine Science and Technology*, 13:127–137, 2008.

[72] M. Manzke, K. Wöckner, J. Schoop-Zipfel, T. Rung, and M. Abdel-Maksoud. Efficient viscous simulation approaches to manoeuvering in seaways. *North Atlantic Treaty Organisation, Research and Technology Organisation, AVT- Specialists' Meeting on Assessment of Stability and Control Prediction Methods for Air and Sea Vehicles*, 2011.

[73] H. Maruo. The drift of a body floating on waves. *Journal of Ship Research*, 4(3):1–10, 1960.

[74] J. N. Newman. Some hydrodynamic aspects of ship maneuverablity. *Symposium on Naval Hydrodynamics*, 6:203–237, 1966.

[75] J. N. Newman. The drift force and moment on ships in waves. *Journal of Ship Research*, 11(11):51–60, 1967.

[76] J. N. Newman. *Marine Hydrodynamics*. The MIT Press, 1977.

[77] P. E. Nikravesh. *Computer-Aided Analysis of Mechanical Systems*. Prentice-Hall, 1988.

[78] K. Nomoto. Ship response in directional control taking account of frequency dependent hydrodynamic derivatives. *International Towing Tank Conference*, 14:408–413, 1975.

[79] T. Ogilvie. Recent progress towards the understanding and prediction of ship motions. *Proc. 5th Symposium on Naval Hydrodynamics*, 1964.

[80] P. Oltmann and K. Wolff. "Computerized Planar Motion Carriage" Anlagenbeschreibung und erste Betriebserfahrungen. *Jahrbuch der Schiffbautechnischen Gesellschaft*, 70:414–441, 1976. in German.

[81] J. F. Otzen and C. D. Simonsen, editors. *Workshop on Verification and Validation of Ship Manoeuvring Simulation Methods, SIMMAN*. FORCE Technology, 2014.

[82] T. Perez and T. I. Fossen. Identification of dynamic models of marine structures from frequency-domain data enforcing model structure and parameter constraints. Technical report, ARC Centre of Excellence for Complex Dynamic Systems and Control, 2009.

[83] A. B. Phillips, S. R. Turnock, and M. Furlong. Evaluation of manoeuvring coefficients of a self-propelled ship using a blade element momentum propeller model coupled to a reynolds averaged navier stokes flow solver. *Ocean Engineering*, 36:1217–1225, 2009.

[84] J. Pinkster. *Low Frequency Second Order Wave Exciting Forces on Floating Structures*. PhD thesis, Netherlands Ship Model Basin, 1980.

[85] F. Pérez and J. A. Clemente. Remarks about the mathematical problems in manoeuvrability. *WEGEMT Summer School - Manoeuvring and manoeuvring devices*, 36, 2001.

[86] A. Ross and T. I. Fossen. Identification of frequency-dependent viscous damping. In *Proceedings of OCEANS'05 MTS/IEEE*, 2005.

[87] N. Salvesen. Second oder steady state forces and moments on surface ships in oblique regular waves. In *International Symposium on the Dynamics of Marine Vehicles and Structures in Waves*, 1974.

[88] N. Salvesen, E. O. Tuck, and O. Faltinsen. Ship motions and sea loads. *SNAME Trans.*, 78:250–287, 1970.

[89] J. Schoop. Numerische Untersuchung des Einflusses der Wassertiefe auf das Manövrierverhalten einer vereinfachten Schiffsform. Master's thesis, Hamburg University of Technology, 2009. in German.

[90] J. Schoop-Zipfel and M. Abdel-Maksoud. A numerical model to determine ship manoeuvring motion in regular waves. In *4th International Conference on Computational Methods in Marine Engineering - MARINE 2011*, 2011.

[91] J. Schoop-Zipfel and M. Abdel-Maksoud. Einfluss der welleninduzierten Kräfte auf das Manövrierverhalten von Schiffen. *Jahrbuch der Schiffbautechnischen Gesellschaft*, 108, 2014. in German.

[92] J. Schoop-Zipfel and M. Abdel-Maksoud. Maneuvering in waves based on potential theory. In *33rd International Conference on Ocean, Offshore and Arctic Engineering (OMAE)*, 2014.

[93] J. Schoop-Zipfel, M. Abdel-Maksoud, and T. Rung. Numerical investigation of the influence of water depth on ship manoeuvring behaviour. In *13th Numerical Towing Tank Symposium*, 2010.

[94] J. Schoop-Zipfel, M. Abdel-Maksoud, and K. Tigges. Stopping simulations and sea trial measurements of a ship with diesel-electric propulsion and controllable pitch propellers. In *International Conference on Marine Simulation and Ship Manoeuvrability, MARSIM*, 2012.

[95] M.-G. Seo and Y. Kim. Numerical analysis on ship maneuvering coupled with ship motion in waves. *Ocean Engineering*, 38:1934–1945, 2011.

[96] R. Skejic. *Maneuvering and Seakeeping of a Single Ship and of Two Ships in Interaction*. PhD thesis, Norwegian University of Science and Technology, 2008.

[97] R. Skejic and O. M. Faltinsen. A unified seakeeping and maneuvering analysis of ships in regular waves. *Journal of Marine Science and Technology*, 13:371–394, 2008.

[98] K.-H. Son and K. Nomoto. On the coupled motion of steering and rolling of a high-speed container ship. *Naval Architecture and Ocean Engineering*, 20:73–83, 1982.

[99] F. Stern and K. Agdrup, editors. *Workshop on Verification and Validation of Ship Manoeuvring Simulation Methods, SIMMAN*. FORCE Technology, 2008.

[100] F. Stern, K. Agdrup, S. Kim, A. Cura Hochbaum, K. Rhee, F. Quadvlieg, P. Perdon, T. Hino, R. Broglia, and J. Gorski. Lessons learnt from the workshop on verification and validation of ship manoeuvring simulation methods - simman 2008. In *International Conference on Marine Simulation and Ship Manoeuvrability, MARSIM*, 2009.

[101] F. Stern, R. V. Wilson, H. W. Coleman, and E. G. Paterson. Comprehensive approach to verification and validation of cfd simulations—part 1: Methodology and procedures. *ASME Journal of Fluids Engineering*, 123:793–802, 2001.

[102] Y. J. Sung. Kvlcc2 pmm tests in deep water. Technical report, Hyundai Maritime Research Institute, 2012.

[103] H. Söding. Eine Modifikation der Streifenmethode. *Schiffstechnik*, 16:15–18, 1969. in German.

[104] H. Söding. Prediction of ship steering capabilities. *Schiffstechnik*, 29:3–29, 1982.

[105] H. Söding. Bewertung der Manövriereigenschaften im Entwurfsstadium. *Jahrbuch der Schiffbautechnischen Gesellschaft*, 78:179–204, 1984. in German.

[106] H. Söding. *Manoeuvring Technical Manual*, chapter Rudder, Fundamental Hydrodynamic Aspects, pages 74–95. Seehafen Verlag, 1993.

[107] H. Söding. Manövrierfähigkeit von Schiffen. Lecture Notes Hamburg University of Technology, 1995. in German.

[108] H. Söding. Limits of potential theory in rudder flow predictions. *Schiffstechnik*, 45:141–155, 1998.

[109] H. Söding. How to integrate free motions of solids in fluids. In *4th Numerical Towing Tank Symposium*, 2004.

[110] H. Söding. Towards fully non-linear floating body simulations by a potential method. In *International Conference on Ocean, Offshore and Arctic Engineering, OMAE*, volume 31, pages 539–549, 2012.

[111] H. Söding and V. Bertram. *Program PDSTRIP: Public Domain Strip Method*, August 2007. http://pdstrip.sourceforge.net/.

[112] M. Tello Ruiz, M. Candries, M. Vantorre, G. Delefortrie, D. Peeters, and F. Mostaert. Ship manoeuvring in waves: A literature review. WL Rapporten, 00.096 Version 2.0, Flanders Hydraulics Research & Ghent University, Antwerp, Belgium, 2012.

[113] The Society of Naval Architects and Marine Engineers. Nomenclature for treating the motion of a submerged body through a fluid. Technical and Research Bulletin No. 1-5, 1952.

[114] M. Ueno, T. Nimura, and H. Miyazaki. Experimental study on manoeuvring motion of a ship in waves. In *International Conference on Marine Simulation and Ship Manoeuvrability, MARSIM*, 2003.

[115] M. Ueno, T. Nimura, H. Miyazaki, K. Nonaka, and T. Haraguchi. Model experiment on steady wave forces and moment acting on a ship at rest. *The Kansai Society of Naval Architects, Japan*, 235:69–77, 2001.

[116] H. Vorhölter. *Numerische Analyse des Nachstroms und der Propellereffektivität am manövrierenden Schiff.* PhD thesis, Hamburg University of Technology, 2011. in German.

[117] F. Wirz. *Simulation und Optimierung des Notstopp-Manövers von Schiffen mit langsamlaufenden Zweitaktmotoren und Festpropellern.* PhD thesis, Hamburg University of Technology, 2011. in German.

[118] K. Wolff. Ermittlung der Manövriereigenschaften fünf repräsentativer Schiffstypen mit Hilfe von CPMC-Modellversuchen. Technical report, Institut für Schiffbau der Universität Hamburg, 1981. in German.

[119] K. Wöckner, M. Greve, M. Scharf, M. Abdel-Maksoud, and T. Rung. Unsteady viscous/inviscid coupling approaches for propeller-flow simulations. In *2nd International Symposium on Marine Ship Propellers smp'11*, 2011.

[120] Y. Xing-Kaeding. *Unified Approach to Ship Seakeeping and Maneuvering by a RANSE Method*. PhD thesis, Hamburg University of Technology, 2006.

[121] Y. Xu, T. Kinoshita, and H. Itakura. A pmm experimental research on ship maneuverability in waves. In *International Conference on Ocean, Offshore and Arctic Engineering, OMAE*, 2007.

[122] H. Yasukawa. Simulations of ship maneuvering in waves (1st report: turning motion). *Journal of the Japan Society of Naval Architects and Ocean Engineers*, 4:127–136, 2006. in Japanese.

[123] H. Yasukawa. Simulations of wave-induced motions of a turning ship. *Journal of the Japan Society of Naval Architects and Ocean Engineers*, 4:117–126, 2006. in Japanese.

[124] H. Yasukawa and Y. Nakayama. 6-dof motion simulations of a turning ship in regular waves. In *International Conference on Marine Simulation and Ship Manoeuvrability, MARSIM*, 2009.

[125] H. Yasukawa and Y. Yoshimura. Introduction of mmg standard method for ship maneuvering predictions. *Journal of Marine Science and Technology*, pages 1–16, 2014.

[126] T.-G. Yen, S. Zhang, K. Weems, and W.-M. Lin. Development and validation of numerical simulations for ship maneuvering in calm water and in waves. *28th Symposium on Naval Hydrodynamics*, 28:12–27, 2010.

[127] Y. Yoshimura and M. Ueno. Circular motion tests (cmt) and pmm test program for kvlcc1 and kvlcc2 in deep water at nmri. Technical report, National Maritime Research Institute (NMRI), Japan, 2007.

[128] W. Zheng. Entwicklung eines in Echtzeit lauffähigen Simulationsmodells für das System Schiff, Motor, Kombinator und Verstellpropeller. *VDI-Verlag, Düsseldorf*, 1991. in German.

[129] R. Zinkmann. Development of an efficient procedure for determination of manoeuvring coefficients based on cfd-methods. Master's thesis, Hamburg University of Technology, 2013.